



TECHNISCHE
UNIVERSITÄT
WIEN

DISSERTATION

Investigation of Electrochemical Migration and Dendrite Growth in Microelectronic Devices

ausgeführt zum Zwecke der Erlangung des akademischen Grades
eines Doktors der Naturwissenschaften unter der Leitung von

Ao. Univ.-Prof. Dipl.-Ing. Dr.techn. Günter FAFILEK
E164 - Institute of Chemical Technologies and Analytics

eingereicht an der Technischen Universität Wien
Fakultät für Technische Chemie

von

Maximilian MAYR, MSc.

Mat-Nr.: 01426129

Wien, 24. September 2024

Maximilian MAYR

Eidesstattliche Erklärung:

Ich erkläre an Eides statt, dass die vorliegende Arbeit nach den anerkannten Grundsätzen für wissenschaftliche Abhandlungen von mir selbstständig erstellt wurde. Alle verwendeten Hilfsmittel, insbesondere die zugrunde gelegte Literatur, sind in dieser Arbeit genannt und aufgelistet. Die aus den Quellen wörtlich entnommenen Stellen sind als solche kenntlich gemacht. Das Thema dieser Arbeit wurde von mir bisher weder im In- noch Ausland einer Beurteilerin/einem Beurteiler zur Begutachtung in irgendeiner Form als Prüfungsarbeit vorgelegt. Diese Arbeit stimmt mit der von den Begutachterinnen/Begutachtern beurteilten Arbeit überein.

Ich nehme zur Kenntnis, dass die vorgelegte Arbeit mit geeigneten und dem derzeitigen Stand der Technik entsprechenden Mitteln (Plagiat-Erkennungssoftware) elektronisch-technisch überprüft wird. Dies stellt einerseits sicher, dass bei der Erstellung der vorgelegten Arbeit die hohen Qualitätsvorgaben im Rahmen der geltenden Regeln zur Sicherung guter wissenschaftlicher Praxis "Code of Conduct" an der TU Wien eingehalten wurden. Zum anderen werden durch einen Abgleich mit anderen studentischen Abschlussarbeiten Verletzungen meines persönlichen Urheberrechts vermieden.

Maximilian MAYR

Acknowledgments

Without you, this work would not exist.

I feel indebted to many people, who have supported me in one way or another so I could come to this point. At times, working on this thesis felt like a roller coaster ride, but with your help I managed to finalize this work.

First and foremost I would like to express my gratitude to my supervisor, Günter Faflek. Your calm attitude and technical knowledge were invaluable. Countless hours of discussions, both professional and casual, lie at the heart of this work.

Another fundamental pillar of support was my research group. Spanning from scientific discussions and technical advice, via fun and relaxing lunch and coffee breaks, to a variety of entertaining leisure activities, you made this time worthwhile. Thank you very much, Andreas, Fabian, Florian, Jakob, Jasmin, Jie, Kathi, Lars, Michael, Sunil, and Thomas.

Throughout this thesis, I worked closely with employees of our cooperation partner. I thank all those who contributed in one way or the other. Special thanks go to Paola and Hasan for the enormous effort we spent on progressing this difficult research topic. It was a pleasure.

You can only achieve a good work-life balance with true friends at your side. I consider myself lucky to have many friends who have been with me for years and who often cheer me up with their presence alone.

I am immensely grateful for having met my partner during the time I spent working for my thesis. Thank you, Viktoria, for believing in me and giving me strength when I needed it. Let us see where our journey together will take us.

Lastly, I want to express my deepest gratitude to my family whose support throughout my studies has been unequivocal and unending. I dedicate this work to my grandparents, both those who are still alive and those who are unfortunately no longer able to experience (the final stage of) this important stage in my career in person. You have shown me love and care that have shaped me like little else. Thank you for being proud of the person I am today.

Abstract

The optimization and miniaturization of semiconductor and microelectronic components lead to ever-increasing demands, especially under extreme operating conditions such as high voltages, temperature, humidity, and contamination. These components consist of various materials, ranging from metals and semiconductors to (in)organic insulators, which facilitate numerous undesirable processes and reactions. One example is the formation of metallic, electrically conductive dendrites, which can cause short circuits and thus component failure. To ensure reliability, it is crucial to understand the reactions in these components caused by external influences.

In this regard, the present work introduces a model and physical/chemical mechanisms that go beyond previous predominantly statistical or phenomenological descriptions. The consideration of ion migration in polymers and electrochemical processes at interfaces contributes to elucidating the causes of failure in microelectronic components, particularly dendrite formation in polymer insulators. The combination of methods enables the quantitative correlation of various influencing parameters with breakdown behavior. For this purpose, high-resolution current measurements are linked with concentration profiles and supported by simulation calculations. Distinguishing between ionic and electronic currents in polymer coatings is difficult, and the influence of ions is often neglected. The method used here allows for estimating the ionic contribution.

This study examined the corrosion mechanisms of copper and the behavior of polyimide coatings under accelerated corrosion conditions, in the form of electrical stress and ionic contamination. Both materials are widely used in today's microelectronics. Experiments were conducted using three different setups to investigate the corrosion and dendrite growth behavior of copper, as well as the penetration of metallic cations into organic coatings and the resulting insulation loss.

The analysis showed that in samples exposed to $\text{AgNO}_{3(\text{aq})}$, the current was predominantly caused by ions. The permeation behavior of three cations in high electric fields ($\sim 70 \text{ MV } \mu\text{m}^{-1}$) was also studied, with Ag^+ exhibiting the highest mobility in the polymer coating, followed by K^+ and Cu^{2+} . The type of cation significantly influenced the current and the time to failure during electrical stress tests. Under certain conditions, ionic contaminants play a crucial role in material failure.

Kurzfassung

Die Optimierung und Miniaturisierung von Halbleiter- und Mikroelektronikbauteilen führt zu stetig steigenden Anforderungen, insbesondere bei extremen Betriebsbedingungen: hohen Spannungen, Temperaturen, Feuchtigkeit und Verunreinigungen. Diese Bauteile bestehen aus verschiedenen Materialien, von Metallen über Halbleiter bis hin zu (an)organischen Isolatoren, was zahlreiche unerwünschte Prozesse und Reaktionen ermöglicht. Ein Beispiel ist die Bildung metallischer, elektrisch leitender Dendriten, die Kurzschlüsse und damit das Bauteilversagen verursachen können. Um die Zuverlässigkeit sicherzustellen, ist es entscheidend, die durch äußere Einflüsse verursachten Reaktionen in diesen Bauelementen zu verstehen.

Die vorliegende Arbeit stellt dahingehend ein Modell und physikalisch/chemische Mechanismen vor, die über bisherige, überwiegend statistische oder phänomenologische, Beschreibungen hinausgehen. Die Berücksichtigung von Ionenmigration in Polymeren und elektrochemischer Prozesse an den Grenzflächen leistet einen bedeutenden Beitrag zur Aufklärung der Ursachen des Versagens mikroelektronischer Bauteile, insbesondere der Dendritenbildung in Polymerisolatoren. Die Kombination von Untersuchungsmethoden ermöglicht es, verschiedene Einflussparameter quantitativ mit dem Durchbruchverhalten zu korrelieren. Dazu werden hoch aufgelöste Strommessungen mit gemessenen Konzentrationsprofilen verknüpft und durch Simulationsrechnungen unterstützt. Die Unterscheidung ionischer und elektronischer Ströme in Polymerbeschichtungen ist schwierig, und der Einfluss von Ionen wird oft vernachlässigt. Die hier verwendete Methode ermöglicht es, den ionischen Beitrag abzuschätzen.

Diese Studie untersuchte die Korrosionsmechanismen von Kupfer und das Verhalten von Polyimidbeschichtungen unter beschleunigten Korrosionsbedingungen, in Form elektrischen Stresses und ionischer Verunreinigungen. Beide Materialien sind in der heutigen Mikroelektronik weit verbreitet. Es wurden Experimente mit drei unterschiedlichen Aufbauten durchgeführt, um das Korrosions- und Dendritenwachstumsverhalten von Kupfer, sowie das Eindringen metallischer Kationen in organische Beschichtungen und den daraus resultierenden Isolationsverlust zu untersuchen.

Die Analyse zeigte, dass bei Proben, die $\text{AgNO}_3(\text{aq})$ ausgesetzt wurden, der Strom überwiegend durch Ionen verursacht wird. Auch das Permeationsverhalten dreier Kationen in hohen elektrischen Feldern ($\sim 70 \text{ MV } \mu\text{m}^{-1}$) wurde untersucht, wobei Ag^+ die höchste Mobilität in

der Polymerbeschichtung aufweist, gefolgt von K^+ und Cu^{2+} . Der Kationentyp beeinflusste den Strom und die Zeit bis zum Ausfall während elektrischer Stresstests maßgeblich. Unter bestimmten Bedingungen spielen ionische Verunreinigungen eine entscheidende Rolle beim Materialversagen.

Contents

1	Introduction	1
2	Theoretical background	3
2.1	Reliability in (micro-) electronic devices	3
2.2	General introduction to corrosion and electrochemistry	6
2.2.1	Thermodynamic aspects	7
2.2.2	2- and 3-electrode setup, potentiostat	13
2.2.3	Kinetic aspects	16
2.2.4	Mass transport	18
2.3	Corrosion of silver and copper	22
2.3.1	Fundamentals of copper and silver corrosion	22
2.3.2	Electrochemical migration and dendrite growth	23
2.4	Polyimides	30
2.4.1	PI - applications	30
2.4.2	PI - chemical structure and properties	30
2.4.3	PI - electrical properties and charge transport	31
2.5	Laser Ablation - Inductively Coupled Plasma - Mass Spectrometry	41
2.5.1	LA-ICP-MS - working principle	41
2.5.2	LA-ICP-MS - advantages and disadvantages	42
2.5.3	LA-ICP-MS - quantification	42
2.6	Electrochemical Impedance Spectroscopy	43
3	Experimental and simulation	47
3.1	Thin Layer Cell	47
3.1.1	TLC - cell design	48
3.1.2	TLC - Making of RE	49
3.1.3	TLC - measurement procedure	51
3.2	Miniaturized Test Chip	51
3.2.1	MTC – sample design	51
3.3	1x1 Interdigitated Test Chip	53
3.3.1	ITC - sample design	54
3.3.2	ITC - cell design	55

3.3.3	ITC - measurement procedure	55
3.4	Laser Ablation - Inductively Coupled Plasma - Mass Spectrometry	58
3.5	Simulation	62
3.5.1	Copper corrosion model (2D)	62
3.5.2	Polymer ion migration and species diffusion model (1D)	63
4	Results and discussion	67
4.1	Thin Layer Cell	67
4.1.1	TLC - experimental	67
4.1.2	TLC - simulation	71
4.2	Miniaturized Test Chip	74
4.2.1	Open MTC (without PI coverage)	74
4.2.2	MTC with PI coverage	75
4.3	1x1 Interdigitated Test Chip	77
4.3.1	ITC - experimental	78
4.3.2	ITC - simulation	101
5	Main findings and conclusion	109
	Bibliography	113
	List of Figures	137
	List of Abbreviations	147
	Appendix	149

1 Introduction

'Corrosion is a major issue for the increase of service life and reliability of metallic materials. A detailed understanding of the mechanisms of corrosion is necessary to solve existing corrosion problems and to prevent future problems.' (Marcus¹, p. *vii*) This citation summarizes the motivation that guided this work in a precise manner. The cost of corrosion is estimated at around 3-4 % of the gross domestic product for different nations.²

One field in which corrosion, conductive filament formation and material degradation play a role is electronics. Stability and reliability of electronic components are crucial for consumers and producers. External environmental influences, such as electrical bias or humidity, are enablers of corrosion processes and lead to accelerated failure. One example is the field-driven electrochemical migration (ECM) of copper (Cu), a material that is widely used for electrical connections. Ionic impurities and the migration of ions in an electric field can drive corrosion processes and ultimately lead to component failure.^{3,4}

The materials investigated in this thesis are such that are typically used in semiconductor devices, especially in high power devices. Metallizations play a key role in these devices, as they function as electric conductors. Encapsulations, for example mold compound or polymer films, are used to encase them and protect them electrically, mechanically and from hazardous environments. However, these materials are imperfect barriers against ion intrusion, and can also degrade over time.^{3,5} It is therefore of interest to better understand ion motion in and the interaction of ions with the encapsulating materials. While insufficient at times at the scale of years of service, the good insulation properties of these materials make their investigation in the laboratory far from trivial and available research on this topic is often contradictory.⁶

In recent years modeling and simulation have received ever increasing attention, as computing power is increasingly easily available. With the aid of models, hypotheses can be challenged and adapted. This leads to better predictability and furthers the in-depth understanding of underlying processes.⁷⁻¹⁰

The aims of this thesis were twofold.

First of, since corrosion is a multifaceted, complex topic, a solid understanding of the basic aqueous electrochemistry of Cu was needed. To this end, the so-called Thin Layer Cell (TLC) was employed. This cell consisted of two Cu plates with a defined gap distance that was filled with an electrolyte. This setup allowed for a controlled environment with limited

electrolyte supply. Application of bias and optical images allowed to control and monitor the corrosion behavior. An electrochemical simulation model was created based on literature and the experimental findings (section 4.1). In addition, experiments on simplified micro-electronic Cu structures without polymer protection were performed. These are described in the Miniaturized Test Chip (MTC) section (section 4.2).

Secondly, a setup and procedure was desired, that allows to drive ionic contaminants into polyimide (PI) protection layers in a controlled manner. This allows to investigate their migration behavior and the impact on time-dependent dielectric breakdown (BD). This was the integral part of this thesis. Experiments on the MTC with PI coating failed due to unwanted corrosion near the bond pad (section 4.2). A new cell was developed for a different test structure, the 1x1 Interdigitated Test Chip (ITC). The 1x1 Interdigitated Test Chip (ITC) consisted of a Cu interdigitated electrode (IDE) structure that was protected by a PI coating. With this cell, an electrolyte could be placed atop the sample, and bias applied between an electrode in the electrolyte and the IDE structure. Continuous current density-versus-time (i - t) data logging, combined with Electrochemical Impedance Spectroscopy (EIS) measurements during the electrical stress tests, provided critical inputs. Additionally, Laser Ablation - Inductively Coupled Plasma - Mass Spectrometry (LA-ICP-MS) measurements after the tests offered further insights. Together, these methods helped understand the migration behavior of the ionic contaminants into and within the organic coating. To further the understanding, a simulation model was developed for this setup, as well (section 4.3).

This work begins by introducing theoretical fundamentals and state-of-the-art knowledge on a variety of relevant topics, as well as the basics of the used electrochemical and analytical methods (chapter 2 - Theoretical background). Following this, the used setups, samples and measurement parameters are introduced, along with the finite element method (FEM) simulation models (chapter 3 - Experimental and simulation). In the next chapter, experimental results are presented and discussed. Findings from the simulations are shown and used to support hypotheses and extract additional information based on the experiments (chapter 4 - Results and discussion). In the final chapter, the main findings are summarized, open questions are addressed, and an outlook on possible future work is provided (chapter 5 - Main findings and conclusion).

2 Theoretical background

This chapter provides the theoretical basis for understanding the work carried out as part of this dissertation and for the interpretation of the results. Entire books have been dedicated to (aspects of) each of the sections of this chapter. This work therefore does not aim to provide an in-depth explanation of all the theoretical foundations, but key aspects are introduced and, when little detail is given, further reading is suggested for the interested reader.

In the first section, a basic overview of reliability in electronic devices is presented (2.1), elaborating in more detail on the motivation described previously in the introduction for the studies conducted in this thesis. Thereafter, concepts of electrochemistry and corrosion are introduced (2.2). An important part of this chapter is a description of mass transport mechanisms and phenomena, which are crucial for this work (section 2.2.4). Important aspects of corrosion of silver and copper will be described (section 2.3), followed by an overview of key aspects regarding polyimides (section 2.4). Additionally, the theoretical basis and some applications of two important experimental techniques in this work are presented: Laser Ablation - Inductively Coupled Plasma - Mass Spectrometry (section 2.5), and Electrochemical Impedance Spectroscopy (section 2.6).

2.1 Reliability in (micro-) electronic devices

Reliability of a product, as well as the predictability of the same, are of crucial importance in today's industry, both for producers, as well as for consumers. This is especially true in the field of electronics, in which the progressive miniaturization of components and devices poses ever new challenges in this regard. The term reliability is defined in Ohring and Kasprzak¹¹, p. 15, 'as the probability of operating a product for a given time period under specified conditions without failure'. Meaningful and precise forecasting of the (un-) reliability is a difficult endeavor. No unified approach to tackle this problem exists, since many internal and external parameters play a role, ranging from base materials and material combinations to temperature and bias, to name a few.^{11,12}

In a similar vein, already the meaning of 'failure' can strongly vary, depending on the different requirements and applications. In a broad definition of this term, Ohring and Kasprzak¹¹, p. 20 state that a 'failure consists of a transition from reliable to failed states'. One common depiction of general failure rate is the so-called bathtub curve (figure 2.1). This curve il-

illustrates different time spans during product life, during which different failure types are predominant. In the early life of a product, a decreasing failure rate is observed. The failures in this category stem mostly from extrinsic causes, such as defective raw materials, or improper handling. In the second region the failure rate remains roughly constant. Random causes can cause the otherwise good product to fail. In the last region, hazard rates increase once again. Failures in this region are dominated by wear-out effects, meaning that aging of the product and its materials ultimately leads to failure. The latter region is the one that is of interest in this work.¹³

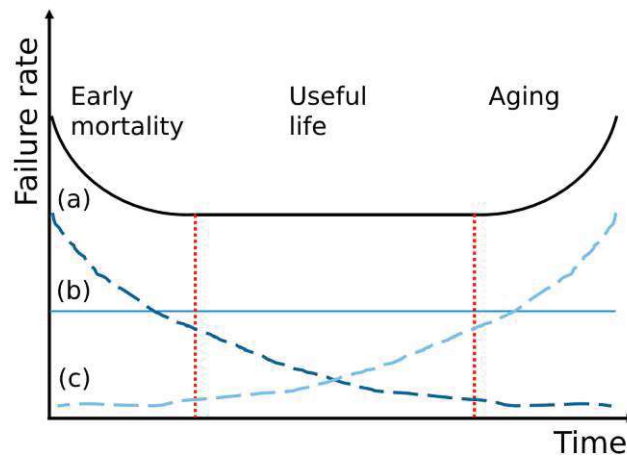


FIGURE 2.1: Schematic drawing of the bathtub curve. Three different regions can be identified in this curve. In each region a different failure type is dominant: (left) extrinsic failures (a), (mid) intrinsic failures (b), (right) wear-out or aging failures (c) dominate. The linear combination of the three failure types results in the bathtub shaped curve. Adapted from Kuo et al.¹³, figure 3.1.

The form that a failure takes is referred to as the failure mode and the how of the occurrence as failure mechanism.¹⁴ Pecht and Gu¹² present a classification into six wear-out failure mechanisms, by which electronics fail:

1. **Fatigue:** often results in fracture, driven by thermal cyclic loads and mechanical vibration.⁴
2. **Corrosion:** can result in electrical shorts or contact loss. Driving factors are, for example, electric fields, humidity and ion mobility. Corrosion is described in detail in sections 2.2 and 2.3.
3. **Electromigration:** describes the movement of atoms, caused by momentum transfer of electrons. Results in hillock or void formation, and in the latter case in open circuits.⁴
4. **Conductive filament formation:** similarly to corrosion, this is a failure observed between metallizations by the formation of a conductive filament. It is also referred to as conductive anodic filament (CAF) formation. It involves the sub-surface growth of

conductive filaments, primarily a copper containing salt, from the anode to the cathode, along a glass/epoxy interface.¹⁵ This phenomenon typically occurs under the influence of an electrical bias in the presence of moisture and is facilitated by the electrochemical migration of metal ions.¹⁴ It was first observed in the 1970s and has still received attention in recent years.^{16,17} A review on this topic is given by Turbini¹⁵.

5. **Stress driven diffusion voiding:** results in open circuits, due to residual stresses, e.g. from manufacturing.⁴
6. **Time dependent dielectric BD:** leads to insulation loss of a dielectric below its breakdown strength. It is influenced by temperature and electrical stress.⁴ This failure mechanism is discussed in more depth in section 2.4.

It should be noted, that the authors do not claim that this list encompasses all existing wear-out mechanisms, but offers only some examples. For the purpose of this work, corrosion, conductive filament formation and time dependent dielectric breakdown are considered to play the most important role. Based on this classification, a recent review of existing models for the description of (time to) failure was put together by Gabriel and Huitink⁴. Suhir¹⁸ addresses the question of electronics reliability in a more generalized way, by presenting the probabilistic design for reliability concept. For the interested reader these works serve as a good starting point to delve into reliability and reliability modeling. In their review, the authors (Gabriel and Huitink⁴) point out the state-of-the-art and shortcomings in this field. For corrosion, they emphasize the lack of consistent standard test procedures and that physics of failure (PoF) (i.e. failure origin) oriented methods have received low attention in this field. With regards to time dependent dielectric breakdown they note a lack of reliability models that consider the effect of field non-uniformity. In general, the authors believe that the combination of experiments, finite element modeling and data-driven prognostics will help to advance in this field.

The aim of reliability modeling is often to find an acceleration factor to predict a real-world device's lifetime based on (laboratory) experiments. A key parameter that is commonly determined is the time-to-failure (TTF), that is the time that passes until the failure condition is met. Two main approaches for reliability prediction exist: the empirical (or traditional) approach and the physics of failure approach. The prior is based on statistics inferred from (historical) reliability databases.¹⁹ This kind of approach has been widely criticized, e.g. by Sinnadurai et al.²⁰. Today, PoF approaches are increasingly important in the reliability of electronics. This demonstrates the need for a sound understanding of the underlying physics (and although omitted from the name, chemistry) of the failure mechanisms. An introduction to this approach is given in Pecht and Dasgupta¹⁴ and further elaborated in Pecht and Gu¹². In Hanif et al.²¹, table II, a comparison between different lifetime prediction methods is given. It shows that, while a PoF approach provides valuable information for predicting expected

lifetime, it requires extensive testing and generation of knowledge, especially in complex systems. This explains, why the traditional approach is still often used. Also for this reason, PoF models often are very specifically tailored to certain needs, and not easily adapted to or not too predictive for other problems.

A commonly used probability distribution function to describe failure rates (or probabilities) is the Weibull distribution. The Weibull distribution is a two-parameter distribution with a time scale parameter, α , and a shape parameter, β . Both parameters are (fitted) constants with values greater than zero. The Weibull probability and cumulative distribution functions, as well as the failure or hazard rate, are given in equation (2.1), (2.2) and (2.3).

$$f(t) = \frac{\beta t^{\beta-1} \exp(-(t/\alpha)^\beta)}{\alpha^\beta} \quad (2.1)$$

$$F(t) = 1 - \exp(-(t/\alpha)^\beta) \quad (2.2)$$

$$\lambda(t) = \frac{\beta t^{\beta-1}}{\alpha^\beta}. \quad (2.3)$$

With this distribution, all three failure types in figure 2.1 can be described: early failures ($\beta < 1$), constant failure rate ($\beta = 1$) and wear out failures ($\beta > 1$). The parameters are obtained by estimating and then fitting them to the experimental data.¹¹

A somewhat dated, but still useful overview over the different approaches for reliability modeling is given in Foucher et al.²². For an up-to-date work on the topic of reliability prediction for microelectronics, a recent book on this topic is recommended (Bernstein et al.¹⁹, Reliability Prediction for Microelectronics).

2.2 General introduction to corrosion and electrochemistry

In a very general definition, corrosion is described in Stansbury and Buchanan²³, p. 1, as "the deterioration of materials due to reactions with their environments". This definition spans all kinds of materials, from metals to organic species such as polymers. The best common knowledge example for a corrosion process is the formation of rust (Fe_2O_3) on iron (Fe), which is described by the following process:



In the above chemical reaction, iron reacts with its environment (oxygen (O_2) in the air, and water (H_2O) that can be present, e.g. in the form of moisture), to form a hydroxide. In an electrochemical process, the Fe metal loses electrons, i.e. it is oxidized ($\text{Fe} \longrightarrow \text{Fe}^{3+} + 3\text{e}^-$).

The reverse process in which a species, for example oxygen, gains one or more electrons is referred to as reduction. In general, for electrochemical corrosion to occur, three prerequisites must be fulfilled:^{23–26}

1. **Electrolyte:** An electrolyte is a conductive solution that allows the flow of ions. Water containing dissolved salts, acids, or bases serves as the electrolyte in most corrosion processes. The electrolyte allows for the movement of ions between the anode and cathode, enabling the electrochemical reactions.
2. **Electron pathway:** For corrosion to occur, there must be an electron conducting path that allows the flow of electrons from the anode to the cathode. This pathway is often the metal itself that is undergoing corrosion.
3. **Presence of anode and cathode:** When electron conducting sites (electrodes) are surrounded by an electrolyte, a potential difference exists at the interface between the surface and the electrolyte. Upon contacting two such sites with an electron conductor, the difference in potential between the two causes the flow of a current. The anode is the site at which oxidation occurs, i.e. a surplus of electrons is generated. An example for this is the oxidation of Fe in the previous example. The cathode is the site at which reduction takes place, i.e. electrons are transferred to the more noble species here.

Based on the mentioned points, one can develop strategies to mitigate corrosion, e.g. by application of coatings to prevent the formation of electrolyte layers on components.¹ However, in hazardous environments, these coatings can lose their protection ability with time, enabling corrosion processes.²⁷

2.2.1 Thermodynamic aspects

Nernst equation

The simplest electrochemical (half) cell consists of an electrode and an ion conductor (electrolyte). At the interface between the two, after a short time, an equilibrium will be reached between ion dissolution and ion deposition. The driving force behind this phenomenon is the so-called electrochemical potential, μ_i^* , which extends the chemical potential by a term for the electric work and is thus described by equation (2.4)

$$\mu_i^* = \left(\frac{\partial G}{\partial n_i} \right)_{p,T,n_j} = \mu_i^0 + RT \ln a_i + z_i F \phi_i \quad (2.4)$$

where

- $\frac{\partial G}{\partial n_i}$ is the partial derivative of the Gibbs free energy of the system with respect to the number of moles of species i , n_i , at constant temperature, pressure and number of moles of all other components, $n_{j \neq i}$.
- μ_i^0 is the standard chemical potential of ion species i (in $J \cdot mol^{-1}$), representing the chemical potential when the ion is in its standard state.
- R is the universal gas constant ($8.314 J \cdot mol^{-1} \cdot K^{-1}$).
- T is the absolute temperature (in K).
- z_i is the charge number of ion species i , representing the number of elementary charges carried by the ion.
- a_i is the activity of the species, which reflects its effective concentration in the solution.
- F is the Faraday constant ($96485 C \cdot mol^{-1}$), the charge of one mole of electrons.
- ϕ_i is the (inner) electric potential of phase i (in V).

Once the system is in equilibrium, the rates of dissolution and deposition will be equal. This means, that the electrochemical potentials of the oxidized species, μ_o^* , and the reduced species, μ_r^* , will be the same.²⁵

$$\mu_o^* = \mu_o^0 + RT \ln a_o + zF\phi_S = \mu_r^0 + RT \ln a_r + zF\phi_C = \mu_r^* \quad (2.5)$$

ϕ_S is the inner potential of the solution phase, and ϕ_C is the inner potential of the conductor (i.e. the electrode). The difference between the two is the (equilibrium) Galvani potential, $\Delta\phi$, and can be arrived at by rearranging equation (2.5):

$$\Delta\phi = \phi_C - \phi_S = \frac{\mu_o^0 - \mu_r^0}{zF} + \frac{RT}{zF} \ln \frac{a_o}{a_r} \quad (2.6)$$

Since μ_o^0 and μ_r^0 represent standard states, the first term is summed up as $\Delta\phi^0$, the standard potential of the given reaction for the given electrode, which leads to:

$$\Delta\phi = \Delta\phi^0 + \frac{RT}{zF} \ln \frac{a_o}{a_r} \quad (2.7)$$

This equation (equation (2.7)) is called Nernst equation, named in honor of Walther Nernst, who first formulated an equation of this form. The equation can be extended to include multiple educts and reaction products. If $\frac{a_o}{a_r} = 1$, the logarithm will be 0 and the second term is eliminated. Thus, one obtains the standard Galvani potential of the given reaction for the given electrode. With the Nernst equation, one can calculate the expected equilibrium

potential for different electrochemical reactions and it is one of the most fundamental equations in the field of electrochemistry.^{1,25,26,28–30} An example for its usage is also given in the subsection on Pourbaix diagrams, later in this chapter.

The electrochemical series

It is not possible to measure the absolute electric potential difference between the electrode and the ion conductor. One can only measure such potentials relative to a reference point, i.e. another potential. A second half-cell, consisting of electrode and ion conductor, is therefore needed. When two electrodes come in contact, however, a contact potential forms at the contact point between the two metals. To reflect this influence, the term electrode potential, E , is introduced to describe an electrode in contact with an arbitrary second 'reference' electrode. It is given as

$$E = \Delta\phi^{C,S} + \phi^{C,C_R} + \phi^{C_R,S_R} \quad (2.8)$$

where, like before, C and S denote the conductor and the solution, and R denotes the reference. ϕ^{C,C_R} is therefore the contact potential between the two electrodes. Since the second and third term in this equation depend on the reference, they can be considered constant, if the same reference is used to investigate different electrodes, resulting in^{25,28}

$$E = \Delta\phi^{C,S} + const \quad (2.9)$$

In order to have comparability between different potential measurements, a common reference point is needed. The standard hydrogen electrode (SHE) is accepted as the primary reference electrode (RE). The standard potential, $\Delta\phi$, of the reaction in this half-cell (hydrogen evolution reaction (HER), equation (2.10)) is, per definition, 0 V.^{1,23}



An exemplary schematic measurement setup of an electrochemical cell for determination of the (standard) electrode potential is given in figure 2.2. In general terms, an electrochemical cell consists of two (or more) electrodes parted by one (or more) electrolyte phase(s).

With the setup shown in the figure, the (standard) electrode potential for the reaction



can be determined via the connected voltmeter. If the activity of the Fe^{2+} ions is 1, the standard electrode potential, E^0 , is obtained (−0.447 V).³¹

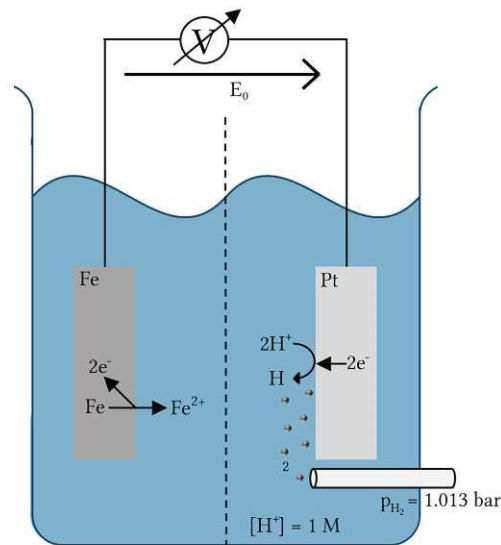


FIGURE 2.2: Exemplary schematic of a measurement setup for the determination of the (standard) electrode potential. In the right half-cell, the standard hydrogen electrode is shown. In the left half-cell the $\text{Fe}|\text{Fe}^{2+}$ electrode is presented. A diaphragm (black dashed line in the center) separates the two half cells. Both half-cells are connected electrically to form an electrochemical cell. Graphic adapted from Marcus¹, p. 22.

The electrochemical series is a collection of standard reduction potentials with respect to the SHE. The more positive a value, the more noble (i.e. more corrosion resistant) the species. The more negative a value, the more ignoble (i.e. more prone to corrosion) the species. This can be well understood based on the relationship between the standard free-energy change, ΔG^0 , and the standard electrode potential (w.r.t. the SHE), E^0 , described in equation (2.12)

$$\Delta G^0 = -nFE^0 \quad (2.12)$$

where n denotes the number of moles of electrons transferred in the redox reaction. This relationship does also hold true for conditions, that are not equal to the standard conditions. $\Delta G < 0$ indicates, that a reaction is energetically favorable (spontaneous), $\Delta G > 0$ is energetically unfavorable and $\Delta G = 0$ means that the reaction is in equilibrium.^{23,28}

It is important to keep in mind, that these values are calculated for standard conditions and that reaction kinetics are not considered here. In table 2.1 an excerpt of the electrochemical series is presented, containing reactions, that are of interest in this work.

A detailed listing of standard reduction potentials with respect to the SHE in the electrochemical series can be found in Vanysek³¹, Table 1-3. More information on the usage of REs is provided in the subsection on 3-electrode setups (2.2.2).

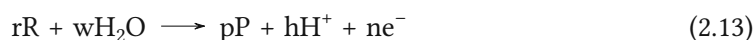
TABLE 2.1: Selected standard reduction potentials for half cell reactions that are of relevance for the work performed in the course of this thesis.

Half cell reaction	Standard potential (V)	Reference
$2\text{H}^+ + 2\text{e}^- \rightleftharpoons \text{H}_2$	0	23
$\text{Ag}^+ + \text{e}^- \rightleftharpoons \text{Ag}$	0.7991	32
$\text{Cu}_2^+ + 2\text{e}^- \rightleftharpoons \text{Cu}$	0.337	33
$\text{Cu}^+ + \text{e}^- \rightleftharpoons \text{Cu}$	0.521	31
$\text{Cu}_2\text{O} + 2\text{H}^+ + 2\text{e}^- \rightleftharpoons 2\text{Cu} + \text{H}_2\text{O}$	0.471	34
$\text{CuO} + 2\text{H}^+ + 2\text{e}^- \rightleftharpoons \text{Cu} + \text{H}_2\text{O}$	0.570	34

Pourbaix diagrams

Pourbaix diagrams, named after their first creator, Marcel Pourbaix, are thermodynamic equilibrium diagrams. In these diagrams, the electrode potential, E , is plotted versus the negative decadic logarithm of the H^+ activity, that is against the pH value. They can yield a lot of insights into the stability of a material of interest in an aqueous system. An exemplary Pourbaix diagram for Cu in uncomplexing media is shown in figure 2.3.

At the heart of such a diagram lies a formulation of the Nernst equation (equation (2.7)) for a general oxidation reaction of the type,



where r moles of the reactant, R, react with w moles of H_2O to form p moles of product, P, and h moles of H^+ ions. n moles of e^- are generated in this process. The formulation of the Nernst equation is then (assuming that $a_{\text{H}_2\text{O}} = 1$) as follows:³³

$$E = E^0 + \frac{0.0591}{n} \log \frac{(a_{\text{P}})^p}{(a_{\text{R}})^r} + \frac{-0.0591h}{n} pH \quad (2.14)$$

Since there is a direct relationship between E^0 and ΔG^0 (equation (2.12)), tabulated thermodynamic data can be taken to calculate the first (constant) term. From this equation three straight-line relationships are possible:³³

1. Vertical straight line: This is the case, when the reaction is influenced by the pH , but not the potential ($n = 0$).
2. Horizontal straight line: When the reaction is influenced by the potential, but not the pH , this shape is obtained ($h = 0$).
3. Straight line with a constant (negative) slope: This is the case, when the reaction is influenced by both the pH and the potential. The slope is then equal to $-0.0591 \frac{h}{n}$.

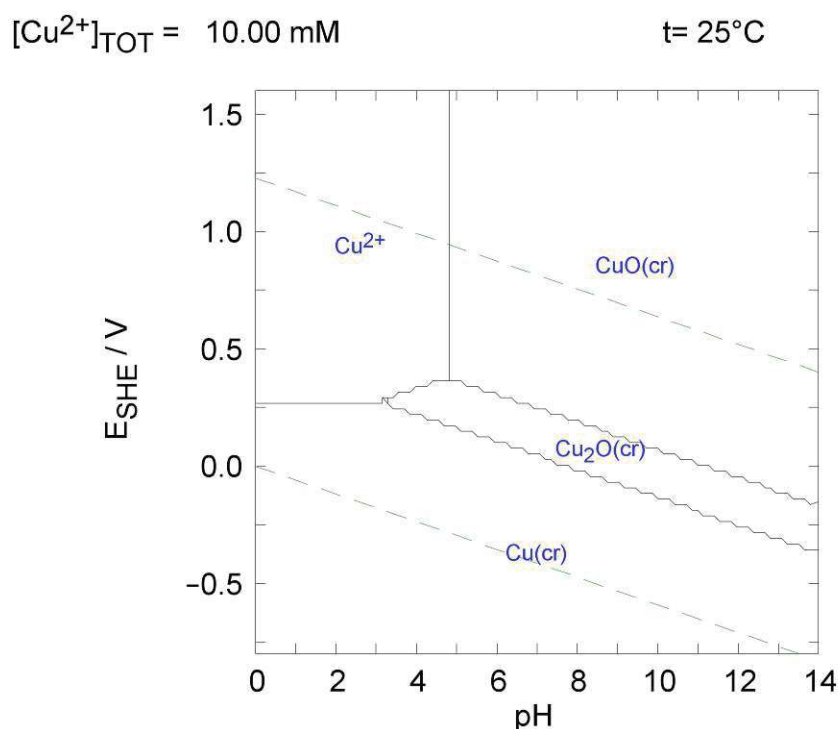


FIGURE 2.3: E_{SHE} (that is E vs. the SHE) vs. pH diagram (Pourbaix diagram) for Cu in aqueous, uncomplexing media at a temperature of 25°C . Concentration of Cu^{2+} ions, $c_{\text{Cu}^{2+}} = 0.01 \text{ mol L}^{-1}$. The dashed green lines indicate the stability region of water, H_2O . Solid lines mark the boundaries at which one species reacts to form another, depending on the change in pH or E_{SHE} . $\text{Cu}(\text{OH})_2$ is not considered in this diagram. This Pourbaix diagram was created using Spana and Database, which are part of the Windows version of Chemical Equilibrium Diagrams (Java), by KTH (the Royal Institute of Technology at Stockholm).

A prerequisite for constructing Pourbaix diagrams is the a priori knowledge of possible educts and products and the availability of thermodynamic data for these. Two reactions form the boundaries within which one can operate in an aqueous environment. These are indicated by dashed green lines in figure 2.3 and constitute the stability region of H_2O . Upon application of increasingly strong reducing conditions, the lower boundary will at some point be reached, at which the hydrogen evolution reaction (equation (2.10)) leads to the decomposition of water. If the potential is strongly oxidizing, the oxygen evolution reaction (OER) will dominate:



It is worth noting, that in an alkaline medium these reactions will actually change, and should be described by



for the hydrogen oxidation reaction³⁵ and



for the oxygen evolution reaction.³⁶ Under reducing conditions, the reactions progress toward the right hand side (i.e. e^- are consumed), for oxidizing conditions, the opposite is true (i.e. progress toward the left, e^- consumption). It can easily be envisioned, by the example of these reactions, that some electrochemical reactions are strongly influenced by (local) pH and will in turn have a strong influence on the same.

2.2.2 2- and 3-electrode setup, potentiostat

2-electrode setup

As the name suggests, a 2-electrode setup consists of two electrodes, namely a working electrode (WE) and a reference electrode (RE). Most of the basics needed to understand such a setup were already introduced in chapter 2.2.1. An example of such an electrochemical cell was also shown in figure 2.2 in the subsection about the Electrochemical Series. Usually, one is primarily interested in the processes occurring at one of the electrodes, namely the working electrode (WE). The RE should be non-polarizable (i.e. its potential does not change when current flows) and (thus) have a known potential, in order to be able to interpret the measured potential drop in terms of the WE. If this is the case, then upon application of an external potential, E_{appl} , the potential drop in the electrochemical cell can be described as

$$E_{\text{appl}}(\text{vs. RE}) = E^0(\text{vs. RE}) + \eta - IR_S \quad (2.18)$$

where

- η is the overpotential. This is described in equation (2.20) in section 2.2.3.
- IR_S reflects the ohmic drop within the electrolyte, stemming from the finite ion conductivity of the electrolyte. I is the current flow in the solution, and R_S the ohmic resistance of the solvent.

If the last term in equation (2.18) is (almost) negligible, and the potential of the RE is stable, then the properties of the WE can be well described.³⁷

However, this is often not the case, for example, when performing solid state measurements. If IR_S is not negligible and E_{RE} is not stable, then one can only describe the overall behavior of the electrochemical cell upon application of an external potential (or current). To overcome these drawbacks and to be able to characterize a single electrode, a 3-electrode setup can be used.

3-electrode setup

In figure 2.4 a schematic of a 3-electrode setup is presented.

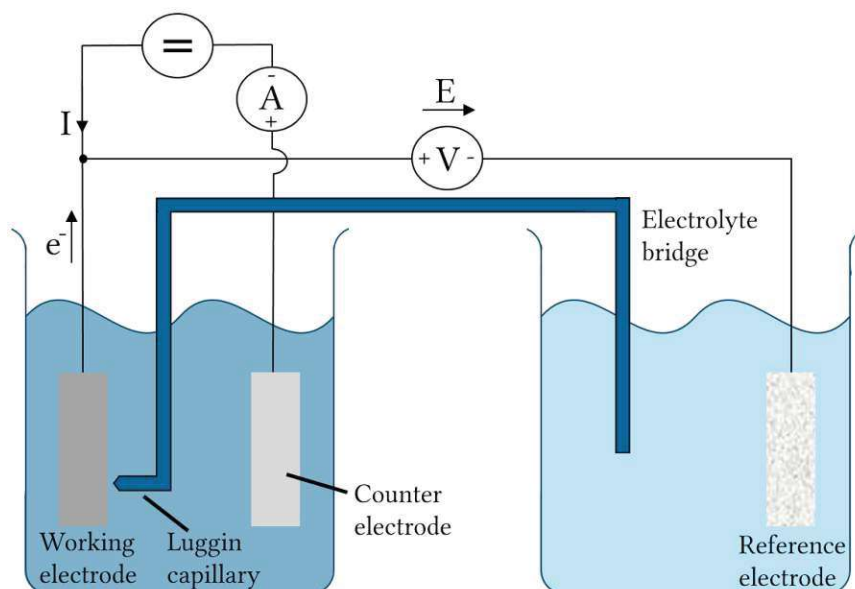


FIGURE 2.4: Schematic drawing of a 3-electrode setup. A counter electrode (CE) is introduced into the system. Current is passed between this electrode and the WE. The RE is therefore not under load and retains a constant potential. The potential difference between WE and RE is measured using a high impedance voltmeter. To minimize ohmic drop within the electrolyte, the RE is brought in close contact with the WE. A Luggin capillary is often employed to this end.

As shown in the schematic, compared to the 2-electrode setup, a third electrode, called counter electrode CE is introduced. The purpose of this additional electrode is to have a counter part for the electrode reaction(s) at the WE that is not the RE. The sole purpose of the CE is to balance the current observed at the WE. The RE therefore is not under load (no current flows through it) and retains a stable potential, which is measured using a high impedance voltmeter. The ohmic drop between the RE and the WE is minimized by placing the RE in the vicinity of the latter. This can be achieved, for example, by using a Luggin capillary.^{29,37,38}

Potentiostatic measurements

In potentiostatic measurements, a constant potential difference is applied between WE and RE. In reality is not quite as simple as that, but to be able to maintain the desired potential difference, a potentiostatic circuit is needed. Simply put, the potential of the WE is constantly monitored using the RE and the potentiostat adjusts the current flow in the cell automatically, if the potential deviates from the desired applied value.²⁵

A more detailed description of the functionality of a potentiostat can be explained with the help of figure 2.5. In this image, a 3-electrode cell is schematically shown, along with two resistances, R_{CE-RE} and R_{RE-WE} . These resistances occur in the electrochemical cell and represent the contribution of the ohmic drop between the two electrodes indicated by the index. Additionally, the charge transfer resistance at the electrode/electrolyte interfaces contribute to these resistances. Now, looking at the electric circuit in figure 2.5, it can be seen, that the WE is held at virtual ground by the current follower, whilst the desired potential is applied to $V_{in}(+)$ and thus indirectly to the RE. The current flow in the system has to pass through both resistors R_{CE-RE} and R_{RE-WE} , forming a voltage divider circuit. The RE is situated at the junction between the two. This voltage is applied to the negative input of the control amplifier, which forms a negative feedback loop. The voltage at the amplifier output is set to the value at which the input voltage difference $V_{in}(+) - V_{in}(-)$ becomes zero. Under this condition V_{out} can be calculated using equation (2.19).

$$V_{out} = \frac{V_{in} (R_{CE-RE} + R_{RE-WE})}{R_{RE-WE}} \quad (2.19)$$

If R_{CE-RE} or R_{RE-WE} change, the output of the control amplifier is adjusted to maintain the applied voltage, V_{in} at the negative input of the amplifier. However, a drawback when using a potentiostat is, that a malfunctioning RE can lead to damage at the WE due to uncontrolled increases of the amplifier output voltage.

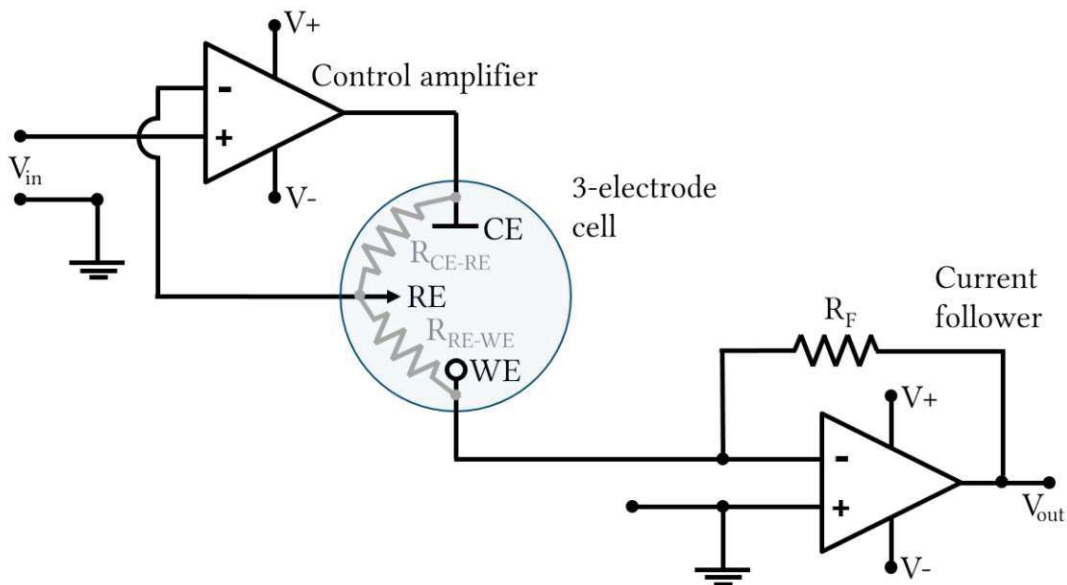


FIGURE 2.5: Electronic circuit for potentiostatic measurements. The control amplifier part is used to maintain the desired potential difference between the WE and the RE. R_{CE-RE} and R_{RE-WE} represent the ohmic drop in the electrolyte between the respective electrodes, as well as the charge transfer resistance at the electrode/electrolyte interfaces. Adapted from Colburn et al.³⁸, Fig. 5(a).

2.2.3 Kinetic aspects

Electrochemical reactions are governed by both thermodynamic and kinetic factors. While thermodynamics dictates the feasibility and direction of a reaction, kinetics determines the rate at which the reaction proceeds.

Overpotential

The overpotential (η) is a key parameter in electrochemistry, representing the excess potential required to drive an electrochemical reaction at a rate higher than its equilibrium state. It is defined as the difference between the actual electrode potential (E) under non-equilibrium conditions and the equilibrium potential (E^0), as expressed by:

$$\eta = E(\text{vs. RE}) - E^0(\text{vs. RE}) \quad (2.20)$$

The existence or rise of overpotential(s) can be attributed to various physical and chemical processes. These include (but are not limited to), charge transfer kinetics, mass transport phenomena (section 2.2.4), and interfacial effects (such as adsorption and desorption). These processes introduce resistances to the flow of charge, necessitating additional driving force (that is the overpotential) for the reaction to proceed at the desired rate. Overpotentials therefore play a key role in electrochemical processes.

The Butler-Volmer Equation

The Butler-Volmer (BV) equation is an empirical description of the relation between the electrode potential and the current density, i (that is the current that flows across a surface area, A , $i = \frac{I}{A}$). It is an empirical relation, even though it can be described based on transition state theory of electron transfer.³⁹ The BV equation will not be discussed in detail here, only fundamental aspects of the version of it used here will be explained. A detailed review of this equation has been provided by (e.g.) Dickinson and Wain³⁹.

To derive the BV equation, the current density of the electrochemical process at the electrode surface, i , must be the sum of independent cathodic and anodic current densities, i_a and i_c , respectively, i.e.

$$i = i_a + i_c \quad (2.21)$$

In addition, the dependence (on potential and concentrations) of these terms must be separable.

The BV equation is expressed as

$$i = i_0 \left[\exp\left(\frac{\alpha_a n F \eta}{RT}\right) - \exp\left(-\frac{(1 - \alpha_a) n F \eta}{RT}\right) \right] \quad (2.22)$$

where:

- i_0 is the exchange current density, a measure of the reaction rate in the equilibrium state ($i_a = -i_c$). It is a critical parameter in the description of the electrode kinetics. It signifies the activity or reactivity of an electrode material for a specific electrochemical reaction. A high i_0 indicates that the electrode material is highly active for the reaction, allowing it to proceed readily even at low overpotentials. Conversely, a low i_0 suggests that the material is less active, requiring higher overpotentials to drive the reaction at significant rates.
- α_a (and α_c) are the anodic (and cathodic) transfer coefficients (dimensionless quantities reflecting the symmetry of the energy barrier for the electrochemical reaction). For a n -electron conversion, $\alpha_a + \alpha_c = n$.

This equation describes how the current density responds to changes in overpotential, highlighting the exponential dependence characteristic of electrochemical charge transfer reactions. The first exponential term represents the anodic contribution to the overall current density, the second term stems from the cathodic contribution. The BV equation exists in various forms, with different approximations forming the basis and different extensions, e.g. to include dependency on species concentrations near the surface as opposed to the bulk solution.^{1,37,39} From this equation, several edge case solutions can be derived, such as the Tafel equation.

The Tafel Equation

For high overpotentials, $|\eta|$, where either the forward or reverse reaction dominates, the Butler-Volmer equation simplifies to the Tafel equation. The high overpotential leads to the clear dominance of the anodic/cathodic branch, leading to a simplified BV equation:

$$i = i_0 \exp\left(\frac{\alpha_a n F \eta}{RT}\right) \quad (2.23)$$

Solving for η results in an equation that provides a linear relationship between overpotential and the logarithm of the current density, the so-called Tafel equation:

$$\eta = \frac{RT}{\alpha F} \ln\left(\frac{i}{i_0}\right) \quad (2.24)$$

This equation plays an important role in electrochemical kinetics, offering insights into reaction mechanisms and rates.¹

The charge transfer resistance

For small overpotentials, linearization of the BV equation is possible, by expansion of the exponentials. This yields:

$$i = i_0 \frac{nF\eta}{RT} \quad (2.25)$$

Since there is a linear, i.e. ohmic, relationship between current and (over)potential near the equilibrium potential, E^0 , this ratio (at $\eta = 0$) is referred to as the charge-transfer resistance, R_{ct} (equation (2.26)).^{29,37} This resistance can be obtained from Electrochemical Impedance Spectroscopy (chapter 2.6) and thus be used to calculate i_0 .

$$R_{ct} = \frac{\eta}{i} = \frac{RT}{nF} \cdot \frac{1}{i_0} \quad (2.26)$$

2.2.4 Mass transport

This section explains phenomena and equations that form the basis for the experiments performed and that provide the fundamental knowledge needed to understand the discussion of the results. A specially emphasized point is the description of mass transport in polymers, since these are of major interest in this work.

Diffusion - Fick's laws

Diffusion describes the process of random molecular motion that results in the transport of matter from one part of a system to another. Since it is a random process, it depends on the concentration of the involved species. If the same fraction of species i randomly moves in any direction, then it logically follows that a higher concentration of a species i , c_i , results in a higher absolute amount of particles moving in either direction than is the case for lower concentrations.⁴⁰ A schematic depiction of a diffusion process is shown on the left in figure 2.6.

The diffusion in an isotropic medium was mathematically described by Fick⁴¹ in 1855 using what is today known as Fick's first law (equation (2.27)) for a one dimensional geometry

$$j_i = -D_i \frac{dc_i}{dx} \quad (2.27)$$

where:

- j_i represents the flux density of species i (in $\text{mol} \cdot \text{m}^{-2} \cdot \text{s}^{-1}$), indicating the amount of substance that flows through a unit area per unit time.
- D_i is the diffusion coefficient of species i (in $\text{m}^2 \cdot \text{s}^{-1}$), which depends on the species and characterizes the ease with which the particles diffuse.

- $\frac{dc_i}{dx}$ is the concentration gradient of species i (in $\text{mol} \cdot \text{m}^{-4}$), that is the change in concentration with respect to position.

In the same paper, Fick also presented his second law (equation (2.28))

$$\frac{\partial c_i}{\partial t} = D_i \frac{\partial^2 c_i}{\partial x^2} \quad (2.28)$$

where:

- $\frac{\partial c_i}{\partial t}$ represents the rate of change of concentration of ion species i (in $\text{mol} \cdot \text{m}^{-3} \cdot \text{s}^{-1}$) with respect to time, indicating how the concentration of the diffusing substance changes over time at a given location.
- $\frac{\partial^2 c_i}{\partial x^2}$ is the second derivative of the concentration with respect to position, representing the curvature of the concentration profile or the spatial rate of change of the concentration gradient.

This partial differential equation predicts the concentration change with respect to time, caused by diffusion. This equation has been modified in many ways, to expand it for use in multi-dimensional spaces, to include a concentration and temperature dependence of the diffusion coefficient or to take into account anisotropy of the medium.⁴⁰

A special type of diffusion is ambipolar diffusion. Ambipolar diffusion is of relevance when interactions occur between oppositely charged species with different diffusion coefficients that are present at the same concentration. If the species diffuse in the same direction (i.e. along a concentration gradient), species with a higher diffusion coefficient are faster. This results in charge separation and the formation of an electric field between them. Slower species are driven by the electric field, resulting in co-diffusion of both positive and negative species, thus maintaining overall charge neutrality.⁴² This process is quantitatively described by the Nernst-Planck equation.

Nernst-Planck equation

The Nernst-Planck (NP) equation can be considered an extension of Fick's first law ((2.27)) to include effects of electrostatic forces on the movement of charged particles (ions) in a fluid.⁴³ Whereas diffusion depends only on the concentration of a species, an additional driving force plays a role in the case of ions. To this end, considerations based on the electrochemical potential, μ_i^* , as well as mass transport in a moving medium (convection) are included.³⁷ Given

$$j_i \propto \nabla \mu_i^* \quad (2.29)$$

and equation (2.4) for the electrochemical potential (where a_i is assumed to be equal to c_i), and

$$j_i = v c_i \quad (2.30)$$

for convection in a system with velocity, v , of the bulk medium, one finally obtains the NP equation for a species i as follows:^{25,28,37}

$$j_i = -D_i \left(\frac{\partial c_i}{\partial x} + \frac{z_i F}{RT} c_i \frac{\partial \phi}{\partial x} \right) + v c_i \quad (2.31)$$

where ϕ is the electric potential (in V), and $\frac{\partial \phi}{\partial x}$ is its gradient with respect to position.

The NP equation is a conservation of mass equation based on continuum theory, in which 'ions are treated as a continuous charge distribution characterized by the concentrations (...) of the ionic species involved' (Coalson and Kurnikova⁴⁴, p.82). As can be seen in the above equation, the total flux of a species i is affected by three different elements: diffusion, migration and convection. These three mass transport processes are schematically depicted in figure 2.6. One should bear in mind, that the NP equation neglects ion-ion interactions and is therefore exact only in the case of infinitely dilute solutions.^{28,37,45} Also, no dependence of electric field strength on ion concentration and vice versa is included. For a more in-depth derivation of this equation, refer to Maex⁴⁶ and Bard and Faulkner³⁷ and references therein.

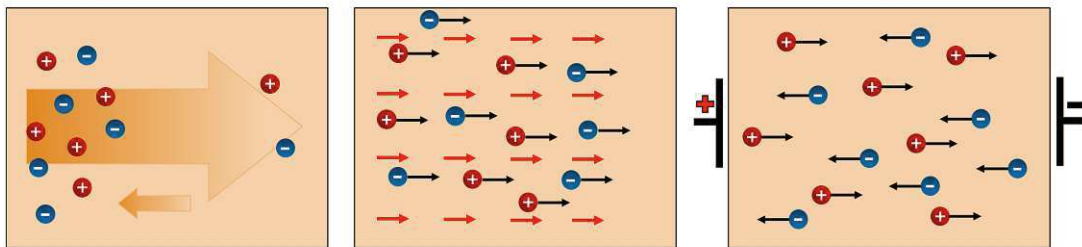


FIGURE 2.6: Schematic drawing of the three possible modes of mass transport included in the NP equation (equation (2.31); image adapted from Jonsson⁴⁷). **(left)** Diffusion along a concentration gradient, **(mid)** convection, driven by movement of the medium, and **(right)** migration, caused by an applied electric field.

Assuming a quiescent solution ($v = 0$), the total flux density for a charged species is then equivalent to a current density, i_i . A system with a cross-sectional area, A (in m^2), is then described using Faraday's law

$$j_i = -\frac{I_i}{z_i F A} \quad (2.32)$$

where I_i is the current of component i . The total current is given by equation (2.33):

$$I = \sum I_i \quad (2.33)$$

Upon introducing these relations into the NP equation, one obtains the following formula for the total current in the system:^{25,37}

$$I = FA \sum z_i D_i \frac{\partial c_i}{\partial x} + \frac{F^2 A}{RT} \cdot \frac{\partial \phi}{\partial x} \sum z_i^2 D_i c_i \quad (2.34)$$

Einstein-Smoluchowski relation

The Einstein-Smoluchowski relation (equation (2.35)) offers a systematic, classical explanation of Brownian motion. It was independently, based on different assumptions, and in varying, but substantially equivalent forms, found by Einstein⁴⁸ and von Smoluchowski⁴⁹ and later named after the two.

$$u_i = \frac{|z_i| F D_i}{RT} \quad (2.35)$$

The equation provides a direct, quantitative relationship between the diffusion coefficient and the mobility of particles in a solution. It is still widely used today.^{37,50} Upon implementation of this relation into the migration term of equation (2.31) the influence of ion mobility on overall flux (and current) is directly seen.

Poisson's equation and its coupling to the Nernst-Planck equation

As mentioned in the introduction of the NP equation above, the influence of (local) ion concentrations on the (local) electric field strength are not taken into account in this equation. However, it has been shown, that even small compositional changes affect $\frac{\partial \phi}{\partial x}$, or, more general, $\nabla \phi$.⁵¹ To overcome this shortcoming and implement gradients in the electric field, the Nernst-Planck equation is often coupled with Poisson's equation for the case of electrostatics. It is described by

$$\nabla^2 \phi = -\frac{\rho}{\varepsilon} = -\frac{F}{\varepsilon} \sum z_i c_i \quad (2.36)$$

where:

- ∇^2 is the Laplace operator, representing the divergence of the gradient of a function, here applied to the electric potential ϕ .
- ρ is the charge density (in $C \cdot m^{-3}$), representing the amount of charge, q , per unit volume. This charge in the system can stem from a variety of sources, such as immobile or mobile ions, but also electronic charge carriers (electrons (e^-) and electron holes (h^+)).

- ε is the permittivity of the material (in $C^2 \cdot N^{-1} \cdot m^{-2}$; e.g. an insulator).

Since

$$\varepsilon = \varepsilon_0 \cdot \varepsilon_r \quad (2.37)$$

where ε_0 is the vacuum permittivity (in $C^2 \cdot N^{-1} \cdot m^{-2}$), a fundamental physical constant that characterizes the ability of the vacuum to permit electric field lines. It is approximately equal to $8.854 \times 10^{-12} C^2 \cdot N^{-1} \cdot m^{-2}$. ε_r is the relative permittivity of the medium (*dimensionless*), which is a measure of how well an insulator stores electric energy in an electric field. ε_r is a quantity that can be extracted from measurements, for example by using dielectric or electrochemical impedance spectroscopy. The latter method is described in chapter 2.6.

The Poisson equation is a useful extension for the NP equation. With equation (2.36), a dependence of the migration part in equation (2.31) on gradients of the electric field is introduced. This way, the influence of concentration changes on the electric field is included, thus adding as a kind of coupled feedback to the concentration changes contained in the NP equation. Usage of this formula, an electrostatic equation, is justified, since the motion of particles in a medium is slow.²⁸

2.3 Corrosion of silver and copper

Throughout this work, the main focus lies on migration processes involving copper and its ions (Cu^+ and Cu^{2+}). Silver and its ion (Ag^+) play a major role in the third and most crucial experimental setup that will be presented in this work. Therefore, an excerpt of the extensive knowledge regarding corrosion processes for these two metals is given, followed by a compilation of insights into an important failure mechanism in microelectronics, namely electrochemical migration.

2.3.1 Fundamentals of copper and silver corrosion

Copper

Copper is a material that is widely used in the fields of electronics, since it combines high electrical and heat conductivity with corrosion resistance. Cu is a noble metal, and the HER (equation (2.10)) therefore does not play a major role in the corrosion process (table 2.1). Copper electrochemistry is more complex than that of other metals, as it is present in two oxidation states, Cu^+ and Cu^{2+} . In an aqueous environment, these two species can be in equilibrium, as described by equation (2.38).



The equilibrium of this reaction lies to the far left ($K_{eq} \approx 10^{-6}$).⁵² As long as there are no complexing ions, such as Cl^- , in the solution, the univalent ion, Cu^+ , plays only a minor role.³³ The Pourbaix diagram, showing the different stability regions of copper has been presented earlier in this work (figure 2.3). It has been shown, that an oxide film forms on a Cu surface, consisting of a mixture of Cu_2O and CuO , when exposed to distilled water at ambient temperature. For lower pH values, a conversion of the mixed oxide to Cu_2O was observed.^{53,54} These oxides form a passive layer that offers protection to the underlying copper.^{33,55}

An in-depth overview over the electrochemistry of Cu, as well as further Pourbaix diagrams, can be found in Bertocci and Turner⁵⁶. The main modes of corrosion for Cu and its alloys in aqueous systems are erosion corrosion, differential aeration corrosion, demetallification and stress corrosion cracking.²⁶ In King⁵⁷ a critical review of the literature dealing with corrosion of Cu in water is undertaken.

Silver

Silver, like copper, has high electrical and heat conductivity, with an even higher corrosion resistance than the latter. As can be seen in the electrochemical series (see table 2.1), silver (Ag) in its solid state is much more stable under standard conditions than its main ion, the univalent Ag^+ . This can also be seen easily upon looking at figure 2.7. Ag^+ is only stable under strongly oxidizing conditions in acidic media. The solubility of Ag in water is at the order of $10^{-6} \text{ mol L}^{-1}$. The most common form of Ag is a type of uniform corrosion, called tarnishing. There, Ag reacts with H_2S to form Ag_2S . In the presence of chlorides it reacts to AgCl . This reaction is important, since it lays the cornerstone for the usage of AgCl reference electrodes (see subsection on making of RE in chapter 3.1).^{24,32}

For more details regarding Ag electrochemistry, the reader is referred to Shumilova and Zhutaeva³².

2.3.2 Electrochemical migration and dendrite growth

Electrochemical migration

Electrochemical migration (ECM) falls in the corrosion category of failure mechanisms mentioned above (section 2.1). ECM and consequent dendrite growth is described in more detail in the following. Alternatively, since a conductive filament is formed, this failure mechanism could also be put in the category of conductive filament formation.

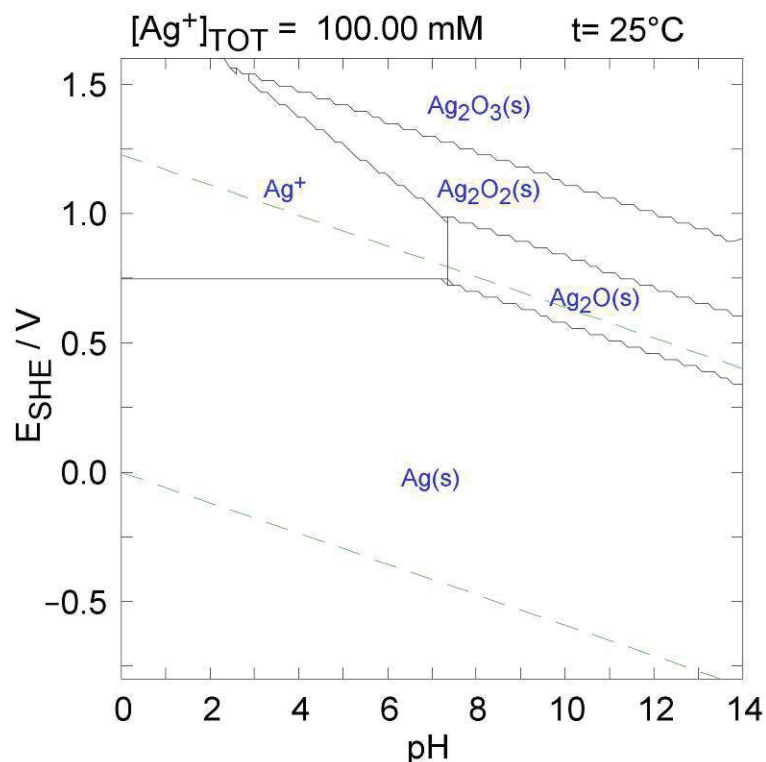


FIGURE 2.7: Pourbaix diagram for Ag in aqueous media at a temperature of 25 °C. Concentration of Ag^+ ions, $c_{Ag^+} = 0.1 \text{ mol L}^{-1}$. The dashed green lines indicate the stability region of water. Solid lines mark the boundaries at which one species reacts to form another, depending on the change in pH or E_{SHE} . This Pourbaix diagram was created using Spana and Database, which are part of the Windows version of Chemical Equilibrium Diagrams (Java), by KTH (the Royal Institute of Technology at Stockholm).

The phenomenon of ECM significantly impacts the reliability and durability of electronic components. It is thus a very active research field even today.^{58,59} Put briefly, ECM is a process whereby metallic ions migrate between two electrodes under the influence of an electric field, leading to the formation of metallic dendrites. These dendritic structures can cause short circuits, leading to the failure of electronic devices.^{3,60}

The most commonly used mechanistic description of ECM involves several key steps, beginning with the formation of an electrolyte layer, dissolution of metal at the anode, ion migration through the electrolyte, and ending with metal deposition at the cathode. This process is influenced by factors such as the presence of moisture, the electric field strength, the type of metal, and the characteristics of the electrolyte.⁶¹

1. **Path formation:** If a continuous water path is present between the conductors, this step is not needed.⁶² If this is not the case, then a continuous water/moisture film has to form, often by adsorption of water molecules on a substrate surface.⁶³ The electrolyte layer thickness can have a significant influence on the ECM behavior.⁶⁴

-
2. **Dissolution of metal at the anode:** Under the influence of an electric field, metal atoms at the anodic site undergo oxidation and dissolve into the electrolyte as metal ions.
 3. **Ion migration:** The ions migrate through the electrolyte toward the cathode, driven by the electric field. The rate of migration and the path followed by the ions can be influenced by the concentration of ions, the electric field strength, and the presence of other ions in the solution.
 4. **Metal deposition at the cathode:** Upon reaching the cathode, the metal ions are reduced and deposit as metal, potentially forming dendritic structures that grow over time. Dendrite growth and shape is influenced by different parameters, such as metal ion concentration and overpotential.⁶⁴

As can be seen by this description, ECM is a form of corrosion, with the prerequisite of an electrical field being present between the conductors.⁶⁵ electrochemical migration should not be confused with electromigration, a different type of (failure) mechanism, that was touched upon in the previous section (2.1) as well. It is worth noting, that the term electrolytic (metal) migration is also often found in literature to describe this phenomenon.

Two 'operation' modes for ECM can be differentiated, based on whether water is present (wet ECM) or only a humidity controlled film (humid ECM).⁶⁶ Harsanyi⁶¹ proposed a total of five subgroups for ECM, namely: classical model (as described here), contaminate induced model (an extension of the classical model to account for ionic impurities), anodic dendritic growth (an anomalous growth observed for Nickel), migration of reduced isolating constituents (stemming from the isolating parts), and virtual migration (reduction of the dielectric by hydrogen ions - the dielectric must be/contain a metal oxide). Steppan et al.³ provides a helpful entry point into this topic with a review on ECM. Two key insights from this review should be highlighted: (a) In Table II in this work, an overview of the migration behavior of several metals is provided, and Cu and Ag are part of the group of metals, that do not require a contaminant to migrate in the electrolyte. (b) Table III of the review lists the susceptibility of different metals towards migration, within which Ag is in first place, meaning that it migrates best. This tendency was found to correlate with the solubility of the metal hydroxide.

A detailed and up-to-date review on this topic has been put together by Lee et al.⁵⁸. This review analyzes the influence that different factors (e.g. electrolyte properties, temperature, electric field,...) have on ECM, as well as possible inhibition strategies (e.g. additives⁶⁷). A more specific review on the test methods used for ECM investigations is given by Zhong et al.⁵⁹. These are: thermal humidity bias (THB), water drop (WD), and thin electrolyte layer (TEL) tests. THB tests is a typical accelerated stress test, for which official standard

procedures exist. In this type of test the device under test (DUT) is exposed to a high temperature and humidity environment. As the name suggests, the WD test, involves a water drop, that is applied as a (local) electrolyte reservoir with a known initial ion concentration (if any). The water drop connects two oppositely biased electrodes. The TEL test is similar to the WD test, but involves a very thin electrolyte layer with a defined geometry (due to an employed housing). Importantly, the role of convection is minimized below a film thickness of 50 μm , while at the same time the growth pattern of filaments is affected.⁶⁸

ECM can affect a wide range of electronic components, including printed circuit boards and integrated circuits. The failure modes associated with ECM can be catastrophic, leading to device malfunction, or complete device failure.^{69,70} As such, understanding and mitigating the risk of ECM is a critical aspect of electronic device design, especially for applications in harsh environments or where high reliability is required.⁵⁸ Table 2.2 provides an overview over factors that affect the ECM mechanism and serves to visualize the variety of possible influential parameters involved in this failure mechanism.

TABLE 2.2: Parameters that influence ECM behavior. Extracted from Lee et al.⁵⁸, Figure 3.

	Material	Electrolyte	Environ- mental	Electric field	Surface conditions
Factors	- electrode - alloying elements	- ionic conductivity - pH - form (e.g. thickness)	- T - RH - conta- minants	- bias voltage - spacing	- roughness - oxidation state - substrate
Plays a role in stage(s)	1, 2, 3, 4	2, 3, 4	1, 2, 3, 4	1, 2, 3, 4	1, 2, 3, 4

When a metallization in an electronic product is covered by a(n organic) barrier coating, corrosion processes are strongly impeded.⁷¹ It is however possible for water and oxygen to penetrate the material and reach the metallization/coating interface.⁷²⁻⁷⁴ This process proceeds relatively swiftly, Dickie⁷⁵ calculated, that the transport rate is roughly equal to the consumption rate of a freely corroding surface. In ? , table 20.1, the permeability of oxygen and water vapor for several resins and coating films is given. At this point it should be noted, that the permeability coefficient, P , can be described by

$$P = D \cdot S \quad (2.39)$$

where D is the diffusion and S the solubility coefficient (in 1 g g^{-1}). S leads to a deviation from ideal Fickian behavior, and represents the interaction with and absorption (of the permeating species) by the polymer.⁷³

The ingress of contaminants into a coating is possible, but much slower.^{76–81} In the literature strongly differing values for the diffusion coefficient for certain chemical elements in electronic packaging material (classes) has been obtained.⁶ Maitland⁷⁶ found two types of conduction behavior in polymer films: direct (D) and indirect (I). This reflected, whether the film resistance was directly or indirectly proportional to the resistance of an electrolyte solution in which the films were submerged. The behavior was found to correlate with the degree of cross-linking, and to affect the amount of absorbed water. A higher percentage of I-areas in a polymer film correlated with higher cross-linking and less absorption of water.⁸² A high crosslinking density was found to play a key role in high-performance barrier coatings.⁸³

Coming back to contaminant diffusion in polymers, the differences were found to be in part due to a lack of standardized procedures in their determination.⁶ It is clear from this, that there is a need for further, and well structured, research in this direction. Challenges are, however, that the low conductivity of these materials require long measurement times, and that depth resolved contamination analysis of coatings has not been widely employed. One possible method for this purpose is LA-ICP-MS, a technique that is presented in section 2.5.⁸⁴

It is often assumed that, for corrosion to occur in the presence of a coating, the adhesion of the latter to the underlying metallization must be weakened (or lost), because otherwise an electrolytic connection cannot be formed.^{60,83,85} According to Leidheiser⁸⁶, already 50 molecules should suffice to initiate a corrosion process. Croll⁸⁷ noted that this roughly coincides with the number of water molecules that are needed to fully hydrate a sodium and a chloride ion. In the same work it is also speculated, that 0.5 nm to 1.0 nm of H₂O, that is the thickness to have bulk properties, might be required to initiate corrosion. Croll⁸⁷ generally presents an interesting review regarding electrolyte transport in polymer barrier coatings and is complemented by Yang et al.⁷³, who focus on (the role of) water and the polymer/metal interface. Many question regarding the role of organic coatings for corrosion protection still remain unanswered, some of which are posed in a brief review by Lyon et al.⁸⁸. One special type of organic coating, namely polyimide, is presented in more detail later in this thesis (2.4).

Dendrite growth

The word dendrite has its origin in the Ancient Greek language, where 'dendron' means tree.⁸⁹ In figure 2.8, some exemplary dendrites are shown. From this image it becomes obvious how the name was inspired.

As mentioned above, dendrite growth can occur as final and (often) detrimental step in the ECM process. Dendritic growth occurs as the result of a metal reduction process at the cathode, i.e.



FIGURE 2.8: Exemplary image of dendrites grown from a CuSO_4 electrolyte.



This is also the reaction that lies at the heart of electrodeposition, in which the metal is reduced uniformly on the substrate. Now the question arises, under which conditions dendritic growth is observed. When looking at the chemical reaction above, it is clear, that it can only proceed, as long as metal ions are present in the electrolyte. It was found that dendrite growth occurs above a critical current density or overpotential⁹⁰⁻⁹² and that the dendritic growth is diffusion controlled, i.e. by the concentration profile of the metal ion near the surface.^{93,94} Steppan et al.³ describes the dendritic growth mechanism as a two step process, consisting of initiation and propagation. During the first step, a dendritic precursor is formed and grows into a protrusion. According to Osenbach⁶⁰ the precursor could be as little as a single deposited atom. Growth at the protrusion is further enhanced with respect to the electrode surface, because³

- of a favored diffusion path of the metal ions from the bulk to the tip. Hence, linear diffusion is replaced by spherical diffusion of metal ions around the tip.
- the electric field strength is increased at the protrusion (tip effect).

Chazalviel⁹⁵ included migration as well as diffusion in his considerations on dendrite growth and demonstrated that a space charge region forms near the cathode because of the depletion of anions. In his work, the author proposed that the required time to establish this space charge region, later referred to as Sand time, τ_s , (equation (2.41)), could explain and predict the incubation time. The Sand time is calculated as

$$\tau_s = \pi D_a \left(\frac{\gamma}{2iu_a} \right)^2 \quad (2.41)$$

where γ is the conductivity, the index a stands for anion, and the other symbols have their previously assigned meanings.⁹⁶ The importance of considering the role of convection when investigating dendrite growth, and strategies how to mitigate its influence have also been

investigated.^{97–102} Jaafar et al.¹⁰³ put together a review on dendrite growth. The review is not written with electrochemistry in mind, but the models presented in there can be and are applied in this field.

For ultra thin electrolyte layers ($\approx 10^{-2}$ μm), it has been shown, that dendrite growth behavior differs significantly as opposed to bulk and thin layer electrolytes. In these experiments, dendrites exhibited 2D-structures and an increased susceptibility to the influence of substrate surface roughness.⁶⁴ This finding highlights that overall ECM processes might behave differently than the dendritic growth phenomena described in the studies above.¹⁰⁴ Additionally, as mentioned before, convection can largely be neglected at film thickness below 50 μm .⁶⁸

Failure models

Different failure models have been developed over the years. In 2014, Bumiller and Hillman¹⁰⁵ published a review of TTF models for ECM. Both empirical and PoF approaches are listed in their work, but it is found by the authors that none of the models comprises all the parameters needed for a generalized model. A possible way to predict failures early on (before they occur), based on surface insulation resistance, and how to calculate TTF based on this has been described for Ag by Yang et al.¹⁰⁶, Yang and Christou¹⁰⁷. A more recent short review on ECM is given by¹⁰⁴. Interesting new developments are shown in there in two respects: (1) New numerical models based on the Nernst-Planck-Poisson (NPP) equation (equation (2.31), (2.36)) have been developed^{62,108}, as well as (2) machine learning based methods.^{109,110} The importance of the latter type of methods for future electronics reliability as a whole is emphasized in Bhat et al.¹¹¹. An attempt specifically to create a generic mathematical framework for ECM through plastic encapsulated microelectronics was given by van Soestbergen et al.⁷. The authors used a combination of generalized Frumkin-BV equation along with NPP theory.

Two recent works on simulations of ECM processes deserve special notice here, as they showcase the increasingly powerful predictive abilities of simulations today. The first is a paper published by Illes et al.¹¹², in which Cu ECM was numerically simulated (in 2D) based on the NP equation. Phases one to three of the ECM process were described in a deterministic manner, for phase 4 (actual dendrite growth) a stochastic approach with given possibilities that depend on the ion concentration was used. water drop experiments were performed to verify the model and good agreement was found. The second paper was written by Cao et al.¹⁰. In this paper, a phase-field model was used to investigate the ECM behavior of Ag-based conductive adhesives. (A word on phase-field: Phase-field models can be used to describe morphology changes at interfaces during phase transitions, and have found increasing attention in research on lithium batteries and associated dendrite growth.^{102,113}) The phase-field model was based on the Allen-Cahn and BV equation. Parameters were determined

based on WD experiments and simulation. With the presented simulation model TTF could be predicted fairly accurately. The authors highlight three advantages of their approach: (1) it provides visualization of the ECM process, including dendrite growth, (2) it is built from fundamental physical and chemical descriptions, and (3) it could be extended to include further processes, if needed.

2.4 Polyimides

Polyimides are a class of high-performance polymers known for their exceptional thermal stability, mechanical properties, and chemical resistance. The first polyimide (PI) was synthesized in 1908 by Bogert and Renshaw¹¹⁴. Since then, these materials have become vital in various industries due to their ability to maintain integrity under extreme conditions.¹¹⁵

2.4.1 PI - applications

Polyimides find extensive applications across various sectors due to their remarkable properties. In the electronics industry, they are used in flexible printed circuits and as insulating films in microelectronics, owing to their excellent electrical insulation and heat resistance. Their ability to maintain performance at high temperatures makes them ideal for components in aerospace and automotive industries. In the field of coatings, PIs provide protective, high-temperature resistant layers for metals and other materials, enhancing their longevity in extreme environments. This is of great relevance in fields like electronics. Their chemical resistance and mechanical strength also make them suitable for use in the chemical processing industry, for e.g. membranes.¹¹⁶

2.4.2 PI - chemical structure and properties

The basic structure of a PI is given in figure 2.9. Polyimides are synthesized through polycondensation, involving the reaction of dianhydrides and diamines. This process results in a polymer chain with imide linkages - characterized by two carbonyl groups (C=O) and one nitrogen atom (N). The robustness of this ring structure is a key factor in the exceptional thermal stability of PIs.¹¹⁷

Polyimides have high thermal stability and exhibit excellent mechanical properties such as high tensile strength and rigidity, which are maintained over a wide temperature range. Chemically, PIs are resistant to solvents, oils, and other chemicals, which enhances their durability in harsh environments. They are less stable in basic environments.²⁴ Furthermore, polyimides possess good electrical insulating properties, making them useful in electronic and electrical industries. The molecular structure of PIs can be changed to alter their

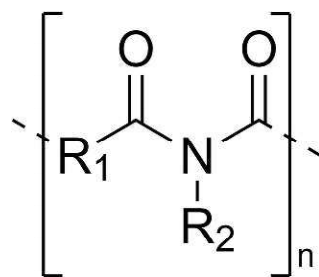


FIGURE 2.9: General chemical structure of PI (structure drawn using ChemDraw®).

properties, making them versatile materials. For instance, adding other chemical groups can enhance their solubility or improve processability without significantly affecting their thermal or mechanical properties.^{117,118}

PIs are known to take up significant amounts of water/moisture. Raju¹¹⁹, p. 234, states that at 100 % RH, PI films absorb ~ 3.3 wt-%, resulting in an up to 20 % increased dielectric constant. The chemical composition of PIs and their linkage have a strong influence on the diffusion coefficient and the uptake of H_2O . In two consecutive studies, involving a number of different PIs, values ranged from $\sim 1.6\text{--}13.5 \times 10^{-10} \text{ cm}^2 \text{ s}^{-1}$ and $\sim 1.5\text{--}5.7$ wt-%.^{120,121}

PIs belong to the class of thermosetting polymers. This means that they are liquid at room temperature, but harden if heated. During this solidification process, new bonds, called crosslinks, are formed. This process is called curing. Other examples of thermosetting polymers include epoxy or polyester resins.¹²²

2.4.3 PI - electrical properties and charge transport

Conduction mechanisms in dielectrics

Polyimides, with their good insulation properties belong to the class of dielectrics. Raju¹²³, p.vii, defines dielectrics as 'materials that do not normally conduct electricity and have the ability to store electrical charge'. Classical band theory is often used to describe polymers and transport phenomena therein. An introduction to the underlying theory for the band structures of polymers is available.^{124–126} An insulator is a material with a large band gap between the valence and the conduction band ($\geq 2 \text{ eV}$). It should be noted that there is not one defined value for E_g to distinguish between insulator and semiconductor. At 0 K, the separation between these bands is perfect and no e^- exist in the conduction band.¹²⁷ In practice, due to imperfections in the crystal lattice (if the material is crystalline at all) it is possible for energy states to exist between those two bands, as illustrated in, e.g., Dissado and Fothergill¹²⁷, Fig. 2.6 and Jaiswal and Menon¹²⁸, Fig. 8. When e^- , h^+ and ions enter such localized states they can get caught in there. Such states are called 'traps'. A simple sketch showing basic band structures and a trap level for both electrons and electron holes is illustrated in fig-

ure 2.10. Depending on how much energy is required to overcome the trapped state, shallow and deep traps are often distinguished, and it can be easily envisioned, that these traps have a potentially significant impact on the conductivity of the polymer.^{127,129}

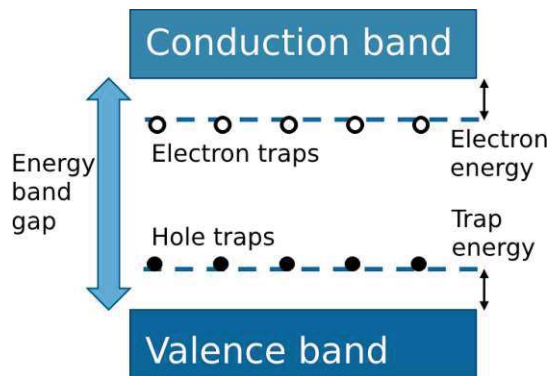


FIGURE 2.10: Schematic drawing of energy band structure with two trap levels, one for e^- and one for h^+ .

Several conduction mechanisms for dielectrics have been proposed and are widely used in literature. They will not be discussed in detail here, but an overview, based on Ohring and Kasprzak¹¹, Table 6.1, and extended with information extracted from Chiu¹³⁰ is compiled in table 2.3. Chiu¹³⁰ generally provides a good, concise overview of charge conduction mechanisms in dielectrics, that serves as a good entry point into this topic for the interested reader. For a more profound picture, refer to Raju¹¹⁹.

It should be noted, that many experiments with dielectrics focus on inorganic materials (such as SiO_2). Without going into too much detail, the different conduction mechanisms will briefly be introduced. Making use of the idealized idea of electron bands, one can imagine electrode limited conduction mechanisms as limited by the energy barrier that a charge has to overcome to be ejected from the metal through the insulator to the other metal or semiconductor. Overcoming this barrier can be achieved via thermal activation (Schottky emission). If the charge carrier does not take up energy to get over the barrier, it still has a finite probability to tunnel through the energy barrier (Fowler-Nordheim and direct tunneling). Thermionic-field emission is a mixture of the two processes.¹³⁰

In the case of bulk limited conduction, similar ideas to electrode limited conduction are employed for a mechanistic description. Poole-Frenkel emission is similar to Schottky emission, but in this conduction process, charge carriers get temporarily caught in traps within the bulk. Upon receiving sufficient thermal energy they escape and continue on to the next trap, and so on, until they successfully traverse the insulator. Similarly, hopping conduction comes from tunneling from one trap to another. Ohmic conduction arises from the small, but not zero, number of e^- that are excited to the conduction band (or h^+ in the valence band).¹³⁰ If charge injection from the electrode is (much) faster than the transport through the bulk,

TABLE 2.3: Overview of possible conduction mechanisms in dielectrics, along with the limiting element, and their dependence on temperature and bias. The table has been adapted from Ohring and Kasprzak¹¹, Table 6.1, and extended with information extracted from Chiu¹³⁰. EL signifies that the conduction mechanism is limited by the electrode, BL by the bulk. l represents the mean free path of an electron, t_d the thickness of the dielectric. $a, a', b, c, d, e, f, g, h, i, m$ are constants that are independent of voltage (V) and temperature (T). E_g is the energy (or band) gap. E_i is the energy needed for creation and motion of an ion. Some of the constants' names had to be adapted, with respect to Ohring and Kasprzak¹¹, Table 6.1, since the order of the mechanisms was changed, and some conduction mechanisms that were only listed in Chiu¹³⁰ were added to the table.

Mechanism	Limitation	Voltage (V), temperature (T) dependence
Schottky emission	EL	$j \propto T^2 \exp\left(\frac{aV^{1/2}-b}{T}\right)$ ($l \geq t_d$)
		$j \propto T^{3/2}V \exp\left(\frac{aV^{1/2}-b}{T}\right)$ ($l < t_d$)
Fowler-Nordheim tunneling	EL	$j \propto V^2 \exp(-c/V)$
Direct tunneling	EL	$j \propto V^2 \exp(-d/V)$
Thermionic-field emission	EL	$j \propto T^{1/2}V \exp\left(\frac{eV^2}{T^3} - \frac{fV}{T}\right)$
Poole-Frenkel emission	BL	$j \propto V \exp\left(\frac{a'V^{1/2}-b}{T}\right)$
Hopping conduction	BL	$j \propto \exp(gV - h)$
Ohmic conduction	BL	$j \propto VT^{3/2} \exp\left(-\frac{hE_g}{T}\right)$
Space charge limited conduction	BL	$j \propto V^{3/2}$
Ionic conduction (low field)	BL	$j \propto \frac{V}{T} \exp\left(-\frac{iE_i}{T}\right)$
Ionic conduction (high field)	BL	$j \propto \sinh\left(\frac{mV}{T}\right) \exp\left(-\frac{iE_i}{T}\right)$

charges can accumulate near the electrode interface (and in the bulk), resulting in the formation of a layer. At sufficiently high voltage the current response will deviate from ohmic behavior and instead be determined by the formed layer. This describes space charge limited conduction. If traps are present in the insulator, this conduction is strongly reduced, since charge is 'stored' in traps. If the voltage is further increased, a point will be reached, when all traps are filled. At this point, the current sharply rises and trap-filled current is obtained.¹¹⁹

The conduction mechanisms described thus far are focused mainly on electronic charge carriers (i.e. h^+ and e^-). Ionic conduction results, as the name suggests, from the transport of ions in an (external) electric field. Traps and defects (e.g. missing ions in a crystal lattice) make room for ions to jump from one site to another, and thus move through the insulator. An applied electric field lowers the energy barrier in one direction, thus facilitating ion jumping in this direction.¹¹⁹ Since ions and electrons are fundamentally different, a distinction between ionic and electronic transport is convenient.¹²⁷ However, differentiating between the two poses a significant challenge in experiments, especially since space charge and polarization effects behave similarly.¹¹⁹ Additionally, Dissado and Fothergill¹²⁷ and Kao¹²⁹ differentiate two types of ionic conduction in polymers, depending on the origin of the ions: (i) intrinsic and (ii) extrinsic ionic conduction. The former proceeds via main-chain or side groups dissociation, followed by H^+ and/or e^- transfer within a hydrogen-bonded network. The latter is driven by the movement of ionic impurities (e.g. from additives) through the structure. Dakin¹³¹ developed a description of ion conduction in dielectrics derived from comparison with electrolyte solutions. As seen in table 2.3, low and high field conduction are differentiated. Low field describes applied voltage gradients of $< 10 \text{ V } \mu\text{m}^{-1}$.¹²³ Low field ionic conduction exhibits low ion mobilities and an initial current decay after voltage application. The latter behavior has been attributed to anion and cation buildup at the electrodes.¹²⁷ It should be noted however, that the cited reference was written before space charge measurements (described in the next paragraph) became popular, undermining the credibility of this assumption. Section 2.3.2 provides some more information on ingress of contaminants into polymers. The next subsection will deal with this topic for the specific case of PI.

To date, many experimenters focus on the investigation of space charges within the protective layers. The techniques used to measure these are reviewed by Ahmed and Srinivas¹³², and, more recently, by Imburgia et al.¹³³. In this context, a distinction is made between homo charges and hetero charges. The former has the same polarity as an adjacent electrode, the latter the opposite.¹³⁴ Homo charges are usually formed by charge injection (e.g. e^- or h^+). Hetero charges can be formed by charge injection, but also due to impurities (e.g. ions), or aging effects in the polymer.¹³⁵ Research on polyethylene films found that space charge behavior is influenced by a variety of factors, including additives, byproducts of cross-linking reactions, oxidation products, surface treatment and the employed electrode material(s).^{136,137} The performance of dielectrics when space charges are present was discussed by Bartnikas¹³⁸, including long term breakdown processes. The role of space charges in insulation failure has been reviewed by Montanari¹³⁴, giving a detailed overview over this topic.

Field distortion due to s inside the insulating material can greatly alter the local electric field and result in a reduced dielectric BD strength of the material.¹³⁷ Correlation between buildup and DC stress related BD of polyethylene was observed by Zhang et al.¹³⁹. also in-

fluences mechanical deformation induced by an electrical field.^{140,141} For polyethylene, the influence of such morphological changes on aging and breakdown have been reviewed and a model has been proposed.^{142,143} An interesting thermodynamic approach, called DMM model (after the authors), was presented and later compared with other models.^{144,145} This model assumes that insulation degradation is caused by local alterations of polymer morphology in moieties, that can result in thermal instability or avalanches. Palit et al.¹⁴⁶ use the thermochemical model developed by McPherson and Mogul¹⁴⁷ to describe time to BD, t_{BD} , in polymers. They show, that t_{BD} depends, among other factors, on relative humidity (RH) and electric field strength. Each factor is inversely proportional to t_{BD} . It has also been shown, that BD strength (of Nylon 6) is reduced by (polar) chemicals.¹⁴⁸ Ieda et al.¹⁴⁹, Fig. 3 shows an illustration of the temperature dependence of various electrical BD processes. In recent years, Shen et al.¹⁵⁰ used simulations in the form of a combination of phase-field modeling and machine learning to further elucidate thermal, electric, and mechanical influences on dielectric BD. They found that the breakdown mechanism of the polymer P(VDF-HFP) changes with increasing temperature, transitioning from a BD that is electrically dominated to an electrothermal breakdown, and finally to an electrical–thermal–mechanical breakdown. Electrical BD strength is strongly reduced at increased temperature. Zuo et al.¹⁵¹ developed a generalized physical framework for simulating electro-thermal aging in polymer dielectrics. They found a strong dependency of the failure pattern on the applied field. The temperature effect was less pronounced in the investigated temperature range (383–433 K). Gallier and Plaud¹⁵² addressed the impact on dielectric BD of loading with randomly dispersed conducting particles. They state that the literature on this type of system is scarce. Their stochastic BD model finds a strong relationship between the geometrical features of the microstructure and the BD strength.

Since traps are considered vital for many (bulk) conduction mechanisms, a good understanding of their nature is important, although still lacking.¹⁵³ Lewis¹⁵⁴ stressed the importance of considering local electrochemical behavior of the polymer materials. Huzayyin¹⁵⁵ presented a density functional theory based approach for polyethylene. Hao et al.¹⁵⁶ proposed a detrapping based method for determining the shallow and deep trap distribution in insulation paper impregnated in oil. Teyssedre et al.¹⁵⁷ reviews different techniques for probing the energy level of traps and provides many examples.

For further reading on charge transport in and breakdown of polymeric insulators, the interested reader is referred to Teyssedre and Laurent¹⁵⁸, Laurent et al.¹⁵³, Sato et al.¹⁵⁹, Zhao et al.¹⁶⁰ and Raju¹¹⁹. Teyssedre and Laurent¹⁶¹ provides a recapitulation of historic progress in polymeric materials for high electric fields.

Electrical properties of polyimides

Polyimides processed at high temperatures have an electrical resistivity of $> 10^{16} \Omega \text{ cm}$, and dielectric constant value, $\epsilon_r = 3.0 - 3.5$ (Table 2.1 in Ohring and Kasprzak¹¹).

As mentioned above, the dielectric constant is influenced (increased) by the uptake of water.^{119,162} Manufacturing and specific treatments, such as plasma treatment or surface fluorination, affect this property as well.^{163,164} Studying the capacitance (which depends on the dielectric properties of the material) versus voltage behavior can yield insights into initially present impurities and charge injection.¹⁶⁵ Modern electronics have a need for even lower dielectric constant materials. Thus, possibilities to reduce this property is an active field of PI research.¹⁶⁶

Possible modes of charge transport, based on the specific chemical components of PI, have been discussed by Salley and Frank¹⁶⁷. Based on both, model systems and experiments with PIs, it is inferred by the authors, that charge transport occurs both inter-, as well as, intramolecularly in PI. Charge is transported between electron acceptors and donors. In the intramolecular case, the donor is the (amine) phenyl component, and the imide on the same chain is the acceptor. Intermolecular charge transport is due to a sandwich type, coplanar configuration of the aforementioned groups on neighboring molecule chains. The latter is illustrated in Georgiev et al.¹⁶⁸, Fig. 4.

In the early days of usage of PI for protection of electronics, a lot of effort was put into investigating the interaction between metals and polyimide. Faupel et al.¹⁶⁹ provides a thorough review on this topic. They state that metals like Cr and Ti do not diffuse into PI. Cu, Ag and Au, and the alkali metal K on the other hand do, and interact only weakly with the polymer. However, Cu diffusion is only pronounced at elevated temperature.¹⁷⁰ Table 2.4 provides a brief summary of diffusion coefficients for ^{67}Cu , $^{110\text{m}}\text{Ag}$, O_2 and H_2O in the stated temperature intervals. From this it can be seen, as was stated earlier in this thesis, that diffusion coefficients for H_2O and O_2 in PI are much higher than those of metals.

TABLE 2.4: Order of magnitude of diffusion coefficients of different chemical species. Extracted from the given sources.

Species	Reported temperature range (K)	Diffusion coefficient range ($\text{m}^2 \text{ s}^{-1}$, order of magnitude)	Source
^{67}Cu	~ 290 – 670	$10^{-23} - 10^{-17}$	Faupel et al. ¹⁶⁹ , Fig. 14
$^{110\text{m}}\text{Ag}$	~ 540 – 770	$10^{-22} - 10^{-17}$	Faupel et al. ¹⁶⁹ , Fig. 14
O_2	~ 400 – 500	$10^{-11} - 10^{-9}$	Faupel et al. ¹⁶⁹ , Fig. 14
H_2O	~ 290 – 333	$10^{-14} - 10^{-13}$	Faupel et al. ¹⁶⁹ , Fig. 14
Na	~ 475 – 600	$10^{-16} - 10^{-11}$	Neuhaus et al. ¹⁷¹
Na	303	$10^{-17} - 10^{-16}$	Schussler et al. ¹⁷²
Cl	303	$10^{-17} - 10^{-16}$	Schussler et al. ¹⁷²

In general, studies on diffusion and migration of contaminants in and through PI are limited. In an early work on the effect of aqueous salt solutions in contact with PI, Sacher¹⁷³ argued that conduction in wet PI samples is due to impurity ions. In dry samples, on the other hand, conduction was stated to originate from protons that are ionized from unreacted polyamic acid groups. The type and amount of residual contaminant ions in the polyimide differ between sample rolls.¹⁷³ The same author investigated trace contaminants in PI and found a variety of potentially detrimental impurities, including Na, K, and Cl.^{174,175} Aqueous extracts of PI were found to be slightly acidic.¹⁷⁵ Several studies investigated the difference in conductivity for Na-doped and clean PI samples. Na was identified as mobile species in PI at room temperature.¹⁷⁶ A mixture of ionic and electronic conduction was observed for Na-doped samples at elevated temperature.^{171,177} Electronic and ionic conductivity were found to depend on the chemical structure of the polymer.¹⁷⁷ Diffusion of Na and Cl was investigated at room temperature and diffusion properties were extracted (see table 2.4).¹⁷² Since no ion selectivity was observed in these experiments, this was interpreted as indication that no fixed ionic charges remained in the bulk matrix.¹⁷² Upon application of electric bias and an acidified electrolyte containing NaCl, Ludwig⁵ observed 'precipitate pathways', consisting of Na and Cl, traversing a PI layer that protected anodically polarized Cu. Ghosh et al.¹⁷⁸ investigated the ingress of (contaminants from) aqueous solutions with Li ions as tracers. A complex penetration behavior was observed, and Li uptake was generally possible. It is known, that the diffusion behavior of solvents and solutes in polymers can be influenced by polymer relaxation, that is the slow rearrangement of the polymer. This can cause non-fickian diffusion behavior.¹⁷⁹ Modern measurement techniques and combinations thereof can help investigate and quantify contaminants (residual and from the outside) in polymer films.^{180–182}

Conductivity of PI films subjected to DC electric fields has been studied in a variety of works. Raju et al.¹⁸³, Table 1 provides an overview of conduction studies on PI at different temperatures and electric fields, and states the proposed conduction mechanisms. The table contains data up to the year 2008. Earlier works, that are not included in this table, and more recent studies will briefly be mentioned. Smith et al.¹⁸⁴ provides a good starting point with their investigation of electrical conduction in dry PI, in the temperature range between 20 and 350 °C, at relatively moderate fields up to 20 MV m⁻¹. They also provide a summary of earlier works. Neuhaus¹⁷⁶ proposed that at $T \leq 40$ °C current in Na-doped PI samples was governed by (Na-) ion transport. Nevin and Summe¹⁸⁵ measured high-field conduction and proposed a combination of Schottky and Poole-Frenkel mechanism below 60 °C, and ionic conduction between 60 and 100 °C. Gaur et al.¹⁸⁶ reported that thermally stimulated discharge current could be governed either by dipolar relaxation or hopping conduction. Their results at polarizing field strengths between 2–20 MV m⁻¹ and 303–473 K hinted at trap-controlled hopping. Vecchio et al.¹⁸⁷ measured plasma-treated PI between 8 and 23 MV m⁻¹ in the temperature range from 298–448 K. They found the best fit for hopping conduction

at low temperatures, and a transition towards Schottky-dominated conduction with increasing temperature. The behavior for plasma-treated and untreated samples was similar, with a higher transition temperature for the treated samples. Fan et al.¹⁸⁸ investigated PI films at -70 MV m^{-1} at 273–123 K. At 273–223 K they proposed that electrode injection stems mainly from Schottky injection, and charge migration is due to hopping. Both are increasingly suppressed with decreasing temperature. Kang and Lee¹⁸⁹ investigated leakage currents along PI layers at the wafer level. They found that the leakage current flow is well described by the Poole-Frenkel mechanism.¹⁹⁰ report that at fields below 140 MV m^{-1} , e^- injection is governed by (Schottky type) thermionic emission. Above this field they state that electron injection mainly results from Fowler-Nordheim tunneling. They propose that electron holes in PI are strongly localized, thus contributing little to electrical conduction, both in high and low field conduction. Recently, the current conduction mechanism of native and nanocomposite PI films were investigated.¹⁹¹ The authors investigated the current density versus bias behavior of Metal-Insulator-Semiconductor (MIS) structures at three temperatures ranging from 328–433 K. They came to the conclusion that the Poole-Frenkel mechanism is most likely for native PI at the lowest temperature.

The influence of curing temperature on the conductivity behavior and dielectric breakdown was investigated, as well as the influence of humidity on the same. The conductivity was found to change by around two orders of magnitude between dry ($\sim 10^{-18} \text{ S cm}^{-1}$) and moist films ($\sim 10^{-15} \text{ S cm}^{-1}$) in the low field region.¹⁹² Moisture was also found to influence the charge transport behavior of the PI, and possible implications are discussed.¹⁹² These findings are in accord with Kaneko et al.¹⁹³ and Bellucci et al.¹⁹⁴. The effect of immersion time in H_2O has also been studied, and a reduction in dielectric breakdown strength was observed.¹⁹⁵ A similar observation was found for different levels of RH.^{173,196} The impact of the water immersion is attributed to the formation of ionic side groups due to hydrolysis. The formation of water trees due to electrical degradation is also a mentioned possibility, however, they were not actually observed.^{195,197} As mentioned earlier, Sacher¹⁷³ proposed that residual impurity ions cause increased conductivity in the wet state. After drying, polyimide films closely resemble non-immersed specimen, indicating reversibility of the influence of immersion.¹⁹⁸ Li et al.¹⁹⁹ used Nuclear Magnetic Resonance measurements, to determine, that water in PI is located primarily in two kinds of sites, γ_1 and γ_2 . γ_1 is uniformly distributed throughout the film, γ_2 is filled only at high humidity and occurs in small molecular clusters. It was found that prolonged exposure of PI films to elevated temperature and relative humidity (85 °C/85 %) changed only the surface properties of the PI, while the bulk remained unchanged.^{200,201}

It was found that below a certain threshold electric field, no accumulation takes place within PI. However, if a certain field strength is exceeded, charges begin to accumulate (as described above, in the previous subsection).²⁰² Zhou et al.²⁰² suggests that below this threshold

field, a component will have a long service life. This hypothesis is supported by conclusions drawn by Bartnikas¹³⁸, for the case of polyethylene cables, in the absence of water or moisture. For PI, the threshold field for accumulation was found to lie between 30 and 40 MV m⁻¹ for two different PIs.²⁰² Other researches obtained roughly similar values.^{192,202–205} Zhou et al.²⁰² relate the threshold field to the dielectric constant. They state that a higher dielectric constant means a higher barrier height and consequently threshold field. formation depends also on the monomer that builds up the PI.²⁰³ For two PIs cured at different temperatures, the threshold value was reduced to ~ 10 and 30 MV m⁻¹, depending on the curing temperature.¹⁹² In the latter case, a change in the DC conductivity behavior was used to assess the threshold field, not s. Humidity and water immersion can enhance the charge injection and charge carrier mobility in PI under the influence of an electric field.^{193,198,203} Fujita and Kamei¹⁹⁸ observed that upon sufficiently long drying, space charge behavior approached the pristine, dry behavior. Wei et al.²⁰⁵ assessed the electric field distribution in a PI thin film sandwiched between two Al electrodes in detail between 25 and 100 MV m⁻¹. They found that for 25 MV m⁻¹ s occurred mainly near the electrodes, but with increased field strength, these charges migrate further into the film. Also, the higher the field, the higher was the total amount of s. In another work, a MIS structure was used and it was shown, that at high electric fields, the internal electric field is significantly enhanced.²⁰⁶ The influence of electrode material (Au and Al) was investigated on Metal-Insulator-Metal (MIM) structures, and no remarkable difference was found at room temperature at 50 MV m⁻¹.²⁰⁷ A markedly different behavior was observed for MIS structures with either p- or n-type Si in the field range of 40–130 MV m⁻¹, owing the doping of the Si. The authors speculate that observed hetero-charges could stem from ions in the PI.²⁰⁸ Locatelli et al.²⁰⁹ investigated MIS structures with p- and n-type Si and Au as well. They used an additional SiO₂ layer between Si and PI to show that the substrate nature determines the charge distribution in the polymer, and not ions. Carrasco et al.²¹⁰ investigated MIS with Au and Al electrodes. The authors believe that the native alumina layer between the Al electrode and the PI acts as electronic barrier. They also state that a direct link between observed space charge dynamics and corresponding conduction phenomena has yet to be established.

Due to their importance in the determination of charge and species transport in polymers, effort has been undertaken in recent years to determine the distribution of trap energy levels in polyimide. Liufu and Kao²¹¹ used a capacitance based method to determine a critical level of field-created traps ($\sim 7 \times 10^{18} \text{ cm}^{-3}$ at room temperature). They speculated that upon reaching this critical value, BD of the PI will occur. Their calculations were based on the assumption of high-field conduction due to Fowler-Nordheim tunneling. Yue et al.²¹² investigated the influence of low-energy proton irradiation on PI deep charge traps using the photo-stimulated discharge technique. They observed degradation of carbonyl groups. He et al.²¹³ and Ma et al.²¹⁴ used the same measurement technique and determined trap levels for

PI mainly between 1.92–3.88 eV and 2.67–3.20 eV, respectively. Fan et al.¹⁸⁸ and Shen et al.²¹⁵ used MIS structures to determine the trap level at 273 and 300 K as 0.88 and 0.84–0.97 eV, respectively. Takada et al.²¹⁶ used quantum chemical simulations to model Kapton® PI. They concluded that trapping sites in this polymer lie along the molecular chain. Gaur et al.¹⁸⁶ used atomic force microscopy to analyze the surface traps of PI. Fan et al.¹⁹⁶ suggested that H₂O molecules do not change the trap levels, but weaken the influence of ρ , thus facilitating carrier movement. This hypothesis was based on the observation that the slope of the I-E curve, was almost the same independent of RH. Amiour et al.²¹⁷ on the other hand noted that with increasing RH the trap energy of both shallow and deep traps was reduced, increasing film conductivity. Amiour et al.²¹⁷, pp.6f provides a short up-to-date overview of the state-of-the-art knowledge regarding the influence of humidity/water on traps and polymer conductivity.

The term dielectric breakdown is used to describe an insulating material that fails (i.e. loses its insulating properties). Determination of dielectric BD strength is often used as a less time-consuming method than measurements of t_{BD} . It is assumed that a material with a higher BD strength will also have a higher t_{BD} .¹⁴⁶ Diahm et al.²¹⁸, Tab. 1 presents an overview over dielectric breakdown fields of PI films reported in literature. The reported values range between ~ 1 and 520 MV m⁻¹. Big differences in experimental conditions can explain the strong scattering of the observed values. Liufu and Kao²¹¹ show the variation of t_{BD} depending on the applied DC stressing field. Hirose²¹⁹ proposed a model for prediction of electrical BD strength based on Weibull distribution and an inverse power model. Hikita et al.²²⁰ observed a rapid (1 ms) current increase before breakdown of PI, at 0 and 90 °C. It was attributed to thermal runaway which results in thermal BD. Evidence of filamentary thermal runaway was provided recently by Diahm et al.²²¹ using infrared thermography. Diahm et al.²¹⁸ investigated the influence of electrode area and film thickness on BD using Weibull statistical analysis. They found that both α and β parameters decreased with increasing area, and only α decreased upon increasing the PI thickness. Min et al.²²² attribute this decrease in electrical BD strength to a more severely distorted electric field due to a higher number of accumulated s. Furthermore, they state that the BD mechanism depends on both molecular displacement dynamics, as well as charge transport. The effect of thermal aging on polyimide BD was investigated by Chen et al.²⁰⁴ and Zhang et al.²²³. Diahm et al.²²⁴ presented a new method for the determination of AC dielectric BD. Based on the results of their measurements the authors claim that the BD mechanism is essentially thickness independent, arguing that a partial discharge in the oil used in common set-ups results in an extrinsic failure of the PI. This should however not alter the findings from DC measurements, but the resulting values become closer to one another. An overview of measured electric (AC and DC) BD strength is provided in Diahm et al.²²⁴, Fig. 1. Immersion in water or (high) RH reduce the dielectric BD strength.^{190,195} Surface fluorination reduced the water uptake and consequently

increased the BD strength.¹⁶⁴ Kishi et al.²²⁵ (probably) measured a MIS structure, although it is not 100 % clear from their description. They observed that hetero-charges always occurred before BD and that electrical properties changed irreversibly due to the electric field stress. Introducing nano-particles into the PI increases the BD strength.²⁰² Fan et al.¹⁹⁶ investigated the BD location on samples that failed in atmospheres with different RH and found that in higher RH environments breakdown spots were smaller. Yun et al.²²⁶ showed that BD in SiO₂ and HfO₂ was significantly reduced in the presence of an aqueous electrolyte containing mono-valent ions, such as Ag⁺. Organic dielectrics could respond similarly to the effect of ionic species, but this has not been thoroughly investigated. BD usually occurs at a single site in the protecting layer, and this is used in the fabrication of nano pores through so-called controlled breakdown. This relatively new technique has been reviewed, and valuable lessons on dielectric BD could potentially be from this field.²²⁷

2.5 Laser Ablation - Inductively Coupled Plasma - Mass Spectrometry

LA-ICP-MS is a technique that was first used in 1985 by Gray²²⁸. It is a versatile method for analyzing the composition of solid materials and tracing elements within them.

2.5.1 LA-ICP-MS - working principle

As depicted in figure 2.11, a Laser Ablation - Inductively Coupled Plasma - Mass Spectrometry (LA-ICP-MS) system consists of three main parts: a laser, an inductively coupled plasma and a mass spectrometer.

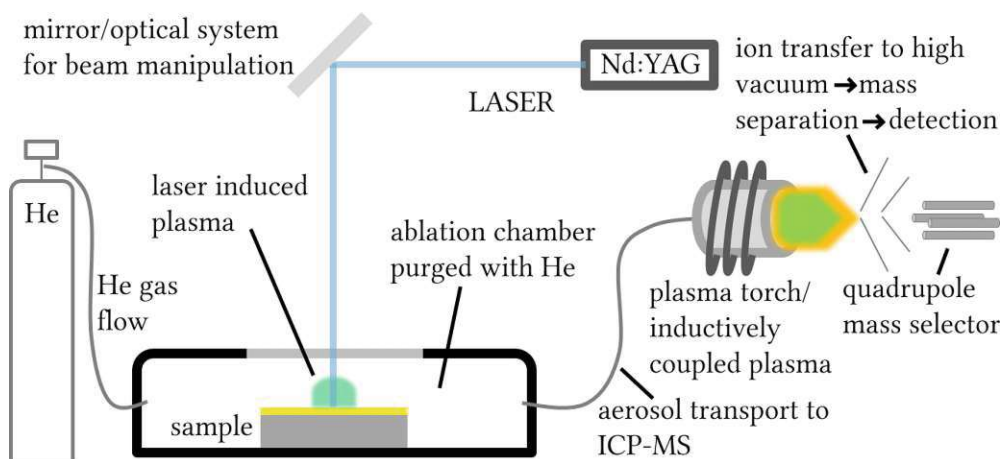


FIGURE 2.11: Schematic drawing of an LA-ICP-MS system.

The pulsed laser source ablates a small area of the sample material. The high energy of the laser results in evaporation and fragmentation/atomization of the ablated material. The released cloud of particles is then transported to the ICP-MS, typically using inert gases like argon (Ar) or helium (He) as carriers. Different mass analyzers can be used for measuring the laser-produced aerosols: quadrupole (Q), sector field, or time-of-flight. Each of these has its own advantages and disadvantages, but the quadrupole is the most commonly used analyzer. It has a linear dynamic range of up to nine orders of magnitude and rapid acquisition cycles.^{229–231}

2.5.2 LA-ICP-MS - advantages and disadvantages

One of the key advantages of LA-ICP-MS is its high sensitivity and spatial resolution, making it an excellent tool for trace element analysis of solid materials.²³² The technique can achieve detection limits at a ppb level, with lateral resolutions in the low μm range and depth resolutions of around 100 nm.²³⁰ It is beneficial for samples where traditional digestion methods are not feasible and offers the capability to analyze the elemental and isotopic composition of various materials without significant sample preparation. Also, this method allows for the rapid 2D- and even 3D-imaging of solid samples, by consecutive ablation of the same area. This can provide crucial data for understanding the distribution and concentration of elements within these materials.^{231,233,234}

Despite its advantages, LA-ICP-MS has some limitations. The formation of a heat-affected zone during laser ablation, especially when analyzing metals and semiconductors, can lead to material redistribution due to thermal diffusion and preferential evaporation of certain constituents. This phenomenon can alter the composition of aerosol particles formed during expansion and affect the accuracy of the analysis. The analyses carried out by LA-ICP-MS are often subject to interference from isobaric isotopes, poly-atomic ions, and doubly charged ions, which affects quantification capabilities and the quality of results.²³⁰ For example, when an Ar plasma is used, when analyzing potassium (K), the ^{41}K isotope has a significant poly-atomic interference from $^{40}\text{Ar}^1\text{H}^+$.²³⁵ Also, the sample matrix has a significant impact on the measurement, since it influences the ablation behavior.^{229,236}

2.5.3 LA-ICP-MS - quantification

Quantification in LA-ICP-MS predominantly relies on the use of external calibration with matrix-matched reference materials. The fundamental principle involves the comparison of the sample signal to that obtained from known standards. Ideally, these standards should closely resemble the sample in terms of composition, as matrix effects can significantly influence the ablation efficiency and ionization process. The development of matrix-matched standards, although challenging, is pivotal in ensuring accuracy.^{229,230,236}

Another critical aspect is the internal standardization method, which involves the use of an internal standard to correct for variations in signal intensity caused by fluctuations in the ablation process or plasma conditions. Elements such as ^{13}C , or ^{29}Si are often used, depending on the matrix and analyte of interest. This internal standard is assumed to behave analogous to the analyte elements during ablation and ionization, thus providing a means to correct for any non-stoichiometric ablation or transport efficiencies.^{237–239}

The introduction of Laser Ablation (LA) in-situ isotope dilution analysis has further improved the quantitative capabilities of LA-ICP-MS. By spiking the sample with a known quantity of isotopically enriched analyte, isotope dilution analysis facilitates the determination of the concentration of the element of interest directly from the isotope ratios, providing high precision and accuracy.^{240–242}

In LA-ICP-MS, the 'dried droplet' approach has been gaining prominence as an innovative quantification method. This technique involves depositing a solution containing known concentrations of analytes onto a substrate, which is then allowed to dry, forming a 'dried droplet'. During the LA-ICP-MS analysis, these dried droplets serve as calibration standards. The key advantage of this approach lies in its ability to simulate the matrix of liquid samples, offering an effective calibration strategy for analyses where traditional solid standards are unavailable or impractical. By mimicking the sample matrix, this method enhances the accuracy of quantification, especially in complex matrices. Additionally, it simplifies the preparation of standards and can be easily adapted for a variety of sample types. The dried droplet method is particularly useful in biological and environmental applications, where matrix-matched standards are crucial for precise quantification.^{243,244}

A recently published method for measuring specific trace elements in polymer samples has been presented by Willner et al.¹⁸¹. Therein, calibration of the ICP-MS was done using matrix-matched polymer standards based on the concept of standard addition. Preparation was done by spraying different levels of analyte and internal standard on top of the polymer standards. This method enabled the acquisition of quantitative results for sulfur in depth profiles of a Kapton® film. The method's capabilities were further explored by the authors in another publication.¹⁸²

A detailed review on different quantification and correction methods for LA-ICP-MS has been compiled by Lin et al.²⁴¹.

2.6 Electrochemical Impedance Spectroscopy

EIS is a non-destructive method that can be used to investigate the properties of an electrochemical system. The impedance, Z , is the resistance when an alternating current (AC) is applied. In the case of AC, voltage, $V(t)$, and current, $I(t)$, do not run in accord, but a phase shift, Θ , can be observed between them (equation (2.42))

$$V(t) = \hat{V} \cos(\omega t) \quad I(t) = \hat{I} \cos(\omega t + \Theta) \quad (2.42)$$

where

- \hat{V} and \hat{I} are the voltage and current amplitude (in Ω and A), respectively.
- $\omega = 2\pi f$ is the angular frequency. f is the frequency of the applied signal (in Hz).
- t is the time (in s).

The basic idea behind EIS is that an electrochemical system can be described in terms of different electric components, such as resistors and capacitances. For example, an electrochemical double layer (DL) needs some time to charge, behaving similar to a capacitor, whereas the charge-transfer resistance, R_{ct} (equation (2.26)), can be represented by an ohmic resistance. In contrast to a resistor, for a capacitor the voltage is proportional to the accumulated charge and not to the current. For sinusoidal signals, this results in a phase shift between current and voltage. In the case of an ideal capacitor, a phase angle shift of $\Theta = 90^\circ$ is observed. The current increases proportional to the frequency. A resistor on the other hand always behaves the same, irrespective of the frequency ($\Theta = 0^\circ$).^{1,245}

In EIS a sinusoidal AC signal with a constant voltage amplitude is applied and the corresponding current response and phase shift are measured. The polarization must be small enough (~ 10 mV), that linearity of the current-voltage curve is given (see description of R_{ct} in section 2.2.3). To investigate the behavior of the system under test at different time scales, a frequency sweep is performed, typically somewhere in the range of 1×10^{-2} Hz to 1×10^7 Hz. To describe the electrochemical system, electrical equivalent circuits are employed. In these, physical processes are modeled using their electric equivalent. A popular example is a parallel RC circuit to model the electrode/electrolyte interface. In figure 2.12 this circuit is depicted and the frequency (i.e. time) dependent current flow is schematically shown. C_{DL} represents the double layer capacitance, R_{ct} the charge transfer resistance. Depending on the applied frequency, charge separation in the capacitor occurs, resulting in an impeded current flow.^{245,246}

The total impedance can be calculated from the measured voltage and current amplitudes and the phase angle ((2.43)).

$$Z(\omega) = \frac{V(\omega)}{I(\omega)} = \frac{\hat{V}(\omega)}{\hat{I}(\omega)} \cdot \exp(j \cdot \Theta) \quad (2.43)$$

Typically in EIS, the impedance is expressed as a complex function (using Euler's relationship).

$$Z = |Z| \cdot \exp(j\Theta) = |Z| (\cos \Theta + j \sin \Theta) = \text{Re}(Z) + j\text{Im}(Z) \quad (2.44)$$

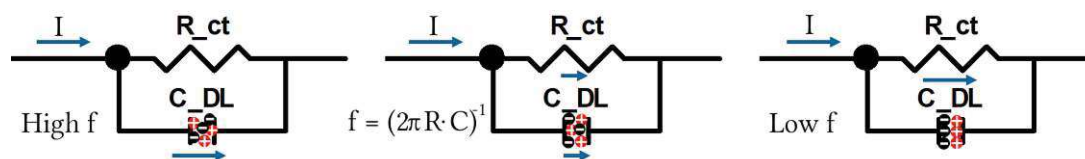


FIGURE 2.12: Exemplary electrical equivalent circuit (parallel RC circuit). **(left)** At high frequencies, the capacitor is quickly charged with alternating polarity and acts like an electric short. **(mid)** At intermediate f (at the characteristic frequency $(2\pi RC)^{-1}$), charge flow through the capacitor starts to be impeded. The current flow is split up equally between R and C . **(right)** At low f , charge separation occurs and the capacitor acts like an insulator. Current flows through the resistor.

where

1. $|Z| = \frac{\hat{V}}{\hat{I}}$ is the absolute value of the impedance.
2. j is the imaginary unit, defined by the property $j = \sqrt{-1}$.
3. $Re(Z)$ and $Im(Z)$ are the real (in-phase) and the imaginary (out-of-phase) part of the impedance, respectively.

From this follows via trigonometry that

$$|Z| = \sqrt{(Re(Z))^2 + (Im(Z))^2} \quad (2.45)$$

$$\tan \Theta = \frac{Im(Z)}{Re(Z)} \quad (2.46)$$

A variety of ways to plot EIS data exist. In electrochemistry and corrosion science, two commonly used representations are the complex plane impedance ('Nyquist') plot, and the Bode representation of the absolute value of the impedance together with the phase angle versus the frequency. An example of these plot types for the simulation of an RC circuit as presented earlier are given in figure 2.13. Looking at the two plots on the right, one can easily identify the characteristic frequency from figure 2.12 (mid), marking the transition zone from capacitive (constant slope, -90°) to resistive (horizontal line, 0°) behavior.²⁴⁶

Any EIS result can be fit using a sufficiently complex equivalent circuit model. The biggest challenge in EIS experiments is therefore often the physically sound attribution of the observed impedance response to meaningful electric components that adequately reflect the electrochemical system.^{247,248}

An advantage of EIS can be applied to a variety of systems. It has been used to obtain information about corrosion susceptibility and behavior of metallic systems.^{249–251} A subsection of this application, the corrosion behavior of Cu in aqueous systems, has been the purpose of many studies.^{55,252–256} Other possible use cases for EIS, that are of relevance for this work, are the characterization of organic coatings^{257–263} and interdigitated electrode structures (the

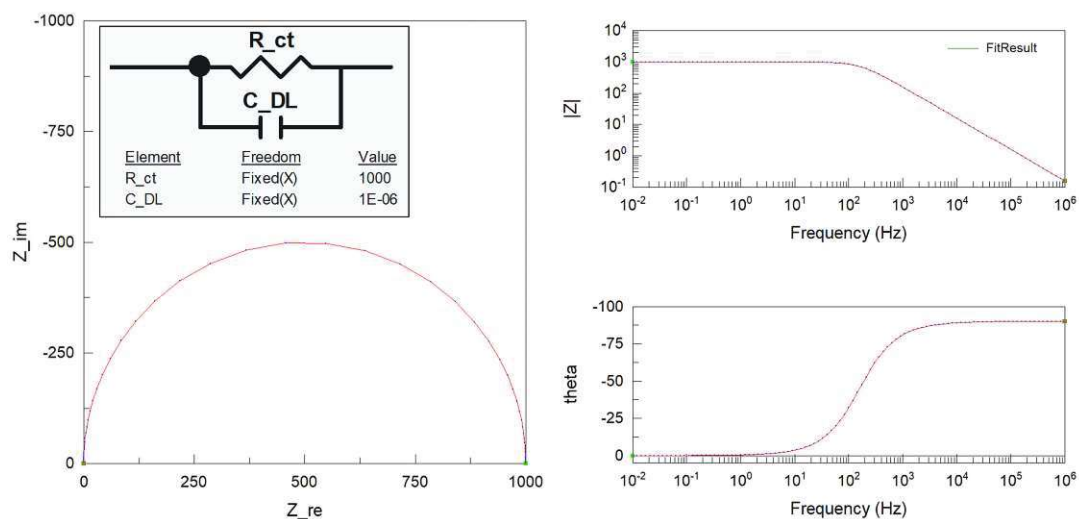


FIGURE 2.13: Simulated result of a (left) Nyquist plot, that is a plot with $Im(Z)$ vs. $Re(Z)$ and (right) the Bode plot, with (top) the logarithm of $|Z|$ and (bot) the phase angle shift, Θ versus the logarithm of the frequency of the applied voltage signal. The inset in the left graph shows the used equivalent circuit and the chosen input parameters for the simulation. The graphic was created using ZView® software from Scribner.

latter are described in section 3.2.^{264–266} EIS, in its classical use, provides information about the system as a whole, but not locally. A variation of this technique, called local EIS, allows to obtain more localized information.²⁶⁷

3 Experimental and simulation

In this chapter the experimental setups, methods and techniques, as well as the simulation methods used in the context of this dissertation are presented. Three different setups were used in this thesis (section 3.1 - Thin Layer Cell, section 3.2 - Miniaturized Test Chip, and section 3.3 - 1x1 Interdigitated Test Chip), and two simulation models were developed (section 3.5). Section 3.4 (Laser Ablation - Inductively Coupled Plasma - Mass Spectrometry) details the procedures and parameters used for measurements employing this analytical technique.

All chemicals used for the experiments conducted in this work were of analytical grade and the metals had a purity of at least 99.95 %.

3.1 Thin Layer Cell

The Thin Layer Cell (TLC) was developed to gain insights on electrochemical migration and corrosion phenomena of copper (Cu) in an aqueous system with reduced convection.

In 2.3.2 and 2.4 it was discussed, that water is assumed to play a major role for failures of insulating materials due to electrochemical processes. Upon direct contact with an aqueous solution or due to high RH the organic coating (OC) has a certain uptake of water, up to a saturation level. As described in the previous chapter, the Nernst-Planck-Poisson (NPP) equation (equation (2.31)) describes the mass transfer in an electrolyte and contains a convection term. Since the amount of water in the polymer and at the polymer/metal interface is limited, convection is reduced, eliminating the convection term from the NPP equation (equation (2.31)). The main idea behind the Thin Layer Cell (TLC) was to create an aqueous electrolyte system in which conditions are similar to those in a polymer system, but that allows better control of the overall system. To this end, a cell was designed, which contains an aqueous electrolyte, but with a limited electrolyte reservoir and less influence of convection. This approach enables better control of the medium properties, such as counter ions and pH, to characterize their influences on the corrosion behavior. At the same time, it gives a fast corrosion response, contrary to measurements on micro-electronic components with organic coatings. Inspiration for the sextup of the cell was taken from Chazalviel et al.⁹⁷.

3.1.1 TLC - cell design

In figure 3.1 a schematic of the developed TLC is depicted.

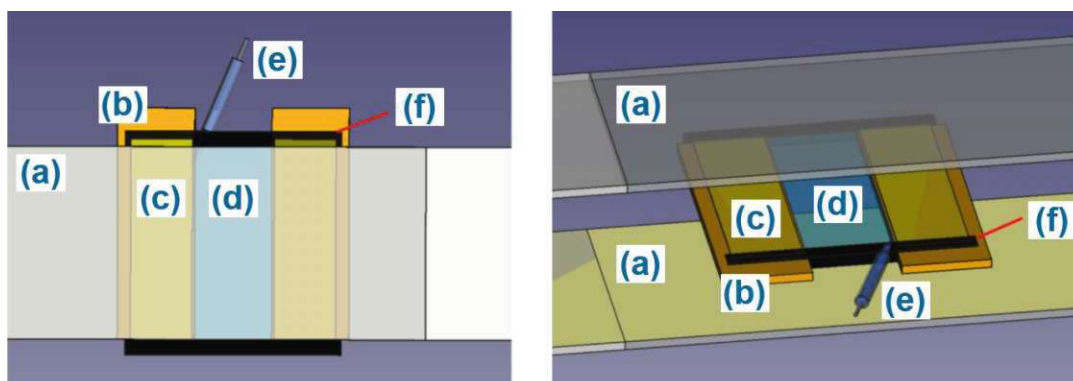


FIGURE 3.1: (left) Schematic top view of the Thin Layer Cell. (right) Schematic, exploded side view of the TLC. a) glass plates, b) Cu plates, c) double-sided tape, d) electrolyte volume, e) RE, f) silicone gel cover.

On the left, the top view of the cell is shown, on the right an exploded side view. The cell consists of two thin, co-planar copper plates (used as working and counter electrode), that are sandwiched between two glass plates, yielding a defined electrolyte volume in between. Connecting wires were soldered to the Cu plates prior to assembly, for easier contacting. The Cu plates had a thickness, h_{cu} , of $170\ \mu\text{m}$ and were fixed on the glass plates using double-sided adhesive tape with a thickness, h_t , of $70\ \mu\text{m}$ (CT-S-1608 by CHEM-TEC). The total thickness of the cell, h_c , therefore amounts to $310\ \mu\text{m}$. The double-sided tape was chosen instead of other forms of fixating the Cu plates (e.g. two component glues) for three reasons. It enables disassembly of the cell after the experiment. It allows for minimization of the bare metal area between the glass plate and the Cu sheet, without risk of accidentally covering the active electrode surface, i.e. the face of the sheet that is in contact with the electrolyte. And, the tape has a defined thickness. The width of the cell, w_c , is $25\ \text{mm}$. 3D-printed spacers were used to set the gap distance, g , between the metal electrodes. In a next step, the bottom side of the cell was sealed using a silicone gel and left to harden for 15 min. The cell was filled with an aqueous electrolyte using a thin glass capillary that was connected to a syringe via a silicone tube. In different experimental series, two types of reference electrodes were used. For most experiments, a self-made Ag|AgCl RE was inserted into the electrolyte volume and positioned next to the copper WE. This RE is described in detail in the following subsection. For one experimental series, a simpler, pseudo RE was used. For this, a Cu stranded wire was inserted into the electrolyte and placed in the center between the two Cu plates. In the final setup step, the top side of the TLC was first sealed with a silicone-free laboratory grease and then again silicone gel, to prevent electrolyte evaporation during the measurement. The grease was used to prevent direct contact between the silicone gel and the aqueous solution,

which could result in ionic impurities, especially during the cross-linking process of the gel. The combination of grease and gel could easily be removed after the measurement and the reference electrode extracted.

The electrolyte volume of the cell, V_c can be calculated using equation (3.1).

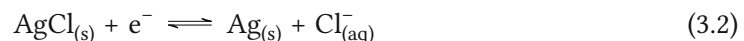
$$V_c = w_c \cdot h_c \cdot g = (w_c \cdot h_{cu} + 2 \cdot w_c \cdot h_t) \cdot g = (A_{ode} + 2 \cdot w_c \cdot h_t) \cdot g \quad (3.1)$$

A_{ode} is the electrode area, all other parameters are defined above. The total thickness of the cell was constant, as was the width of the cell. A_{ode} equals 4.25 mm^2 . Only the gap distance was varied between measurements. The correct value is stated in the corresponding discussion of the experimental results (section 4.1).

3.1.2 TLC - Making of RE

In figure 3.2 the manufacturing process of the Ag|AgCl reference electrode is shown.

The manufacturing process involved several steps. First, a glass capillary with an inner diameter of 1 mm was elongated in its middle part. This was done using a single stage glass microelectrode puller model PP-830 by Narishige Japan. The partially elongated capillary was carefully scratched in the middle and then broken in two, resulting in two 'µCapillaries' with fine tips ($0.12 \pm 0.02 \text{ mm}$ inner diameter). The µCapillary was filled by drawing up a Nafion™ solution ($w_{Nafion} = 20\%$) using a syringe and a tube. Since the Nafion™ came in the form of a solution, the solvent was evaporated in a drying chamber at $60 \text{ }^\circ\text{C}$ for one week. This long period of time was used to mitigate the risk of air inclusion in the tip of the µCapillary. Next, the µCapillary was filled with a saturated KCl solution ($\sim 3.5 \text{ mol L}^{-1}$). This was achieved by inserting a glass capillary, that was connected to a syringe, with a very long, fine tip into the µCapillary. A Ag wire was anodized in a solution of 0.1 mol HCl using a bias of 2 V against a Pt wire that was inserted into the same solution. This was done for 1.25 min to oxidize the surface of the Ag wire to AgCl, as per equation (3.2).³²



The wire was then inserted into the filled µCapillary and sealed with parafilm® to prevent evaporation of the KCl solution. The potential of this type of RE is known to lie at $E_{\text{Ag|AgCl}(sat.KCl)} = +0.197 \text{ V}$ vs. SHE. Functionality and stability of the RE was tested using a commercial Ag|AgCl RE stored in $3 \text{ mol L}^{-1} \text{ KCl}$ (QCM.REF.EL) by Metrohm Autolab.

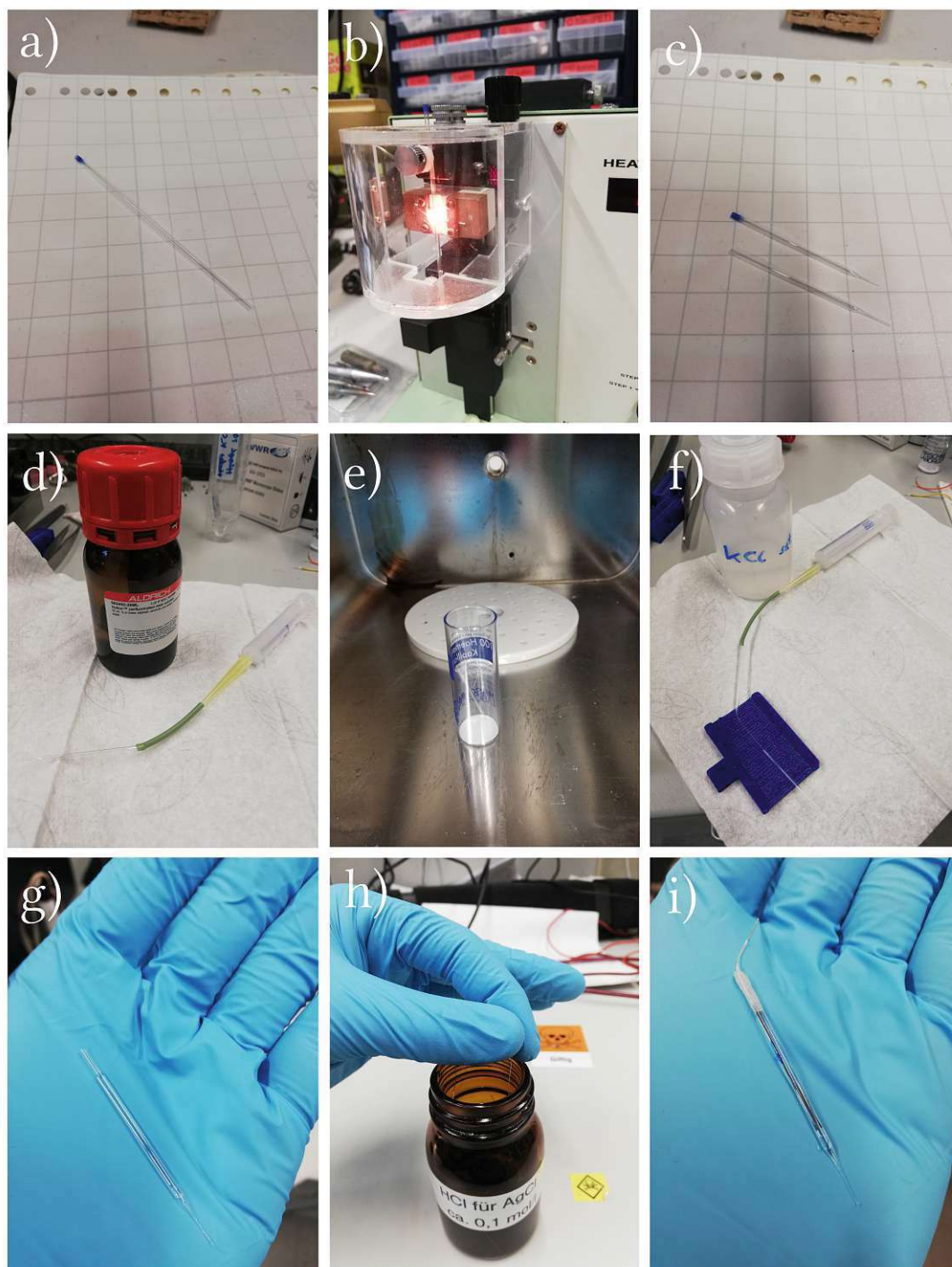


FIGURE 3.2: Manufacturing steps of the reference electrode. a) Used glass capillary, b) drawing of fine tips, c) resulting capillaries with fine tips, d) filling of the μ Capillary by drawing up a Nafion™ solution, e) evaporation of the solvent at 60 °C in a drying chamber, f) filling of the μ Capillary with a saturated KCl solution, g) filled μ Capillary, h) anodization of a Ag wire, i) finalized μ Capillary: the anodized Ag wire is inserted in the μ Capillary, parafilm® is used for sealing.

3.1.3 TLC - measurement procedure

Open circuit, potentiostatic and EIS measurements were performed using a potentiostat/galvanostat PGSTAT204 by Metrohm Autolab, extended with the FRA32M EIS module. Two cameras were used to capture imagery during the measurements, both a top view and a side view at an angle of $\sim 60^\circ$. Each TLC experiment was performed in a three electrode setup and began with an open-circuit potential (OCP) measurement until stabilization was achieved, followed by the acquisition of an electrochemical impedance spectrum. Then, a fixed bias was applied between the WE and the RE. Both current flow and voltage drop were recorded between CE and WE. At the same time, images were taken at set time intervals. Additionally, in the experiments performed with the Ag|AgCl RE, after a fixed time span, EIS measurements were performed during polarization, resulting in alternating acquisition of current density-versus-time (*i-t*), and EIS data. The exact parameter values that were used for each measurement series are stated in the corresponding section of the results and discussion chapter (4.1) for the *i-t*, and in table 5.2.

The findings from these measurements were used to develop an electrochemical simulation using COMSOL Multiphysics®. The model setup and parameters are described in chapter 3.5, and the findings discussed in section 4.1.

3.2 Miniaturized Test Chip

The Miniaturized Test Chip (MTC) samples were provided by the industrial partner Infineon. The basic idea for utilization of these samples was to investigate the influence of small geometries on the corrosion behavior of Cu electrodes.

3.2.1 MTC – sample design

The MTC samples consisted of various Cu structures, deposited on 3 mm · 3 mm Si substrate using the dual damascene process. The structures presented in this doctoral thesis are pairs of flat-band Cu electrodes, separated by a gap distance, w_{gap} , between 0.5 μm and 50 μm . The electrodes themselves had a width, w_{ode} , of $1.6 \cdot w_{gap}$ and a length, L_{ode} , of 50 or 100 μm . The utilized structures are referred to as *bd1* through *bd4*. In addition, an IDE structure was available. IDE structures consist of two comb-like electrode arrays that are individually addressable²⁶⁸. Such structures are often employed, for example, in sensor applications, since they offer high sensitivity at low cost.²⁶⁸ This specific IDE differs from other such structures by having an additional Cu meander in between the two sides of the comb. This structural type as a whole will be referred to as comb-meander (*cm*) structure. The width of each finger, w_f , was 60 μm and the gap between finger and meander, g_{mf} , was 50 μm . The 3x3 samples were glued on a ceramic package and bonded to the respective contacts. The bond pads

were then covered with an epoxy resin for protection. An exemplary build with and without the epoxy resin protection is shown in figure 3.3 (a, c). The samples were received by the industrial partner in the way shown in (c). On the right hand side in the same figure (b), a top view of the MTC sample is depicted.

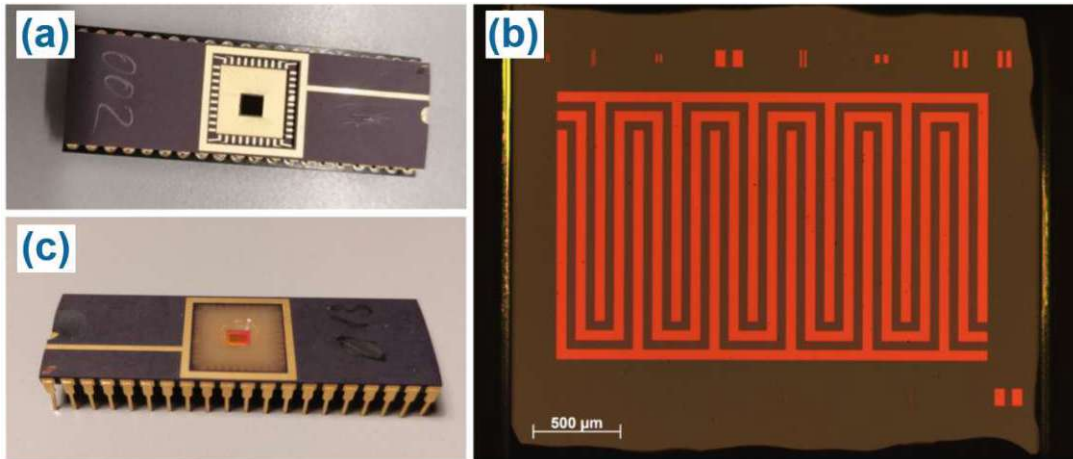


FIGURE 3.3: (a) MTC mounted on ceramic package, without epoxy protecting layer. The bond wires leading from the sample to the lead frame can faintly be made out. (b) MTC on ceramic package, with epoxy protecting layer. (c) Top view of the MTC.

MTC - open structures

Serial dilution and i-t experiments were chosen to confirm the functionality of the structures and test their sensitivity. For the former, 100 μL of solutions with different concentrations of CuSO_4 were applied on top of the MTC and the EIS response was recorded at some of the structures. The measurements were performed in order from lowest (pure H_2O) to highest concentration. The EIS parameters are given in table 5.2 in the appendix. For the i-t experiments, bias was applied between the conductors and the current response was measured and normalized to the active area.

Next, different CuSO_4 electrolyte concentrations in acidic or neutral environment were used to probe the corrosion response. To this end, EIS measurements were first performed in the initial state. Then, bias was applied and current density-versus-time and EIS were measured alternately until the sample short-circuited or the measurement was interrupted. The applied bias, electrolyte concentration and the investigated structure are specified for each experiment in the course of presenting the results in section 4.2.

MTC - polyimide covered structures

A number of different types of experiments were performed on this sample type: autoclavation, electrical stressing with electrolyte drop, and electrical stressing with a 3D printed electrolyte reservoir.

In the experiments with autoclave treatment, 20 μL electrolyte were placed on the sample surface using a pipette. 0.1 mol L^{-1} solutions of either $\text{Cu}(\text{NO}_3)_2$ or CuCl_2 were applied. Then the samples were stored in an autoclave for 48 h at 121 $^\circ\text{C}$, 2 atm, and 100 % RH.

Electrical stressing with electrolyte drop and with a 3D printed electrolyte reservoir followed a similar principle. In the former, an O-ring with an inner diameter of 7 mm was glued onto a microscope slide, with a metal wire introduced between the O-ring and the glass plate. This wire, either made of Cu or Ag, later served as anode for the electrical stress tests. Next, a layer of grease was applied to the other side of the O-ring. 100 μL electrolyte solution were dropped onto the MTC sample using a volumetric pipette and covered by placing the O-ring assembly on top of the epoxy resin surrounding the sample. Either CuSO_4 or AgNO_3 were used as salts in this experimental series. Then, the same silicone gel that was used as sealant in the TLC experiments was placed around the O-ring to fix it in position and enhance the tightness. That way, the solution did not evaporate, even over the course of multiple days, ensuring constant contact between the electrolyte and the electrode wire. Using a glass slide as cover allowed to visually ensure that the electrolyte had not evaporated during the experiment. For the stress tests, bias was applied between (a) selected structure(s) on the test chip (cathode) and the wire (anode).

The 3D printed reservoir had a rectangular open area of $2.68 \cdot 1.74 \text{ mm}^2$ at the socket, and a wall thickness of 0.2 mm. The small dimensions were predetermined by the MTC and the placement of the bond pads on it. The printed reservoirs were glued onto the samples. Special care was taken to avoid flow of excess glue into the desired open area of the reservoir before solidification. Then the same electrolytes as in the previous paragraph were used to fill the cell volume. A plastic cap through which a metal wire was introduced, was employed to cover the reservoir and prevent evaporation. The stress tests were performed in the exact same manner as described in the experiments with electrolyte drop.

3.3 1x1 Interdigitated Test Chip

The samples described in this section were provided by the semiconductor manufacturing company Infineon Technologies AG. A detailed description of an older, but only slightly different version of these samples and how they were manufactured can be found in the thesis by Elke Ludwig⁵. A shorter description is given in the following subsection.

3.3.1 ITC - sample design

Figure 3.4 shows a microscope image of the 1x1 Interdigitated Test Chip (ITC). In figure 3.5 a schematic cross section of the chip is illustrated.

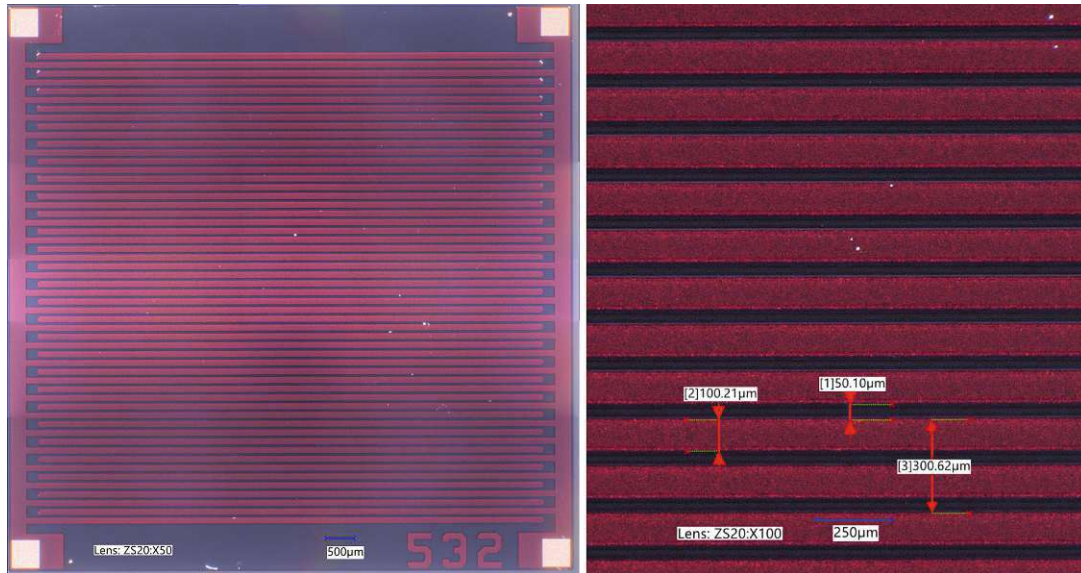


FIGURE 3.4: (left) Panoramic micrograph of an ITC sample (x50 magnification). (right) Microscope image of a section of the sample including dimensions (x100 magnification).



FIGURE 3.5: Schematic cross section of the used test chip. Sizes are not to scale. The cross section shows the substrate (grey), with the Cu comb fingers (orange) and a PI protection layer (yellow) on top.

The ITC samples are square pieces cut from a silicon wafer with an area of $1 \text{ cm} \cdot 1 \text{ cm}$ and a thickness, t_{wafer} , of $\sim 500 \mu\text{m}$. On each wafer piece there is a Cu IDE structure. From this the metallization ratio, α , can be calculated as follows:

$$\alpha = \frac{w_f}{w_f + g_{ff}}$$

Inputting the given parameters yields a value of 0.67 for α . On each side of the IDE, there was a total, n_f , of 27 fingers. The whole sample was covered with a PI layer with a thickness, t_{PI} , of $\sim 7.7 \mu\text{m}$ above the fingers. Only the corners of the samples were left uncovered for electrical contacting, as seen in the figure. Each comb side can therefore be contacted via two of the corners. A successfully established electrical contact between pins and comb (side) was tested by confirming a short circuit between the two pins on the same comb side.

3.3.2 ITC - cell design

In figure 3.6 a schematic of the ITC is depicted.

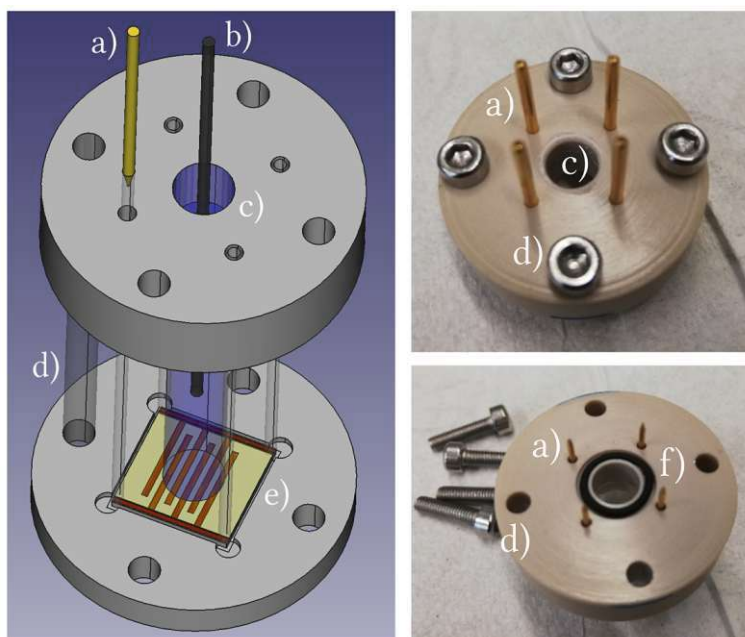


FIGURE 3.6: (left) Schematic of the cell used for the 1x1 Interdigitated Test Chip experiments. (right) Images of the (top) upper side and the (bottom) underside of the top component of the cell. a) contacting pin with spring, b) CE, c) electrolyte volume, d) screw for fixation, e) sample position, f) O-ring for leak-tightness.

The cell consists of two separate parts, referred to as bottom and top part or component. A tailored groove on the upper side of the bottom part allows for placement of the ITC sample, as seen on the left in the figure. On the underside of the top component there is a circular cutout, compliant with standards, where a Viton® O-ring is placed to prevent leakage of the electrolyte after the final assembly (bottom right in figure 3.6). The inner diameter of the O-ring is 7 mm. Four stainless steel screws are used for connecting and fixing the two individual parts. Gold plated precision test pins with an integrated spring mechanism are used to electrically contact the samples. The pins are a fixed element of the upper part. They were pressed in so that all four protrude at the same level, as can be seen on the bottom right image in figure 3.6. This allows for a stable electrical contact, while not exerting so much force as to break the samples.

3.3.3 ITC - measurement procedure

Three experimental series, differentiated mainly by the used aqueous electrolytes, were performed with this setup. The investigated electrolytes were: $\text{AgNO}_{3(\text{aq})}$, $\text{KNO}_{3(\text{aq})}$, and $\text{Cu}(\text{NO}_3)_2(\text{aq})$. From each of the metal salts, aqueous solutions with $\sim 0.1 \text{ mol L}^{-1}$ were prepared using ana-

lytical grade chemicals. Doubly distilled water was used as solvent. For the experiments, the cell that was described in the previous subsection was used. The ITC samples were placed in the groove on the upper side of the bottom part of the cell. The cell parts were then assembled using the screws. Care was taken to avoid over-tightening the screws and to ensure that they were all at the same height in order to exert even pressure on the O-ring used to achieve leak tightness. The assembled cell was then filled with one of the three electrolytes mentioned above, depending on the experimental series. 140 ± 10 mg were used, resulting in a filling height of about 50 % of the total height of the upper part of the cell. The diameter of the (electrolyte) exposed sample area, d_{expo} , was determined to be ~ 8.04 mm.

To prevent evaporation, the cell space above the electrolyte had to be enclosed. Also, an electrode had to be inserted into the electrolyte solution for the intended biasing from the top during the experiment. To fulfill both of these requirements, a metal wire was fed through a rubber stopper in the shape of a truncated cone. The employed metal wire depended on the experimental series: For the $\text{Cu}(\text{NO}_3)_2(\text{aq})$ experiments, a Cu wire was used, Ag for $\text{AgNO}_3(\text{aq})$, and Pt for $\text{KNO}_3(\text{aq})$. The wires were coiled up on one side. An exemplary image of a Ag spool and rubber stopper is depicted on the right side of figure 3.7. Finally, the rubber stopper-metal wire combination was used to enclose the electrolyte space while dipping the coil into the electrolyte at the same time. The fully assembled cell can be seen on the left hand side of the figure.



FIGURE 3.7: (left) Fully assembled ITC cell with contacted clamps. (right) Image of the rubber stopper with metal coil.

The assembled cell was placed in a Faraday cage and EIS measurements were performed. A Solartron1250 frequency response analyzer unit in combination with a Keithley428-PROG programmable current amplifier were used for this purpose. The measurement settings are summarized in table 5.1 in the appendix. The current amplifier was utilized to obtain a sensitive measurement. This is necessary because the electrical impedance of the investigated samples is very high. Two different kinds of EIS measurements were performed: between the two sides of the IDE (referred to as EIS type A), as well as between the biased side of the

IDE and the metal spool in the electrolyte (referred to as EIS type B). Impedance measurements were performed before electrically stressing the samples, after set soaking or stress times, and after BD. An 'as received' measurement between the two comb sides was also performed in the beginning, before the electrolyte was applied on top of the sample. In doing so, functionality and initial properties of the sample were tested.

After the initial EIS measurements, the sample was electrically stressed, either for a pre-determined period of time, or until the failure criterion was reached. The metal spool in the electrolyte served as the anode or positive electrical pole. One side of the IDE was utilized as cathode or negative pole, the other side was left untouched. A constant bias of 550 V was applied in all experiments, resulting in an electrical field of $\sim 72 \text{ MV m}^{-1}$ within the imide coating. A Keithley2470 source measure unit (SMU) was used for application of the bias. The device was programmed to measure the current while applying the bias, and to automatically turn off the source, as soon as the time limit or a threshold current of 100 nA was reached. In the latter case, at this point in time, named t_{BD} or breakdown time, the sample failed. Then, the same EIS measurements as before the electrical stress test were carried out. Then, the cell was disassembled and the sample was rinsed with doubly distilled water. The samples were stowed in a plastic tray until further investigations were performed. Regardless of whether the impedance measurements were performed as type A or type B, the voltage stress was always applied between the wire placed in the electrolyte and one side of the IDE, never between the two comb sides. The active metallized area, A_{met} , for the i-t measurements is calculated according to equation (3.3).

$$A_{met} = 0.5 \cdot \alpha \cdot \left(\frac{d_{expo}}{2}\right)^2 \pi \quad (3.3)$$

The factor 0.5 in the equation stems from the fact that only one side of the IDE was biased during the electrical stress tests. For the given setup, A_{met} equals $1.692 \times 10^{-5} \text{ m}^2$. Although a faraday cage was used, noise affected the measured signal at times. Therefore, a median filter with a window width of 50 data points and no boundary condition was used to smooth the signal using dedicated software (OriginPro, Version 2021b, OriginLab Corporation, Northampton, MA, USA). This filter is advantageous as it is robust against outliers, while preserving important structural attributes, provided that the number of noisy data points is not too similar in quantity to the actual signal. Omitting a boundary condition ensures that the signal structure at the beginning and the end of the measurements is retained.

With the findings from these measurements an electrochemical simulation using COM-SOL Multiphysics® was developed. The model setup and parameters are described in the corresponding section in chapter 3.5, and the findings are discussed in the simulation part of section 4.3.

3.4 Laser Ablation - Inductively Coupled Plasma - Mass Spectrometry

The major analytical technique employed throughout the experimental work for this dissertation was the so-called Laser Ablation - Inductively Coupled Plasma - Mass Spectrometry (LA-ICP-MS). The theoretical foundation of this method is described in chapter 2.5. LA-ICP-MS measurements were performed with the samples described in the previous section 3.3, that is with the ITC samples.

For the measurements, an 'imageGEO193' LA system from Elemental Scientific Laser was used. PTFE tubing directly coupled this system to an 'iCAP Q' Inductively Coupled Plasma (ICP)-Mass Spectrometry (MS) system from ThermoFisher Scientific. Data processing and analysis was done using the software Iolite 4. For all measurements, unless stated otherwise, the same settings for the ablation were used, as per table 5.4 in the appendix.

Both, line scans and images were ablated. For the line scans the ablation depth per pass (or layer) was ~ 185 nm. This was determined using a Bruker DektakXT® stylus profilometer. 20 layers were ablated (denominated L1 through 20) along the same line, resulting in a total ablated thickness, d_{abl} of ~ 3.7 μm per measured line scan (depth profile). A total of nine depth profiles were recorded per sample, in pairs of three each. Each triplet consisted of one line above a finger that was biased during the electrical stressing, one line above an unbiased finger, and one line in between these two fingers. The three triplets were spread evenly across the area of the ITC that was exposed to the aqueous electrolyte during the electrical stress testing. All samples that were exposed to the same electrolyte were measured in one run to ensure comparability of the measurements. For each ablation pass, the median value of the signal intensity of the element of interest was calculated and normalized to the median value of ^{13}C . The normalization mitigates the influence of fluctuations in ablation behavior. Finally, the mean of the three measurements on the same sample was calculated. A schematic cross section and a top view of the line scan measurements are illustrated in figure 3.8 (a), (b). For the images, an area to map was defined, and the defined area was ablated three times (L1, L2 and L3). The mapped area is indicated in figure 3.8 (b), and a pseudo-3D representation is shown in figure 3.8 (c). The denomination 'unbiased' and the minus sign on the IDE indicate the polarity of the respective comb side during the electrical stress tests that were performed prior to LA-ICP-MS analysis. Normalization to ^{13}C was done for the maps as well.

The measured elements were partially varied, depending on the aqueous electrolyte that was applied in the preceding experiments.

- $\text{Cu}(\text{NO}_3)_{2(\text{aq})}$: ^{13}C , ^{63}Cu , ^{65}Cu
- $\text{AgNO}_3(\text{aq})$: ^{13}C , ^{107}Ag , ^{109}Ag , ^{151}Eu , ^{153}Eu
- $\text{KNO}_3(\text{aq})$: ^{13}C , ^{39}K , ^{63}Cu , ^{65}Cu , ^{195}Pt

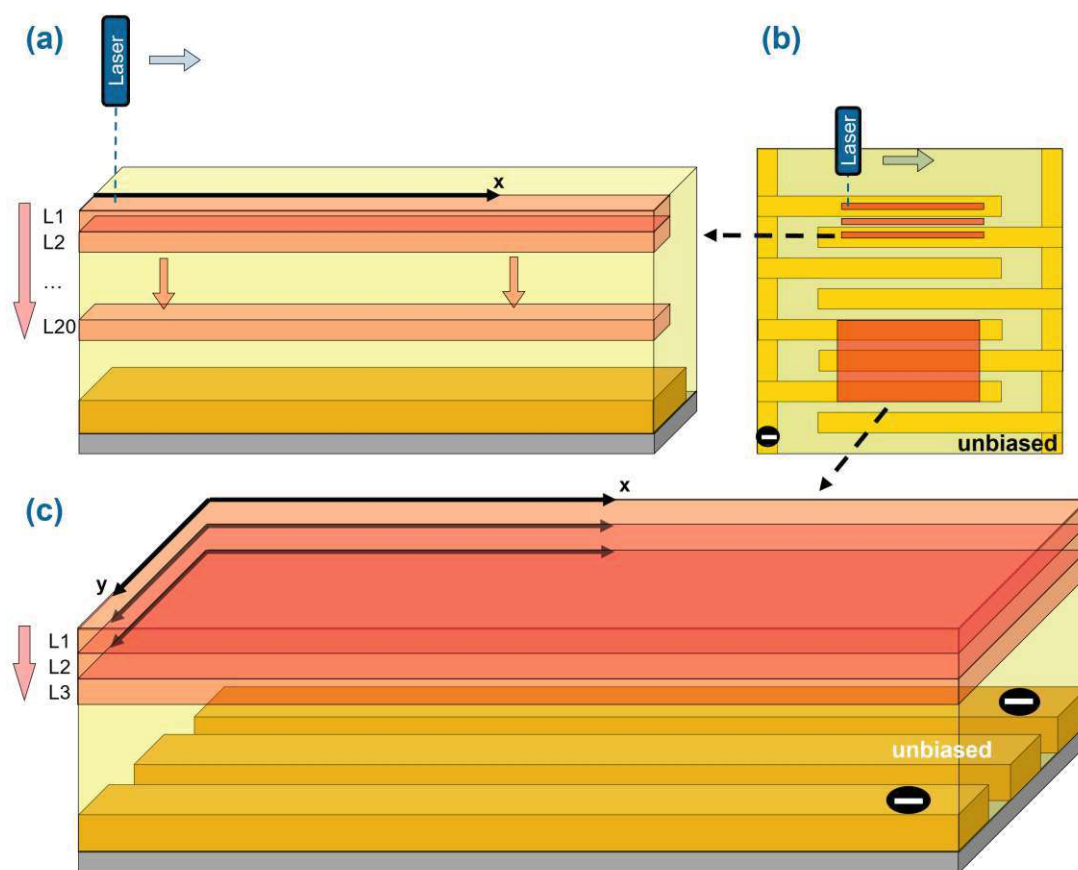


FIGURE 3.8: Schematics of the ablation patterns used for Laser Ablation measurements. **(a)** Cross section illustrating a line scan ablation pattern. A total of 20 layers was ablated along the same line per line scan, highlighted in red. **(b)** Top view of the sample, indicating both a line scan triplet (one pattern above a biased electrode finger, one between the combs, and one above an unbiased finger), and an area that was ablated for imaging. The denomination 'unbiased' and the minus sign on the IDE indicate the polarity of the respective comb side during the electrical stress tests that were performed prior to LA-ICP-MS analysis. **(c)** Pseudo-3D representation of the imaged part of the sample, with the three ablated layers indicated in red.

LA-ICP-MS - Quantitative measurements

For quantitative LA-ICP-MS measurements the preparation of standards is necessary. Quantification was done for Ag only. A standard addition method for matrix-matched standards was employed throughout this doctoral thesis. The method was developed and is described in detail by Willner et al.¹⁸¹. Sample preparation was done using the same instruments and steps described therein.

An isopropanol solution, with a mass fraction of 30 %, was prepared, as well as two stock solutions. Stock A contained a mixture of isopropanol, polyethylene glycol and europium, with a volume fraction of 30 %, 1 % and 10 µg/g, respectively. Europium was added as an internal standard to compensate for potential inhomogeneities in the distribution of the standard

residues by the applied spraying procedure. Stock B was a solution of isopropanol, with a mass fraction of 30 %, containing 1000 µg/g Ag. These two stock solutions were mixed in different ratios, along with the isopropanol solution, to obtain four solutions with different concentrations of Ag. The weights and resulting concentrations of the standard solutions are provided in table 5.5 in the appendix.

Each standard solution was then sprayed on a pristine ITC sample to get the final matrix-matched standard. These standards were measured with LA-ICP-MS during the run in which all samples from the electrical treatment with the $\text{AgNO}_{3(\text{aq})}$ electrolyte were analyzed. The same instrument settings were used for the measurement of the standards, except for the overlap, which was set to 19 µm for measuring the standards. The number of passes was consequently decreased from 20 to 1. This results in the ablation of the same total volume as for the treated samples, but in one pass. This is necessary since the standard solution is sprayed on the surface of the sample and is fully ablated after the first ablation pass. The concentration of Ag in the prepared standard solutions does not equal the concentration on the sample surface. Instead, it has to be related to the mass of ablated polymer matrix and the analyte coverage of the standard's surface. Willner et al.¹⁸¹ found a correction factor of ~2.3 for their prepared Kapton® samples with a thickness of 13 µm. This means, that the concentration of analyte on the surface, relative to the sample thickness and density, is 2.3 times higher than in the standard solution. Determining this factor from scratch involved a couple of more or less complicated steps, as described in the paper. However, for the works in this thesis, not all of the steps had to be repeated. Since comparable standard concentrations and the same spraying unit and settings were employed, differences in the surface coverage should be negligibly low. Also, in both cases a polyimide matrix was used. Since for the samples investigated in this thesis the density is not exactly known, it was assumed to be equal in both cases ($\rho_{\text{polyimide}} = 1.38 \text{ g/cm}^3$). The key difference between Willner et al.¹⁸¹ and the measurements in here lie in the thickness of the ablated polymer layer for quantification. The correction factor was therefore calculated from the one in the literature using the following equation (3.4)

$$cf = cf_0 \cdot \frac{t_0}{t} \quad (3.4)$$

where cf and t are the calculated correction factor and ablated film thickness, respectively, in this work, and cf_0 and t_0 are the correction factor and the ablated film thickness, respectively, that were employed by Willner et al.¹⁸¹. This correction factor was then used to correct the concentrations of the matrix-matched standards with respect to the used standard solutions. The ^{107}Ag signal was first normalized to ^{13}C for each standard, and then corrected based on the ratio of ^{151}Eu to the average ^{151}Eu signal, to minimize sample-to-sample variations based on differences in the ablation behavior. The concentrations in the solutions and

on the sample, along with the determined values for the linear calibration, are summarized in table 5.6. The calibration curve is plotted in figure 5.1. The native Ag content in the untreated samples was below the limit-of-detection of the LA-ICP-MS, which lies in the low ppb region. It was therefore assumed that the concentration of Ag in the sample, without standard addition, was zero. Accordingly, the linear calibration was forced through the origin.

Possible limitations of the here mentioned quantification method and assumptions made are taken up and discussed later, in section 4.3.

Comparison i-t and LA-ICP-MS data

Obtaining information on both the current flow across and the ion distribution within the PI protection layer allows for a comparison of the consumed charges. Assuming that the current flow is ionic in nature, both methods should yield the same result. The charge was calculated from i-t measurements and LA-ICP-MS data.

For the former, the current was integrated over the measured time period using the trapezoidal rule. Additionally, charges were calculated after excluding a set period of time at the beginning of the measurement to account for potential initial transients. The nature of such transients is elaborated in the corresponding discussion section (4.3).

For the LA-ICP-MS data, the concentration of the investigated ion as a function of depth was first converted from parts per million (ppm) to grams per cubic meter (g m^{-3}), considering $\rho_{polyimide}$. The moles of Ag^+ per unit area were then calculated for each depth. The total moles were obtained by integrating these values over the ablated depth, and the corresponding charge was calculated using Faraday's law. The calculation steps are summarized in equation (3.5)

$$Q = n \cdot F \cdot A_{met} \cdot \int_0^{d_{abl}} \frac{C(x) \cdot \rho_{polyimide}}{M_{\text{Ag}^+}} dx \quad (3.5)$$

where:

- Q is the total charge (Coulombs).
- $n = 1$ is the number of electrons transferred per Ag^+ ion.
- $C(x)$ is the concentration of Ag^+ ions at depth x (in parts per million, ppm).
- M_{Ag} is the molar mass of silver (107.8682 g/mol).
- d_{abl} is the total ablated depth (in meters).

3.5 Simulation

Simulation models were created to gain more profound insights of the investigated systems. COMSOL Multiphysics®, a FEM based software, was used for this purpose. Version 6.2 was used throughout the presented work. In short, the FEM breaks a real-world space- and time-dependent system down into a number of numerically solvable linearized problems (differential equations) by means of discretization. The real-world geometry is approximated using a mesh, consisting of a finite number of small, interconnected elements. At this point, a trade-off has to be made. The elements must be chosen small enough to give viable, physically sound results, but large enough to avoid overly large computational effort.²⁶⁹

Two different models have been developed. The first model was designed to describe corrosion and ECM in an aqueous system containing Cu electrodes, as well as Cu²⁺ and Cu¹⁺ ions. This was calibrated using the data obtained from the TLC and MTC measurements. The second developed model describes the diffusion and migration of cat- and anions through a polymer. It was calibrated using the ITC data.

3.5.1 Copper corrosion model (2D)

The model developed here uses the tertiary current distribution (TCD) physics interface, which is integrated into COMSOL Multiphysics®. This interface is used to describe the current and potential distribution in the model system and is based on the NP equations. The influence of convection was neglected in this case. For charge conservation water-based electroneutrality was used. The transport of charged and neutral species in the model is described by the NP equations, neglecting the convection terms. The chosen physics interface also allows for the description of electrode kinetics for charge transfer reactions. To this end, the Nernst equation is solved, as well as the BV or Tafel equation. An double layer capacitance feature is implemented to account for transient non-faradaic currents due to the formation of an electrochemical double layer upon biasing. A 2D representation of the cross-section of the TLC with a Ag|AgCl RE was modeled (figure 3.9 (left)). The electrode reactions that were implemented in the simulation model are given in table 3.1.

TABLE 3.1: Simulated electrochemical reactions at the cathode, the anode and in the bulk.

Cathode	Anode
$2\text{H}^+ + 2\text{e}^- \longrightarrow \text{H}_2$	
$\text{Cu}^{2+} + 2\text{e}^- \longrightarrow \text{Cu}$	$\text{Cu} \longrightarrow \text{Cu}^{2+} + 2\text{e}^-$
$2\text{Cu}^{2+} + \text{H}_2\text{O} + 2\text{e}^- \longrightarrow \text{Cu}_2\text{O} + 2\text{H}^+$	$\text{Cu}_2\text{O} + 2\text{H}^+ \longrightarrow 2\text{Cu}^{2+} + \text{H}_2\text{O} + 2\text{e}^-$
$\text{Cu}_2\text{O} + 2\text{H}^+ + 2\text{e}^- \longrightarrow 2\text{Cu} + \text{H}_2\text{O}$	$2\text{Cu} + \text{H}_2\text{O} \longrightarrow \text{Cu}_2\text{O} + 2\text{H}^+ + 2\text{e}^-$
Equilibrium reaction	
$\text{Cu}^{2+} + \text{Cu} \rightleftharpoons 2\text{Cu}^+$	$\text{H}_2\text{O} \rightleftharpoons \text{H}^+ + \text{OH}^-$

The electric circuit module was used to integrate the potentiostatic control with the reference electrode. The corresponding electric circuit is depicted in figure 3.9 (right). For more details on the working principle circuit refer to the description of a potentiostat in section 2.2.2.

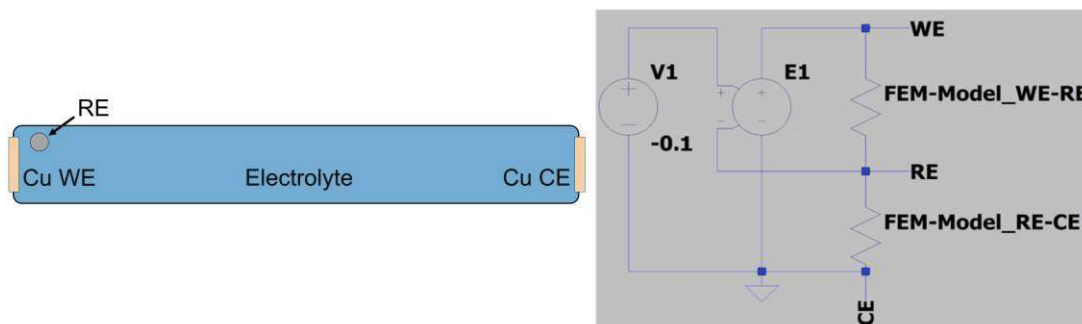


FIGURE 3.9: (left) Schematic cross-section of the TLC used in the simulation model. The geometry is not to scale. In the model, the RE is implemented as a point node, CE and WE as boundary nodes. (right) Representation of the electric circuit model that was used for implementation of potentiostatic control via the RE in the simulation model. The electric circuit was drawn using LTspice XVII(x64), version 17.0.37.0, by Analog Devices, Inc.

The parameters and variables used for setting up the model are given in table 5.7.

3.5.2 Polymer ion migration and species diffusion model (1D)

The model developed here is intended as a 1D representation of the setup used for the ITC measurements. It describes a line along the cross-section of the experimental system across the z -axis. The model developed here also uses the TCD physics interface that was mentioned in the previous subsection. The influence of convection was neglected in this case, too. For charge conservation the Poisson equations were included. The transport of charged and neutral species in the model is therefore described by the NPP equations, neglecting the convection terms. As before, electrode kinetics for charge transfer reactions are also described by this interface.

In total, four species are included in the simulation: Two positively and two negatively charged species. One positive species has a charge (z_{cat}) of $z+$, that is either $+1$ or $+2$, reflecting the metal cation used in the experiment: Cu^{2+} , Ag^+ or K^+ . The associated anion has a charge (z_{an}) of -1 and models the NO_3^- ion. The other two species, one negative and one positive, are both singly charged. These can be thought of as e^- and h^+ , respectively, that can move inside the polymer, but cannot enter the aqueous electrolyte. This assumption was based on literature.^{270,271} It is discussed and challenged in the simulation part of section 4.3.

In figure 3.10 a schematic of the model geometry is shown, detailing key features that are included in the simulation. Starting from left to right, the system consists of: a) a point node with a fixed electrolyte potential and a set concentration of a fully dissolved metal salt, b) an aqueous electrolyte with a defined initial metal salt concentration equal to the concentration in a), c) a polymer separator and d) an electrode surface point.

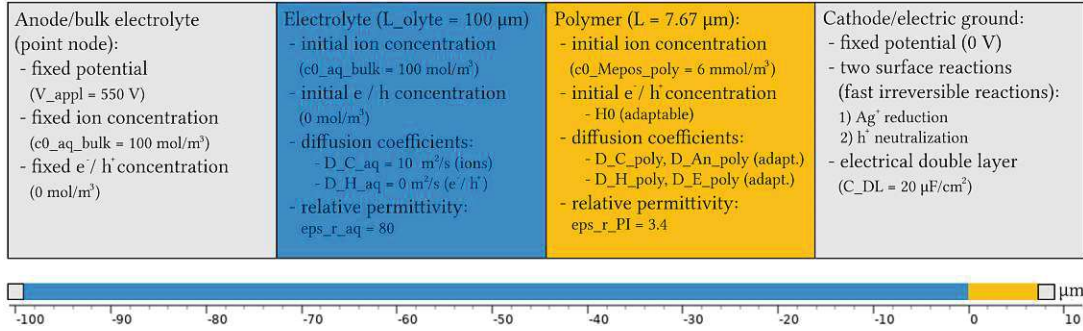


FIGURE 3.10: Sketch of the 1D model used for simulation of ITC experiments. Descriptions of the boundaries and domains are given in the colored boxes. Initial values and values to be fitted ('adaptable') are given.

The leftmost node reflects the anode, that is the metal coil from the experiment, as well as the transition to the bulk of the electrolyte. A positive potential, V_{appl} , is applied here. No electrode reactions are included at this node. The assumption is made, that possible anodic reactions (metal dissolution, oxygen evolution or metal oxidation) do not have a significant influence on the measurement results. Therefore they were excluded in the simulation. This assumption was based on and supported by experimental findings. Furthermore, it is presumed, that the ion concentration in the bulk electrolyte does not (significantly) change during the course of the experiment, since the currents flowing during the experiment are low (at the order of 10 nA). This is implemented in the form of a fixed cation concentration,

$$c_{cat_mob} = c_{0_aq_bulk} \quad (3.6)$$

at this leftmost point, where $c_{0_aq_bulk}$ is the concentration in the bulk of the aqueous electrolyte. The assumption of a constant ion concentration in the bulk of the electrolyte is plausible, given the low current flow. $c_{0_aq_bulk}$ is set to 0.1 mol L^{-1} for the cationic species for all simulations, reflecting the electrolyte concentrations used in the experiments. For the anionic concentration, c_{an_mob} , this concentration is adjusted by the charge of the cation, to be stoichiometrically correct.

$$c_{an_mob} = c_{0_aq_bulk} \cdot z_{cat} \quad (3.7)$$

Since electrons and electron holes cannot enter the aqueous electrolyte, their concentrations, c_{elect_mob} and c_{hole_mob} , are set to 0 mol L^{-1} at this boundary node.

Next to the anode, the aqueous electrolyte is represented by a corresponding domain in the simulation. A length, L_{olyte} , of $100\ \mu\text{m}$ was assigned to it. For this domain, initial species concentration values and electrolyte properties are set. The initial values for the ionic species are set to $c0_{aq_bulk}$, e^- and h^+ are again set to $0\ \text{mol L}^{-1}$, reflecting the practical experiments and the lack of electronic charge carriers in the aqueous electrolyte. The electrolyte properties define the migration, diffusion and dielectric behavior of the electrolyte. e^- and h^+ are immobile in this domain. For both the cation and the anion the diffusion coefficient, D_{C_aq} , is set to $1 \times 10^{-9}\ \text{m}^2\ \text{s}^{-1}$. Since species transport is limited by the polymer and not the aqueous electrolyte, this value, although not exact, was chosen as it is at the typical order of magnitude of ion diffusion coefficients in water.³¹ Migration properties of the ions are described by the Nernst-Einstein relation (equation (2.35)), that was introduced in section 2.2.3. The relative permittivity of the electrolyte was set to 80, the observed value for water at 293.15 K.

Adjacent to the aqueous electrolyte a separator domain is used to model the polymer coating of the ITC. A length, L , equal to t_{PI} (i.e. $7.7\ \mu\text{m}$) was assigned to it, fitting the thickness of the actual coating. Similarly to the electrolyte, initial species concentration values and separator properties have to be set here. However, most of these properties are not known a priori, neither from literature nor the experimental setup. These parameters were extracted from the experiments, either directly (initial cation concentration, $c0_{Mepos_poly}$) or by fitting the simulation to the experiment (initial electron holes concentration $H0$, diffusion coefficient of cation, anion, h^+ and e^- , D_{C_poly} , D_{An_poly} , D_{H_poly} , and D_{E_poly}). The initial anion concentration was equal to the cation concentration. The relative permittivity of the polymer, eps_r_PI , is known and was set to 3.4 accordingly.

The last geometric feature seen in figure 3.10 is another point node, representing the Cu comb. This electrode is grounded, thus making it the lower potential node and therefore the cathode. Here, electrode reactions are defined and a double layer is implemented. Two electrode reactions are implemented: The previously defined equation (2.40), indicative of metal deposition/dissolution at the electrode, as well as the following recombination reaction:



Both reactions are considered to be fast irreversible electrode reactions. The implemented electrical double layer has a capacitance represented by C_{DL} with a number of z_{cat} participating ions and stoichiometric coefficients set to -1, -1, 1 and 1 for the cation, h^+ , anion, and e^- , respectively. The temperature for the whole simulation system was set to a constant 293.15 K, reflecting the laboratory conditions.

4 Results and discussion

In this chapter the experimental results and derived findings are discussed and simulations that were developed for some of the experiments are presented and used to support and enhance the findings.

4.1 Thin Layer Cell

This section is dedicated to the results and findings obtained with the Thin Layer Cell described in chapter 3.1 and the corresponding part of chapter 3.5.

4.1.1 TLC - experimental

The main goal of the TLC experiments was to provide experimental data to verify the developed 2D electrochemical simulation model with. Additionally they served to better understand the Cu electrochemistry in electrolyte layers.

Experiments with pseudo reference electrode

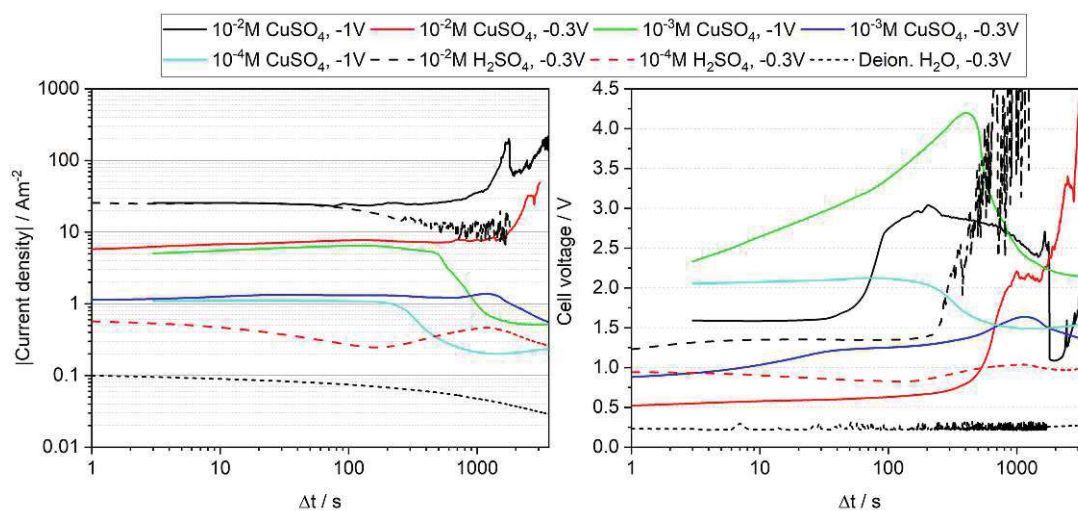


FIGURE 4.1: TLC results with pseudo RE. Different electrolytes and voltages were used, as given in the legend. The CuSO_4 samples were dissolved in 10^{-4} M H_2SO_4 . **(left)** Double logarithmic current density-vs-time for the given electrolyte and applied bias. **(right)** Cell voltage-vs-time for the given electrolyte and applied bias. A logarithmic x-axis was chosen.

Figure 4.1 presents the experimental results from TLC measurements performed in aqueous solutions, at different applied biases, in acidic or neutral pH and varying electrolyte concentrations. A Cu stranded wire was used as pseudo-RE in this experimental series. CuSO_4 concentrations between 10^{-2} M and 10^{-4} M dissolved in 10^{-4} M H_2SO_4 were used, as well as two different concentrations of H_2SO_4 and pure deionized water. -0.3 or -1.0 V were applied between WE and pseudo-RE. The gap distance was set to 10.0 mm in this series resulting in V_c equal to 77.5 mm^3 .

Increasing the concentration tenfold leads to a similar increase in overall current density in the first ~ 100 s, both for H_2SO_4 and CuSO_4 . In all cases but pure H_2O , the cell voltage was significantly higher than the value that was applied between the WE and RE. Throughout the measured period, overpotentials were needed to maintain the applied potential. Optical images that were taken in parallel to the i - t measurements revealed dendritic growth at the cathode in solutions with 10^{-2} M CuSO_4 (figure 4.2 (d, f)). The growth of dendrites is reflected as a rise in the overpotential (figure 4.1 (right)), and with some retardation also in a current density gain (figure 4.1 (left)). Ultimately, the cell is short circuited by bridging of the main dendrite, from the cathode to the anode side. This behavior was observed both at 0.3 V and at 1.0 V, with similar initial growth. At lower Cu concentrations, as well as in 10^{-4} M H_2SO_4 and deionized water, precipitates occur near the anode (figure 4.2 (a, c, e)). Based on the color (greenish/black), these are likely CuO , or a mixture of CuO and Cu_2O . Precipitation occurs due to differences in local pH and block ion motion in the cell. Precipitation depletes the cell volume of ions and reduces the conductivity of the electrolyte. This results in a decreasing current density and an increase in cell voltage to maintain the potentiostatic control. Figure 4.2 (b) shows strong hydrogen gas evolution at the cathode, which effectively reduces the available reaction surface area, thus also resulting in a decreased current density and a strong cell voltage rise. Overall, the observed reactions results were mostly in accordance with what could be expected from Cu in aqueous bulk solutions. However, in contrast to the bulk solution, precipitation and gas evolution can significantly impact the cell behavior due to the closely confined space.

Experiments with Ag|AgCl reference electrode

In figure 4.3 the experimental results from TLC measurements performed in aqueous CuSO_4 solutions with varying concentrations, at -0.3 V, are depicted. A Ag|AgCl RE was employed throughout this experimental series. The gap distance was 5.0 mm, consequently V_c was equal to 38.8 mm^3 . Application of -0.3 V was chosen to generate conditions under which copper reduction is favored at the working electrode, and the HER is suppressed.

Similarly to the previous set of experiments, the Cu^{2+} concentration is the main factor determining the current density. A direct relationship between the concentration and the current density is observed. Between 0.01 M and 0.1 M a minimum is observed at ~ 1000 s.



FIGURE 4.2: Exemplary images during the electrochemical experiment with the TLC with pseudo RE. Cathode and anode side are denoted with + and - symbols, respectively. Different electrolytes and voltages were used. The CuSO_4 samples were dissolved in 10^{-4} M H_2SO_4 . Information for (a-f) is in the format electrolyte concentration, applied voltage. (a) Deionized water, -0.3 V, (b) 10^{-2} M H_2SO_4 , -0.3 V, (c) 10^{-4} M H_2SO_4 , -0.3 V, (d) 10^{-2} M CuSO_4 , -0.3 V, (e) 10^{-3} M CuSO_4 , -0.3 V, (f) 10^{-2} M CuSO_4 , -1.0 V.

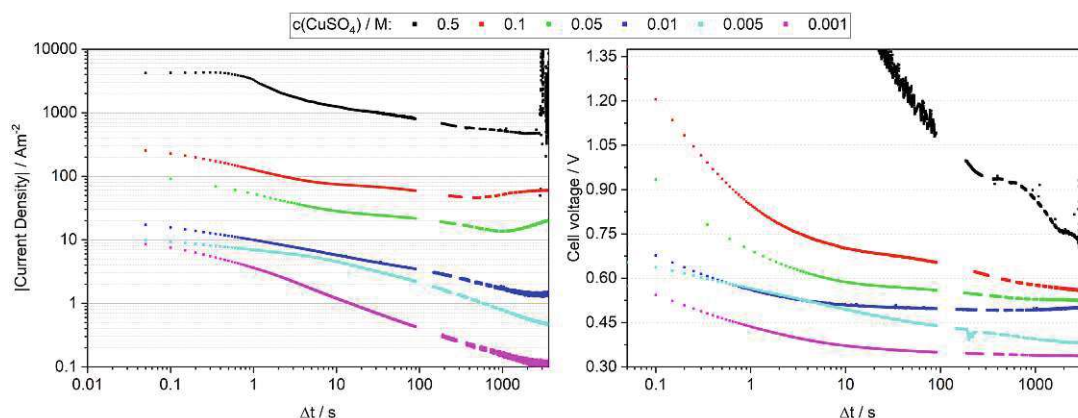


FIGURE 4.3: TLC results with $\text{Ag}|\text{AgCl}$ RE. Different electrolyte concentrations were used, as given in the legend. -0.3 V were set between the WE and RE. The CuSO_4 samples were dissolved in H_2O . (left) Double logarithmic current density-vs-time for the stated electrolyte concentration. (right) Cell voltage-vs-time for the given electrolyte concentration. A logarithmic x-axis was chosen.

Correlating this with optical imagery revealed the onset of dendrite growth or Cu deposition at the cathode surface. At higher concentrations a denser, more uniform layer was deposited

(figure 4.4 (b)), at lower concentrations dendritic onsets occur (figure 4.4 (f)). This indicates that at 0.01 M with the given applied voltage, a diffusion layer forms near the cathode surface. As described as part of the theory (section 2.3.2), such a diffusion layer is typically a prerequisite for dendrite growth. Upon further reducing the concentration, no copper deposition was observed. Contrary to the previous measurements, no, or hardly any, hydrogen evolution was observed. Looking at figure 2.3, this does not come as a surprise, as Cu reduction is thermodynamically possible at the chosen conditions, while the HER is not. The sample solutions were not acidified, hence providing less H^+ for the HER. On the anode side a slight reddening of the Cu was observed, which was attributed to the formation of Cu_2O . Compared to the previous experimental series, differences are observable both in the i - t behavior, as well as the cell voltage. In figure 4.3 both curves show an initial decrease, before ebbing off or reversing the trend. Also, no dendrite bridging was observed. The low cell voltage in the system is not high enough to maintain continual growth, because of the depletion of Cu ions that is not compensated by dissolution on the anode side. This is in line with literature.^{91,272}

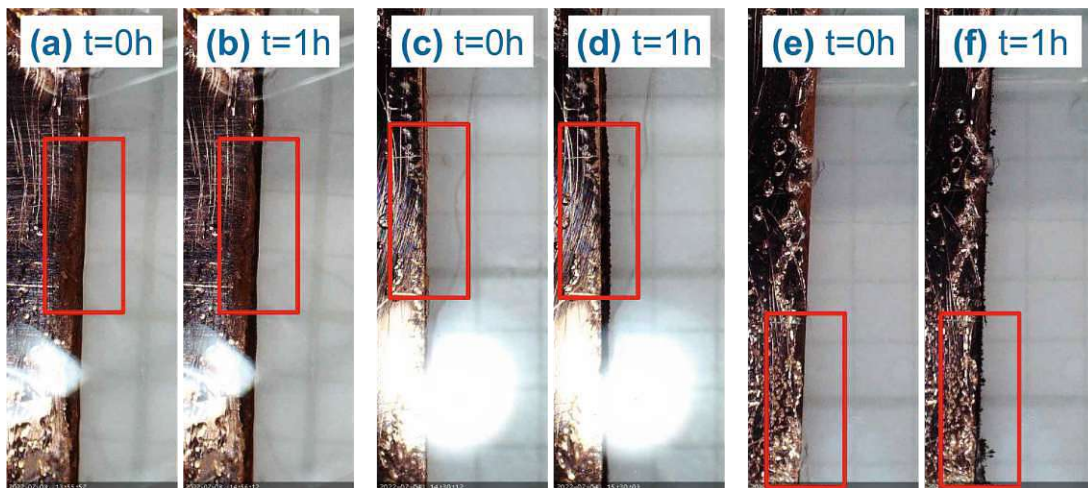


FIGURE 4.4: TLC images of the cathodically polarized side. Three different $CuSO_4$ concentrations at two different times during the electrochemical experiment are depicted. -0.3 V were set between the WE and $Ag|AgCl$ RE. The $CuSO_4$ was dissolved in deionized H_2O . (a) 0.1 M, at the beginning of the measurement. (b) 0.1 M, 1 h after initiating the measurement. (c) 0.05 M, at $t = 0$ h. (d) 0.05 M, 1 h after beginning the measurement. (e) 0.01 M, at the beginning of the measurement. (f) 0.01 M, after stressing for 1 h.

The interruptions in the i - t measurements are due to the intermediary EIS measurements that were performed. Figure 4.5 shows the capacitance versus measurement cycle or time for five different electrolyte concentrations. The capacitance, C , was calculated using equation (4.1) with $f = 100$ Hz.

$$C = \frac{1}{2\pi f|Z|} \quad (4.1)$$

The capacitance strongly increases in the measured interval for the 5×10^{-1} M sample, and roughly doubles for $\geq 5 \times 10^{-2}$ M. A $\sim 50\%$ gain is observed at $\geq 5 \times 10^{-3}$ M. This capacitance is connected to the electrochemical double layer at the electrode surface. The gain is therefore attributed to an increasing Cu surface area due to metal deposition. The initial surface was polished Cu. Formation of a rougher deposition layer leads to surface area growth and consequently to a higher capacitance value.

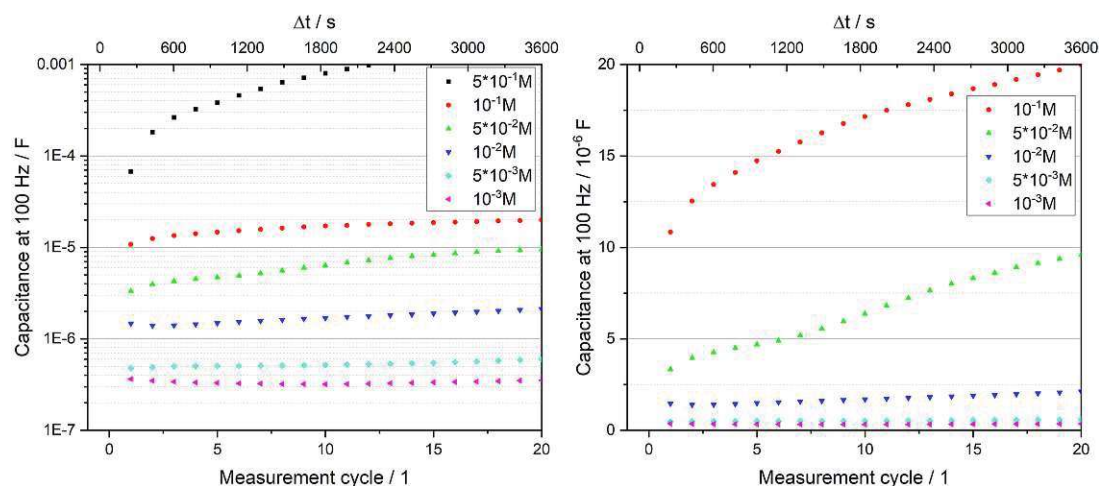


FIGURE 4.5: Capacitance versus cycle number (bottom x-axis) or versus time (top x-axis) for different CuSO_4 concentrations, as indicated in the legend. (left) Logarithmic y-axis. (right) Linear y-axis. Only a section of the left hand diagram is shown.

4.1.2 TLC - simulation

The data that was obtained from experiments, and presented above, together with information extracted from literature, served as the basis for the development of a 2D multi-element FEM simulation. The simulation model was described in the corresponding methods section (section 3.5). As stated there, thermodynamic (NP) and kinetic (Nernst and BV) equations were used to solve the simulation. The simulation was run for five different initial concentrations of Cu^{2+} , that were also measured experimentally, ranging from 0.1 mol L^{-1} to $10^{-3} \text{ mol L}^{-1}$.

In figure 4.6, both, experimentally determined and simulated, current density-versus-time as well as cell voltage-versus-time are depicted. The simulation supported the finding that the observed current response is mainly determined by the reduction/oxidation reaction $\text{Cu}^{2+} + 2 e^- \rightleftharpoons \text{Cu}$. Potential side reactions, like the HER, were found to contribute to the overall current density by less than one per mil. Looking at the figure, the fit is evidently imperfect. The complexity and in parts still insufficient understanding of the copper corrosion/deposition system make the simulation of this system complicated.^{273,274} A number of shortcomings of the implemented model can be identified. Copper precipitation in the bulk,

along pH gradients can deplete the solution of ions, and consequently increase the electrolyte resistivity. This is not implemented, but could explain the lower predicted cell voltage, compared to the experimental observation. The experimental *i-t* curves show multiple distinct regions for the higher initial concentrations of Cu^{2+} . The model includes neither surface inhomogeneities, nor surface changes. However, the microscope images showed changes both at the anode and at the cathode. As was seen in figure 4.5, the capacitance changes over time during the experiment, indicating that the surface area increases. While this effect was not included in the simulation, the plotted experimental current density was area corrected based on a curve fit of the observed capacitance change. The uncorrected values are those that were presented in figure 4.3. A similar effect at the anode surface has not been taken into account, that is oxide layer growth. The formation of an oxide layer reduces the supply of Cu^{2+} ions from the underlying copper surface, resulting in a diffusion limitation, and affects the electrode kinetics as a whole by changing the substrate. The formation of the Cu_2O layer was considered in the form of an increasing resistance due to the film growth, but the formation and growth of the layer itself were not included. With a value of $4.3 \times 10^{-10} \text{ m}^2 \text{ s}^{-1}$, the diffusion coefficient for Cu^{2+} is on the low side, but within the range of values reported in literature.²⁷⁵ For the exchange current density of the main reaction, a value of 8 A m^{-2} was found, again being reasonable when compared to other works.²⁵³ Both of these parameters were taken as fixed, with no concentration dependency. For the above reasons, increasing the complexity of the simulation could likely lead to a better fit, but was beyond the scope of this work.

With the simulation it was clearly shown, that the copper concentration is the most influential factor, determining the reactions occurring in the cell. The reduction of copper is the main reaction occurring at the cathode, and its reverse reaction is predominant at the anode. The formation of Cu_2O plays a critical role at this electrode, as well. The almost neutral environment ($\text{pH} = 5.5$, assuming saturation with CO_2) does not provide sufficient H^+ to drive the HER at significant rates.

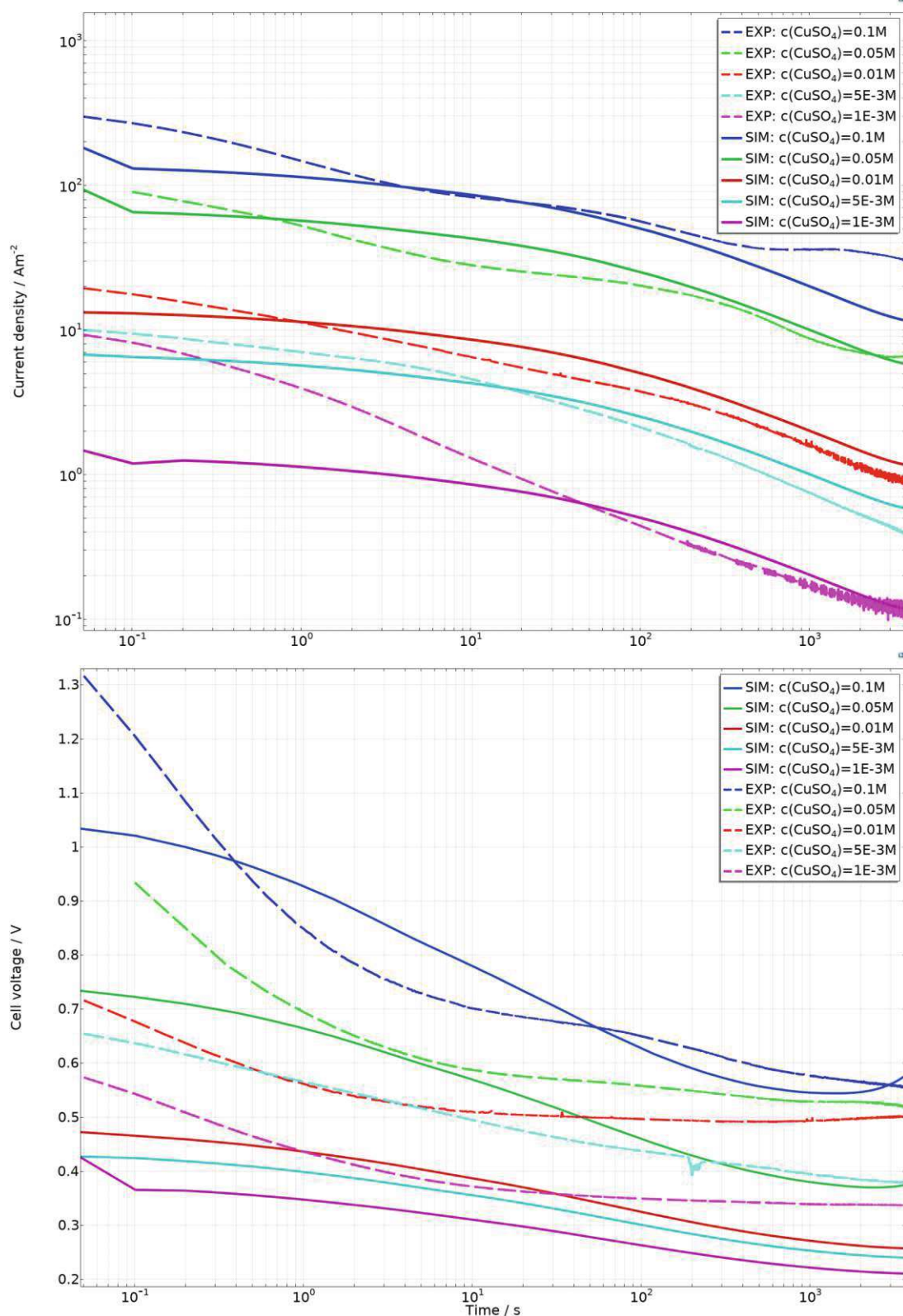


FIGURE 4.6: Comparison of experimental and simulated TLC results with -0.3 V vs. Ag|AgCl RE . **(top)** current density-versus-time. **(bottom)** Cell voltage-versus-time.

4.2 Miniaturized Test Chip

The TLC was intended to give a solid understanding of Cu electrochemistry in thin electrolyte layers. The MTC was designed as the next step to be able to investigate even smaller structures, at a scale that is found in electronic components. The first set of samples, without polymer protection, was used to ensure the functionality of and perform electrochemical measurements on the 'open' test structures. The second set of samples was covered with a thin organic coating, and was intended for stress tests and corrosion investigations in the presence of such a protecting layer.

4.2.1 Open MTC (without PI coverage)

As described in the methods chapter (3.2), solutions with different concentrations of CuSO_4 were applied on top of the MTC and the EIS response was recorded. These measurements were used to proof the functionality of the developed test structures.

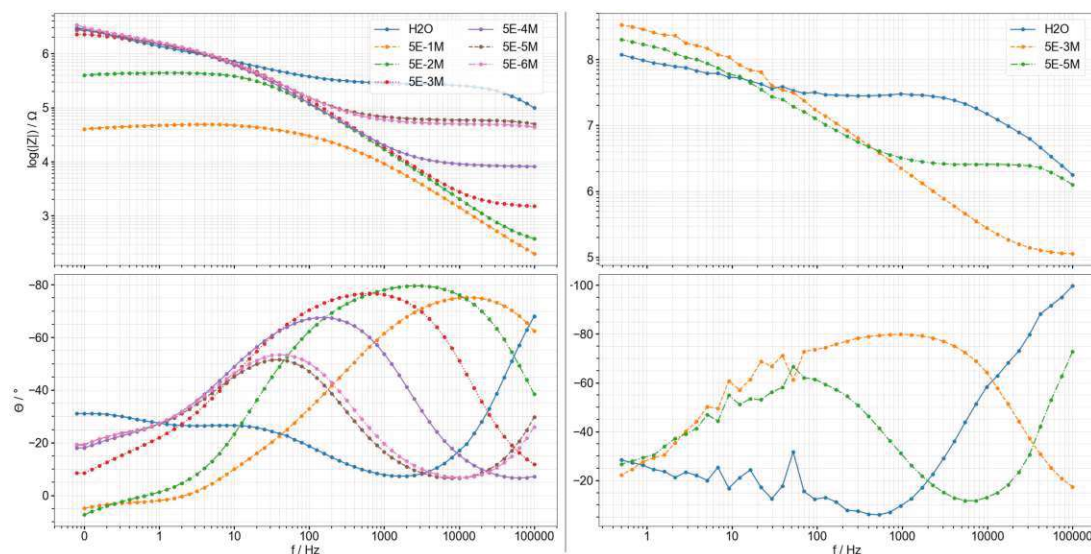


FIGURE 4.7: Bode plots obtained from EIS measurements on the open MTC. The applied CuSO_4 concentration is indicated in the legend. **(left)** Measurements performed on the *cm* structure. **(right)** Measurements performed on the *bd3* structure.

Figure 4.7 shows resulting Bode plots obtained for two different structures. The results clearly show a concentration dependency and confirm the functionality of the test structures. For example, extending the horizontal curve region observed for most curves in the upper graphs until they intersect the ordinate allows to extract the electrolyte resistance.

Two key differences in corrosion behavior between the TLC and the open MTC became evident during the experiments performed with this setup:

1. The anode (Cu sheet) used in the TLC was like an infinite Cu reservoir from which Cu^{2+} ions could be generated. On the MTC on the other hand, the supply of Cu was limited and anodic dissolution played a major role. This is evidenced by microscopic images (a), (b), (f), and (h) in figure 4.8.
2. Building on the previous point, at high CuSO_4 concentrations ($\geq 10^{-3} \text{ mol L}^{-1}$) no dendrite growth was observed. Instead, the anode dissolved fully, and a homogeneous deposition layer was formed on the cathode. In the TLC setup, dendrite growth had been observed under similar conditions. In the MTC setup, dendrite growth was only observed once the initial Cu^{2+} concentration was reduced to $10^{-4} \text{ mol L}^{-1}$ or below (figure 4.8 (b)-(i)). Considering that the structures are shrunk by a factor of $\sim 100 - 1000$ compared to the TLC, this finding can be explained. As mentioned earlier, a diffusion limited zone is usually needed for dendrites to form. Due to the much smaller geometry, high concentrations result in a complete dissolution of the anode before a sufficiently large depletion, i.e. diffusion limited, zone can form near the cathode to change from uniform deposition to the formation of electric trees. Since an electrolyte drop is applied in this setup, the bulk solution is much larger in relation to the electrode area compared to the TLC, which further reduces the depletion of ions.

One of the structures, *bd3*, deviated markedly from the rest of the observations (figure 4.8 (g)). No dendrite growth was observed, instead strong discoloration and a corrosion front around the cathode. In between the electrodes of this structure, three small, open Cu bands had been placed to sense capacitance and potential changes in the electrolyte. While these sensing bands were not actively biased during the electrochemical experiments, they appeared to influence the measurement results. This structure, and similarly designed ones, were therefore deemed not functional. The rest of the tested structures was found to be operational and sensitive to changes in their environment, especially when they were shorted due to dendrite growth.

4.2.2 MTC with PI coverage

After testing the general functionality of the various structures on the open MTC, the focus was laid on the MTC with a polyimide protection layer. Two types of electrolytes were applied in these experiments, containing ions of commonly used metals in the semiconductor industry: Cu and Ag. Adding silver as ion to investigate seemed like a reasonable choice, based on the available literature. Literature on ECM, and related topics suggest that Ag migrates more easily than Cu, therefore potentially making it suitable as a faster model system than Cu. Its electrochemistry is also less complex since it has only one relevant oxidation state (Ag^+), as opposed to two for Cu (Cu and Cu^{2+}). This results in a reduced number of possible reactions.

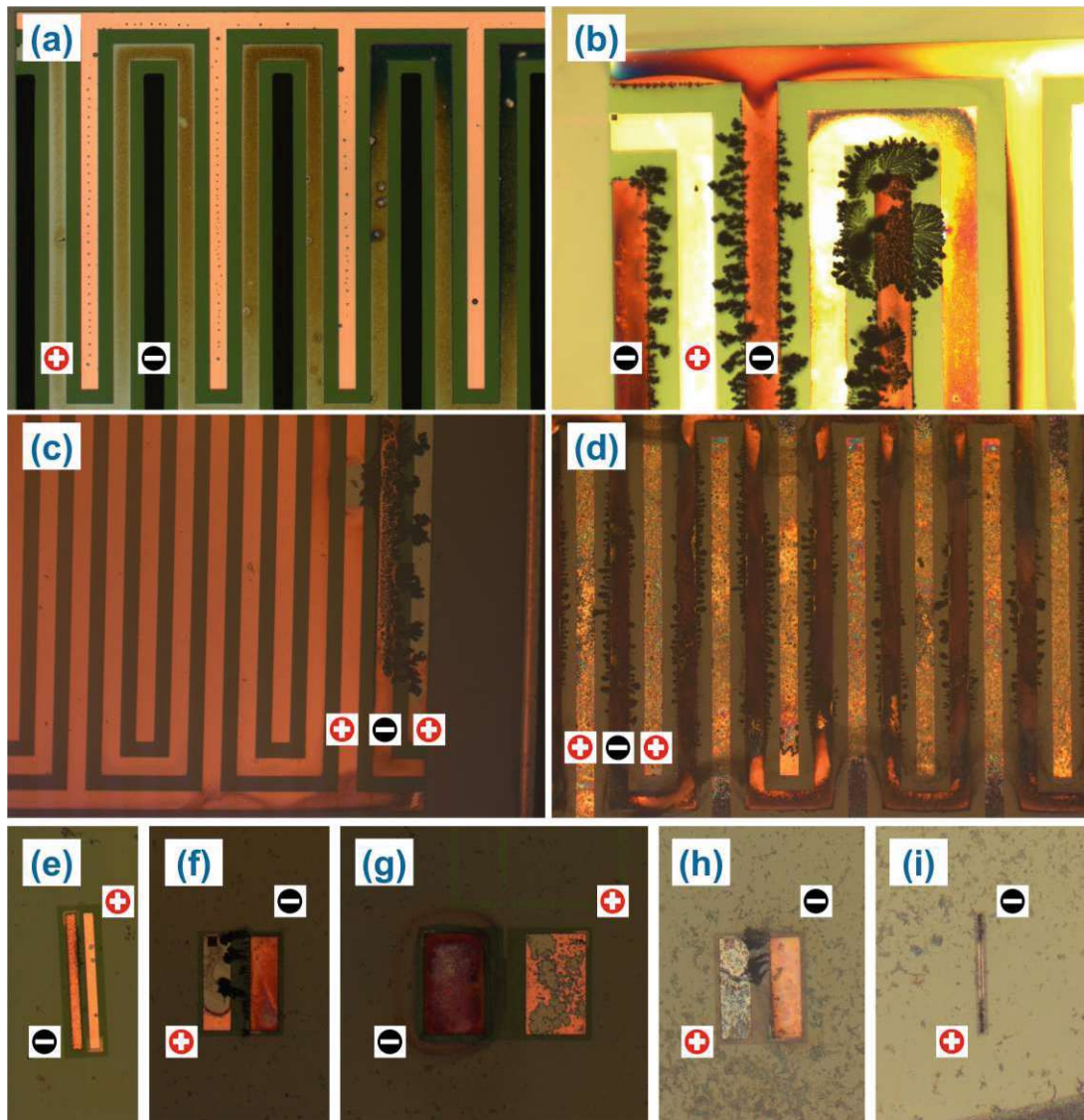


FIGURE 4.8: Exemplary microscopic images depicting the observed corrosion phenomena after electrical stress tests at selected MTC structures. (a) *cm* structure: 0.5 V bias, $10^{-2} \text{ mol L}^{-1} \text{ CuSO}_4$ (in $10^{-4} \text{ mol L}^{-1} \text{ H}_2\text{SO}_4$) solution dropped on the sample surface. (b) *cm* structure: 0.5 V bias, $10^{-4} \text{ mol L}^{-1} \text{ CuSO}_4$ (in $10^{-4} \text{ mol L}^{-1} \text{ H}_2\text{SO}_4$). (c) *cm* structure: 1 V bias, $10^{-4} \text{ mol L}^{-1} \text{ CuSO}_{4(\text{aq})}$. (d) *cm* structure: 1 V bias, $5 \times 10^{-6} \text{ mol L}^{-1} \text{ CuSO}_{4(\text{aq})}$ (in ultra-pure water). (e) *bd1* structure: same conditions as (b). (f) *bd2* structure: same conditions as (c). (g) *bd3* structure: same conditions as (c). (h) *bd2* structure: same conditions as (d). (i) *bd4* structure: same conditions as (d).

To better understand the detrimental influence of ionic impurities on the performance of electronic components, a controlled metal loading was desired. Autoclavation was tested as a possible method, but proved unsuitable to this end. An increased conductivity was observed with EIS for some samples, but not in a reproducible, well controlled manner. This method was therefore not further used.

Next, driving ions into the organic coating was tested. This experimental procedure is described in section 3.2. These experiments revealed a significant shortcoming of the given test setup. Putting an electrolyte on top of the polymer coating and applying bias resulted in shorts, but not, as intended, at the biased structures. Instead, the interface PI/electrolyte/epoxy resin proved to be a weak spot, allowing for corrosion at the bond pads. An example of such a failure, with the electrolyte still on top of the sample, is depicted in figure 4.9 (left).

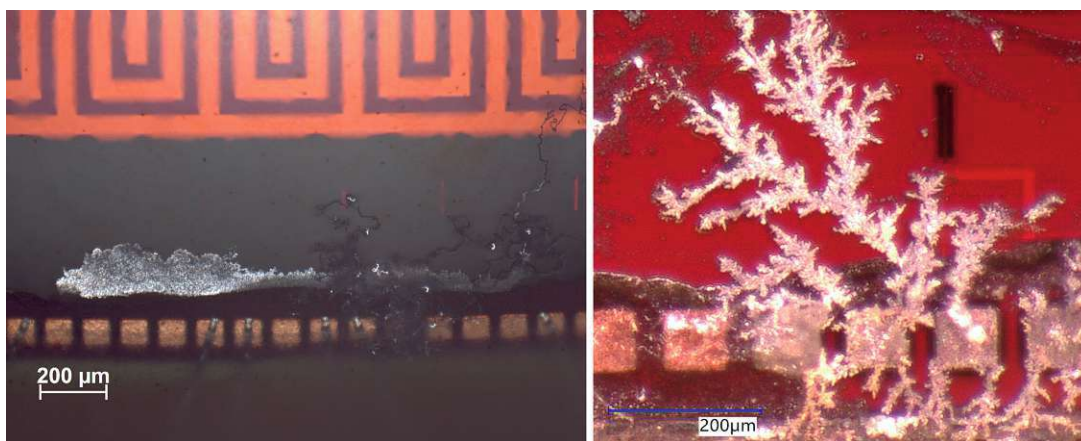


FIGURE 4.9: Exemplary short circuits near the bond pads on the MTC. **(left)** Ag deposit and filaments observed after application of 20 V for seven days with $0.1 \text{ mol L}^{-1} \text{ AgNO}_3$. **(right)** Dendrites observed after application of 100 V for 19 days.

To circumvent this issue, small electrolyte reservoirs were 3D printed with an epoxy resin printer. These were then glued on the sample. Great care was taken to not accidentally place the reservoir on the structures that were to be investigated. This was checked under a microscope, and only samples where this was achieved successfully were used for further tests. Notwithstanding, similar issues as before were encountered when performing the electrical stress tests, albeit after longer measurement periods. Post-mortem analysis revealed that imperfections in the glue layer allowed for electrolyte paths, which in turn enabled a similar failure mechanism as in the prior experimental series (figure 4.9 (right)).

The combination of samples and methods tested with the MTC proved unsuitable for achieving a controlled, ion assisted/driven failure. The decision was made to explore other options. In the end, a suitable alternative was found in the form of the ITC.

4.3 1x1 Interdigitated Test Chip

In this section the results obtained with the 1x1 Interdigitated Test Chip are presented and discussed. While establishing a satisfactory setup and procedure for controlled ion migration for the MTC samples proved troublesome, such a setup was successfully developed in parallel

for the ITC samples. Details about this setup and the procedure are provided in the respective methods section (section 3.3). The simulation setup was described in the corresponding part of chapter 3.5.

4.3.1 ITC - experimental

Since the investigated currents were expected and found to be low (i.e. (sub-) nano range), at first the stray current of the used instruments and setup was determined. To this end, the cell was assembled as per the description in the method section, and the wire and one comb side were connected. However, no electrolyte was filled into the cell, leaving an air-filled gap between the two electrodes. The desired bias voltage (550 V) was applied and the current was measured for 15 h. The results are depicted in figure 4.10. From these, the limit of detection for the current measurements can be set at (the order of 1 to) roughly 10 pA.

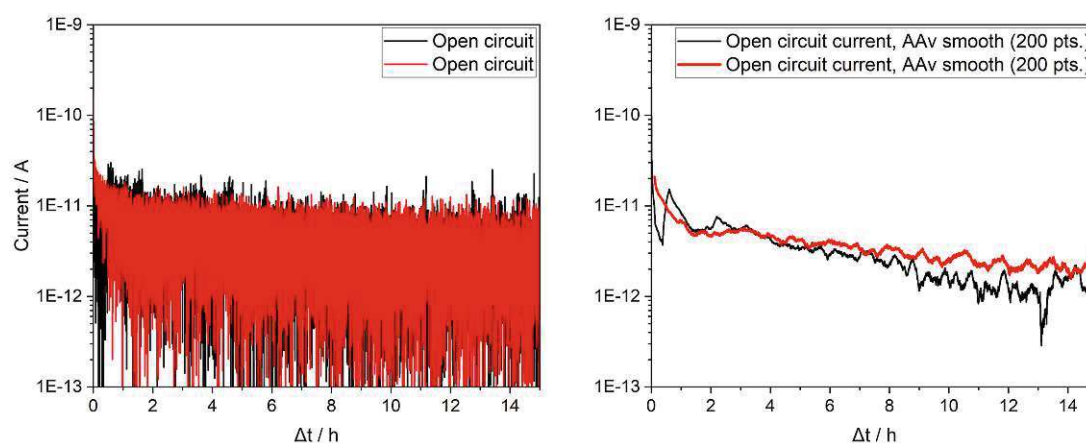


FIGURE 4.10: Two independent open circuit current versus time measurement results. Both electrodes were connected, but no electrolyte was filled into the cell electrolyte volume, leaving an air gap between the two electrodes. **(left)** Original and **(right)** smoothed (adjacent average, window width = 200) measurement signal.

Electrochemical Impedance Spectroscopy measurements between the two IDE sides were used to probe the initial properties of the polymer protection layer and to test, whether irregularities in the initial state of a sample were observed (EIS type A). If irregularities were observed, the sample was not used. All samples presented in the ITC part of this chapter originated from the same wafer. The median value for the stray capacitance of the cell and cables was determined to be 15 pF. To determine this value, one comb side was connected to the instrument, and the clamp for contacting the second comb side was placed next to the sample, without establishing contact.

For each electrolyte the following measurements were performed: (i) current density-versus-time (i-t) at constant bias, (ii) Electrochemical Impedance Spectroscopy (EIS), and (iii) Laser Ablation - Inductively Coupled Plasma - Mass Spectrometry (LA-ICP-MS). As stated

in chapter 3.3, two variants of EIS measurements were performed: between the two sides of the IDE (EIS type A), as well as between the side of the IDE that was biased during i-t measurements and the metal spool in the electrolyte (EIS type B).

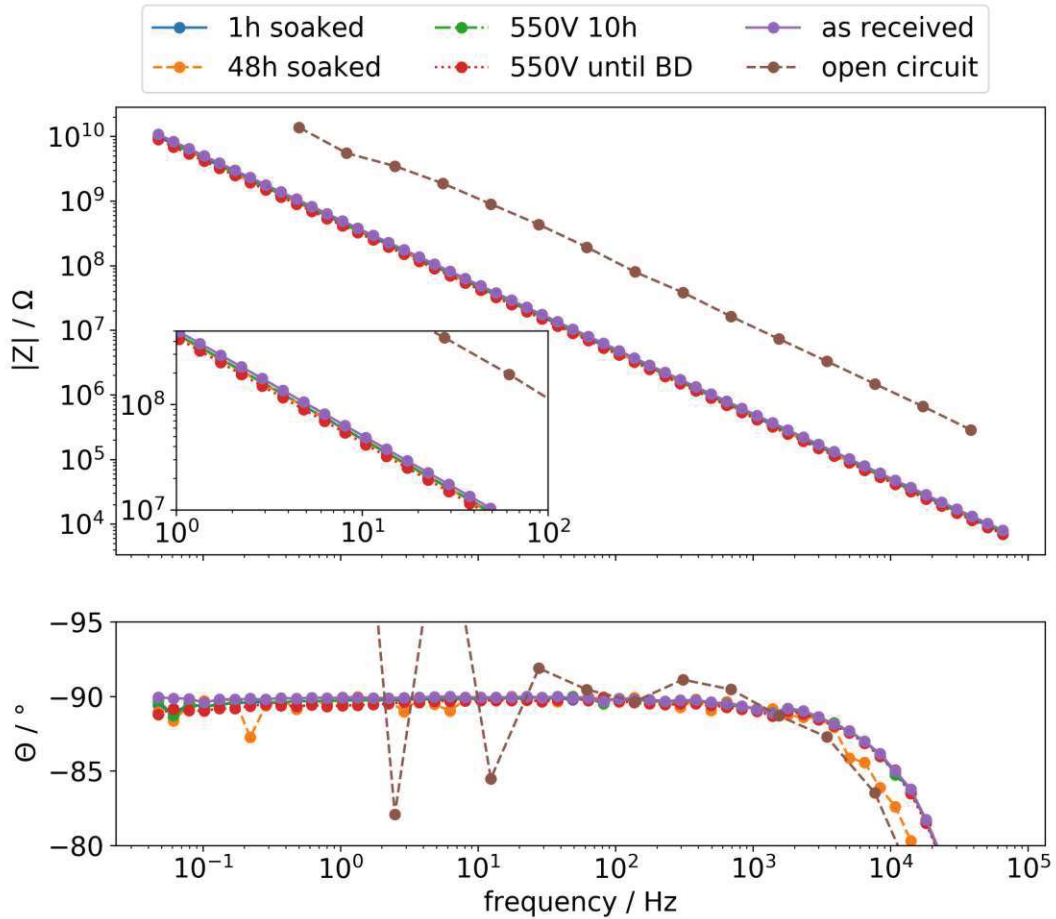


FIGURE 4.11: Bode plot of typical EIS results (EIS type A) after subjecting the samples to the given stress conditions for the given time span. **(top)** Absolute value of the impedance versus frequency. The inset magnifies a part of the given spectrum. **(bottom)** Phase angle versus frequency.

Figure 4.11 depicts representative EIS spectra for selected stress conditions and time spans (EIS type A). Unsurprisingly, the figure reveals a distinct difference between open circuit measurements and measurements with the sample cell connected. However, with the bare eye, curves in the dry and wet state, as well as in the (wet) treated state are barely discernible. Both, phase angle and absolute value of the impedance show a purely capacitive behavior at frequencies below 1000 Hz. The deviation in the phase angle at higher frequencies originates from the used current amplifier, and hence does not contain meaningful information about the sample. Since the impedance behavior in the spectra is purely capacitive (in the measured frequency region), a very simple electrical equivalent circuit was at first chosen to fit the data. A parallel circuit consisting of two capacitors, C_{stray} and C_{sample} , was used (figure 4.12).

The former was estimated through an open circuit measurement during which the electric circuit was not closed after the sample cell. This approach allows to distinguish between the influence of the leads on the total capacitance, represented by C_{stray} , and the contribution of the sample itself, C_{sample} , and is needed because parallel capacitors can not be separately determined in a single measurement.

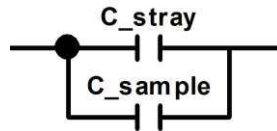


FIGURE 4.12: Electric equivalent circuit used for fitting the impedance data obtained during the ITC experiments. The circuit was drawn using ZView®, version 3.5g, by Scribner Associates, Inc.

Putting together the results from all measurements with different electrolyte solutions, box plots were created. Figure 4.13 portrays the results for (left) EIS type A and (right) EIS type B (left) experiments.

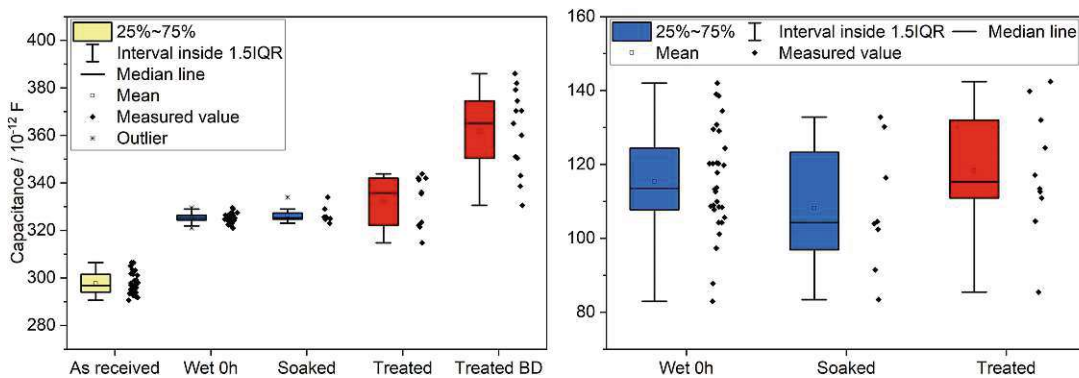


FIGURE 4.13: Box chart diagrams depicting the fitted values for C_{sample} . Underlying data points for the individual box plots are shown to the right of the corresponding boxes. Samples are categorized in 5 groups. (1) 'As received': The cell was assembled, but no electrolyte had been added. (2) 'Wet 0h': The sample was measured within the first hour after addition of the electrolyte to the cell. (3) 'Soaked': Samples were left standing with electrolyte on top for 24 or 48 h. (4) 'Treated': In addition to the electrolyte the samples were biased at 550 V for 5, 10 or 20 h. (5) 'Treated BD': Samples were measured after the failure criterion had been reached. (left) Results from EIS type A experiments. (right) Results from EIS type B experiments.

Looking at the top graph, the capacitance of the samples increases by ~ 10 % or 30 pF upon addition of the electrolyte, with respect to the 'as received' state. Increased soaking times do not further increase this value. With

$$t \sim \frac{t_{PI}^2}{2 \cdot D_{H_2O,PI}}$$

and $D_{H_2O,PI} \sim 10^{-10} \text{ cm}^2 \text{ s}^{-1}$ (see table 2.4), the diffusion time, t , through the whole PI layer with a thickness, t_{PI} , of $7.7 \mu\text{m}$, lies at $\sim 2800 \text{ s}$. Therefore, especially since the samples were not dried before use, it can be assumed, that the sample is widely saturated with H_2O from the beginning. Hence, no difference is observed for prolonged soaking times. Exposing the sample to several hours of electrical stress without BD increases the scattering of the observed values. In the type A experiments, the median is slightly increased, but not significantly (figure 4.13 (left)). After the BD, the median value of the sample capacitance increases once more, by another $\sim 10 \%$ or 30 pF compared to the 'as received' samples. The box plot diagrams depicted in the bottom graph (EIS type B experiments) on the same figure do not reveal any differences. 'As received' measurements were not possible in this setup, as they would essentially be equal to open circuit measurements (without electrolyte). 'Treated BD' samples were not included, since the BD effectively resulted in a short circuit. Findings regarding BD and failure of the insulation will be discussed in more detail later in this chapter.

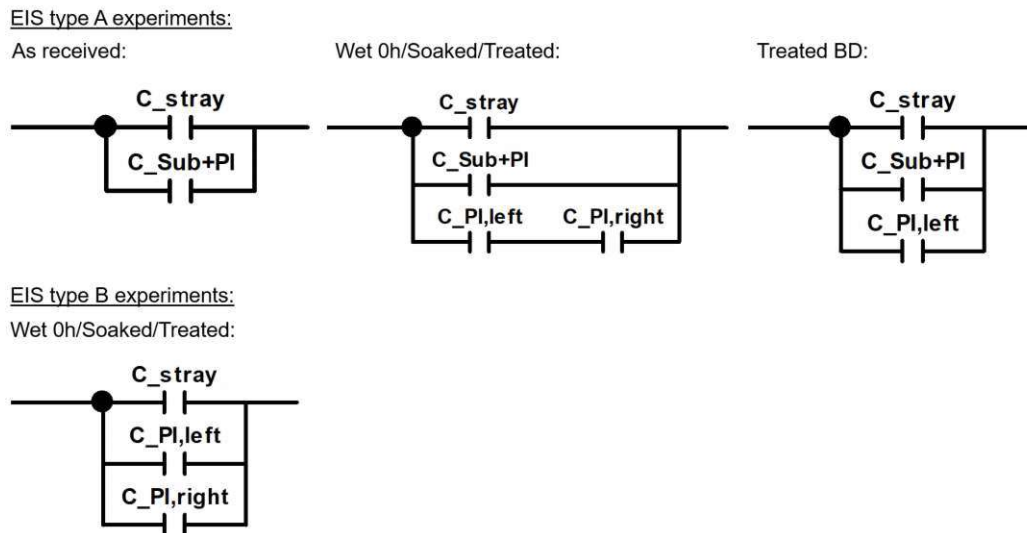


FIGURE 4.14: Revised electrical equivalent circuits used for evaluating the impedance data obtained during the ITC experiments. Circuits were drawn using ZView®, version 3.5g, by Scribner Associates, Inc.

Based on the observed impedance response, revised equivalent circuit models were developed for the different states (figure 4.14). The underlying considerations are presented in figure 4.15. The schematic cross sections in the figure describe bulk resistances and capacitances for (a-c) EIS type A and (d) type B experiments. The designations ' $R \gg$ ' and ' $R \ll$ ' indicate that the expected value of that resistance is very high or low, respectively. Since the behavior observed in the EIS spectra (figure 4.11) is purely capacitive, paths containing ' $R \gg$ ' were not included in the equivalent circuits. Very low resistance values essentially behave as electric shorts and are therefore not explicitly represented in the models in fig-

ure 4.14, either. Two conduction paths, via the substrate, and across the PI layer between the electrodes contribute in all schematics in figure 4.15. However, they can not be separated with the available EIS measurements. They form a collective variable, C_{Sub+PI} , in figure 4.14. Application of an aqueous electrolyte opens up a conduction path orthogonally to the electrode fingers, which plays an important role for measurements between the combs. The twofold polyimide thickness above the electrodes is smaller than the distance between the IDE fingers (15.4 μm and 50 μm , respectively). In the type B experiments, C_{Sub+PI} can be neglected as it lies in parallel between (only) $C_{PI,right}$ and $C_{PI,left}$, as evident from figure 4.15. With the revised equivalent circuits, the three distinct capacitance levels observed in figure 4.13 (left) can be well described. C_{Sub+PI} was calculated and lies slightly below 300 pF, $C_{PI,right}$ and $C_{PI,left}$ are equivalent, with values of ~ 55 pF.

To facilitate understanding, the remaining results and observations for each of the investigated electrolytes are first presented and discussed separately, before general findings and their validity are proposed and challenged. As mentioned in the corresponding 'experimental' section (3.3), 550 V were used in all i-t stress tests.

Copper electrolyte

All measurements presented in this subsection were performed with an electrolyte containing 0.1 mol L⁻¹ Cu(NO₃)_{2(aq)}. A total of 14 samples was used in the experimental series. Four samples were soaked, two for 24 h and 48 h each, another four samples were electrically biased, again two for 10 h and two for 20 h. A total of six samples was stressed until BD was observed, i.e. until the insulation failed.

Figure 4.16 depicts two graphs. Both contain the obtained i-t data for the experiments with a Cu(NO₃)_{2(aq)} electrolyte, with a logarithmic x-axis in the top graph. Before BD, the measured current response shows a similar behavior for all samples and the order of magnitude is the same. Four regions can be identified:

1. **Decrease** ($t < 0.5-1$ h): During the first (half) hour, a decrease in current density is observed.
2. **Constant** ($0.5 - 1 \leq t < 4-10$ h): After the initial decrease, the current evens off. In this stage the current flow remains widely constant.
3. **Decrease** ($4-10 \text{ h} \leq t < t_{BD}$): In this intermediary region, the current density decreases once more. For some samples, this decrease is followed by another current density plateau, before the final stage is reached.

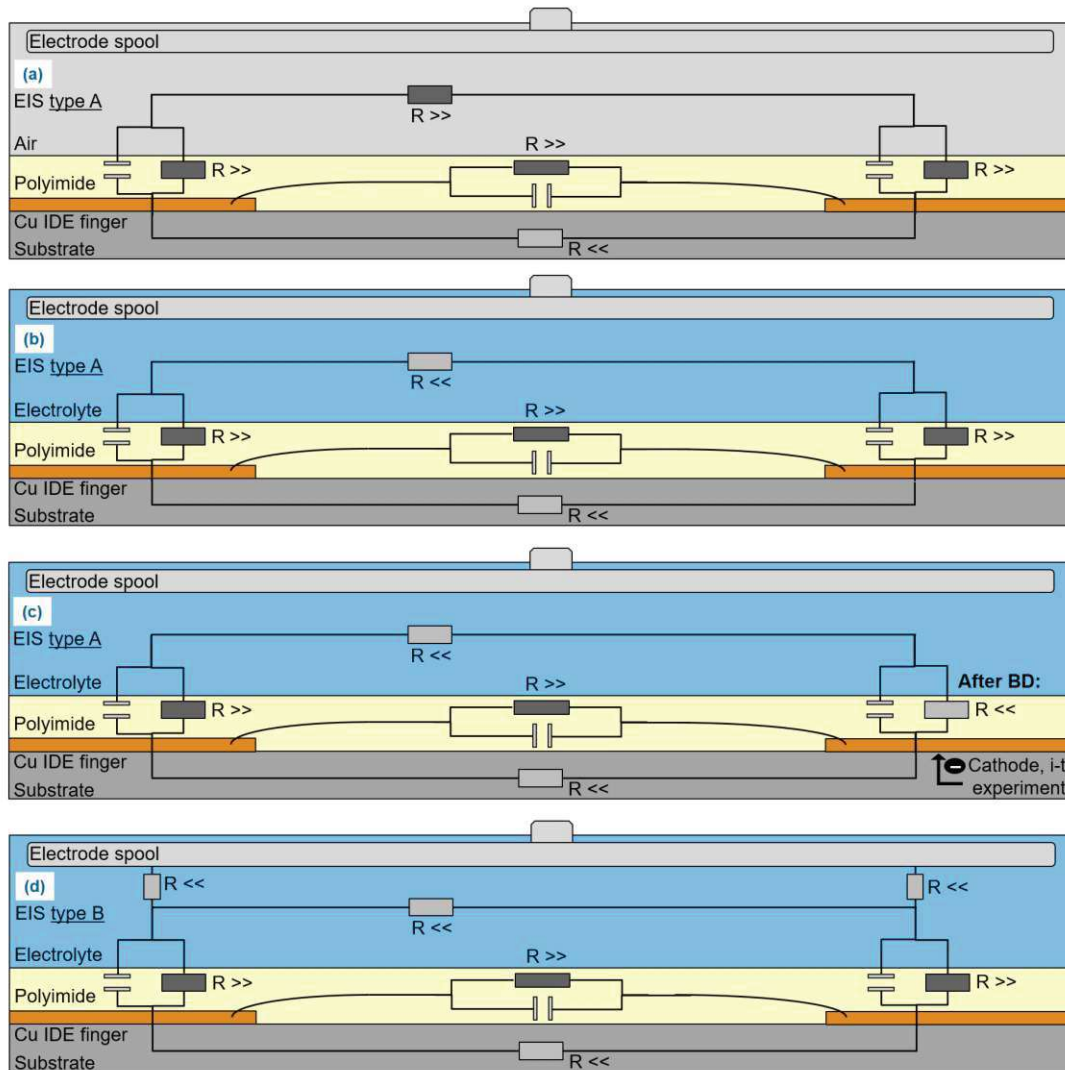


FIGURE 4.15: Schematic cross sections of the cell for different conditions and experimental setups. Expected bulk resistances and capacitances are included. Cross sections (a-c) represent EIS type A, and the cross section in (d) corresponds to EIS type B experiments. (a) Schematic for 'as received' experiments. Since no electrolyte is present, a very high resistance is observed in the (air filled) electrolyte volume and the conduction paths leading orthogonally through the PI layer are eliminated. The impedance signal is dominated by the substrate, and in part by the polymer. (b) Schematic for 'wet 0h''/soaked''/treated' experiments. The presence of a low resistance electrolyte opens up a new conduction path via the electrolyte. (c) Schematic for 'treated BD' experiments. BD of the electrical insulation results in a low resistance pathway along the failed IDE side (cathode in the i-t measurements). This renders the influence of this comb side negligible. (d) Schematic for 'wet 0h''/soaked''/treated' EIS experiments (type B). Two conduction paths are formed. One through the electrolyte, across the polymer, and directly to the connected IDE side. The other, indirect path first leads through the electrolyte and across the polymer as well, but is then indirectly coupled via the disconnected IDE side, via the substrate or polymer layer.

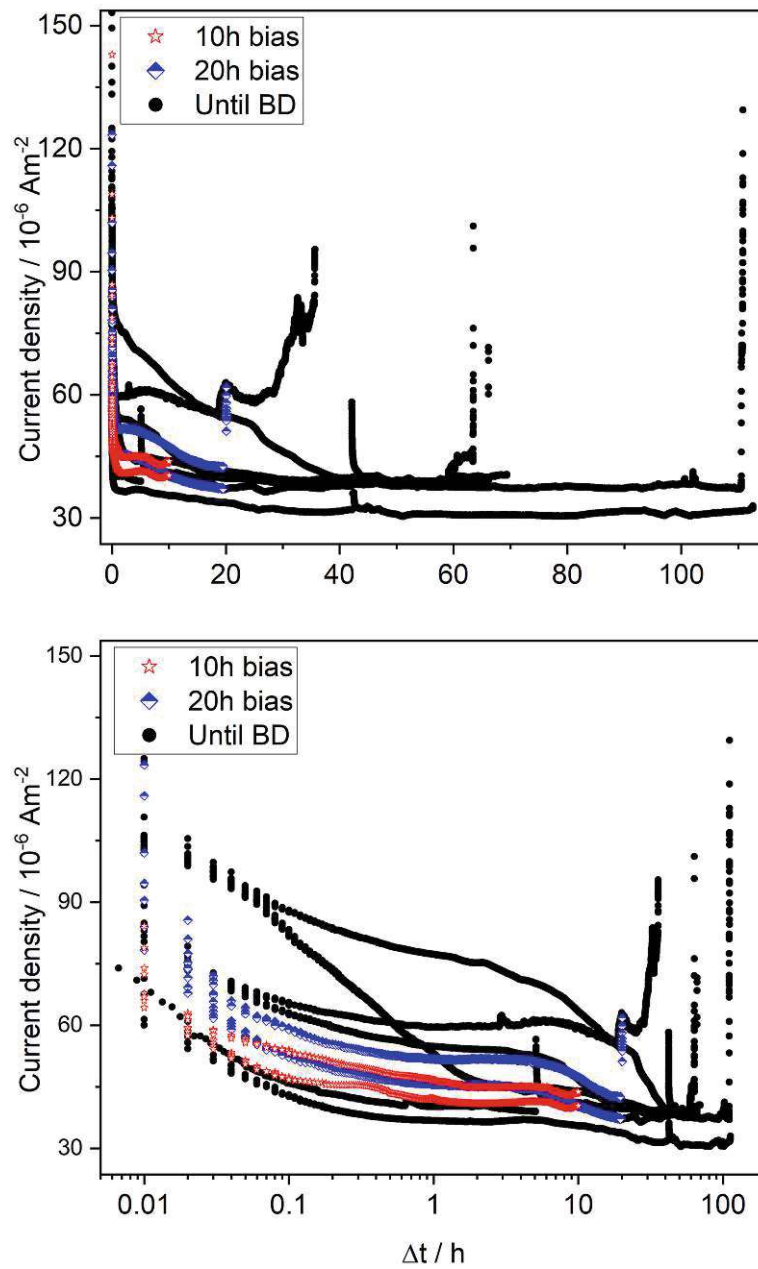


FIGURE 4.16: Current density-versus-time relationship obtained for experiments with a $\text{Cu}(\text{NO}_3)_2(\text{aq})$ electrolyte at 550 V bias. The samples are grouped based on the duration of the electric stress tests. Samples in the same group use the same colors and markers. **(top)** Both axes are given in a linear scale. **(bottom)** A logarithmic x-axis is used.

- Increase and breakdown ($t \sim t_{BD}$):** The time before BD is characterized by a slightly increasing current density. This increase takes between minutes up to several hours. Finally, there is a steep current increase, reaching the set limit at 105 nA, signaling that the insulation has failed.

In stage 1 a linear decay is observed (figure 4.16 (bottom)), indicating an exponentially decreasing current. This behavior is typical for the charging of a capacitor and is (likely) controlled by the formation of space charges in the (water saturated) PI protection layer near the interfaces (metal and aqueous electrolyte). This assumption can be based, e.g., on the findings by Kaneko et al.¹⁹³, obtained for a water-treated PI film in a MIS structure at room temperature. The behavior and order of magnitude of the current density agrees well with their observations. It should be noted that the maximum electric field gradient in their measurements was 50 MV m^{-1} , which is lower than the $\sim 70 \text{ MV m}^{-1}$ used in this work. Furthermore, a constant current region can be observed in their experimental curves after roughly 20 min application of bias voltage, similar to that in stage 2 of this work. In their work, the behavior did not notably change until the end of their measurements (after 90 min).¹⁹³ According to Guinane et al.¹⁹² and references therein, the decay could be explained by the gradual filling of trap sites in the polyimide, likely with electronic charge carriers. The additional minor decrease in stage 3 cannot unambiguously be attributed. It is possible that at this point the cation from the electrolyte show a significant influence. Cu^{2+} ions are driven from the aqueous electrolyte reservoir into the bulk of the polymer, and substitute mobile ionic or electronic species. Another possibility is that no ions enter the polymer film from the electrolyte. Instead, initially present residual, mobile ionic contaminants are available at first, but consumed by the end of stage 2. Both options explain a decreasing overall current flow, assuming that Cu^{2+} is less mobile in the PI film than the substituted species. Electronic charge carriers (e^- or h^+) likely play a role for mechanism 1, and are strictly necessary for mechanism 2. In fact, if the second proposed mechanism holds true, this would implicitly mean that BD is caused electrically and not ionically, since no ions would be present at t_{BD} .

To better elucidate the role of the aqueous cation that is available in the electrolyte solution, LA-ICP-MS was employed. This method allows for relatively quick analysis of various elements in μm thick polymer layers. It is described in detail in the corresponding section (3.4).

To assess the impact of the aqueous electrolyte on the copper content in the PI film, LA-ICP-MS 'images' were created. To this end, the same area was ablated three consecutive times. Each ablation pass is referred to as 'layer', and the layers were enumerated L1, L2, and L3, where L1 is the topmost layer, i.e. the layer that was in direct contact with the aqueous electrolyte. The sampled area extended from one biased comb finger to another, encompassing one of the unbiased IDE fingers. The idea was that, if the ions contained in the electrolyte entered the polymer, they would enter above the electrode fingers of the biased comb side toward the same. On the other hand, the polymer film above the unbiased film should not be affected (as much). Therefore, a difference should be observable between biased and unbiased electrode, as well as in the gap between. The results are depicted in figure 4.17.

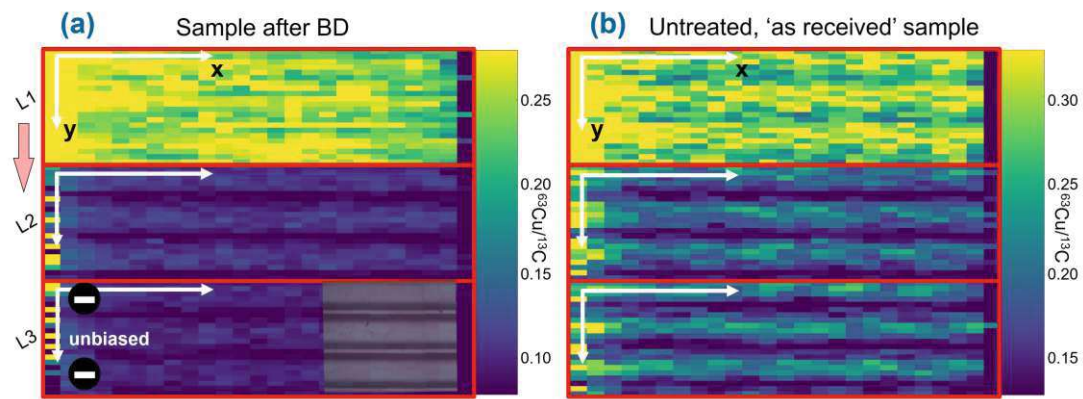


FIGURE 4.17: LA-ICP-MS images of ITC samples. Each image consists of three ablated layers. L1 to L3 denominate the ablation passes, where L1 is the topmost layer. A schematic illustration is shown in figure 3.8. **(a)** LA-ICP-MS image of a sample that was electrically stressed until BD, with a $\text{Cu}(\text{NO}_3)_2(\text{aq})$ electrolyte on top of the sample. The colors represent the measured ^{63}Cu signal normalized to ^{13}C . The denomination 'unbiased' and the minus sign on the IDE indicate the polarity of the respective comb side during the electrical stress tests that were performed prior to LA-ICP-MS analysis. The inset in the bottom right of this graph shows an overlaid optical micrograph. **(b)** LA-ICP-MS image of an untreated, 'as received' sample. The colors represent the measured ^{63}Cu signal normalized to ^{13}C .

Looking at figure 4.17 (a) allows a number of observations:

1. In all three layers a strong Cu signal is observed, indicating the presence of Cu in either the ionic or atomic state.
2. The topmost layer (L1) of the sample clearly shows an increase in Cu content, when compared to the underlying layers.
3. In L2 and L3 an increased Cu signal is observed above the combs, compared to the gap region.
4. There is barely a change in Cu signal intensity from L2 to L3.

At first glance, observations 1 and 2 imply that Cu^{2+} ions from the electrolyte enter the polymer film during the treatment. However, upon comparison with figure 4.17 (b) it becomes clear, that the same effect is observed in the untreated, 'as received' sample. It is not surprising that the PI already contains a measurable amount of Cu ab initio, since this is a well known observation for PI in direct contact with this metal.¹⁶⁹ Since the increased Cu signal in the top most region is observed both in the treated and the untreated sample, this is apparently an inherent property of the PI films as well, and not a result of the electrolyte reservoir. In both samples in L2 and L3 the underlying comb structure becomes visible. This is the same for both samples, and no difference between biased and unbiased fingers are observable. Thus, observation 3 is likely an effect of the curing step, in which Cu is dissolved by the polymer.

Concluding, the images reveal that a high amount of Cu is prevalent already in the native PI film, but the electrical stress in the presence of an aqueous electrolyte does not result in an additional increase. Either, no ions migrate or diffuse into the protective layer, or the initial Cu content is too high for Cu to detect a significant difference with respect to this baseline. As this analytical technique cannot distinguish between atomic and ionic states, no information about the oxidation state of the samples can be obtained. Further LA-ICP-MS analyses on soaked, stressed and untreated samples confirmed these observations and conclusions.

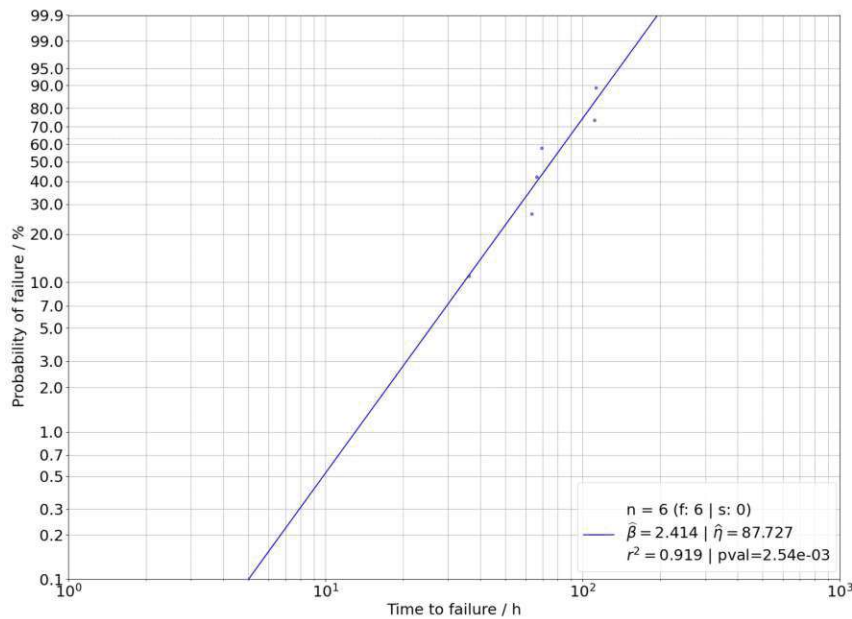


FIGURE 4.18: Weibull plot and calculated values based on the TTF obtained for the electrical stress tests with $\text{Cu}(\text{NO}_3)_2(\text{aq})$ electrolyte.

From the electrical stress tests, the TTF was extracted, at the point in time at which BD of the insulating film occurred. With this information, a Weibull plot was created and failure parameters were extracted, see figure 4.18. The $\hat{\eta}$ value, signifying a 63.2 % failure probability, lies at ~ 88 h. The $\hat{\beta}$ value of 2.4 indicates that it is a wear-out or aging type of failure, corresponding to the third region of figure 2.1. This is the type of failure that would be expected and aimed for in the performed type of experiments. As a caveat, it should be noted that the sample size was limited to six values, which certainly poses a limitation to the certainty with which conclusions based on statistics can be drawn.

Identification of the location(s) of BD was not possible using an (optical) microscope, without an additional step. Therefore, the cells were assembled once again, and $\text{Ag}_{(s)}$ was electrodeposited for a minute from a $\text{AgNO}_3(\text{aq})$ solution. This allowed for localization of the failure location with the microscope, as the Ag deposits strongly reflect light. It was found, that BD occurred at a single point on the sample. Identification of and findings regarding the failure location will be discussed in more detail in the following section, with $\text{AgNO}_3(\text{aq})$.

Silver electrolyte

All measurements presented in this subsection were performed with an electrolyte containing $0.1 \text{ mol L}^{-1} \text{ AgNO}_{3(\text{aq})}$. A total of 16 samples was investigated. Four samples were soaked, two for only 1 h, the other two for 24 h. Another four samples were electrically biased, two for 5 h and two for 10 h. Eight samples were electrically stressed until BD was observed, i.e. until the insulation failed.

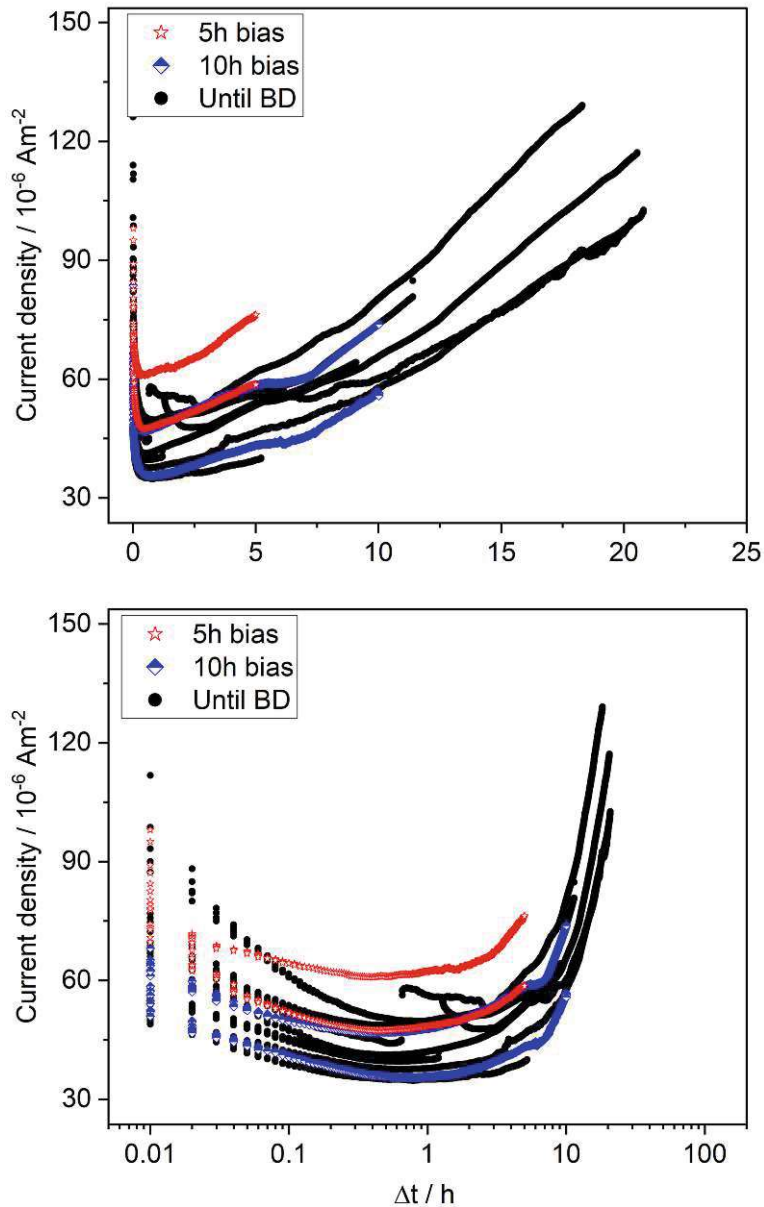


FIGURE 4.19: Current density-versus-time relationship obtained for experiments with a $\text{AgNO}_{3(\text{aq})}$ electrolyte at 550 V bias. The samples are grouped based on the duration of the electric stress tests. Samples in the same group use the same colors and markers. **(top)** Both axes are given in a linear scale. **(bottom)** A logarithmic x-axis is used.

Figure 4.19 shows the results from the experimental series that was measured with the Ag^+ ions containing electrolyte. For better comparison, the same style was chosen as in the previous figure that detailed the Cu measurements (figure 4.16). Once again, a number of common features was observed in between the Ag experiments:

1. **Decrease** ($t < 0.5\text{--}1\text{ h}$): During the first (half) hour, a decrease in current density is observed.
2. **Increase** ($0.5 - 1 \leq t < 5\text{ h}$): After the initial decrease, the trend inverses. In this stage, the current flow increases.
3. **Constant** ($5 \leq t < 6\text{--}10\text{ h}$): In this intermediary region, some curves exhibit a current density plateau. Other curves do not have a constant current region, but changes in the slope are observable.
4. **Increase and breakdown** ($6 - 10\text{ h} \leq t \leq t_{BD}$): The time before BD is characterized by a notably increasing current density. This increase continues over the course of several hours. At the point of BD, at t_{BD} , the sampled signal increases almost instantly, reaching the set limit at 105 nA. The insulation has failed.

The stage 1 behavior of these samples is very similar to the behavior observed for the Cu electrolyte samples. This strengthens the previous assumptions, that this stage is dominated by the dielectric properties of the (water saturated) polymer film. To show this more clearly, the measured current density during the first 0.5 h of the 10 h electrically stressed samples is portrayed in figure 4.20, for both electrolytes. In the first 0.1 h (6 min), a strong decrease of the current is observed, the result of charging effects in the dielectric. Later this effect is less pronounced, resulting in only a weak decrease and flattening off of the curve, towards the end of stage 1.

After the first stage, the behavior observed in this experimental series deviated markedly from that of the previous experiments with copper. This points at a significant influence of the employed cation provided via the electrolyte. As stated in chapter 2.4, a similar influence, namely of Ag ions on the stability of thin inorganic dielectrics in electric fields has been reported before.²²⁶ Two mechanisms have been proposed to explain the decreasing current densities observed in stage 3 of the previous, first ITC experimental series: substitution of mobile ionic or electronic species by the cation in the electrolyte (mechanism 1), or total consumption of initially available mobile contaminants in the polymer film, without ingress of cations from the electrolyte (mechanism 2). If the second mechanism was the key driver, then a similar behavior should be observed, irrespective of the available electrolyte. Instead, the current increases monotonously in the later stages of the electrical stress tests with Ag. The first proposed mechanism explains the observed behavior, if Ag ions permeate the PI

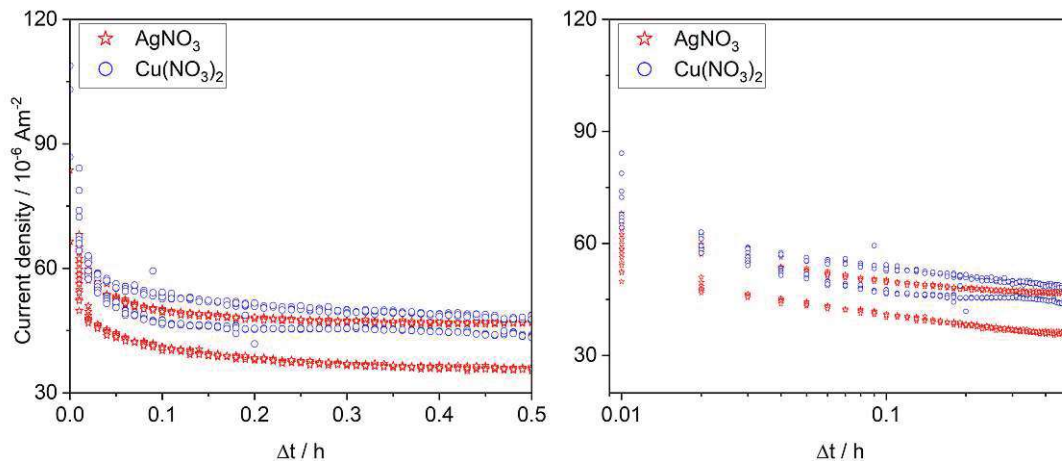


FIGURE 4.20: Current density-versus-time relationship obtained for the first 0.5 h of experiments with a $\text{AgNO}_3(\text{aq})$ electrolyte (red stars) and $\text{Cu}(\text{NO}_3)_2(\text{aq})$ electrolyte (blue circles) at 550 V bias. The samples are grouped based on the type of electrolyte that was used. Samples in the same group use the same colors and markers. **(left)** Both axes are given in a linear scale. **(right)** A logarithmic x-axis is used.

film more easily than other available charge carriers. Since Ag has been found to be more susceptible to ion migration than Cu in ECM studies, this is plausible.³ The intermediary ebbing off of the current density gain during stage 3 is not explained by this mechanism. The reason can only be speculated at this point, but it is possible that this is due to the initial presence of charge carrying species with varying mobility inside the coating. In stage 4, the current increases notably, until the sample fails rapidly and irreversibly. The gain is in line with what can be expected based on mechanism 1, assuming that Ag continuously enters the PI. The acquisition rate was $\sim 0.125 \text{ s}^{-1}$ (i.e. \sim one data point every 8 s). As the current density jumped from $\sim 50 \mu\text{A m}^{-2}$ to the current limit in between two data points, the ultimate failure occurred at a time scale that is smaller than this sampling rate. The proposed origin of this rapid increase is further discussed at a later point.

Hoping to be able to reach more conclusive results than with Cu, further LA-ICP-MS experiments were performed. First tests with line scans revealed that initially no Ag was present in the PI films. After stressing the sample electrically in the presence of the electrolyte, a Ag signal was clearly identified, proofing the presence of Ag in the insulating material. On the left hand side of figure 5.2 in the appendix, depth profiles (i.e. multiple line scans along the same area, as per 3.4) of both an untreated and a treated sample are shown (figure 5.2 (a) and (c)). On the right, the second ablated layer of the untreated and treated sample, respectively, is magnified (figure 5.2 (b) and (d)). Since they proofed to yield valuable information and are more time efficient than 3D-mappings, the rest of the LA-ICP-MS measurements was performed as line scans, according to the procedure described in section 3.4. Additionally, calibration standards were prepared for quantification of the measured signal. This method

was developed by Willner et al.¹⁸¹ and is detailed in the corresponding part of section 3.4, as well. With the obtained calibration line, the ¹¹⁷Ag signal intensity was converted to mass concentrations.

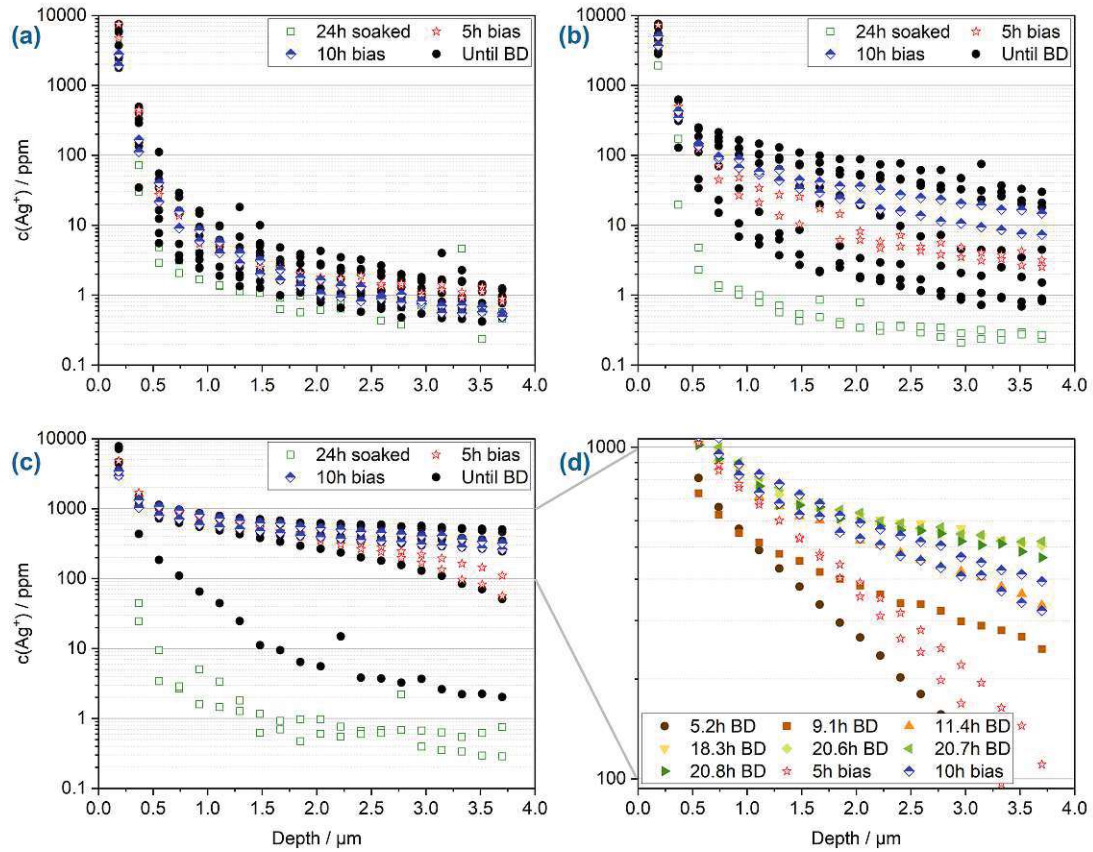


FIGURE 4.21: LA-ICP-MS depth profiles of ITC samples, determined as per section 3.4. Samples are grouped based on the type of stress they were exposed to. LA-ICP-MS depth profiles obtained from measurements (a) above the IDE side that was left unbiased during the electrical stress test, (b) in the gap between treated and untreated IDE fingers, and (c) above the IDE side that was biased during the electrical stress test. (d) A concentration range (indicated by the grey connecting lines) of (c) is magnified. The BD samples are not grouped. Instead they can be distinguished. Their t_{BD} is given in the legend.

The resulting depth profiles obtained from the ablation are depicted in figure 4.21. The samples are grouped based on the type of treatment they have been exposed to, and the subplots in the figure show results obtained (a) above the unbiased IDE side, (b) in the gap between the IDE fingers, and (c) above the biased side. Even though LA-ICP-MS cannot differentiate oxidation states, the y-axes are labeled 'c(Ag⁺)'. Since the initial Ag content is 0, all measured Ag signal is the result of the undergone treatment. Looking at figure 4.21 is informative in a number of ways:

- In (a) an increase of Ag signal is observed in the top layers for all samples, including the 24 h soaked samples. This indicates, that Ag^+ penetrates the polymer via ambipolar diffusion. Since the behavior of the stressed samples is similar, it stands to reason, that diffusion is the governing process, or at least plays an important role, for these samples as well. This is plausible, considering that the underlying IDE fingers were not (negatively) biased. However, fringing electric fields could play a role, explaining the small increase observed for many of the samples. The high signal in the top layer could also be the result of residual Ag at the surface. The samples were thoroughly rinsed after disassembly of the cells, but surface impurities could still play a role.
- Also in (a), a sort of minimum concentration is observed at ~ 1 ppm. This is likely a measurement artifact. When measuring LA-ICP-MS depth profiles, the ablation of each layer is not perfect. Therefore, ablation of the small remainder of previous layers can have an impact on the concentration measured in the current layer. Seeing as the concentration range spans four orders of magnitude, it is not surprising, that even small quantities of ablated material from upper layers results in a measurable amount of Ag^+ in lower layers. This imperfect ablation is one disadvantage of LA-ICP-MS depth profiling. However, as concentration changes can clearly be observed, the impact on the measurements performed for this thesis is deemed negligible.
- Comparison of the samples that were soaked for 24 h reveals a very similar behavior, irrespective of the position on the sample, at which the measurements were performed. This is further proof of diffusion, since no bias was applied to these samples.
- From the previous observations it follows, that Ag^+ concentrations notably higher than 1 ppm at a depth $\geq 1.5 \mu\text{m}$ are the consequence of migration in the applied electric field.
- Looking at (b) in the same figure ostensibly shows increased concentrations. With a few exceptions, one sees a stronger concentration increase with prolonged duration of the stress tests. There is one thing that should be borne in mind for this type of sampling (i.e. between two IDE fingers): Care was taken, to place the samples in the chamber as parallel to the laser beam path as possible. However, this could not perfectly be achieved. Thus, for some samples, the laser ablation pattern ended in closer proximity to a biased IDE finger, than for others. This can result in potentially higher measured concentrations. As the width of the fingers was twice as large as that of the gap, this problem was not encountered when measuring upon the IDE fingers. For this reason, the focus was laid on the results obtained above the fingers of the biased IDE side.

- A clear Ag^+ gain can be seen for all but the soaked samples and one BD sample in (c). As before, an increase can be observed from 5 h to 10 h. After 10 h a plateau seems to be reached, that rises only slowly with prolonged stress duration.
- Two BD samples in (c) differ notably from the rest of their group. From one a concentration profile just slightly above the soaked samples was obtained, the other one was similar to the 5 h treated samples. Their behavior can be well explained when their t_{BD} is considered. The values were 1.2 h, and 5.2 h, respectively. As the bulk properties were probed in the LA-ICP-MS measurements, and not the (vicinity of the) location of failure, these two behaviors are in line with the rest of the results. 1.2 h application of electric bias results in an increase with respect to the soaked samples, but well below the level achieved after 5 h. The early BD of this sample can be explained. During assembly of the cell, this sample was accidentally scratched with tweezers in the area that was later in contact with the electrolyte. As was expected, the sample later broke down at this weak point. However, the sample was included for LA-ICP-MS measurements since it is quite instructive and provides additional information on the time dependency of Ag^+ migration in the investigated PI film. The sample that failed after 5.2 h is almost identical to one of the samples that was stressed for 5 h without BD. It is unclear why this sample failed relatively early. No indication to explain this was found.
- The remaining BD samples in (c) show very similar behaviors and concentrations. A closer look at the t_{BD} of the different samples in (d) reveals a clear pattern. With increasing stress duration before the sample fails, the Ag^+ concentration deeper inside the bulk increases. However, after 18-21 h a level seems to be reached, at which the polymer is saturated. At this point little to no concentration increase is observed anymore.

The findings from this figure (figure 4.21) are very interesting when it comes to determining the permeation behavior of cations in PI films, as well as the failure of these organic insulating films. The conduction mechanism is not (solely) electronic in nature, but at least in part ionic. This further supports the proposed mechanism 1, and falsifies mechanism 2, as Ag^+ is clearly driven into the PI. Progression of the Ag^+ concentration gain ever deeper inside the sample with increased time can also explain the rising current density observed in figure 4.19. The differences in t_{BD} hint at critical variations between the samples (e.g. due to fluctuations during processing) or the influence of chance. Mechanical damaging of a sample significantly reduces its expected lifetime. Small variations in PI film thickness are therefore one candidate that influences the TTF. The polymer protection can take up a certain impurity amount,

before a plateau is reached. At this point, or soon after, BD occurs. Assuming that this BD is caused by dendritic growth, this plateau or critical (minimum) concentration is in line with the findings from the TLC experiments (section 4.1).

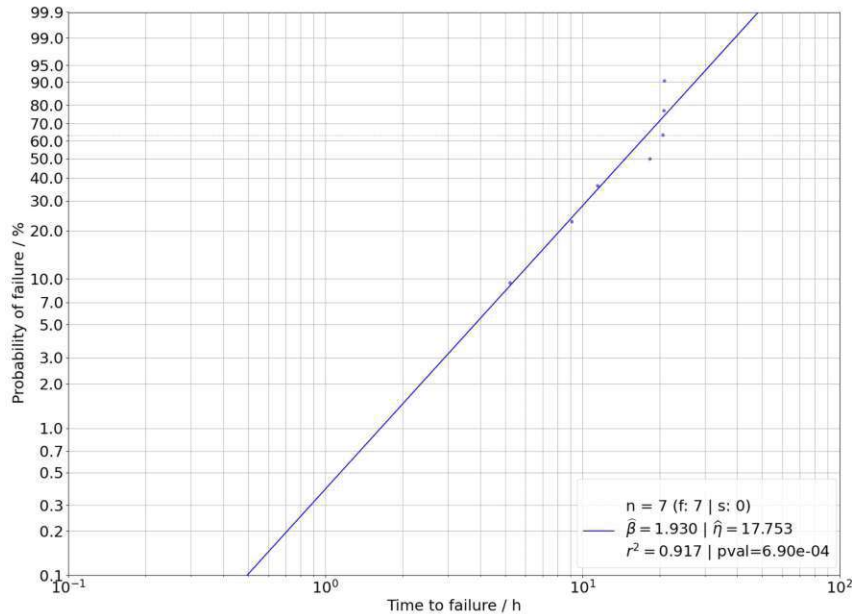


FIGURE 4.22: Weibull plot and calculated values based on the TTF obtained for the electrical stress tests with $\text{AgNO}_{3(\text{aq})}$ electrolyte.

With the available information, a comparison between the *i-t* and the LA-ICP-MS data is possible. The consumed charge was calculated for the former measurement and the theoretical charge to consume the total amount of available ions for the latter. The calculation is detailed in the corresponding methods section (3.3). The calculation was done for the two samples that were stressed for 5 h during the electrical stress test. No concentration information is available below $3.7 \mu\text{m}$. Since the concentration profile is ebbing off for the 5 h samples, the influence of the lower layers is assumed to be negligible. This assumption would clearly not hold for samples that were stressed for a longer period of time. The resulting amount of charge agrees well for both samples (table 4.1). The consumed charge was calculated both with and without consideration of the space charge contribution on the current (stage 1). Excluding this initial current in this comparison is reasonable, since it does not stem from ion flow. The calculated charge is higher for the LA-ICP-MS measurements in both analyzed cases, regardless of whether or not the initial current is considered. It is equal to roughly two to four times the value obtained from the *i-t* measurements, even though the concentration of the lower PI layers was assumed to be negligible. The most likely explanation for this discrepancy lies in the aforementioned imperfect ablation, resulting in an overestimation of the concentration of Ag^+ . Overall, the matching order of magnitude for both measurements further supports the hypothesis that the observed current is (primarily) ionic in nature.

TABLE 4.1: Comparison of calculated charges from i-t and LA-ICP-MS measurements.

Sample	q (i-t) / C	q (i-t, excl. 0.5 h) / C	q (LA-ICP-MS) / C
5h_S1	1.63×10^{-5}	1.45×10^{-5}	4.58×10^{-5}
5h_S2	2.06×10^{-5}	1.85×10^{-5}	4.20×10^{-5}

Same as before with Cu, the TTF or t_{BD} was extracted from the electrical stress tests. The resulting Weibull plot is shown in figure 4.22. The sample that was mechanically damaged and failed after 1.2 h was excluded from the calculations. For Ag^+ , the $\hat{\eta}$ value is equal to ~ 18 h. The $\hat{\beta}$ value of ~ 1.9 again indicates a wear-out or aging type of failure. $\hat{\eta}$ is much lower for Ag, than for Cu ($\sim 1/4$ of the time). This dependency on the type of electrolyte, or, more precisely, cation, strengthens the argument that ions play an important role in the observed insulation failure under the given conditions. One obvious difference between Ag^+ and Cu^{2+} is the oxidation state. It is possible, that a monovalent ion enters and permeates the organic film more easily than a divalent ion. However, bearing in mind the findings from Yun et al. ²²⁶, it seems more likely that there is another reason, since they compared monovalent cations and still found the strongest effect for silver. To clarify this matter, an additional experimental series with another monovalent cation, K^+ , was performed. The results from these experiments will be presented shortly.

In the case of silver, the failure locations could easily be determined. Optical microscopy revealed strongly reflecting metal deposits. For all samples only a single failure site was found. Selected examples are shown in figure 4.23. Importantly, the investigation of the failure sites proved that BD occurred inside the area that was exposed to the electrolyte, and neither outside, nor along the outline of the O-ring. The former serves as additional proof that the cell is leak proof, while the latter indicates that mechanical stress introduced by the cell assembly is negligible. Screwing the cell too tightly during assembly might introduce significant stress, but care was taken to avoid this. Figure 4.23 (a) shows that even though the sample was rinsed after disassembly, some residual Ag is evident, likely in the uppermost layers of the PI film. This could in part explain the high concentrations that were measured in the LA-ICP-MS experiments (figure 4.21.) A discoloration of the IDE finger at which the failure occurred was observed as well. This phenomenon can be explained as follows: Once the sample failed, the bias voltage was automatically turned off by the instrument. However, the cables were not disconnected and the electrolyte was not directly removed. The BD results in a metallic connection between electrolyte and IDE finger. Since Ag is a nobler metal than Cu (see table 2.1), Ag^+ ions in the electrolyte are reduced, and metallic Cu is dissolved at the IDE finger, in the presence of H_2O .

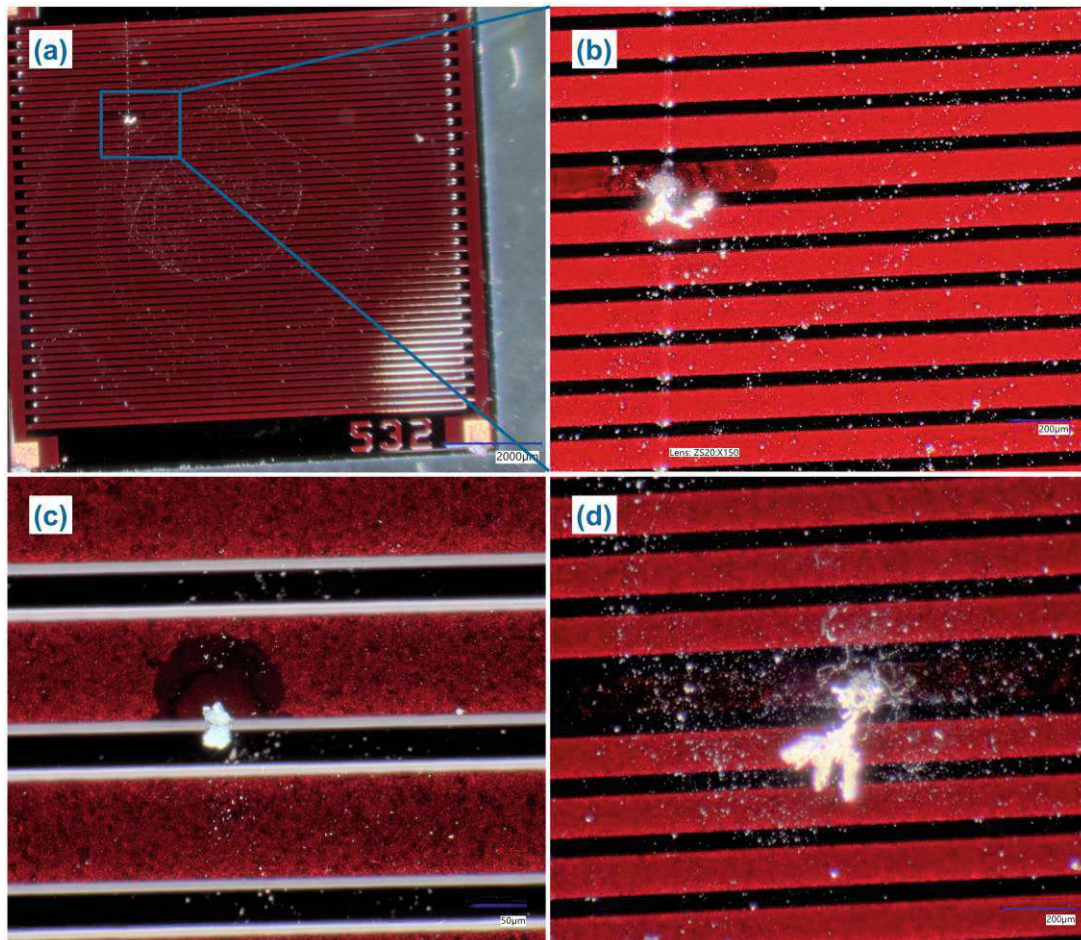


FIGURE 4.23: Microscopic images of ITC samples after BD of the PI insulation film. **(a)** Overview of the ITC sample that failed after 1.2 h due to mechanical damage. The damage is visible in the top left, in the form of a scratch that reflects light differently than the rest of the protection layer, and is also partially highlighted in the blue box. In the blue inset, a metal deposit is seen, indicating the location at which BD occurred. **(b)** Further magnification of the BD location, as indicated by the blue inset in **(a)**. **(c, d)** BD sites of two more samples.

Based on these findings, mechanism 1 can be extended with regards to failure of the dielectric. A few seconds or less before t_{BD} , a critical ion concentration at the metal/polymer interface is locally exceeded. The transported cation (i.e. Ag^+) is deposited at this location on the electrode, forming an anchor point for further deposition. The tip effect leads to rapid growth of a metal filament from this nucleus, through the dielectric film. Once the protection layer is bridged at t_{BD} , a short-circuit is formed resulting in insulation loss. Alternatively, filamentary thermal runaway (see section 2.4) could cause the failure, with the Ag deposit being a side product, once a conductive path is formed. The role the cation would play in this case to explain the differences in t_{BD} is unclear. One possible explanation lies in the works of Kishi et al.²²⁵ and Takada et al.²¹⁶. They reported the appearance of hetero charges in electrically stressed PI shortly before BD. They used a MIS structure and applied higher voltage

gradients than were employed in this work ($\geq 110 \text{ MV m}^{-1}$) and measured in a dry environment. According to the authors, hetero charges form by charge separation inside the bulk in their case. They do not elaborate on the exact nature of the breakdown. In this thesis, the migrating cation could take on the role of the critical hetero charge that forms a layer near the cathode. Briefly after a critical concentration is reached, BD occurs. The migration speed of a cation would therefore play a key part in the failure as it determines the build-up speed of the hetero charge layer. In this way, a cation dependent filamentary thermal runaway could be explained. Effort should be undertaken in the future to ascertain the cause of BD.

Potassium electrolyte

The final ITC experimental series was performed with an electrolyte containing $0.1 \text{ mol L}^{-1} \text{ KNO}_{3(\text{aq})}$. A total of 10 samples was investigated. Two samples were soaked for 24 h. Four samples were electrically biased, two for 10 h and two for 20 h. Four samples were stressed until BD.

Figure 4.24 depicts the i - t data obtained for the $\text{KNO}_{3(\text{aq})}$ experiments, again in the same style as the previous graphs of the same type. In this series, the sample to sample variation was more pronounced than in the other series. Using the same approach as previously, three regions were roughly determined:

1. **Decrease** ($t < 0.5\text{--}1 \text{ h}$): As in the previous series, a current decrease is observed after the onset of the bias application.
2. **Constant** ($0.5 - 1 \leq t < 3\text{--}50 \text{ h}$): In this region, the current remains fairly constant over an extended period of time. The duration varies strongly from sample to sample. This region is not observed in the 10 h treated samples.
3. **Increase and breakdown** ($4\text{--}50 \text{ h} \leq t \leq t_{BD}$): The time before the sample fails exhibits increasing current densities. The gain continues over the course of several (tens of) hours, rising faster as time progresses. At t_{BD} the current density rises sharply.

The stage 1 behavior of these samples is very much alike the one observed in the other two series. In the second stage, a current plateau is reached, during which there is neither a net decrease nor increase in current density, for most samples. Neither of the 10 h stressed samples exhibits this behavior. Instead, these two samples behave very similarly to those exposed to Ag^+ . It is unclear, why these two samples behaved differently than the rest. It is also unknown whether this would have affected their t_{BD} , as the stress test was interrupted before this point was reached. One of the two samples generally exhibited an unusually high base current density. Focusing instead on stages 2 and 3 of the rest of the investigated samples, key differences are observed, upon comparison with the previous series. Stage 2 looks similar to the same stage of the $\text{Cu}(\text{NO}_3)_{2(\text{aq})}$ samples, stage 3 is much alike stage 4 of

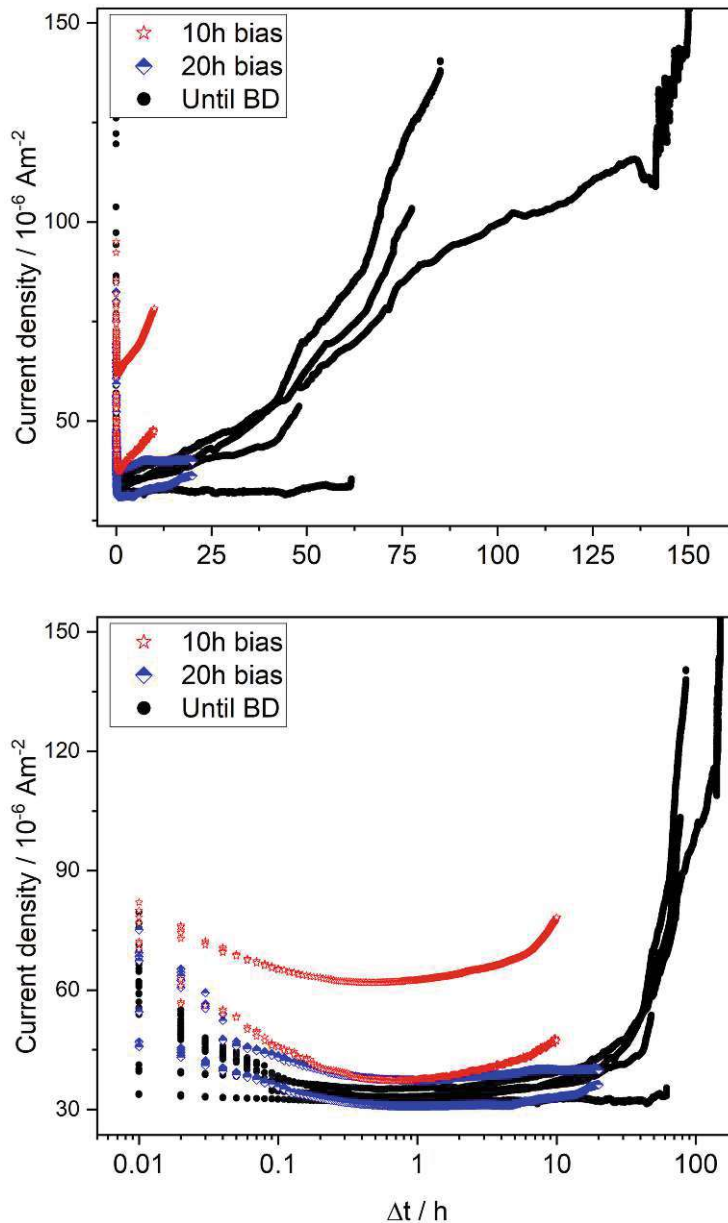


FIGURE 4.24: Current density-versus-time relationship obtained for experiments with a $\text{KNO}_3(\text{aq})$ electrolyte at 550 V bias. The samples are grouped based on the duration of the electric stress tests. Samples in the same group use the same colors and markers. **(top)** Both axes are given in a linear scale. **(bottom)** A logarithmic x-axis is used.

the $\text{AgNO}_3(\text{aq})$ samples. While the trend in the last stage resembles the Ag^+ experiments, the TTF is closer to that in the Cu^{2+} experiments. This is in line with the previously mentioned expectation that was based on the work by Yun et al.²²⁶: The valency is not the key factor that determines the cation's influence on t_{BD} . It could still impact the migration and permeation properties of the species in the PI film. Mechanism 1, that was proposed earlier, explains the observed behavior in stages 2 and 3. If the permeability of K^+ is roughly equal to that of

the charge carriers that are initially present in the polymer, then exchanging these species will not impact net current flows (stage 2). The increase in stage 3 likely is governed by a different mechanism than for Ag^+ . K^+ ions are not expected to deposit and form dendrites, instead the formation of OH^- is favorable. In this stage, the accumulation of K^+ ions at the metal/polymer interface and their diffusion into the pi (together with OH^- ions formed at this interface) progressively increase the overall conductivity and consequently the current. This is further elaborated later in this section.

Again, LA-ICP-MS experiments were undertaken. Preliminary line scans revealed the absence of K in the 'as received' PI films. After the stress tests, a K signal was found, proving that potassium, like silver, entered the insulating material. Same as before, calibration standards were prepared for quantification of the measured signal. However, problems with the spraying instrument during the preparation of the standards rendered these useless. For this reason only qualitative results are shown, that is the obtained ^{39}K signal normalized to ^{13}C .

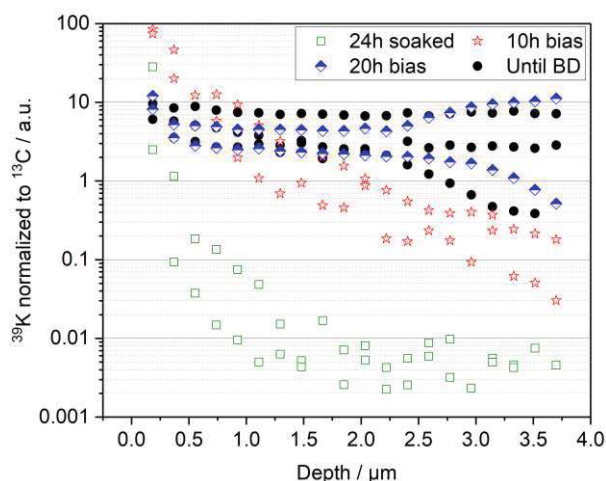


FIGURE 4.25: LA-ICP-MS depth profiles of ITC samples exposed to $\text{KNO}_{3(\text{aq})}$, determined as per section 3.4. Samples are grouped based on the undergone treatment. LA-ICP-MS depth profiles were obtained from measurements above the IDE side that was biased during the electrical stress test.

Figure 4.25 presents the resulting depth profiles obtained from the ablation experiments. Once again, the samples are grouped according to the type of treatment. Only the resulting measurements from above the biased IDE finger are shown, as the other two measurements (above the unbiased fingers, and in between) revealed the same picture as the previous measurements with Ag . Initially there is no K present in the polymer. Consequently, the measured signal gain can be attributed to the exposure to $\text{KNO}_{3(\text{aq})}$. The observations in this figure are:

- The 24 h soaked samples exhibit a diffusion driven ingress of K into the organic coating. The penetration depth during this time span is roughly $1.25\ \mu\text{m}$. This matches the previous finding of the samples with Ag^+ in the electrolyte.

- In all but the soaked samples the potassium signal is clearly enriched. An increase is observed from 10 to 20 h electrical stress, but there is no clear trend between 20 h and until BD.
- Like the i-t curves, the measured results vary more strongly than during the Ag measurements. The 10 h curves exhibit a different trend in the upper layers than the samples that were treated for a longer period of time. The 20 h and until BD treated samples display similar trends with notable sample to sample variations.
- A plateau is observed in ≥ 20 h stressed samples, at depths between 0.5 and 2.5 μm . The height of this plateau exhibited differences from sample to sample.

The LA-ICP-MS measurements paint a picture that is similar to that in figure 4.21 (c). The K data is not quantitative, allowing only for a qualitative comparison between the two. While in the Ag exposed samples a plateau is observed after ~ 10 h, this is the case only after ≥ 20 h for the samples presented in this section. It is plausible that formation of such a plateau occurs after the initially prevalent charge carriers are exchanged by the introduced cations. The same polymer was investigated both with $\text{AgNO}_{3(\text{aq})}$ and $\text{KNO}_{3(\text{aq})}$, suggesting that this number is at the same order of magnitude. From this the following hypotheses can be derived: (i) The concentration plateau is reached more swiftly when Ag^+ is available. That is, initial charge carrier exchange progresses faster with Ag^+ , than with K^+ . Consequently, the permeability of Ag^+ is higher than that of K^+ . (ii) Soon after the plateau is reached, BD will occur. Before this saturation level is reached in the upper half of the polymer layer, failure is unlikely.

As for the previous electrolytes, a Weibull plot was generated based on the obtained t_{BD} values (figure 4.26).

In table 5.8 in the appendix, the TTF for all measured samples for all electrolytes are given. $\hat{\eta}$ equals ~ 113 h. The $\hat{\beta}$ value is ~ 2.1 . The $\hat{\eta}$ value is the highest of all three electrolytes. As stated before, the low number of samples results in a strong sensitivity of the calculated parameters on every single data point, making the results prone to potential outliers. However, the mean TTF is definitely lower for samples exposed to Ag^+ than to K^+ . The failure locations were not be identified for this experimental series.

Concerning the different i-t response depending on the cation and the variability of the TTF, the electrochemical nature of the investigated cation can play a distinct role. Both Ag^+ and Cu^{2+} lie at positive values in the electrochemical series, while K is negative. The noble metals are therefore likely to be reduced once a sufficient concentration is surpassed at the surface. The observed dendrite growth in the $\text{AgNO}_{3(\text{aq})}$ experiments supports this. K^+ on the other hand is more likely to accumulate near the interface. Many years ago, Steppan et al.³ reported the hypothesis of the formation of an alkaline zone near the cathode in the presence of potassium in thin, contaminated water films. Delamination processes and the

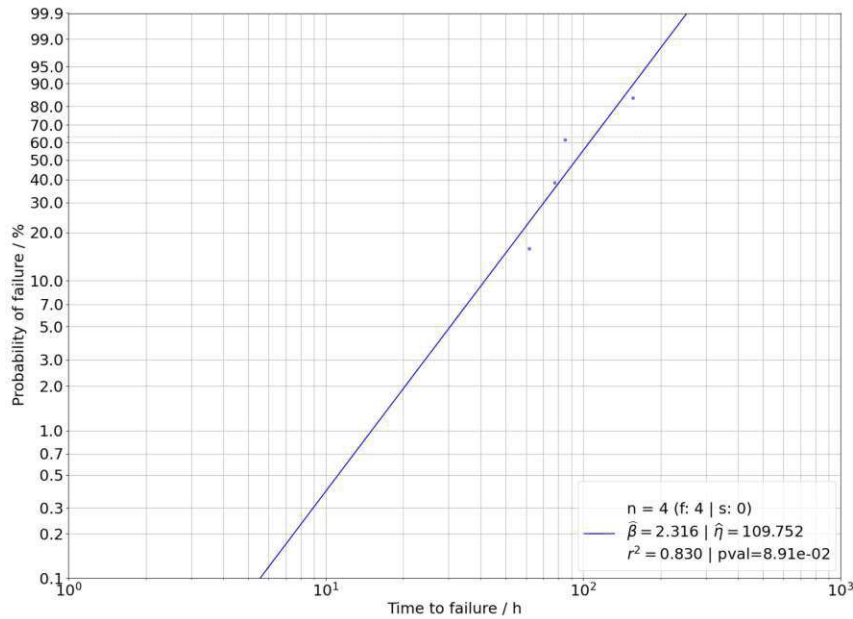


FIGURE 4.26: Weibull plot and calculated statistical parameters based on the TTF obtained for the electrical stress tests with $\text{KNO}_{3(\text{aq})}$ electrolyte.

formation of hydroxide through the reduction of water at the interface could play a key role in insulation failure in this case, especially considering that PI is known to be less stable in alkaline environments.²⁴ Assuming this alkalization takes place, the increase in stage 3 of the i-t curves could be connected to a loss of the insulation properties of the PI due to attack by OH^- ions and an accumulation of ions at and near the interface. The increasing K signal inside the polymer observed in some curves that were exposed to extended electrical stress (figure 4.25) further supports this hypothesis. The extended mechanism 2 is no plausible candidate to explain the failure in the case of K^+ , as it does not form dendrites. Filamentary thermal BD or conductive paths, like the ones described by Ludwig⁵, are other possible explanations. Future LA-ICP-MS investigations should measure the ion content down to the interface metal/coating, to see whether differences exist between the cations.

4.3.2 ITC - simulation

The setup and simulation details of the model have been described earlier in this work (section 3.5). Initially, the idea was to implement the learning from the TLC measurements and simulation and to use these as basis for the modeled developed here. However, as strong field gradients are used, a description using BV kinetics does not run stably due to the non-linearity of the equation. Instead, the interface was treated in a simplified manner, assuming fast, irreversible reduction reactions of the available cationic species. The simulation was compared with and parameters adjusted based on the data that was available from the ex-

perimental part. Both i-t and LA-ICP-MS measurement results, where available, were used to this end. Parametric sweeps were performed for H_0 , D_C_poly , D_{An_poly} , D_H_poly , and D_E_poly , to achieve a good agreement of the simulation with the measured values.

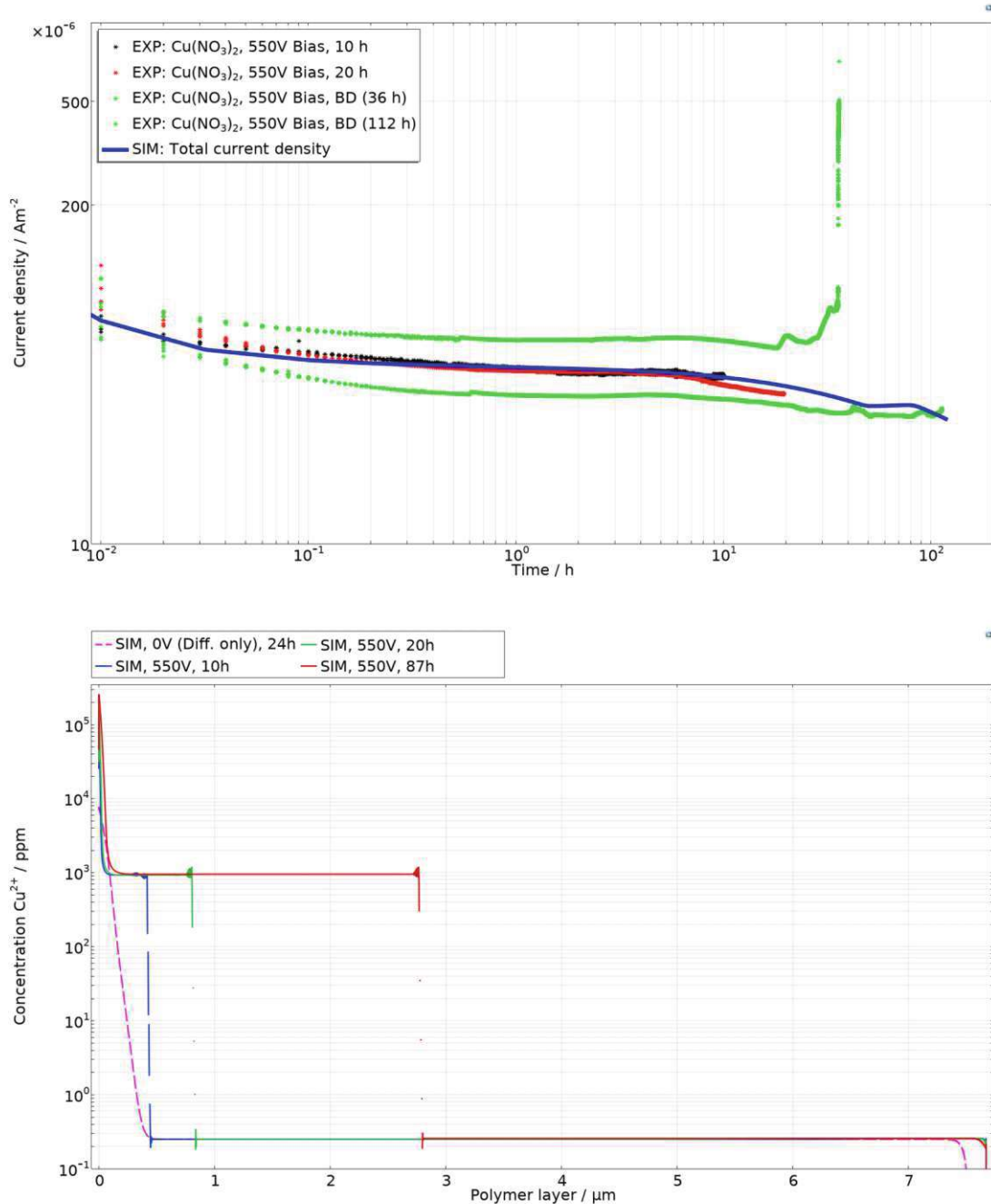


FIGURE 4.27: Comparison of ITC experimental data ($\text{Cu}(\text{NO}_3)_2(\text{aq})$) and simulation results. **(top)** current density-versus-time curves. For better clarity only selected experimental curves are given (colored *). The simulated curve is shown in blue. **(bottom)** Simulated LA-ICP-MS profiles after different stress test times. The graph in pink was obtained for 24 h simulation without application of bias. No experimental data of this type is available for comparison.

All simulation parameters in figure 4.27-4.29 are the same, except for the diffusion coefficient of the cation, D_{C_poly} . This choice was made since the samples and setup are the same for all of the investigated electrolytes, with the sole differentiating factor being the cation: Cu^{2+} , Ag^+ , and K^+ . The idea was to find a fixed set of parameters that describes the immersed polyimide system, and then optimize a variable parameter that describes the influence of the different cations. The top graphs of the figures present the experimental i - t curves (*) and a simulated i - t curve (line). On the bottom of the figures, LA-ICP-MS derived experimental and simulated concentration profiles are depicted, where available.

As discussed in the experimental part, the i - t behavior evolved over multiple stages with certain characteristics for all investigated samples. The first (and the second, for Cu^{2+} and K^+) stage were attributed to the response of the PI coating, independently of the type of electrolyte. Hence this stage should not be determined by ions stemming from the electrolyte, but only the charge carriers that are initially present in the PI. The usage of an electrochemical double layer combined with defined initial impurity concentrations, and values for D_{H_poly} and D_{E_poly} resulted in a good fit of the experimental curves, as seen in the top graph of all three figures. Adapting the initial (electronic) charge carrier or impurity concentration levels in the model allows to achieve a better fit. Doing this for every sample would be necessary to fit each experimental curves, since there is clear sample-to-sample variation. As it is, a starting value was chosen, that resulted in i - t curves that lay in between the experimental extrema. H_0 , was determined to be 44 mol m^{-3} . This number is of interest since it presents a quantifiable number of available charge carriers or reactive sites of the polymer under the given conditions. As stated earlier when presenting the simulation model (section 3.5), the charge carriers were considered as electrons and electron holes. The actual nature of these mobile charge carriers is unknown. This was already discussed during the presentation of the experimental results. Since there is notable sample-to-sample variation, the obtained H_0 value should be treated as order of magnitude and not an absolute. D_{H_poly} and D_{E_poly} were chosen in combination with H_0 , to approximate the initial current densities well. The values for these two parameters are $4.3 \times 10^{-21} \text{ m}^2 \text{ s}^{-1}$ and $2.2 \times 10^{-21} \text{ m}^2 \text{ s}^{-1}$, respectively. The anion mobility plays a role in the later stages of the experiment. Since the same anion was used in all experiments, one fixed parameter value was used for D_{An_poly} : $1.5 \times 10^{-20} \text{ m}^2 \text{ s}^{-1}$.

Looking at each figure separately allows to further elucidate the findings discussed earlier based solely on the experiments. Figure 4.27 (top) reveals the models ability to predict the dip observed in stage 3 of the experiments (see figure 4.16 (bottom)). The (effective) diffusion coefficient of Cu in the polymer part of the simulation is the input parameter that drives the i - t behavior at this point. Thus, adapting this parameter to achieve a good fit to the experiment allows to extract the diffusion and migration properties of Cu in the PI matrix. A value of $6 \times 10^{-22} \text{ m}^2 \text{ s}^{-1}$ was obtained. In stage 4, a deviation of the simulation from the measured

i-t values is observed. This does not come as a surprise, since the actual BD process is not simulated in this simulation. This should be the subject of further investigation, to be able to fully predict the impact of ion migration on dielectric failure. Since no experimental values could be extracted from LA-ICP-MS measurements for this electrolyte, figure 4.27 (bottom) presents only the simulated Cu^{2+} concentration curves. The simulation predicts a slowly moving Cu^{2+} front. It should be noted that the experimentally observed background Cu signal was not taken into account in the calculation of the concentration of Cu^{2+} . It is assumed that this background is present in a non-ionic state that does not contribute to the measured i-t signal and is therefore not reflected in the simulation. For example, Faupel et al.²⁷⁶ and Ludwig⁵ presented microscopic images that show copper precipitates or agglomerates in the polyimide.

Figure 4.28 (top) shows exemplary experimental i-t curves measured with $\text{AgNO}_3(\text{aq})$ electrolyte (*), combined with the simulation results obtained for an adapted diffusion coefficient value for the electrolyte cation (line). The current onset is again well described by the simulation. The second and fourth experimental stage, during which the current rises, is approximated reasonably well, too. However, no plateau formation is observed. This indicates that the model complexity should be further increased to allow for more degrees of freedom. One avenue lies in the addition of another cationic charge carrier with an intermediary mobility, lying between the initially present contaminant and the Ag^+ . First tests proved this to be a promising approach, but further adaptations of the model will be the aim of future work. The concentration curves in figure 4.28 (bottom) show a good agreement between the measured and the predicted concentration values. In this case, the quantified values can be directly compared, allowing to analyze not only the curve shape, but also the absolute values. Since the base level in the LA-ICP-MS measurements never went back to 0 ppm if there was an increased amount in the upper layers, a cation base concentration of 0.5 ppm was assumed to be prevalent in the PI for simulation purposes. This explains the base line that is seen for all curves. The results for diffusion only agree well in the upper layers. In lower layers the simulation does not predict an increased ion content. This is again likely to be in part attributable to the carryover from upper layers. As mentioned in the experimental section, one of the samples had a surface damage and failed already after 1.2 h. Once again the uppermost layers are well described by the simulation, but no ion ingress below $\sim 1 \mu\text{m}$ is predicted. Carryover does not provide a good explanation for this observation, as it would not be expected to result in higher concentrations than the ones observed for the 'diffusion only' sample. As it is, this stronger drop-off cannot be well explained. At prolonged times the ion ingress in both simulation and experiment progresses ever deeper into the PI. After ~ 8 h ions reach the cathode surface. After 21 h the simulated concentration at this surface is roughly equal to the value of the concentration plateau observed experimentally. At this stage the samples failed without exception. It is likely that a critical Ag^+ content near the cathode surface

plays a key role in BD of the samples. This value was found to lie at ~ 500 ppm of Ag^+ . This value essentially corresponds to the concentration of initially available charge carriers in the PI coating. It follows that at this point the initially available positive charge carriers have been fully substituted by Ag^+ ions. The (effective) diffusion coefficient of Ag^+ used in this simulation was set to $6.25 \times 10^{-20} \text{ m}^2 \text{ s}^{-1}$.

Figure 4.29 (top) presents experimental (*) and simulated (line) i-t data for the $\text{KNO}_{3(\text{aq})}$ experiments. Looking at this figure, it is apparent that the calculated total current density is higher than those observed in the experiments. The starting values of the simulation could have been adapted to achieve a better fit. However, since only the cation diffusion coefficient was varied in between the presented simulations for better comparison, this was not done. Also, aside from being slightly overestimated, the i-t behavior is still modeled appreciably well. Contrary to the previous figures, for the $\text{KNO}_{3(\text{aq})}$ series two y-axes are used to present the LA-ICP-MS data (figure 4.29 (bottom)). The left axis shows calculated K^+ concentration profiles, the right one the measured ^{39}K signal (normalized to ^{13}C). Since determining the concentrations from experiment failed, a direct comparison of measured and simulated signal is not possible. However, assuming a linear relationship between signal ratio and concentration, as was the case for Ag , the axes were set to span the same order of magnitude. Doing so results in a relatively good fit between the measured and simulated values. However, since the experimental results scattered more than with $\text{AgNO}_{3(\text{aq})}$, further experiments are desirable to improve the security with which conclusions can be drawn from the simulation. As it is, the (effective) diffusion coefficient of K^+ through the investigated PI was determined as $1.75 \times 10^{-20} \text{ m}^2 \text{ s}^{-1}$.

TABLE 4.2: Collection of diffusion coefficients extracted from simulation, for each of the three electrolytes used in ITC experiments.

Electrolyte	Ion	Diffusion coefficient ($10^{-20} \text{ m}^2 \text{ s}^{-1}$)	Mobility ($10^{-18} \text{ m}^2 \text{ V}^{-1} \text{ s}^{-1}$)
$\text{Cu}(\text{NO}_3)_{2(\text{aq})}$	Cu^{2+}	0.06	3.89
$\text{AgNO}_{3(\text{aq})}$	Ag^+	6.25	2.43
$\text{KNO}_{3(\text{aq})}$	K^+	1.75	0.68

The diffusion coefficients obtained from simulation for all three investigated electrolytes are summarized in table 4.2. The calculated order of magnitude, based on the experimental results, is in good agreement with the range presented in table 2.4 for Cu. No room temperature values were found for comparison for the other two elements.

As stated before, the initially present charge carriers in the PI could be electronic in nature, but also ionic. Thanks to the simulation, the (effective) diffusion coefficients and, via equation (2.35), the mobility of the charge carriers are known. In literature, the mobility of electronic charge carriers has been reported to be at the order of $10^{-14} \text{ m}^2 \text{ V}^{-1} \text{ s}^{-1}$.²⁷⁷ The

mobility values calculated based on the diffusion coefficients, D_{H_poly} and D_{E_poly} , are $1.68 \times 10^{-19} \text{ m}^2 \text{ V}^{-1} \text{ s}^{-1}$ and $8.57 \times 10^{-20} \text{ m}^2 \text{ V}^{-1} \text{ s}^{-1}$, respectively. Clearly, these values are orders of magnitude lower, than the values found in literature. Seeing as their is an order of magnitude difference, this indicates a different nature of the species that is mobile inside the polyimide. This makes ionic impurities or side groups more likely candidates. This is also plausible in context with the effect of humidity or immersion that was suspected in literature (section 2.4). However, it is also possible that this reveals a shortcoming of the used model. In the current state of the model, trapping, charge injection and relaxation effects are not considered. Instead, an effective mobility and diffusion coefficient are used and extracted. To establish the nature of the inherent charge carriers beyond doubt, the model has to be adapted to include the effect of charge trapping and recombination in the PI bulk, along with the tertiary current distribution or transport of diluted species for the description of the transport of ionic species. Electronic charge carriers also likely impact the BD behavior of the PI in the investigated field region. The field strength is in a range that lies above the degradation threshold described by Zhou et al.²⁰². An important difference between their measurements and the experiments performed in this work lies in the usage of an aqueous environment, which influences the PI layer significantly. While the lack of detail for the description of electronic charge carriers likely constitutes a shortcoming of the employed model, the agreement of the order of magnitude of the chemical species diffusion coefficients with literature values supports the validity of the model for a simplified macroscopic description.

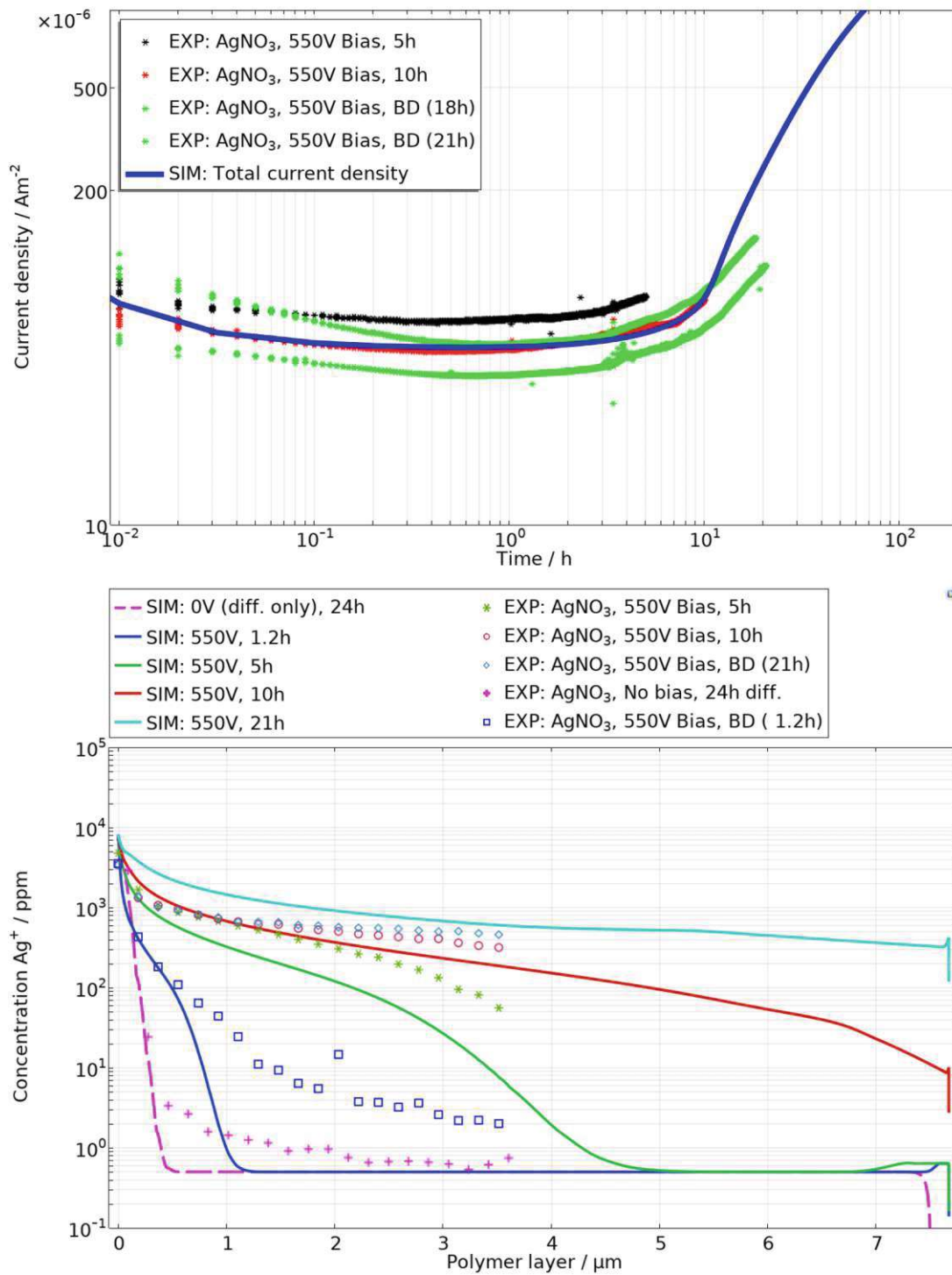


FIGURE 4.28: Comparison of ITC experimental data ($\text{AgNO}_{3(\text{aq})}$) and simulation results. **(top)** current density-versus-time curves. Selected experimental curves (colored *) and the simulated curve (blue line) are depicted. **(bottom)** LA-ICP-MS profiles. Selected experimental curves are shown (colored scatter plots). The simulated curves obtained after the same time are shown as line plots, using the same colors as for the experimental curves. The pink graphs were obtained for 24 h soaked samples without application of bias.

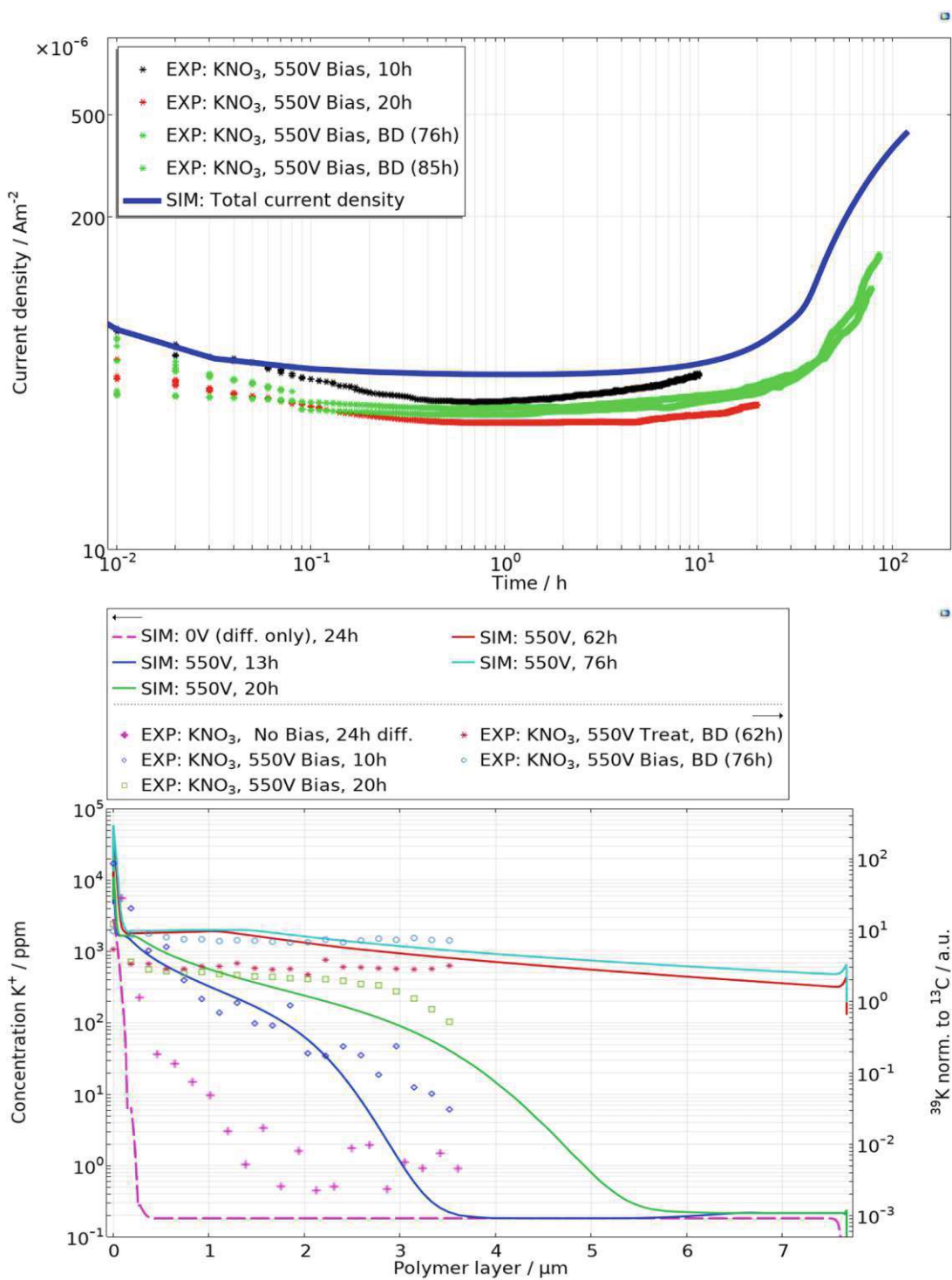


FIGURE 4.29: Comparison of ITC experimental data (KNO_{3(aq)}) and simulation results. **(top)** current density-versus-time curves. Only selected experimental curves are given (colored *), along with the simulated curve (blue line). **(bottom)** LA-ICP-MS profiles. Again, only selected experimental curves are given (colored scatter plots). The simulated curves obtained after the same time are shown as line plots. The same colors are used both for experiment and simulation after the same stress duration. The graphs in pink were obtained for 24 h soaked samples without application of bias.

5 Main findings and conclusion

In the course of this work, three different experimental setups were used for experimental investigations. Using a combination of electrochemical and analytical methods, along with simulation allowed to further the understanding of the behavior of metal cations in thin electrolyte layers. Most importantly, in the third part of this work, a method is presented that allows for controlled stressing and metal loading of polymer coatings on wafer substrates. This makes the technique of potential interest for corrosion scientists or the semiconductor industry.

For the first part of this thesis, a so-called Thin Layer Cell (TLC) was used. With this cell, dendrite growth regimes for dilute, neutral or acidic aqueous solutions under potentiostatic control were determined. It was found, that a critical concentration of Cu^{2+} had to be exceeded for copper dendrites to grow. Dendrite growth is accompanied by a significant increase of the cell voltage, followed by an increasing current density. At lower concentrations, or without the addition of copper ions, precipitation of Cu_2O and sometimes CuO was observed. A low cathodic overpotential strongly limited dendrite growth, in line with expectations based on literature.^{91,92,272} The simulation proved that the reduction and oxidation of $\text{Cu}|\text{Cu}^{2+}$ was the main reaction in the electrochemical cell. Side reactions, like the HER, played only a negligible role.

In the second part of the thesis, a Miniaturized Test Chip (MTC) was intended to be used to investigate simple metal structures, with and without PI coating, that were manufactured with techniques employed in the micro-electronics industry. The functionality of these structures was successfully tested on samples without organic coating. However, the usage of the coated structures was not successful, as unintended stray current paths proved troublesome on the assembled MTC. Countermeasures did not yield the intended outcome, either. Therefore, the experiments with the MTC setup were sidelined.

The third setup was referred to as 1x1 Interdigitated Test Chip (ITC). A PI coated copper comb structure on a Si substrate was used for these measurements. The aim of these experiments was threefold: 1) design a cell that enables the controlled ingress of metal cations into the organic coating and degradation of the same, 2) measure different cations and find similarities or differences between them, and 3) develop a simulation model, that describes the permeation behavior of the cation and the measured current flow. The final cell design consisted of an electrolyte bath on top of the organic coating, with a metal electrode dipped

into the same. A bias was applied between this electrode and one of the two sides of the IDE structure, with the latter operating as the cathode. The imposed potential acted as a strong force, driving cations from the electrolyte into the polyimide. The ITC samples were biased for a defined period of time, or until BD occurred. The current density was logged and after finishing the electrical stress, LA-ICP-MS measurements were performed to determine the cation content in the coating.

Three electrolytes were investigated: $\text{Cu}(\text{NO}_3)_2(\text{aq})$, $\text{AgNO}_3(\text{aq})$, and $\text{KNO}_3(\text{aq})$. Taking the same anion for all measurements allowed to focus on the influence of the cation. The *i*-onset showed a reproducible behavior for all cations, showing that this part is determined by the dielectric properties of the coating. In the later stages, a clear impact of the choice of cation was found. While *j* increased for Ag^+ , it stagnated for K^+ , and decreased over time for Cu^{2+} . $\hat{\eta}$ was determined as 17.8, 109.8, and 87.7 h, for Ag^+ , K^+ , and Cu^{2+} , respectively. It should be noted that a higher number of experiments is desirable to strengthen the statistical reliability of these values. LA-ICP-MS measurements were unsuccessful for the analysis of copper ion ingress into the organic coating. This was due to a high base level of copper in the PI, which can be explained due to the direct contact with the copper comb.^{169,276} Both Ag^+ and K^+ were not present in untreated ITC samples, and LA-ICP-MS measurements yielded insightful results. By measuring the PI film directly above the treated and the untreated side of the IDE structure, it was proven that migration was the main driver of ions into the film, while diffusion played a measurable, but only minor role. With increasing time, the ions progressed ever further into the PI, and overall concentrations increased. After sufficiently long electrical stress duration, a concentration plateau was observed, indicating a maximum uptake of cations of the coating.

A significant advantage and novelty of this work is the correlation of current measurements with concentration profiles. Differentiating between ionic and electronic currents in polymer coatings is typically challenging, and the ionic contribution is often overlooked. The methodologies and calculations presented in this thesis make it possible to distinguish these currents. The analysis clearly shows that, for ITC samples exposed to $\text{AgNO}_3(\text{aq})$, the current is primarily ionic. Therefore, under certain conditions, the influence of ionic contaminants becomes not just relevant, but a critical factor in shaping the observed behavior.

A 1D FEM simulation model was developed to generate more in-depth insights for the ITC experiments. With the simulation an effective diffusion coefficient for the cations and the anion was extracted, as well as the inherent charge carrier (or reactive site) density and their diffusion coefficient in the PI. H_0 was determined as 44 mol m^{-3} and for the diffusion coefficients the following order was obtained: $D_{\text{Ag}^+} > D_{\text{K}^+} > D_{\text{H}_2\text{O}} > D_{\text{E}_-} > D_{\text{Cu}^{2+}}$. At the point of creating the simulation, electronic charge carriers were considered most likely to be available in the polymer bulk. However, comparison of literature values and the mobility values calculated based on the diffusion coefficients, imply a different nature for the

charge carriers, since the extracted mobility values are significantly lower.²⁷⁷ The different *i-t* response, depending on the type of cation, was explained in terms of the exchange or substitution of inherent charge carriers by the migrating cation from the aqueous electrolyte. By attributing differing mobilities to these inside the PI, a similar current response was simulated, lending support to this assumption. Dielectric BD was not modeled. However, the simulated and measured cation concentration profiles imply that failure occurs once a critical concentration is exceeded at the interface between the organic coating and the cathode.

While the work performed for this thesis provides a good starting point to delve deeper into the investigation of the influence of metal cations on coating failure, a lot of work remains to be done. The setup used for the ITC measurements and the samples themselves offer interesting possibilities. Two major challenges in investigating corrosion in complex coated systems are reproducibility and time. Reliability is often an issue at the scale of years, and accelerated stress tests at times yield strongly varying results. One avenue that opens up with this setup is loading of the coating with metal particles, similar to what can happen over extended periods of time during service life. This loading can be achieved in the same, controlled way that was used in this work, but by electrically stressing the samples only for a period of time that does not lead to BD of the sample. This results in a coating with a relatively defined amount of cationic impurity, offering a reproducible baseline. In a next step, the electrolyte could be removed, or kept, and bias applied between the two sides of the IDE. This way, corrosion processes could be investigated, for example, depending on the amount of introduced contaminants. To mitigate the risk of failure due to field-induced BD, the electric field could be reduced to levels below the critical threshold reported by Zhou et al.²⁰².

On the simulation side, a lot of work remains to be done, as well. To test the hypothesis of non-electronic charge carriers, the semiconductor interface offered by COMSOL Multiphysics® should be implemented for describing the polymer, instead of the tertiary current. In the current model, electronic charge trapping is not considered. While the order of magnitude of the diffusion coefficient is plausible for ionic charge transport at room temperature, this is not the case for electronic charge carriers. It is possible that the extracted (effective) diffusion coefficient for e^- and h^+ results from a reduction of the (effective) mobility due to trapping, an effect that is currently excluded in the model.

Ultimately, introducing a BD condition and preceding changes inside the polymer film into the simulation would allow to encompass and predict the whole lifetime of the investigated sample. To this end, Zuo et al.¹⁵¹ and Gallier and Plaud¹⁵² could serve as valuable starting points.

Bibliography

- [1] Marcus, P. P. *Corrosion mechanisms in theory and practice.*; CRC Press, 2012.
- [2] Koch, G. In *Trends in Oil and Gas Corrosion Research and Technologies*; El-Sherik, A., Ed.; Woodhead Publishing Series in Energy; Woodhead Publishing: Boston, 2017; pp 3–30.
- [3] Steppan, J. J.; Roth, J. A.; Hall, L. C.; Jeannotte, D. A.; Carbone, S. P. A review of corrosion failure mechanisms during accelerated tests: Electrolytic metal migration. *Journal of the Electrochemical Society* **1987**, *134*, 175.
- [4] Gabriel, O. E.; Huitink, D. R. Failure Mechanisms Driven Reliability Models for Power Electronics: A Review. *Journal of Electronic Packaging, Transactions of the ASME* **2023**, *145*.
- [5] Ludwig, E. Accelerated corrosion testing of the copper/polyimide system in semiconductor devices. Ph.D. thesis, TU Wien, 2018.
- [6] Herrmann, A.; van Soestbergen, M.; Erich, S. J.; van der Ven, L. G.; Huinink, H. P.; van Driel, W. D.; Mavinkurve, A.; Buyl, F. D.; Adan, O. C. Elucidating the large variation in ion diffusivity of microelectronic packaging materials. *Microelectronics Reliability* **2022**, *136*.
- [7] van Soestbergen, M.; Mavinkurve, A.; Rongen, R. T. H.; Ernst, L. J.; Zhang, G. Q. Modeling electrochemical migration through plastic microelectronics encapsulations. 2009 International Conference on Electronic Packaging Technology and High Density Packaging. 2009; pp 1079–1082.
- [8] Huang, Y.; Jämbeck, J.; Unge, M. Understanding the Ionic Conduction in Dielectric Polymers at High Electric Fields Using Molecular Dynamics Simulations. *ACS Macro Letters* **2017**, *6*, 571–574.
- [9] Varain, L. Electrochemical Investigation and Modeling of Ion-and Water Transport Through Polymer Membranes. Ph.D. thesis, TU Wien, 2022.

- [10] Cao, C.; Yang, M.; Liang, C.; Zhang, D.; Chen, X.; Zhao, X.; Lee, C. C.; Huo, Y. A phase-field model of electrochemical migration for silver-based conductive adhesives. *Electrochimica Acta* **2023**, *471*.
- [11] Ohring, M.; Kasprzak, L. *Reliability and failure of electronic materials and devices*, 2nd ed.; Academic Press, 2015.
- [12] Pecht, M.; Gu, J. Physics-of-failure-based prognostics for electronic products. *Transactions of the Institute of Measurement and Control* **2009**, *31*, 309–322.
- [13] Kuo, W.; Chien, W.-T. K.; Kim, T. *Reliability, yield, and stress burn-in: a unified approach for microelectronics systems manufacturing and software development*; Springer Science and Business Media, 2013.
- [14] Pecht, M.; Dasgupta, A. Physics-of-failure: an approach to reliable product development. *Journal of the IES* **1995**, *38*, 30–34.
- [15] Turbini, L. J. Conductive anodic filament (CAF) formation: an historic perspective. *Circuit World* **2006**, *32*, 19–24.
- [16] Boddy, P. J.; Delaney, R. H.; Lahti, J. N.; Landry, E. F.; Restricks, R. C. Accelerated life testing of flexible printed circuits. 14th International Reliability Physics Symposium. 1976; pp 108–117.
- [17] Zou, L. C.; Hunt, C. A new approach to investigate conductive anodic filament (CAF) formation. *Soldering and Surface Mount Technology* **2015**, *27*, 22–30.
- [18] Suhir, E. Could electronics reliability be predicted, quantified and assured? *Microelectronics Reliability* **2013**, *53*, 925–936.
- [19] Bernstein, J. B.; Bensoussan, A.; Bender, E. *Reliability Prediction for Microelectronics*; John Wiley and Sons, 2024.
- [20] Sinnadurai, N.; TWI, S. M. I.; Kulicke, C. A. A. S.; Pecht, M.; Ieee, F. A critique of the reliability analysis center failure-rate-model for plastic encapsulated microcircuits. *IEEE Transactions on reliability* **1998**, *47*, 110–113.
- [21] Hanif, A.; Yu, Y.; DeVoto, D.; Khan, F. A comprehensive review toward the state-of-the-art in failure and lifetime predictions of power electronic devices. *IEEE Transactions on Power Electronics* **2018**, *34*, 4729–4746.
- [22] Foucher, B.; Boullie, J.; Meslet, B.; Das, D. A review of reliability prediction methods for electronic devices. *Microelectronics reliability* **2002**, *42*, 1155–1162.

- [23] Stansbury, E. E.; Buchanan, R. A. *Fundamentals of electrochemical corrosion*; ASM International, 2000.
- [24] Fontana, M. G. *Corrosion engineering*; McGraw-Hill, 1986.
- [25] Bagotsky, V. S. *Fundamentals of electrochemistry*, 2nd ed.; John Wiley and Sons, 2005.
- [26] Revie, R. W. *Uhlig's corrosion handbook*, 3rd ed.; John Wiley and Sons, Inc., 2011.
- [27] Bellucci, F.; Nicodemo, L.; Monetta, T.; Kloppers, M. J.; Latanision, R. M. A study of corrosion initiation on polyimide coatings. *Corrosion science* **1992**, *33*, 1203–1226.
- [28] Bard, A. J.; Stratmann, M.; Calvo, E. J. *Encyclopedia of electrochemistry. Vol. 2. Interfacial kinetics and mass transport*; 2003; Vol. 2.
- [29] Schmickler, W.; Santos, E. *Interfacial Electrochemistry*, 2nd ed.; 2010.
- [30] Vidal-Iglesias, F. J.; Solla-Gullón, J.; Rodes, A.; Herrero, E.; Aldaz, A. Understanding the Nernst equation and other electrochemical concepts: An easy experimental approach for students. *Journal of Chemical Education* **2012**, *89*, 936–939.
- [31] Vanysek, P. In *CRC handbook of chemistry and physics*, 86th ed.; Lide, D. R., Ed.; Taylor and Francis Group LLC, 2006; Chapter 8, pp 20–29.
- [32] Shumilova, N. A.; Zhutaeva, G. V. In *Encyclopedia of Electrochemistry of the Elements*, 1st ed.; Bard, A. J., Ed.; Marcel Dekker, 1973; Vol. 8; Chapter 1, pp 1–147.
- [33] Revie, R. W.; Uhlig, H. H. *CORROSION AND CORROSION CONTROL: An Introduction to Corrosion Science and Engineering*, 4th ed.; John Wiley and Sons, Inc., 2008.
- [34] Ives, D. J. G.; Rawson, A. E. Copper corrosion: III. electrochemical theory of general corrosion. *Journal of the Electrochemical Society* **1962**, *109*, 458.
- [35] Rossmeisl, J.; Chan, K.; Skulason, E.; Bjorketun, M. E.; Tripkovic, V. On the pH dependence of electrochemical proton transfer barriers. *Catalysis Today* **2016**, *262*, 36–40.
- [36] Liang, Q.; Brocks, G.; Bieberle-Hütter, A. Oxygen evolution reaction (OER) mechanism under alkaline and acidic conditions. *Journal of Physics: Energy* **2021**, *3*.
- [37] Bard, A. J.; Faulkner, L. R. *Electrochemical Methods: Fundamentals and applications*; Wiley New York, 2001; Vol. 2.
- [38] Colburn, A. W.; Levey, K. J.; O'Hare, D.; Macpherson, J. V. Lifting the lid on the potentiostat: a beginner's guide to understanding electrochemical circuitry and practical operation. *Physical Chemistry Chemical Physics* **2021**, *23*, 8100–8117.

- [39] Dickinson, E. J.; Wain, A. J. The Butler-Volmer equation in electrochemical theory: Origins, value, and practical application. *Journal of Electroanalytical Chemistry* **2020**, *872*.
- [40] Crank, J. *The mathematics of diffusion*, 2nd ed.; Oxford University Press, 1975.
- [41] Fick, A. Ueber Diffusion. *Annalen der Physik* **1855**, *170*, 59–86.
- [42] Kerner, R. A.; Rand, B. P. Ionic-Electronic Ambipolar Transport in Metal Halide Perovskites: Can Electronic Conductivity Limit Ionic Diffusion? 2018.
- [43] Schiesser, W. E. *Spline Collocation Methods for Partial Differential Equations*; John Wiley and Sons Inc., 2017; Chapter 7, pp 261–286.
- [44] Coalson, R. D.; Kurnikova, M. G. Poisson-Nernst-Planck theory approach to the calculation of current through biological ion channels. *IEEE Transactions on Nanobioscience* **2005**, *4*, 81–92.
- [45] Zheng, Q.; Wei, G. W. Poisson-Boltzmann-Nernst-Planck model. *Journal of Chemical Physics* **2011**, *134*.
- [46] Maex, R. In *Encyclopedia of Computational Neuroscience*; Jaeger, D., Jung, R., Eds.; Springer New York: New York, NY, 2013; pp 1–7.
- [47] Jonsson, A. *Organic electronics for precise delivery of neurotransmitters*; Linköping University Electronic Press, 2016.
- [48] Einstein, A. Über die von der molekularkinetischen Theorie der Wärme geforderte Bewegung von in ruhenden Flüssigkeiten suspendierten Teilchen. *Annalen der Physik* **1905**, *4*.
- [49] von Smoluchowski, M. Zur kinetischen Theorie der Brownschen Molekular Bewegung und der Suspensionen. *Ann. d. Phys.* **1906**, *21*, 756–780.
- [50] Evangelista, L. R.; Lenzi, E. K.; Barbero, G.; Scarfone, A. M. On the Einstein–Smoluchowski relation in the framework of generalized statistical mechanics. *Physica A: Statistical Mechanics and its Applications* **2024**, *635*, 129491.
- [51] Pellicer, J.; Mafé, S.; Aguilera, V. M. Ionic transport across porous charged membranes and the Goldman constant field assumption. *Berichte der Bunsengesellschaft für physikalische Chemie* **1986**, *90*, 867–872.
- [52] Ciavatta, L.; Ferri, D.; Palombari, R. On the equilibrium $\text{Cu}_{2++} \text{Cu} (s) \leftrightarrow 2\text{Cu}^+$. *Journal of Inorganic and Nuclear Chemistry* **1980**, *42*, 593–598.

- [53] Kruger, J. The Oxide Films Formed on Copper Single Crystal Surfaces in Pure Water: I. Nature of the Films Formed at Room Temperature. *Journal of the Electrochemical Society* **1959**, *106*, 847.
- [54] Feng, Y.; Siow, K.-S.; Teo, W.-K.; Tan, K.-L.; Hsieh, A.-K. Corrosion mechanisms and products of copper in aqueous solutions at various pH values. *Corrosion* **1997**, *53*.
- [55] Feng, Y.; Teo, W.-K.; Siow, K.-S.; Tan, K.-L.; Hsieh, A.-K. The corrosion behaviour of copper in neutral tap water. Part I: corrosion mechanisms. *Corrosion Science* **1996**, *38*, 369–385.
- [56] Bertocci, U.; Turner, D. In *Encyclopedia of Electrochemistry of the Elements*, 1st ed.; Bard, A., Ed.; Marcel Dekker, 1973; Vol. 2; Chapter 6, pp 383–497.
- [57] King, F. Critical review of the literature on the corrosion of copper by water. 2010; www.skb.se.
- [58] Lee, E. L.; Goh, Y. S.; Haseeb, A. S. M. A.; Wong, Y. H.; Sabri, M. F. M.; Low, B. Y. Review—Electrochemical Migration in Electronic Materials: Factors Affecting the Mechanism and Recent Strategies for Inhibition. *Journal of The Electrochemical Society* **2023**, *170*, 021505.
- [59] Zhong, X.; Yu, S.; Chen, L.; Hu, J.; Zhang, Z. Test methods for electrochemical migration: a review. *Journal of Materials Science: Materials in Electronics* **2017**, *28*, 2279–2289.
- [60] Osenbach, J. W. Corrosion-induced degradation of microelectronic devices. *Semiconductor Science and Technology* **1996**, *11*, 155–162.
- [61] Harsanyi, G. Electrochemical Processes Resulting in Migrated Short Failures in Microcircuits. *IEEE TRANSACTIONS ON COMPONENTS, PACKAGING, AND MANUFACTURING TECHNOLOGY-PART A* **1995**, *18*.
- [62] He, X.; Azarian, M. H.; Pecht, M. G. Analysis of the kinetics of electrochemical migration on printed circuit boards using Nernst-Planck transport equation. *Electrochimica Acta* **2014**, *142*, 1–10.
- [63] Lauser, S.; Richter, T.; Vadimas, V.; Ambat, R. Electrochemical impedance spectroscopy (EIS) for monitoring the water load on PCBAs under cycling condensing conditions to predict electrochemical migration under DC loads. Proceedings - Electronic Components and Technology Conference. 2019; pp 515–521.
- [64] Warren, G. W.; Wynblatt, P.; Zamanzadeh, M. The Role of Electrochemical Adsorption on the Reliability Substrates Migration and Moisture of Metallized Ceramic. *Journal of Electronic Materials* **1989**, *18*.

- [65] Hong, M. S.; Kim, J. G. Method for Mitigating Electrochemical Migration on Printed Circuit Boards. *Journal of Electronic Materials* **2019**, *48*, 5012–5017.
- [66] Krumbein, S. J. Metallic Electromigration Phenomena. *IEEE TRANSACTIONS ON COMPONENTS, HYBRIDS, AND MANUFACTURING TECHNOLOGY* **1988**, *11*.
- [67] Song, S. J.; Choi, S. R.; Kim, J. G. The effect of organic additives for the prevention of copper electrochemical migration. *Journal of Electroanalytical Chemistry* **2019**, *832*, 75–86.
- [68] Huth, J. M.; Swinney, H. L.; McCormick, W. D.; Kuhn, A.; Argoul, F. Role of convection in thin-layer electrodeposition. *Physical Review E* **1995**, *51*, 3444.
- [69] Ambat, R. A review of Corrosion and environmental effects on electronics. 2006.
- [70] Jellesen, M. S.; Verdingovas, V.; Conseil, H.; Piotrowska, K.; Ambat, R. Corrosion in electronics: Overview of failures and countermeasures. European Corrosion Congress. 2014.
- [71] Bierwagen, G. P. Reflections on corrosion control by organic coatings. *Progress in Organic Coatings* **1996**, *28*, 43–48.
- [72] Wel, G. K. V. D.; Adan, O. C. G. Moisture in organic coatings - a review. *Progress in Organic Coatings* **1999**, *37*, 1–14.
- [73] Yang, C.; Xing, X.; Li, Z.; Zhang, S. A comprehensive review on water diffusion in polymers focusing on the polymer–metal interface combination. *Polymers* **2020**, *12*, 138.
- [74] Wit, J. H. W. D.; der Weijde, D. H.; Ferrari, G. In *Corrosion Mechanisms in Theory and Practice*, 3rd ed.; Marcus, P., Ed.; CRC Press, 2011; Chapter 20, pp 863–905.
- [75] Dickie, R. A. In *Applied Polymer Science*; Tess, R. W., Poehlein, G. W., Eds.; ACS Publications, 1985; Chapter 32, pp 773–799.
- [76] Maitland, C. C. Factors affecting the electrolytic resistance of polymer films. *Official Digest* **1962**, *34*, 972.
- [77] Iwamoto, M. Transient current across insulating films with long-range movements of charge carriers. *Journal of applied physics* **1996**, *79*, 7936–7943.
- [78] Gilbert, R.; Crine, J.-P.; Noirhomme, B.; Péliou, S. Measurement of organic and inorganic ions in cable insulation and shields. Conference on Electrical Insulation and Dielectric Phenomena., 1989; pp 235–240.

- [79] Hu, J.-M.; Zhang, J.-T.; Zhang, J.-Q.; Cao, C.-N. A novel method for determination of diffusion coefficient of corrosive species in organic coatings by EIS. *Journal of Materials Science* **2004**, *39*, 4475–4479.
- [80] Motta, V.; Schäfer, M.; Noll, F.; Hampp, N.; Weitzel, K.-M. Pathways for Alkali Ion Transport in Mold Compounds. *ECS Journal of Solid State Science and Technology* **2020**, *9*, 053001.
- [81] Mamun, M. A. Z.; Mavinkurve, A.; van Soestbergen, M.; Alam, M. A. Transient Leakage Current as a Non-destructive Probe of Wire-bond Electrochemical Failures. 2023 IEEE International Reliability Physics Symposium (IRPS). 2023; pp 1–7.
- [82] Kinsella, E. M.; Mayne, J. E. O. Ionic conduction in polymer films I. Influence of electrolyte on resistance. *British polymer journal* **1969**, *1*, 173–176.
- [83] Sorensen, P. A.; Kiil, S.; Dam-Johansen, K.; Weinell, C. E. Anticorrosive coatings: A review. *Journal of Coatings Technology and Research* **2009**, *6*, 135–176.
- [84] Mayr, M. Investigation of polymer and copper degradation under corrosive conditions using LIBS and LA-ICP-MS. M.Sc. thesis, TU Wien, 2019.
- [85] Funke, W. Toward a unified view of the mechanism responsible for paint defects by metallic corrosion. *Industrial and Engineering Chemistry Product Research and Development* **1985**, *24*, 343–347.
- [86] Leidheiser, H. J. In *Polymeric Materials for Corrosion Control*; Dickie, R., Floyd, F., Eds.; ACS Publications, 1986; Chapter 12, pp 124–135.
- [87] Croll, S. G. Electrolyte transport in polymer barrier coatings: perspectives from other disciplines. 2018.
- [88] Lyon, S. B.; Bingham, R.; Mills, D. J. Advances in corrosion protection by organic coatings: What we know and what we would like to know. *Progress in Organic Coatings* **2017**, *102*, 2–7.
- [89] Trivedi, R.; Kurz, W. Dendritic growth. *International Materials Reviews* **1994**, *39*, 49–74.
- [90] Barton, J. L.; Bockris, M. The Electrolytic Growth of Dendrites from Ionic Solutions. *Source: Proceedings of the Royal Society of London. Series A, Mathematical and Physical Sciences* **1962**, *268*, 485–505.
- [91] Popov, K. I.; Djukic, L. M.; Pavlovic, M. G.; Maksimovic, M. D. The critical overpotential for copper dendrite formation. *Journal of Applied Electrochemistry* **1979**, *9*, 527–531.

- [92] Popov, K. I.; Pavlovic, M. G. Comparison of the critical conditions for initiation of dendritic growth and powder formation in potentiostatic and galvanostatic copper electrodeposition. *Journal of Applied Electrochemistry* **1982**, *12*, 25–531.
- [93] Mathews, H. I.; de S Mutucumarana, T.; Wilman, H. Orientated crystal growth in electrodeposits, in relation to ionic diffusion in the electrolyte. *Acta Crystallographica* **1961**, *14*, 636–640.
- [94] Nishikawa, K.; Chassaing, E.; Rosso, M. Evolution of the Morphology of Electrodeposited Copper at the Early Stage of Dendritic Growth. *Journal of The Electrochemical Society* **2013**, *160*, D183–D187.
- [95] Chazalviel, J.-N. Electrochemical aspects of the generation of ramified metallic electrodeposits. *Physical Review A* **1990**, *42*, 15.
- [96] Devos, O.; Gabrielli, C.; Beitone, L.; Mace, C.; Ostermann, E.; Perrot, H. Growth of electrolytic copper dendrites. III: Influence of the presence of copper sulphate. *Journal of Electroanalytical Chemistry* **2007**, *606*, 95–102.
- [97] Chazalviel, J.-N.; Rosso, M.; Chassaing, E.; Fleury, V. A quantitative study of gravity-induced convection in two-dimensional parallel electrodeposition cells. *Journal of Electroanalytical Chemistry* **1996**, *407*, 61–73.
- [98] Gonzalez, G.; Rosso, M.; Chassaing, E.; Chazalviel, J.-N. Experimental and theoretical study of the onset of the growth of an irregular metal electrodeposit. *Electrochimica acta* **2007**, *53*, 141–144.
- [99] Marshall, G.; Mocskos, P. Growth model for ramified electrochemical deposition in the presence of diffusion, migration, and electroconvection. *Physical Review E* **1997**, *55*, 549.
- [100] Marshall, G.; Mocskos, P.; Swinney, H. L.; Huth, J. M. Buoyancy and electrically driven convection models in thin-layer electrodeposition. *Physical Review E* **1999**, *59*, 2157.
- [101] Rosso, M.; Chassaing, E.; Chazalviel, J.-N. Role of buoyancy in the onset of dendritic growth in thin layer electrodeposition. *Physical Review E* **1999**, *59*, 3135.
- [102] Dubrovski, O.; Manor, O. Convective mitigation of dendrite growth. *Physical Review Materials* **2021**, *5*.
- [103] Jaafar, M. A.; Rouse, D. R.; Gibout, S.; Bedecarrats, J.-P. A review of dendritic growth during solidification: Mathematical modeling and numerical simulations. *Renewable and Sustainable Energy Reviews* **2017**, *74*, 1064–1079.

- [104] Gharaibeh, A.; Illes, B.; Geczy, A.; Medgyes, B. Numerical Models of the Electrochemical Migration: A short review. 2020 IEEE 26th International symposium for design and technology in electronic packaging (SIITME). 2020; pp 178–183.
- [105] Bumiller, E.; Hillman, C. A review of models for time-to-failure due to metallic migration mechanisms. *DfR Solutions* **2009**,
- [106] Yang, S.; Wu, J.; Christou, A. Initial stage of silver electrochemical migration degradation. *Microelectronics Reliability* **2006**, *46*, 1915–1921.
- [107] Yang, S.; Christou, A. Failure Model for Silver Electrochemical Migration. *IEEE Transactions on Device and Materials Reliability* **2007**, *7*.
- [108] Ma, H.; Kunwar, A.; Chen, J.; Qu, L.; Wang, Y.; Song, X.; Råback, P.; Ma, H.; Zhao, N. Study of electrochemical migration based transport kinetics of metal ions in Sn-9Zn alloy. *Microelectronics Reliability* **2018**, *83*, 198–205.
- [109] Zhou, Y.; Chen, Y.; Xie, Q.; Li, Y. Modeling Research of Electrochemical Migration Failure on Printed Circuit Board. Proceedings - 2018 Prognostics and System Health Management Conference, PHM-Chongqing 2018. 2018; pp 209–214.
- [110] Zhou, Y.; Yang, L.; Li, Y.; Lu, W. Exploring the Data-Driven Modeling Methods for Electrochemical Migration Failure of Printed Circuit Board. Proceedings - 2019 Prognostics and System Health Management Conference, PHM-Paris 2019. 2019; pp 100–105.
- [111] Bhat, D.; Muench, S.; Roellig, M. Application of machine learning algorithms in prognostics and health monitoring of electronic systems: A review. *e-Prime - Advances in Electrical Engineering, Electronics and Energy* **2023**, *4*.
- [112] Illes, B.; Medgyes, B.; Dusek, K.; Busek, D.; Skwarek, A.; Geczy, A. Numerical simulation of electrochemical migration of Cu based on the Nernst-Plank equation. *International Journal of Heat and Mass Transfer* **2022**, *184*.
- [113] Chen, L.; Zhang, H. W.; Liang, L. Y.; Liu, Z.; Qi, Y.; Lu, P.; Chen, J.; Chen, L.-Q. Modulation of dendritic patterns during electrodeposition: A nonlinear phase-field model. *Journal of Power Sources* **2015**, *300*, 376–385.
- [114] Bogert, M. T.; Renshaw, R. R. 4-AMINO-0-PHTHALIC ACID AND SOME OF ITS DERIVATIVES. *Journal of the American Chemical Society* **1908**, *30*, 1135–1144.
- [115] Wilson, D.; Stenzenberger, H. D.; Hergenrother, P. M. *Polyimides*; Springer, 1991.
- [116] Hicyilmaz, A.; Bedeloglu, A. Applications of polyimide coatings: a review. *SN Applied Sciences* **2021**, *3*.

- [117] Ghosh, M. K.; Mittal, K. L. *Polyimides: fundamentals and applications*, 1st ed.; CRC Press, 1996.
- [118] Zha, J.-W.; Dang, Z.-M. *High Temperature Polymer Dielectrics: Fundamentals and Applications in Power Equipment*, 1st ed.; Wiley-VCH GmbH, 2023.
- [119] Raju, G. G. *Dielectrics in electric fields*, 2nd ed.; CRC press, 2017.
- [120] Seo, J.; Cho, K.-Y.; Han, H. Dependence of water sorption in polyimides on the internal linkage in the diamine component. *Polymer degradation and stability* **2001**, *74*, 133–137.
- [121] Seo, J.; Han, H. Water sorption behaviour of polyimide thin films with various internal linkages in the dianhydride component. *Polymer degradation and stability* **2002**, *77*, 477–482.
- [122] Pascault, J.-P.; Williams, R. J. J. In *Handbook of Polymer Synthesis, Characterization, and Processing*; Saldívar-Guerra, E., Vivaldo-Lima, E., Eds.; John Wiley and Sons, Inc., 2013; Chapter 28, pp 519–533, Wiley Online Books.
- [123] Raju, G. G. *Dielectrics in electric fields*, 1st ed.; Marcel Dekker, 2003.
- [124] Duke, B. J.; O’leary, B. The Band Structure of Polymers: Its Calculation and Interpretation Part 1. Foundation. *Journal of Chemical Education* **1988**, *65*, 319–321.
- [125] Duke, B. J.; O’leary, B. The Band Structure of Polymers: Its Calculation and Interpretation Part 2. Calculation. *Journal of Chemical Education* **1988**, *65*, 379–383.
- [126] Duke, B. J.; O’leary, B. The Band Structure of Polymers: Its Calculation and Interpretation Part 3. Interpretation. *Journal of Chemical Education* **1988**, *65*, 513–516.
- [127] Dissado, L. A. L. A.; Fothergill, J. C. J. C. *Electrical degradation and breakdown in polymers*; P. Peregrinus, 1992.
- [128] Jaiswal, M.; Menon, R. Polymer electronic materials: A review of charge transport. *Polymer International* **2006**, *55*, 1371–1384.
- [129] Kao, K. C. Electrical conduction and breakdown in insulating polymers. Proceedings of the 6th International Conference on Properties and Applications of Dielectric Materials (Cat. No. 00CH36347). 2000; pp 1–17.
- [130] Chiu, F. C. A review on conduction mechanisms in dielectric films. *Advances in Materials Science and Engineering* **2014**, 2014.

- [131] Dakin, T. W. Conduction and Polarization Mechanisms and Trends in Dielectrics. *IEEE Electrical Insulation Magazine* **2006**, *22*, 11–28.
- [132] Ahmed, N. H.; Srinivas, N. N. Review of Space Charge Measurements in Dielectrics. *IEEE Transactions on Dielectrics and Electrical Insulation* **1997**, *4*, 644–656.
- [133] Imburgia, A.; Miceli, R.; Sanseverino, E. R.; Romano, P.; Viola, F. Review of space charge measurement systems: Acoustic, thermal and optical methods. *IEEE Transactions on Dielectrics and Electrical Insulation* **2016**, *23*, 3126–3142.
- [134] Montanari, G. C. Bringing an Insulation to Failure: the Role of Space Charge. *IEEE Transactions on Dielectrics and Electrical Insulation* **2011**, *18*, 339–364.
- [135] Li, W.; Li, J.; Wang, X.; Li, S.; Chen, G.; Zhao, J.; Ouyang, B. Physicochemical origin of space charge dynamics for aged XLPE cable insulation. *IEEE Transactions on Dielectrics and Electrical Insulation* **2014**, *21*, 809–820.
- [136] Mizutani, T. Space charge measurement techniques and space charge in polyethylene. *IEEE Transactions on Dielectrics and Electrical Insulation* **1994**, *1*, 923–933.
- [137] Nie, Y.; Yang, L.; Zhao, N.; Min, D.; Li, S. Effect of surface state on DC breakdown of LDPE films. *IEEE Transactions on Dielectrics and Electrical Insulation* **2017**, *24*, 2522–2530.
- [138] Bartnikas, R. Performance Characteristics of Dielectrics in the Presence of Space Charge. *IEEE Transactions on Dielectrics and Electrical Insulation* **1997**, *4*, 544–557.
- [139] Zhang, Y.; Lewiner, J.; Alquie, C.; Hampton, N. Evidence of Strong Correlation Between Space-charge Buildup and Breakdown in Cable Insulation. *IEEE Transactions on Dielectrics and Electrical Insulation* **1996**, *3*, 778–783.
- [140] Anh, T. T.; Berquez, L.; Boudou, L.; Martinez-Vega, J. Effect of trapped space charge on mechanical deformation induced by electric field. *IEEE Transactions on dielectrics and electrical insulation* **2011**, *18*, 1416–1422.
- [141] Tran, T. S.; Tran, A. T.; Nguyen, H. K. Correlation between Space Charge and Induced Mechanical Deformation by DC Electric Field on Electron Irradiated PTFE Thin Film. Conference Proceedings - 2023 IEEE Asia Meeting on Environment and Electrical Engineering, EEE-AM 2023. 2023.
- [142] Jones, J. P.; Llewellyn, J. P.; Lewis, T. J. The Contribution of Field-Induced Morphological Change to the Electrical Aging and Breakdown of Polyethylene. *IEEE Transactions on Dielectrics and Electrical Insulation* **2005**, *12*, 951–966.

- [143] Lewis, T. J.; Llewellyn, J. P.; der Sluijs, M. J. V.; Freestone, J.; Hampton, R. N. A new model for electrical ageing and breakdown in dielectrics. Seventh International Conference on Dielectric Materials, Measurements and Applications (Conf. Publ. No. 430). 1996; pp 220–224.
- [144] Dissado, L. A.; Mazzanti, G.; Montanari, G. C. The Role of Trapped Space Charges in the Electrical Aging of Insulating Materials. *IEEE Transactions on Dielectrics and Electrical Insulation* **1997**, *4*, 496–506.
- [145] Mazzanti, G.; Montanari, G. C.; Dissado, L. A. Electrical Aging and Life Models: The Role of Space Charge. *IEEE Transactions on Dielectrics and Electrical Insulation* **2005**, *12*, 876–890.
- [146] Palit, S.; Varghese, D.; Guo, H.; Krishnan, S.; Alam, M. A. The Role of Dielectric Heating and Effects of Ambient Humidity in the Electrical Breakdown of Polymer Dielectrics. *IEEE Transactions on Device and Materials Reliability* **2015**, *15*, 308–318.
- [147] McPherson, J. W.; Mogul, H. C. Underlying physics of the thermochemical E model in describing low-field time-dependent dielectric breakdown in SiO₂ thin films. *Journal of Applied Physics* **1998**, *84*, 1513–1523.
- [148] Ding, R.; Bowler, N. Permittivity and Electrical Breakdown Response of Nylon 6 to Chemical Exposure. *IEEE Transactions on Dielectrics and Electrical Insulation* **2015**, *22*.
- [149] Ieda, M.; Nagao, M.; Hikita, M. High-field Conduction and Breakdown in Insulating Polymers Present Situation and Future Prospects. *IEEE Transactions on Dielectrics and Electrical Insulation* **1994**, *1*.
- [150] Shen, Z. H.; Wang, J. J.; Jiang, J. Y.; Huang, S. X.; Lin, Y. H.; Nan, C. W.; Chen, L. Q.; Shen, Y. Phase-field modeling and machine learning of electric-thermal-mechanical breakdown of polymer-based dielectrics. *Nature Communications* **2019**, *10*.
- [151] Zuo, Z.; Dissado, L. A.; Yao, C.; Chalashkanov, N. M.; Dodd, S. J.; Gao, Y. Emergent failure patterns at sub-critical fields in polymeric dielectrics. *Journal of Materials Science* **2020**, *55*, 4748–4761.
- [152] Gallier, S.; Plaud, M. Modeling the Breakdown of Dielectrics Loaded With Conducting Particles. *IEEE Transactions on Dielectrics and Electrical Insulation* **2023**, *30*, 709–716.
- [153] Laurent, C.; Teyssedre, G.; Roy, S. L.; Baudoin, F. Charge Dynamics and its Energetic Features in Polymeric Materials. *IEEE Transactions on Dielectrics and Electrical Insulation* **2013**, *20*, 357–381.

- [154] Lewis, T. J. Charge transport, charge injection and breakdown in polymeric insulators. *Journal of Physics D: Applied Physics* **1990**, *23*, 1469.
- [155] Huzayyin, A. Effect of Chemical Impurities on the Solid State Physics of Polyethylene. Ph.D. thesis, University of Toronto, 2011.
- [156] Hao, J.; Zou, R.; Liao, R.; Yang, L.; Liao, Q. New method for shallow and deep trap distribution analysis in oil impregnated insulation paper based on the space charge detrapping. *Energies* **2018**, *11*.
- [157] Teysse, G.; Zheng, F.; Boudou, L.; Laurent, C. Charge trap spectroscopy in polymer dielectrics: A critical review. *Journal of Physics D: Applied Physics* **2021**, *54*.
- [158] Teysse, G.; Laurent, C. Charge transport modeling in insulating polymers: from molecular to macroscopic scale. *IEEE Transactions on Dielectrics and Electrical Insulation* **2005**, *12*, 857–875.
- [159] Sato, K.; Tanaka, Y.; Maeno, T. Study on generation of electro-chemical migration in layered insulating films for flexible printed circuit. 2017 1st International Conference on Electrical Materials and Power Equipment (ICEMPE). 2017; pp 192–197.
- [160] Zhao, L.; Su, J. C.; Liu, C. L. Review of developments on polymers' breakdown characteristics and mechanisms on a nanosecond time scale. *AIP Advances* **2020**, *10*.
- [161] Teysse, G.; Laurent, C. Advances in High-Field Insulating Polymeric Materials Over the Past 50 Years. **2013**, *29*, 26–36.
- [162] Wu, S.-Y.; Denton, D. D. Dielectric Modeling of Polyimide Exposed to Environmental Stress. *IEEE Transactions on Electrical Insulation* **1992**, *27*, 362–373.
- [163] Wu, S.-Y.; Denton, D. D.; Souza-Machado, R. D. Dielectric behavior of O₂/CF₄ plasma etched polyimide exposed to humid environments. *Journal of Vacuum Science and Technology A: Vacuum, Surfaces, and Films* **1993**, *11*, 291–300.
- [164] Du, B. X.; Guo, Y. G. Effects of Surface Fluorination on Dielectric Properties and Surface Charge Behavior of Water Absorbed Polyimide Film. *IEEE Transactions on Dielectrics and Electrical Insulation* **2015**, *22*.
- [165] Tu, N.-R. High field electric conduction in polyimide. M.Sc. thesis, University of Manitoba, 1995.
- [166] Li, Y.; Sun, G.; Zhou, Y.; Liu, G.; Wang, J.; Han, S. Progress in low dielectric polyimide film – A review. *Progress in Organic Coatings* **2022**, *172*.

- [167] Salley, J. M.; Frank, C. W. In *Polyimides: Fundamentals and Applications*, 1st ed.; Ghosh, M., Mittal, K., Eds.; CRC Press, 1996; Chapter 11, pp 279–308.
- [168] Georgiev, A.; Dimov, D.; Spassova, E.; Assa, J.; Dineff, P.; Danev, G. *Chemical and physical properties of polyimides: biomedical and engineering applications*; InTech, 2012.
- [169] Faupel, F.; Willecke, R.; Thran, A. Diffusion of metals in polymers. *Materials Science and Engineering R: Reports* **1998**, *22*, 1–55.
- [170] Tromp, R. M.; Legoues, F.; Ho, P. S. Interdiffusion at the polyimide–Cu interface. *Journal of Vacuum Science and Technology A: Vacuum, Surfaces, and Films* **1985**, *3*, 782–785.
- [171] Neuhaus, H. J.; Day, D. R.; Senturia, S. D. Sodium transport in polyimide-SiO₂ systems. *Journal of electronic materials* **1985**, *14*, 379–404.
- [172] Schussler, A.; Bellucci, F.; Senturia, S. D.; Latanision, R. M. Na⁺ and Cl⁻ transport across polyimide films. *Journal of Applied Polymer Science* **1991**, *42*, 1567–1577.
- [173] Sacher, E. Dielectric Properties of Polyimide Film. II. DC Properties. *IEEE Transactions on Electrical Insulation* **1979**, *14*, 85–93.
- [174] Sacher, E. The determination of trace contaminants in polymers. Conference on Electrical Insulation and Dielectric Phenomena-Annual Report 1980. 1980; pp 131–135.
- [175] Sacher, E. The Determination of Trace Inorganic Contaminants in Polyimides. *IEEE Transactions on Electrical Insulation* **1983**, *4*, 369–373.
- [176] Neuhaus, H. J. Electrical conduction in polyimide. **1989**,
- [177] Beuhler, A. J.; Burgess, M. J.; Fjare, D. E.; Gaudette, J. M.; Roginski, R. T. Moisture and purity in polyimide coatings. *MRS Online Proceedings Library (OPL)* **1989**, *154*, 73.
- [178] Ghosh, S.; Klett, R.; Fink, D.; Dwivedi, K. K.; Vacik, J.; Hnatowicz, V.; Cervena, J. On the penetration of aqueous solutions into pristine and radiation damaged polyimide. *Radiation Physics and Chemistry* **1999**, *55*, 271–284.
- [179] Borrmann, D.; Danzer, A.; Sadowski, G. Generalized Diffusion–Relaxation Model for Solvent Sorption in Polymers. *Industrial and Engineering Chemistry Research* **2021**, *60*, 15766–15781.
- [180] Chia, V. K. F.; Wilkus, T.; Huerta, L.; Rivello, W.; Jew, J.; Li, F.; Gotts, H.; Hsu, I.-H.; Anderson, S. Contamination Troubleshooting for Microelectronics Packaging. 54th International Symposium on Microelectronics. 2021; pp 286–291.

- [181] Willner, J.; Brunnbauer, L.; Larisegger, S.; Nelhiebel, M.; Marchetti-Deschmann, M.; Limbeck, A. A versatile approach for the preparation of matrix-matched standards for LA-ICP-MS analysis – Standard addition by the spraying of liquid standards. *Talanta* **2023**, *256*.
- [182] Willner, J.; Brunnbauer, L.; Quarles, C. D.; Nelhiebel, M.; Larisegger, S.; Limbeck, A. Development of a simultaneous LA-ICP-MS and LIBS method for the investigation of polymer degradation. *Journal of Analytical Atomic Spectrometry* **2023**, *38*, 2028–2037.
- [183] Raju, G. G.; Shaikh, R.; Haq, S. U. Electrical Conduction Processes in Polyimide Films-I. *IEEE Transactions on Dielectrics and Electrical Insulation* **2008**, *15*, 663–670.
- [184] Smith, F. W.; Neuhaus, H. J.; Senturia, S. D.; Feit, Z.; Day, D. R.; Lewis, T. J. Electrical conduction in polyimide between 20 and 350 C. *Journal of electronic materials* **1987**, *16*, 93–106.
- [185] Nevin, J. H.; Summe, G. L. DC conduction mechanisms in thin polyimide films. *Microelectronics Reliability* **1981**, *21*, 699–705.
- [186] Gaur, M. S.; Ramlal,; Tiwari, R. K. Study of trap structure of thermally polarized polyimide. *Journal of Applied Polymer Science* **2012**, *125*, 520–526.
- [187] Vecchio, M. A.; Meddeb, A. B.; Ounaies, Z.; Lanagan, M. T. Conduction through plasma-treated polyimide: analysis of high-field conduction by hopping and Schottky theory. *Journal of materials science* **2019**, *54*, 10548–10559.
- [188] Fan, L.; Tu, Y.; Chen, B.; Yi, C.; Qin, S.; Wang, S. Space charge behavior of polyimide at cryogenic temperatures. *IEEE Transactions on Dielectrics and Electrical Insulation* **2020**, *27*, 891–899.
- [189] Kang, T. K.; Lee, H. G. Reduction of Leakage Current Along Polyimide Layers in Wafer Level Packaging. *Transactions on Electrical and Electronic Materials* **2019**, *20*, 124–131.
- [190] Tu, N. R.; Kao, K. C. High-field electrical conduction in polyimide films. *Journal of applied physics* **1999**, *85*, 7267–7275.
- [191] Akram, S.; Haq, I. U.; Castellon, J.; Nazir, M. T. Examining the Mechanism of Current Conduction at Varying Temperatures in Polyimide Nanocomposite Films. *Energies* **2023**, *16*.
- [192] Guinane, L.; Tofail, S. A. M.; Stenson, B.; O'Malley, J.; Glynn, C.; Geary, S.; Diahm, S. Electric field DC conductivity dependency of polyimide films. *IEEE Transactions on Dielectrics and Electrical Insulation* **2020**, *27*, 1440–1445.

- [193] Kaneko, K.; Ozaki, T.; Nakane, E.; Mizutani, T. Effects of absorbed water on space charge and conduction phenomena in polyimide films. CEIDP'05. 2005 Annual Report Conference on Electrical Insulation and Dielectric Phenomena, 2005. 2005; pp 657–660.
- [194] Bellucci, F.; Khamis, I.; Senturia, S. D.; Latanision, R. M. Moisture effects on the electrical conductivity of kapton polyimide. *Journal of the Electrochemical Society* **1990**, *137*, 1778.
- [195] Li, L.; Bowler, N.; Hondred, P. R.; Kessler, M. R. Statistical Analysis of Electrical Breakdown Behavior of Polyimide Following Degrading Processes. *IEEE Transactions on Dielectrics and Electrical Insulation* **2011**, *18*, 1955–1962.
- [196] Fan, Y.; xiao Yang, R.; Chen, H.; liang Zhang, H. The impact of air relative humidity on corona-resistant polyimide film. Proceedings of 2011 6th International Forum on Strategic Technology. 2011; pp 80–83.
- [197] Kamalov, A. M.; Borisova, M. E. The influence of moisture on charge relaxation in modified polyimide films. *St. Petersburg Polytechnical University Journal: Physics and Mathematics* **2016**, *2*, 188–192.
- [198] Fujita, S.; Kamei, Y. Electrical properties of polyimide with water absorption. Proceedings. 11th International Symposium on Electrets. 2002; pp 275–278.
- [199] Li, S. Z.; Pak, Y. S.; Adamic, K.; Greenbaum, S. G.; Lim, B. S.; Xu, G.; Nowick, A. S. Diffusion and Deuteron Nuclear Magnetic Resonance Study of the Distribution of Water Molecules in Polyimide Films. *J. Electrochem. Soc* **1992**, *139*, 662–667.
- [200] Buncick, M. C.; Denton, D. D. Effects of aging on polyimide: A study of bulk and interface chemistry. *Journal of Applied Polymer Science* **1992**, *46*, 271–280.
- [201] Denton, D. D.; Buncick, M. C.; Pranjoto, H. Effects of process history and aging on the properties of polyimide films. *Journal of Materials Research* **1991**, *6*, 2747–2754.
- [202] Zhou, L. R.; Wu, G. N.; Gao, B.; Zhou, K.; Liu, J.; Cao, K. J.; Zhou, L. J. Study on Charge Transport Mechanism and Space Charge Characteristics of Polyimide Films. *IEEE Transactions on Dielectrics and Electrical Insulation* **2009**, *16*, 1143–1149.
- [203] Fukunaga, K.; Maeno, T. Space charge observation of polyimide films under DC electric fields. Proceedings of the 2004 IEEE International Conference on Solid Dielectrics, 2004. ICSD 2004. 2004; pp 178–181.
- [204] Chen, Y.; Wang, Y.; Wu, J.; Yin, Y. Study on conduction current characteristics of corona-resistant polyimide film before and after thermal aging. 2017 International Symposium on Electrical Insulating Materials (ISEIM). 2017; pp 605–608.

- [205] Wei, Q.; Zheng, F.; Zhang, Y. Measurement of Electric Field Distribution in Thin Polyimide Film. ICD 2022 - IEEE 2022 4th International Conference on Dielectrics, Proceedings. 2022; pp 518–521.
- [206] Tajiri, K.; Muto, H.; Carrasco, F.; Berquez, L.; Marty-Dessus, D.; Locatelli, M.-L.; Diahham, S.; Griseri, V.; Lebey, T.; Teyssedre, G. Electric field enhancements due to space charge in thin polyimide film. 2019 IEEE Conference on Electrical Insulation and Dielectric Phenomena (CEIDP). 2019; pp 781–784.
- [207] Kaneko, K.; Shiomi, R.; Suzuoki, Y.; Mizutani, T.; Shiota, H.; Muto, H. Effects of electrode material on injection and space charge formation in polyimide. 2007 IEEE International Conference on Solid Dielectrics. 2007; pp 518–521.
- [208] Pham, C.-D.; Locatelli, M.-L.; Berquez, L.; Diahham, S.; Teyssedre, G. Space charge distributions in Polyimide thin films determined by FLIMM. 2011 Annual Report Conference on Electrical Insulation and Dielectric Phenomena. 2011; pp 121–124.
- [209] Locatelli, M.-L.; Pham, C.-D.; Diahham, S.; Berquez, L.; Marty-Dessus, D.; Teyssèdre, G. Space charge formation in polyimide films and polyimide/SiO₂ double-layer measured by LIMM. *IEEE Transactions on Dielectrics and Electrical Insulation* **2017**, *24*, 1220–1228.
- [210] Carrasco, F.; Berquez, L.; Tajiri, K.; Muto, H.; Marty-Dessus, D.; Locatelli, M.-L.; Diahham, S.; Griseri, V.; Lebey, T.; Teyssedre, G. Effect of film thickness and electrode material on space charge formation and conductivity in polyimide films. 2019 IEEE International Workshop on Integrated Power Packaging (IWIPP). 2019; pp 102–106.
- [211] Liufu, D.; Kao, K. C. Capacitance transient spectroscopy in metal-insulator-metal systems and its application to the determination of trap parameters in polyimide films. *Journal of Applied Physics* **1999**, *85*, 1089–1094.
- [212] Yue, L.; Wang, X.; Wu, Y.; Cao, J.; Liu, Y.; Sun, C.; Yang, J. Study on evolution of deep charge traps in polyimide irradiated by low-energy protons using photo-stimulated discharge technique. *Journal of Physics D: Applied Physics* **2013**, *46*, 145502.
- [213] He, L. J.; Yang, X.; Niu, H. Q.; Yuan, Z. H.; Li, D. W.; Chen, C. T. Influence of photoconductivity on the study of trap levels in polyimide films by photo-stimulated discharge. *Modern Physics Letters B* **2016**, *30*.
- [214] Ma, P.; Zhang, Y.; Zheng, F.; An, Z.; Lei, Q. Investigation of surface and bulk charge traps of polyimide film by using the photo-stimulated discharge method. *Europhysics Letters* **2015**, *109*, 27006.

- [215] Shen, H.; Wu, J.; Yin, Y. Temperature Effect on Space Charge Behavior of Polyimide Films under DC High Electric Field. 2023 IEEE 4th International Conference on Electrical Materials and Power Equipment, ICEMPE 2023. 2023.
- [216] Takada, T.; Kikuchi, H.; Miyake, H.; Tanaka, Y.; Yoshida, M.; Hayase, Y. Determination of charge-trapping sites in saturated and aromatic polymers by quantum chemical calculation. *IEEE Transactions on Dielectrics and Electrical Insulation* **2015**, *22*, 1240–1249.
- [217] Amiour, N.; Ziari, Z.; Sahli, S. Traps energy distribution in Kapton HN polyimide films through surface potential decay model under humidity conditions. *Journal of Electrostatics* **2021**, *109*.
- [218] Diahm, S.; Zelmat, S.; Locatelli, M.-L.; Dinculescu, S.; Decup, M.; Lebey, T. Dielectric Breakdown of Polyimide Films: Area, Thickness and Temperature Dependence. *IEEE Transactions on Dielectrics and Electrical Insulation* **2010**, *17*, 18–27.
- [219] Hirose, H. A method to estimate the lifetime of solid electrical insulation. *IEEE Transactions on Electrical Insulation* **1987**, 745–753.
- [220] Hikita, M.; Hirose, T.; Ito, Y.; Mizutani, T.; Ieda, M. Investigation of electrical breakdown of polymeric insulating materials using a technique of pre-breakdown current measurements. *Journal of Physics D: Applied Physics* **1990**, *23*, 1515.
- [221] Diahm, S.; Belijar, G.; Locatelli, M. L.; Lebey, T. Filamentary electrical conduction in polyimide films detected by infrared thermography before thermal breakdown. *Applied Physics Letters* **2017**, *110*.
- [222] Min, D.; Li, Y.; Yan, C.; Xie, D.; Li, S.; Wu, Q.; Xing, Z. Thickness-dependent DC electrical breakdown of polyimide modulated by charge transport and molecular displacement. *Polymers* **2018**, *10*.
- [223] Zhang, L.; Zhou, Y.; Mo, Y.; Zhou, Z.; Sha, Y.; Lu, Z.; Cheng, Z. Dielectric property and charge evolution behavior in thermally aged polyimide films. *Polymer Degradation and Stability* **2018**, *156*, 292–300.
- [224] Diahm, S.; Lambkin, P.; O’Sullivan, L.; Chen, B. Intrinsic AC Dielectric Breakdown Strength of Polyimide Films at the Extreme: New Breakthrough Insights on Thickness Dependence. *Advanced Materials Interfaces* **2023**,
- [225] Kishi, Y.; Hashimoto, T.; Miyake, H.; Tanaka, Y.; Takada, T. Breakdown and space charge formation in polyimide film under DC high stress at various temperatures. *Journal of Physics: Conference Series*. 2009.

- [226] Yun, J.; Lee, J. G.; Oh, K.; Kang, K.; Chung, T. D. Aqueous ionic effect on electrochemical breakdown of Si-dielectric–electrolyte interface. *Scientific Reports* **2020**, *10*.
- [227] Ying, C.; Ma, T.; Xu, L.; Rahmani, M. Localized Nanopore Fabrication via Controlled Breakdown. *Nanomaterials* **2022**, *12*.
- [228] Gray, A. L. Solid sample introduction by laser ablation for inductively coupled plasma source mass spectrometry. *The Analyst* **1985**, *110*, 551–556.
- [229] Hill, S. J. *Inductively coupled plasma spectrometry and its applications*; Blackwell Pub, 2006.
- [230] Koch, J.; Günther, D. In *Encyclopedia of Spectroscopy and Spectrometry (Third Edition)*, third edition ed.; Lindon, J. C., Tranter, G. E., Koppenaal, D. W., Eds.; Academic Press: Oxford, 2017; pp 526–532.
- [231] Chew, D.; Drost, K.; Marsh, J. H.; Petrus, J. A. LA-ICP-MS imaging in the geosciences and its applications to geochronology. *Chemical Geology* **2021**, *559*.
- [232] Watling, R. J.; Herbert, H. K.; Abell, I. D. The application of laser ablation-inductively coupled plasma-mass spectrometry (LA-ICP-MS) to the analysis of selected sulphide minerals. *Chemical geology* **1995**, *124*, 67–81.
- [233] Burger, M.; Gundlach-Graham, A.; Allner, S.; Schwarz, G.; Wang, H. A.; Gyr, L.; Burgener, S.; Hattendorf, B.; Grolimund, D.; Günther, D. High-Speed, High-Resolution, Multielemental LA-ICP-TOFMS Imaging: Part II. Critical Evaluation of Quantitative Three-Dimensional Imaging of Major, Minor, and Trace Elements in Geological Samples. *Analytical Chemistry* **2015**, *87*, 8259–8267.
- [234] Brunnbauer, L.; Mayr, M.; Larisegger, S.; Nelhiesel, M.; Pagnin, L.; Wiesinger, R.; Schreiner, M.; Limbeck, A. Combined LA-ICP-MS/LIBS: powerful analytical tools for the investigation of polymer alteration after treatment under corrosive conditions. *Scientific Reports* **2020**, *10*.
- [235] May, T. W.; Wiedmeyer, R. H. A table of polyatomic interferences in ICP-MS. *ATOMIC SPECTROSCOPY-NORWALK CONNECTICUT-* **1998**, *19*, 150–155.
- [236] Jochum, K. P.; Stoll, B. Reference materials for elemental and isotopic analyses by LA-(MC)-ICP-MS: Successes and outstanding needs. *Laser Ablation ICP-MS in the Earth Sciences: Current practices and outstanding issues* **2008**, *40*, 147–168.
- [237] Pearce, N. J. G.; Perkins, W. T.; Abell, I.; Duller, G. A. T.; Fuge, R. Communication. Mineral microanalysis by laser ablation inductively coupled plasma mass spectrometry. *Journal of Analytical Atomic Spectrometry* **1992**, *7*, 53–57.

- [238] Williams, J. G.; Jarvis, K. E. Preliminary assessment of laser ablation inductively coupled plasma mass spectrometry for quantitative multi-element determination in silicates. *Journal of Analytical Atomic Spectrometry* **1993**, *8*, 25–34.
- [239] Jackson, S. E.; Pearson, N. J.; Griffin, W. L.; Belousova, E. A. The application of laser ablation-inductively coupled plasma-mass spectrometry to in situ U–Pb zircon geochronology. *Chemical geology* **2004**, *211*, 47–69.
- [240] Tibi, M.; Heumann, K. G. Isotope dilution mass spectrometry as a calibration method for the analysis of trace elements in powder samples by LA-ICP-MS. *Journal of Analytical Atomic Spectrometry* **2003**, *18*, 1076–1081.
- [241] Lin, J.; Liu, Y.; Yang, Y.; Hu, Z. Calibration and correction of LA-ICP-MS and LA-MC-ICP-MS analyses for element contents and isotopic ratios. *Solid Earth Sciences* **2016**, *1*, 5–27.
- [242] Zheng, L.-N.; Feng, L.-X.; Shi, J.-W.; Chen, H.-Q.; Wang, B.; Wang, M.; Wang, H.-F.; Feng, W.-Y. Single-cell isotope dilution analysis with LA-ICP-MS: a new approach for quantification of nanoparticles in single cells. *Analytical Chemistry* **2020**, *92*, 14339–14345.
- [243] Yang, L.; Sturgeon, R. E.; Mester, Z. Quantitation of trace metals in liquid samples by dried-droplet laser ablation inductively coupled plasma mass spectrometry. *Analytical chemistry* **2005**, *77*, 2971–2977.
- [244] Guo, L.; Li, Q.; Chen, Y.; Zhang, G.; Xu, Y.; Wang, Z. Dried droplet calibration approach for the analysis of inorganic nonmetallic materials by laser ablation-inductively coupled plasma-mass spectrometry. *Journal of Analytical Atomic Spectrometry* **2020**, *35*, 1441–1449.
- [245] Lvovich, V. F. *Impedance spectroscopy: applications to electrochemical and dielectric phenomena*; John Wiley and Sons, 2012.
- [246] Orazem, M. E.; Tribollet, B. *Electrochemical impedance spectroscopy*, 2nd ed.; John Wiley and Sons, 2008; Vol. 1.
- [247] Wang, S.; Zhang, J.; Gharbi, O.; Vivier, V.; Gao, M.; Orazem, M. E. Electrochemical impedance spectroscopy. *Nature Reviews Methods Primers* **2021**, *1*.
- [248] Orazem, M. E.; Agarwal, P.; Garcia-Rubio, L. H. Critical issues associated with interpretation of impedance spectra. *Journal of Electroanalytical Chemistry* **1994**, *378*, 51–62.
- [249] Mansfeld, F. Recording and analysis of AC impedance data for corrosion studies. *Corrosion* **1981**, *37*, 301–307.

- [250] Mansfeld, F.; Kendig, M. W.; Tsai, S. Recording and analysis of AC impedance data for corrosion studies. *Corrosion* **1982**, *38*, 570–580.
- [251] GABRIELLI, C.; KEDDAM, M.; TAKENOUTI, H. In *Corrosion: Aqueous Processes and Passive Films*; SCULLY, J., Ed.; Treatise on Materials Science and Technology; Elsevier, 1983; Vol. 23; pp 395–451.
- [252] Amin, M. A.; Khaled, K. F. Copper corrosion inhibition in O₂-saturated H₂SO₄ solutions. *Corrosion Science* **2010**, *52*, 1194–1204.
- [253] Gerth, L.; Lopicque, F. Importance of surface preparation in electrochemical investigations of the copper system in dilute copper sulfate solutions. *Journal of the Electrochemical Society* **1996**, *143*, 3910.
- [254] Sharifi-Asl, S.; Macdonald, D. D. Investigation of the kinetics and mechanism of the hydrogen evolution reaction on copper. *Journal of The Electrochemical Society* **2013**, *160*, H382–H391.
- [255] Naseer, A.; Khan, A. Electrochemical impedance spectroscopic studies of the passive layer on the surface of copper as a function of potential. *Turkish Journal of Chemistry* **2010**, *34*, 815–824.
- [256] Benzbiria, N.; Zertoubi, M.; Azzi, M. Oxygen reduction reaction kinetics on pure copper in neutral sodium sulfate solution. *SN Applied Sciences* **2020**, *2*, 1–17.
- [257] Loveday, D.; Peterson, P.; Rodgers, B. Evaluation of organic coatings with electrochemical impedance spectroscopy - Part 2: Application of EIS to Coatings. *JCT coatings tech* **2004**, 88–93.
- [258] Loveday, D.; Peterson, P.; Instruments, B. R.-G. Evaluation of organic coatings with electrochemical impedance spectroscopy Part 3: Protocols for Testing Coatings with EIS. *JCT coatings tech* **2005**, 22–27.
- [259] Mansfeld, F. Use of electrochemical impedance spectroscopy for the study of corrosion protection by polymer coatings. *Journal of Applied Electrochemistry* **1995**, *25*, 187–202.
- [260] Akbarinezhad, E.; Faridi, H. R. Different approaches in evaluating organic paint coatings with electrochemical impedance spectroscopy. *Surface Engineering*, 2008; pp 280–286.
- [261] Su, C.; Wu, W.; Li, Z.; Guo, Y. Prediction of film performance by electrochemical impedance spectroscopy. *Corrosion Science* **2015**, *99*, 42–52.

- [262] Margarit-Mattos, I. C. EIS and organic coatings performance: Revisiting some key points. *Electrochimica Acta* **2020**, 354.
- [263] Bongiorno, V.; Michailidou, E.; Curioni, M. Evaluating organic coating performance by EIS: Correlation between long-term EIS measurements and corrosion of the metal substrate. *Materials and Corrosion* **2023**, 75, 156–173.
- [264] Lauser, S.; Eckold, P.; Richter, T.; Verdingovas, V.; Ambat, R. Implementation of electrochemical impedance spectroscopy (EIS) for assessment of humidity induced failure mechanisms on PCBAs. EUROCOR 2018-Applied science with constant awareness. 2018.
- [265] Dizon, A.; Orazem, M. E. On the impedance response of interdigitated electrodes. *Electrochimica Acta* **2019**, 327.
- [266] Dizon, A.; Orazem, M. E. On experimental determination of cell constants for interdigitated electrodes. *Electrochimica Acta* **2020**, 337.
- [267] Huang, V. M.; Wu, S. L.; Orazem, M. E.; Pébre, N.; Tribollet, B.; Vivier, V. Local electrochemical impedance spectroscopy: A review and some recent developments. *Electrochimica Acta* **2011**, 56, 8048–8057.
- [268] Mazlan, N. S.; Ramli, M. M.; Abdullah, M. M.; Halin, D. S.; Isa, S. S.; Talip, L. F.; Darnial, N. S.; Murad, S. A. Interdigitated electrodes as impedance and capacitance biosensors: A review. AIP Conference Proceedings. 2017.
- [269] Logan, D. L. *A first course in the finite element method*; Thomson, 2007; Vol. 4.
- [270] Wang, X.; Shapiro, B.; Smela, E. Development of a model for charge transport in conjugated polymers. *The Journal of Physical Chemistry C* **2009**, 113, 382–401.
- [271] Ganjovi, A.; Khezripour, S. Description of Characteristics of the Charge Transfer within solid Insulating Materials. *Technical and Physical Problems of Engineering* **2014**, 6, 46–55.
- [272] Lawson, W. The effects of design and environmental factors on the reliability of electronic products. **2007**, 1–152.
- [273] Velasco-Velez, J.-J.; Skorupska, K.; Frei, E.; Huang, Y.-C.; Dong, C.-L.; Su, B.-J.; Hsu, C.-J.; Chou, H.-Y.; Chen, J.-M.; Strasser, P. The electro-deposition/dissolution of CuSO₄ aqueous electrolyte investigated by in situ soft X-ray absorption spectroscopy. *The Journal of Physical Chemistry B* **2018**, 122, 780–787.

- [274] Scherzer, M.; Girgsdies, F.; Stotz, E.; Willinger, M.-G.; Frei, E.; Schloegl, R.; Pietsch, U.; Lunkenbein, T. Electrochemical surface oxidation of copper studied by in situ grazing incidence X-ray diffraction. *The Journal of Physical Chemistry C* **2019**, *123*, 13253–13262.
- [275] Quickenden, T. I.; Xu, Q. Toward a reliable value for the diffusion coefficient of cupric ion in aqueous solution. *Journal of the Electrochemical Society* **1996**, *143*, 1248.
- [276] Faupel, F.; Gupta, D.; Silverman, B. D.; Ho, P. S. Direct measurements of Cu diffusion into a polyimide below the glass transition temperature. *Applied Physics Letters* **1989**, *55*, 357–359.
- [277] Ziwei, G.; Daomin, M.; Lingyu, Y.; Yanan, D.; Qingzhou, W.; Shenlong, Z.; Shaorui, Q. Charge Transport and Energy Accumulation Breakdown Probability Distribution Characteristics of Polyimide. *Lecture Notes in Electrical Engineering*. 2023; pp 1089–1107.
- [278] Bockris, J. O.; Enyo, M. Mechanism of electrodeposition and dissolution processes of copper in aqueous solutions. *Transactions of the Faraday Society* **1962**, *58*, 1187–1202.
- [279] Situmorang, R. S.; Seri, O.; Kawai, H. Estimation of exchange current density for hydrogen evolution reaction of copper electrode by using the differentiating polarization method. *Applied Surface Science* **2020**, *505*, 144300.
- [280] Institute, M. H. Concentration and Solubility of H₂. <https://molecularhydrogeninstitute.org/concentration-and-solubility-of-h2/>, 2023; Accessed: June 12, 2024.
- [281] Jaehne, B.; Heinz, G.; Dietrich, W. Measurement of the diffusion coefficients of sparingly soluble gases in water. *Journal of Geophysical Research: Oceans* **1987**, *92*, 10767–10776.
- [282] Keil, P.; Lutzenkirchen-Hecht, D.; Frahm, R. Investigation of room temperature oxidation of Cu in air by Yoneda-XAFS. *AIP conference proceedings*. 2007; pp 490–492.
- [283] Brandt, I. S.; Tumelero, M. A.; Pelegrini, S.; Zangari, G.; Pasa, A. A. Electrodeposition of Cu₂O: growth, properties, and applications. *Journal of Solid State Electrochemistry* **2017**, *21*, 1999–2020.

List of Figures

2.1	Schematic drawing of the bathtub curve. Three different regions can be identified in this curve. In each region a different failure type is dominant: (left) extrinsic failures (a), (mid) intrinsic failures (b), (right) wear-out or aging failures (c) dominate. The linear combination of the three failure types results in the bathtub shaped curve. Adapted from Kuo et al. ¹³ , figure 3.1.	4
2.2	Exemplary schematic of a measurement setup for the determination of the (standard) electrode potential. In the right half-cell, the standard hydrogen electrode is shown. In the left half-cell the Fe Fe ²⁺ electrode is presented. A diaphragm (black dashed line in the center) separates the two half cells. Both half-cells are connected electrically to form an electrochemical cell. Graphic adapted from Marcus ¹ , p. 22.	10
2.3	<i>E</i> _{SHE} (that is <i>E</i> vs. the SHE) vs. pH diagram (Pourbaix diagram) for Cu in aqueous, uncomplexing media at a temperature of 25 °C. Concentration of Cu ²⁺ ions, <i>c</i> _{Cu²⁺} = 0.01 mol L ⁻¹ . The dashed green lines indicate the stability region of water, H ₂ O. Solid lines mark the boundaries at which one species reacts to form another, depending on the change in pH or <i>E</i> _{SHE} . Cu(OH) ₂ is not considered in this diagram. This Pourbaix diagram was created using Spana and Database, which are part of the Windows version of Chemical Equilibrium Diagrams (Java), by KTH (the Royal Institute of Technology at Stockholm).	12
2.4	Schematic drawing of a 3-electrode setup. A CE is introduced into the system. Current is passed between this electrode and the WE. The RE is therefore not under load and retains a constant potential. The potential difference between WE and RE is measured using a high impedance voltmeter. To minimize ohmic drop within the electrolyte, the RE is brought in close contact with the WE. A Luggin capillary is often employed to this end.	14
2.5	Electronic circuit for potentiostatic measurements. The control amplifier part is used to maintain the desired potential difference between the WE and the RE. <i>R</i> _{CE-RE} and <i>R</i> _{RE-WE} represent the ohmic drop in the electrolyte between the respective electrodes, as well as the charge transfer resistance at the electrode/electrolyte interfaces. Adapted from Colburn et al. ³⁸ , Fig. 5(a).	15

2.6	Schematic drawing of the three possible modes of mass transport included in the NP equation (equation (2.31); image adapted from Jonsson ⁴⁷). (left) Diffusion along a concentration gradient, (mid) convection, driven by movement of the medium, and (right) migration, caused by an applied electric field.	20
2.7	Pourbaix diagram for Ag in aqueous media at a temperature of 25 °C. Concentration of Ag ⁺ ions, $c_{Ag^+} = 0.1 \text{ mol L}^{-1}$. The dashed green lines indicate the stability region of water. Solid lines mark the boundaries at which one species reacts to form another, depending on the change in pH or E_{SHE} . This Pourbaix diagram was created using Spana and Database, which are part of the Windows version of Chemical Equilibrium Diagrams (Java), by KTH (the Royal Institute of Technology at Stockholm).	24
2.8	Exemplary image of dendrites grown from a CuSO ₄ electrolyte.	28
2.9	General chemical structure of PI (structure drawn using ChemDraw®).	31
2.10	Schematic drawing of energy band structure with two trap levels, one for e ⁻ and one for h ⁺	32
2.11	Schematic drawing of an LA-ICP-MS system.	41
2.12	Exemplary electrical equivalent circuit (parallel RC circuit). (left) At high frequencies, the capacitor is quickly charged with alternating polarity and acts like an electric short. (mid) At intermediate f (at the characteristic frequency $(2\pi RC)^{-1}$), charge flow through the capacitor starts to be impeded. The current flow is split up equally between R and C. (right) At low f, charge separation occurs and the capacitor acts like an insulator. Current flows through the resistor.	45
2.13	Simulated result of a (left) Nyquist plot, that is a plot with $Im(Z)$ vs. $Re(Z)$ and (right) the Bode plot, with (top) the logarithm of $ Z $ and (bot) the phase angle shift, Θ versus the logarithm of the frequency of the applied voltage signal. The inset in the left graph shows the used equivalent circuit and the chosen input parameters for the simulation. The graphic was created using ZView® software from Scribner.	46
3.1	(left) Schematic top view of the Thin Layer Cell. (right) Schematic, exploded side view of the TLC. a) glass plates, b) Cu plates, c) double-sided tape, d) electrolyte volume, e) RE, f) silicone gel cover.	48

3.2	Manufacturing steps of the reference electrode. a) Used glass capillary, b) drawing of fine tips, c) resulting capillaries with fine tips, d) filling of the μ Capillary by drawing up a Nafion™ solution, e) evaporation of the solvent at 60 °C in a drying chamber, f) filling of the μ Capillary with a saturated KCl solution, g) filled μ Capillary, h) a anodization of a Ag wire, i) finalized μ Capillary: the anodized Ag wire is inserted in the μ Capillary, parafilm® is used for sealing.	50
3.3	(a) MTC mounted on ceramic package, without epoxy protecting layer. The bond wires leading from the sample to the lead frame can faintly be made out. (b) MTC on ceramic package, with epoxy protecting layer. (c) Top view of the MTC.	52
3.4	(left) Panoramic micrograph of an ITC sample (x50 magnification). (right) Microscope image of a section of the sample including dimensions (x100 magnification).	54
3.5	Schematic cross section of the used test chip. Sizes are not to scale. The cross section shows the substrate (grey), with the Cu comb fingers (orange) and a PI protection layer (yellow) on top.	54
3.6	(left) Schematic of the cell used for the 1x1 Interdigitated Test Chip experiments. (right) Images of the (top) upper side and the (bottom) underside of the top component of the cell. a) contacting pin with spring, b) CE, c) electrolyte volume, d) screw for fixation, e) sample position, f) O-ring for leak-tightness.	55
3.7	(left) Fully assembled ITC cell with contacted clamps. (right) Image of the rubber stopper with metal coil.	56
3.8	Schematics of the ablation patterns used for Laser Ablation measurements. (a) Cross section illustrating a line scan ablation pattern. A total of 20 layers was ablated along the same line per line scan, highlighted in red. (b) Top view of the sample, indicating both a line scan triplet (one pattern above a biased electrode finger, one between the combs, and one above an unbiased finger), and an area that was ablated for imaging. The denomination 'unbiased' and the minus sign on the IDE indicate the polarity of the respective comb side during the electrical stress tests that were performed prior to LA-ICP-MS analysis. (c) Pseudo-3D representation of the imaged part of the sample, with the three ablated layers indicated in red.	59

3.9	(left) Schematic cross-section of the TLC used in the simulation model. The geometry is not to scale. In the model, the RE is implemented as a point node, CE and WE as boundary nodes. (right) Representation of the electric circuit model that was used for implementation of potentiostatic control via the RE in the simulation model. The electric circuit was drawn using LTspice XVII(x64), version 17.0.37.0, by Analog Devices, Inc.	63
3.10	Sketch of the 1D model used for simulation of ITC experiments. Descriptions of the boundaries and domains are given in the colored boxes. Initial values and values to be fitted ('adaptable') are given.	64
4.1	TLC results with pseudo RE. Different electrolytes and voltages were used, as given in the legend. The CuSO_4 samples were dissolved in 10^{-4} M H_2SO_4 . (left) Double logarithmic current density-vs-time for the given electrolyte and applied bias. (right) Cell voltage-vs-time for the given electrolyte and applied bias. A logarithmic x-axis was chosen.	67
4.2	Exemplary images during the electrochemical experiment with the TLC with pseudo RE. Cathode and anode side are denoted with + and - symbols, respectively. Different electrolytes and voltages were used. The CuSO_4 samples were dissolved in 10^{-4} M H_2SO_4 . Information for (a-f) is in the format electrolyte concentration, applied voltage. (a) Deionized water, -0.3 V, (b) 10^{-2} M H_2SO_4 , -0.3 V, (c) 10^{-4} M H_2SO_4 , -0.3 V, (d) 10^{-2} M CuSO_4 , -0.3 V, (e) 10^{-3} M CuSO_4 , -0.3 V, (f) 10^{-2} M CuSO_4 , -1.0 V.	69
4.3	TLC results with Ag AgCl RE. Different electrolyte concentrations were used, as given in the legend. -0.3 V were set between the WE and RE. The CuSO_4 samples were dissolved in H_2O . (left) Double logarithmic current density-vs-time for the stated electrolyte concentration. (right) Cell voltage-vs-time for the given electrolyte concentration. A logarithmic x-axis was chosen.	69
4.4	TLC images of the cathodically polarized side. Three different CuSO_4 concentrations at two different times during the electrochemical experiment are depicted. -0.3 V were set between the WE and Ag AgCl RE. The CuSO_4 was dissolved in deionized H_2O . (a) 0.1 M, at the beginning of the measurement. (b) 0.1 M, 1 h after initiating the measurement. (c) 0.05 M, at $t = 0$ h. (d) 0.05 M, 1 h after beginning the measurement. (e) 0.01 M, at the beginning of the measurement. (f) 0.01 M, after stressing for 1 h.	70
4.5	Capacitance versus cycle number (bottom x-axis) or versus time (top x-axis) for different CuSO_4 concentrations, as indicated in the legend. (left) Logarithmic y-axis. (right) Linear y-axis. Only a section of the left hand diagram is shown.	71

4.6	Comparison of experimental and simulated TLC results with -0.3 V vs. Ag AgCl RE. (top) current density-versus-time. (bottom) Cell voltage-versus-time.	73
4.7	Bode plots obtained from EIS measurements on the open MTC. The applied CuSO_4 concentration is indicated in the legend. (left) Measurements performed on the <i>cm</i> structure. (right) Measurements performed on the <i>bd3</i> structure.	74
4.8	Exemplary microscopic images depicting the observed corrosion phenomena after electrical stress tests at selected MTC structures. (a) <i>cm</i> structure: 0.5 V bias, 10^{-2} mol L $^{-1}$ CuSO_4 (in 10^{-4} mol L $^{-1}$ H_2SO_4) solution dropped on the sample surface. (b) <i>cm</i> structure: 0.5 V bias, 10^{-4} mol L $^{-1}$ CuSO_4 (in 10^{-4} mol L $^{-1}$ H_2SO_4). (c) <i>cm</i> structure: 1 V bias, 10^{-4} mol L $^{-1}$ $\text{CuSO}_{4(\text{aq})}$. (d) <i>cm</i> structure: 1 V bias, 5×10^{-6} mol L $^{-1}$ $\text{CuSO}_{4(\text{aq})}$ (in ultra-pure water). (e) <i>bd1</i> structure: same conditions as (b) . (f) <i>bd2</i> structure: same conditions as (c) . (g) <i>bd3</i> structure: same conditions as (c) . (h) <i>bd2</i> structure: same conditions as (d) . (i) <i>bd4</i> structure: same conditions as (d)	76
4.9	Exemplary short circuits near the bond pads on the MTC. (left) Ag deposit and filaments observed after application of 20 V for seven days with 0.1 mol L $^{-1}$ AgNO_3 . (right) Dendrites observed after application of 100 V for 19 days.	77
4.10	Two independent open circuit current versus time measurement results. Both electrodes were connected, but no electrolyte was filled into the cell electrolyte volume, leaving an air gap between the two electrodes. (left) Original and (right) smoothed (adjacent average, window width = 200) measurement signal.	78
4.11	Bode plot of typical EIS results (EIS type A) after subjecting the samples to the given stress conditions for the given time span. (top) Absolute value of the impedance versus frequency. The inset magnifies a part of the given spectrum. (bottom) Phase angle versus frequency.	79
4.12	Electric equivalent circuit used for fitting the impedance data obtained during the ITC experiments. The circuit was drawn using ZView®, version 3.5g, by Scribner Associates, Inc.	80

- 4.13 Box chart diagrams depicting the fitted values for C_{sample} . Underlying data points for the individual box plots are shown to the right of the corresponding boxes. Samples are categorized in 5 groups. (1) 'As received': The cell was assembled, but no electrolyte had been added. (2) 'Wet 0h': The sample was measured within the first hour after addition of the electrolyte to the cell. (3) 'Soaked': Samples were left standing with electrolyte on top for 24 or 48 h. (4) 'Treated': In addition to the electrolyte the samples were biased at 550 V for 5, 10 or 20 h. (5) 'Treated BD': Samples were measured after the failure criterion had been reached. **(left)** Results from EIS type A experiments. **(right)** Results from EIS type B experiments. 80
- 4.14 Revised electrical equivalent circuits used for evaluating the impedance data obtained during the ITC experiments. Circuits were drawn using ZView®, version 3.5g, by Scribner Associates, Inc. 81
- 4.15 Schematic cross sections of the cell for different conditions and experimental setups. Expected bulk resistances and capacitances are included. Cross sections **(a-c)** represent EIS type A, and the cross section in **(d)** corresponds to EIS type B experiments. **(a)** Schematic for 'as received' experiments. Since no electrolyte is present, a very high resistance is observed in the (air filled) electrolyte volume and the conduction paths leading orthogonally through the PI layer are eliminated. The impedance signal is dominated by the substrate, and in part by the polymer. **(b)** Schematic for 'wet 0h'/'soaked'/'treated' experiments. The presence of a low resistance electrolyte opens up a new conduction path via the electrolyte. **(c)** Schematic for 'treated BD' experiments. BD of the electrical insulation results in a low resistance pathway along the failed IDE side (cathode in the i-t measurements). This renders the influence of this comb side negligible. **(d)** Schematic for 'wet 0h'/'soaked'/'treated' EIS experiments (type B). Two conduction paths are formed. One through the electrolyte, across the polymer, and directly to the connected IDE side. The other, indirect path first leads through the electrolyte and across the polymer as well, but is then indirectly coupled via the disconnected IDE side, via the substrate or polymer layer. 83
- 4.16 Current density-versus-time relationship obtained for experiments with a $\text{Cu}(\text{NO}_3)_2(\text{aq})$ electrolyte at 550 V bias. The samples are grouped based on the duration of the electric stress tests. Samples in the same group use the same colors and markers. **(top)** Both axes are given in a linear scale. **(bottom)** A logarithmic x-axis is used. 84

4.17	<p>LA-ICP-MS images of ITC samples. Each image consists of three ablated layers. L1 to L3 denominate the ablation passes, where L1 is the topmost layer. A schematic illustration is shown in figure 3.8. (a) LA-ICP-MS image of a sample that was electrically stressed until BD, with a $\text{Cu}(\text{NO}_3)_{2(\text{aq})}$ electrolyte on top of the sample. The colors represent the measured ^{63}Cu signal normalized to ^{13}C. The denomination 'unbiased' and the minus sign on the IDE indicate the polarity of the respective comb side during the electrical stress tests that were performed prior to LA-ICP-MS analysis. The inset in the bottom right of this graph shows an overlaid optical micrograph. (b) LA-ICP-MS image of an untreated, 'as received' sample. The colors represent the measured ^{63}Cu signal normalized to ^{13}C.</p>	86
4.18	<p>Weibull plot and calculated values based on the TTF obtained for the electrical stress tests with $\text{Cu}(\text{NO}_3)_{2(\text{aq})}$ electrolyte.</p>	87
4.19	<p>Current density-versus-time relationship obtained for experiments with a $\text{AgNO}_3(\text{aq})$ electrolyte at 550 V bias. The samples are grouped based on the duration of the electric stress tests. Samples in the same group use the same colors and markers. (top) Both axes are given in a linear scale. (bottom) A logarithmic x-axis is used.</p>	88
4.20	<p>Current density-versus-time relationship obtained for the first 0.5 h of experiments with a $\text{AgNO}_3(\text{aq})$ electrolyte (red stars) and $\text{Cu}(\text{NO}_3)_{2(\text{aq})}$ electrolyte (blue circles) at 550 V bias. The samples are grouped based on the type of electrolyte that was used. Samples in the same group use the same colors and markers. (left) Both axes are given in a linear scale. (right) A logarithmic x-axis is used.</p>	90
4.21	<p>LA-ICP-MS depth profiles of ITC samples, determined as per section 3.4. Samples are grouped based on the type of stress they were exposed to. LA-ICP-MS depth profiles obtained from measurements (a) above the IDE side that was left unbiased during the electrical stress test, (b) in the gap between treated and untreated IDE fingers, and (c) above the IDE side that was biased during the electrical stress test. (d) A concentration range (indicated by the grey connecting lines) of (c) is magnified. The BD samples are not grouped. Instead they can be distinguished. Their t_{BD} is given in the legend.</p>	91
4.22	<p>Weibull plot and calculated values based on the TTF obtained for the electrical stress tests with $\text{AgNO}_3(\text{aq})$ electrolyte.</p>	94

4.23	Microscopic images of ITC samples after BD of the PI insulation film. (a) Overview of the ITC sample that failed after 1.2 h due to mechanical damage. The damage is visible in the top left, in the form of a scratch that reflects light differently than the rest of the protection layer, and is also partially highlighted in the blue box. In the blue inset, a metal deposit is seen, indicating the location at which BD occurred. (b) Further magnification of the BD location, as indicated by the blue inset in (a) . (c, d) BD sites of two more samples.	96
4.24	Current density-versus-time relationship obtained for experiments with a $\text{KNO}_{3(\text{aq})}$ electrolyte at 550 V bias. The samples are grouped based on the duration of the electric stress tests. Samples in the same group use the same colors and markers. (top) Both axes are given in a linear scale. (bottom) A logarithmic x-axis is used.	98
4.25	LA-ICP-MS depth profiles of ITC samples exposed to $\text{KNO}_{3(\text{aq})}$, determined as per section 3.4. Samples are grouped based on the undergone treatment. LA-ICP-MS depth profiles were obtained from measurements above the IDE side that was biased during the electrical stress test.	99
4.26	Weibull plot and calculated statistical parameters based on the TTF obtained for the electrical stress tests with $\text{KNO}_{3(\text{aq})}$ electrolyte.	101
4.27	Comparison of ITC experimental data ($\text{Cu}(\text{NO}_3)_{2(\text{aq})}$) and simulation results. (top) current density-versus-time curves. For better clarity only selected experimental curves are given (colored *). The simulated curve is shown in blue. (bottom) Simulated LA-ICP-MS profiles after different stress test times. The graph in pink was obtained for 24 h simulation without application of bias. No experimental data of this type is available for comparison.	102
4.28	Comparison of ITC experimental data ($\text{AgNO}_{3(\text{aq})}$) and simulation results. (top) current density-versus-time curves. Selected experimental curves (colored *) and the simulated curve (blue line) are depicted. (bottom) LA-ICP-MS profiles. Selected experimental curves are shown (colored scatter plots). The simulated curves obtained after the same time are shown as line plots, using the same colors as for the experimental curves. The pink graphs were obtained for 24 h soaked samples without application of bias.	107

4.29	Comparison of ITC experimental data ($\text{KNO}_{3(\text{aq})}$) and simulation results. (top) current density-versus-time curves. Only selected experimental curves are given (colored *), along with the simulated curve (blue line). (bottom) LA-ICP-MS profiles. Again, only selected experimental curves are given (colored scatter plots). The simulated curves obtained after the same time are shown as line plots. The same colors are used both for experiment and simulation after the same stress duration. The graphs in pink were obtained for 24 h soaked samples without application of bias.	108
5.1	Calibration curve obtained for LA-ICP-MS measurements of Ag.	151
5.2	Exemplary depth profiles obtained from LA-ICP-MS line scans above an IDE finger of an ITC sample. Each 'peak' corresponds to one ablated layer. (a) Depth profile obtained from an 'as-received' sample (i.e. untreated). (b) Magnification of a single ablated layer of the untreated sample. (Highlighted yellow area in (a)). (c) Depth profile obtained from a sample that was biased at 550 V until BD (i.e. treated). The line scan pattern was placed above an IDE finger that had served as cathode during the electrical stress test. (d) Magnification of a single ablated layer of the treated sample. (Highlighted in yellow in (c)).	153

List of Abbreviations

TLC	Thin Layer Cell
ECM	electrochemical migration
NP	Nernst-Planck
NPP	Nernst-Planck-Poisson
ITC	1x1 Interdigitated Test Chip
MTC	Miniaturized Test Chip
LA-ICP-MS	Laser Ablation - Inductively Coupled Plasma - Mass Spectrometry
LA	Laser Ablation
ICP	Inductively Coupled Plasma
MS	Mass Spectrometry
EIS	Electrochemical Impedance Spectroscopy
i-t	current density-versus-time
Ag	silver
Cu	copper
Ar	argon
He	helium
RH	relative humidity
OC	organic coating
RE	reference electrode
WE	working electrode
CE	counter electrode
IDE	interdigitated electrode
PI	polyimide
K	potassium
Q	quadrupole

OC	organic coating
BD	breakdown
FEM	finite element method
TCD	tertiary current distribution
e⁻	electrons
h⁺	electron holes
SMU	source measure unit
SHE	standard hydrogen electrode
BV	Butler-Volmer
AC	alternating current
DL	double layer
HER	hydrogen evolution reaction
PoF	physics of failure
OER	oxygen evolution reaction
CAF	conductive anodic filament
THB	thermal humidity bias
WD	water drop
TEL	thin electrolyte layer
DUT	device under test
TTF	time-to-failure
MIS	Metal-Insulator-Semiconductor
MIM	Metal-Insulator-Metal
OCP	open-circuit potential
<i>cm</i>	comb-meander

Appendix

TABLE 5.1: Electrochemical Impedance Spectroscopy parameters for ITC measurements

Parameter	Value	Parameter	Value
Perturbation amplitude	1 V	Integration cycles	5
Start frequency	1E5 Hz	Measurement cycles	2
End frequency	0.05 Hz	Wave form	Sine

TABLE 5.2: Electrochemical Impedance Spectroscopy parameters for TLC and MTC measurements

Parameter	Value	Parameter	Value
Perturbation amplitude	0.01 V	Integration cycles	5
Start frequency	1E5 Hz	Measurement cycles	2
End frequency	0.05 Hz	Wave form	Sine

TABLE 5.3: Frequency ranges and current amplification

Frequency / Hz	Current amplification / $V A^{-1}$
> 1500	5
1500 - 250	6
250 - 2.5	7
2.5 - 0.2	8
0.2 - 0.05	9

TABLE 5.4: Laser Ablation Measurement Parameters

Parameter	Value	Parameter	Value
Spot size	20 μm	Repetition rate	80 Hz
Shape	Rectangular	Overlap	0 μm
Laser energy	10%	Number of passes	20
Warm up	1 s		

TABLE 5.5: Theoretical and practical concentrations of solution standards and stock solutions

Theory	c_{Stock} / ppm	v_{Stock} / mL	c_{Std}	v_{Std}	v_{PEG10000}	v_{IP30}
	1000	5	500	10	5	0
	1000	0.5	50	10	5	4.5
	10	5	5	10	5	0
	10	0.5	0.5	10	5	4.5
Actual	983	4.971	500.5	9.768	4.797	0
	1004	0.498	50.9	9.806	4.812	4.496
	10	4.917	4.8	9.732	4.816	0
	10	0.498	0.5	9.842	4.856	4.488
Stock solution: AgNO₃ dissolved in 30 vol-% Isopropanol (IP30)						
M(AgNO ₃)	169.873 g/mol		w%: 0.63			
M(Ag)	107.868 g/mol		1/w%: 1.57			
Theory: 15.8 mg AgNO ₃ filled up to 10g with IP30 to obtain 1000 ppm ($\mu\text{g/g}$)						
Stock	$m(\text{AgNO}_3)_{\text{th}}$	$m_{\text{tot,th}}$	$c(\text{Ag}^+)_{\text{th}}$	$m(\text{AgNO}_3)_{\text{pr}}$	$m_{\text{tot,pr}}$	$c(\text{Ag}^+)_{\text{pr}}$ / ppm
Stock1	15.5 mg	10 g	1E-3 g/g	15.5 mg	10.009 g	983
Stock2	15.8 mg	10 g	1E-3 g/g	15.8 mg	9.996 g	1004
Stock1/100*	100 mg	10 g	1E-5 g/g	96.9 mg	10.004 g	10

*for the 5 ppm and 0.5 ppm standards, the Stock1 solution was diluted 1/100 with 30% Isopropanol

TABLE 5.6: Data for the calibration curve and extracted values. The linear fit was forced through the origin (i.e. $d = 0$).

c_{STD}	$^{107}\text{Ag}/^{13}\text{C}$ mean	Corr. factor (^{151}Eu)	$^{107}\text{Ag}/^{13}\text{C}$ (Eu corr.)	$c_{STD_corr}(\text{Eu}, cf)$
0.4822	0.0146	1.3903	0.0204	3.8971
0.4822	0.0139	1.1439	0.0159	3.8971
0.4822	0.0189	0.9831	0.0186	3.8971
4.8121	0.1999	1.2661	0.2530	38.8866
4.8121	0.1992	1.2837	0.2557	38.8866
4.8121	0.1879	1.3642	0.2563	38.8866
50.9230	2.8251	0.9883	2.7920	411.5126
50.9230	2.8072	0.9398	2.6384	411.5126
50.9230	3.2030	0.8617	2.7600	411.5126
500.4600	30.1411	0.8169	24.6234	4044.2577
500.4600	28.2408	0.8397	23.7151	4044.2577
500.4600	34.3528	0.6962	23.9179	4044.2577
Correction factor polymer mass (cf), according to equation (3.4)			8.1	
Calibration	k	0.0060	R^2	0.9994

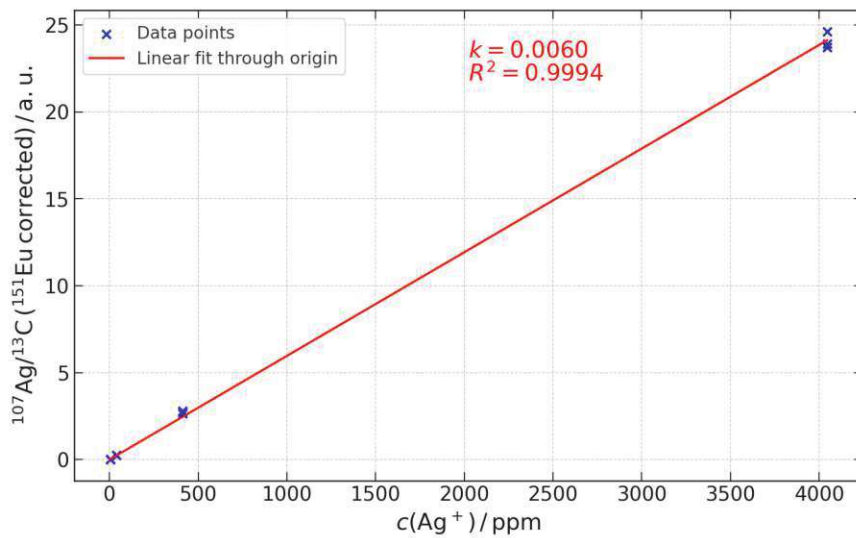


FIGURE 5.1: Calibration curve obtained for LA-ICP-MS measurements of Ag.

TABLE 5.7: Parameters and descriptions used for the TLC simulation. 'est.' means the value was estimated, 'var.' that the value was variable, 'exp.' was defined by the experiment.

Parameter	Value	Description	Source
A_ode	$4.25 \times 10^{-6} \text{ m}^2$	electrode surface area	exp.
ATC_Cu2p	1.45	anodic transfer coefficient (Cu Cu ²⁺)	est. ²⁷⁸
ATC_H2	0.55	anodic transfer coefficient (HER)	279
c_cu2plus_ref	var. mol m ⁻³	Cu ²⁺ initial concentration	exp.
C_dl	1 F m ⁻²	double layer capacitance	est.
c_H2_ini	$4.33 \times 10^{-4} \text{ mol m}^{-3}$	H ₂ initial concentration	280
c_SO4_2m_ini	var. mol m ⁻³	SO ₄ ²⁻ initial concentration	exp.
D_cu2plus	$4.28 \times 10^{-10} \text{ m}^2 \text{ s}^{-1}$	Cu ²⁺ diffusion coefficient	275
D_cuplus	$1.38 \times 10^{-9} \text{ m}^2 \text{ s}^{-1}$	Cu ⁺ diffusion coefficient	est.
D_H2	$5.11 \times 10^{-9} \text{ m}^2 \text{ s}^{-1}$	H ₂ diffusion coefficient (aq)	281
D_Hpos	$9.3 \times 10^{-9} \text{ m}^2 \text{ s}^{-1}$	H ⁺ diffusion coefficient	COMSOL
D_OHneg	$5.3 \times 10^{-9} \text{ m}^2 \text{ s}^{-1}$	OH ⁻ diffusion coefficient	COMSOL
d_REWE	$5 \times 10^{-5} \text{ m}$	distance between RE and WE	-
D_SO4_2m	$1.07 \times 10^{-9} \text{ m}^2 \text{ s}^{-1}$	SO ₄ ²⁻ diffusion coefficient	275
Eeq_Cu2O_red	0.471 V	equilibrium potential, Cu ₂ O reduction	56
Eeq_Cu2O_ox	0.203 V	equilibrium potential, Cu ²⁺ formation from Cu ₂ O	56
Eeq_cu	0.34 V	equilibrium potential, Cu Cu ²⁺	56
gain	1.00×10^6	voltage controlled voltage source gain	-
Height	$3.1 \times 10^{-4} \text{ m}$	height of electrolyte (Cu + 2*tape)	-
i0_cu	8 A m^{-2}	Exchange current density, Cu surface	253
i0_Cu2O	3.5 A m^{-2}	exchange current density (Cu ₂ O formation)	est.
i0_Cu2OCu2p	1 A m^{-2}	exchange current density (Cu ₂ O oxidation)	est.
i0_H2	0.07 A m^{-2}	exchange current density (HER)	279
Keq_DisprCu	5.6×10^{-7}	equilibrium constant (Cu ²⁺ + Cu(s) ↔ Cu ⁺)	56
L	$1.7 \times 10^{-4} \text{ m}$	height of the Cu plate	exp.
length	0.025 m	length of the Cu plate	exp.
molar_mass_cu	$0.06355 \text{ kg mol}^{-1}$	copper molar mass	-
pH_init	5.5	initial pH value	-
rho_cu2o	6000 kg m^{-3}	Cu ₂ O density	-
s0	$3 \times 10^{-9} \text{ m}$	initial Cu ₂ O layer thickness, anode	est. ²⁸²
sigma_cu2O	$8 \times 10^{-7} \text{ S m}^{-1}$	electrical conductivity Cu ₂ O	283
V_ext	-0.1 V	external electric potential (vs. SHE)	exp.
width	0.005 m	electrode gap (= electrolyte width)	exp.
z_Cu1p	1	charge number (Cu ²⁺)	-
z_Cu2p	2	charge number (Cu ⁺)	-
z_SO42m	-2	charge number (SO ₄ ²⁻)	-

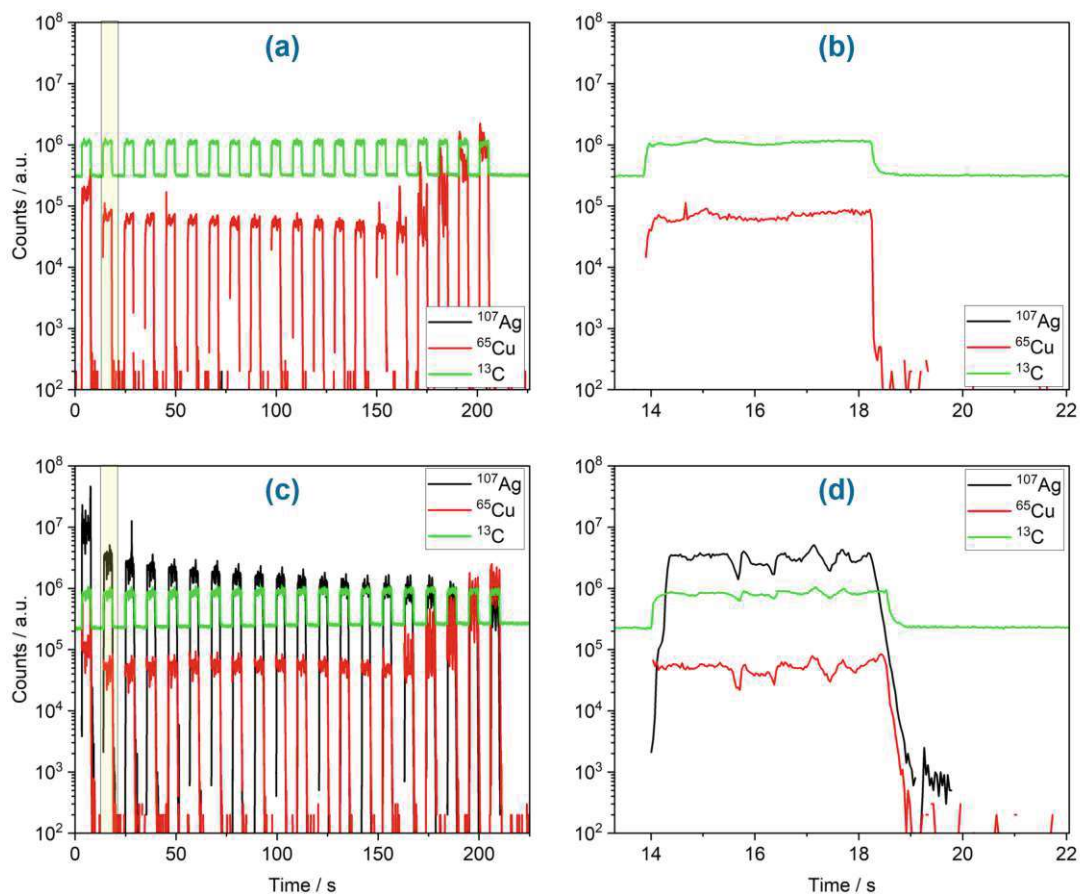


FIGURE 5.2: Exemplary depth profiles obtained from LA-ICP-MS line scans above an IDE finger of an ITC sample. Each 'peak' corresponds to one ablated layer. **(a)** Depth profile obtained from an 'as-received' sample (i.e. untreated). **(b)** Magnification of a single ablated layer of the untreated sample. (Highlighted yellow area in **(a)**). **(c)** Depth profile obtained from a sample that was biased at 550 V until BD (i.e. treated). The line scan pattern was placed above an IDE finger that had served as cathode during the electrical stress test. **(d)** Magnification of a single ablated layer of the treated sample. (Highlighted in yellow in **(c)**).

TABLE 5.8: Collection of measured TTFs for all three electrolytes used in ITC experiments.

Electrolyte	No. of BD samples	TTF (h)
$\text{Cu}(\text{NO}_3)_2(\text{aq})$	6	112.6, 110.9, 63.5, 36.0, 69.4, 66.2
$\text{AgNO}_3(\text{aq})$	7	5.2, 11.4, 20.8, 20.7, 18.3, 20.6, 9.1
$\text{KNO}_3(\text{aq})$	4	61.7, 77.5, 85.1, 156.2